UNIVERSIDADE FEDERAL DE MINAS GERAIS
INSTITUTO DE GEOCIÊNCIAS
PROGRAMA DE PÓS-GRADUAÇÃO EM GEOLOGIA

TESE DE DOUTORADO

ÁREA DE CONCENTRAÇÃO: GEOLOGIA ECONÔMICA E APLICADA

EVOLUÇÃO E GÊNESE DO MINÉRIO DE FERRO HIDROTERMAL NOS DEPÓSITOS DA SERRA NORTE, PROVÍNCIA MINERAL CARAJÁS

AUTORA: Rosaline Cristina Figueiredo e Silva

ORIENTADORA: Profa. Dra. Lydia Maria Lobato (UFMG)
CO-ORIENTADOR: Prof. Dr. Carlos Alberto Rosière (UFMG)
CO-ORIENTADOR: Prof. Dr. Steffen Hagemann (UWA)

BELO HORIZONTE
30/01/2009

Nº 13

UNIVERSIDADE FEDERAL DE MINAS GERAIS
INSTITUTO DE GEOCIÊNCIAS
PROGRAMA DE PÓS-GRADUAÇÃO EM GEOLOGIA

ROSALINE CRISTINA FIGUEIREDO E SILVA

EVOLUÇÃO E GÊNESE DO MINÉRIO DE FERRO HIDROTERMAL NOS DEPÓSITOS DA SERRA NORTE, PROVÍNCIA MINERAL CARAJÁS

Tese apresentada ao Programa de Pós-Graduação em Geologia da Universidade Federal de Minas Gerais, como requisito parcial à obtenção do Título de DOUTOR, Área de concentração Geologia Econômica e Aplicada

Orientadora: Prof. Dra. Lydia Maria Lobato (UFMG)
Co-orientador: Prof. Dr. Carlos Alberto Rosière (UFMG)
Co-orientador: Prof. Dr. Steffen Hagemann (UWA)

BELO HORIZONTE
30 de Janeiro de 2009

S586e
2009

Figueiredo e Silva, Rosaline Cristina.

Evolução e gênese do minério de ferro hidrotermal nos depósitos da Serra Norte, província mineral Carajás [manuscrito] / Rosaline Cristina Figueiredo e Silva. - 2009.

xxiv, 236 f., enc. : il., fots. (color.), mapas (color.), tabs. (color.).

Orientadora: Lydia Maria Lobato.

Co-orientadores: Carlos Alberto Rosière.

Steffen Hagemann.

Tese (doutorado) - Universidade Federal de Minas Gerais, Instituto de Geociências, 2009.

Área de concentração: Geologia Econômica e Aplicada.

Bibliografia: f. 47-57.

Inclui 4 anexos contendo artigos da autora.

1. Geologia econômica – Teses. 2. Minérios de ferro – Carajás, Serra dos, Região (PA) – Teses. 3. Depósitos hidrotermais – Teses. I. Lobato, Lydia Maria. II. Rosière, Carlos Alberto. III. Hagemann, Steffen. IV. Universidade Federal de Minas Gerais, Instituto de Geociências. V. Título.

CDU: 553.31

Tese defendida e aprovada, em 30 de janeiro de 2009, pela Banca Examinadora constituída pelos professores:

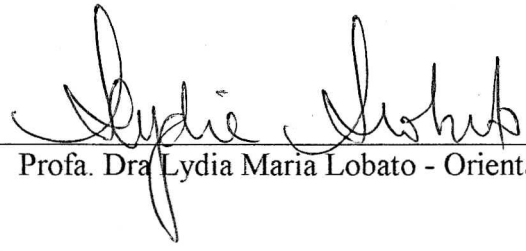

Profa. Dra. Lydia Maria Lobato - Orientadora

Profa. Dra. Lena Virgínia Soares Monteiro

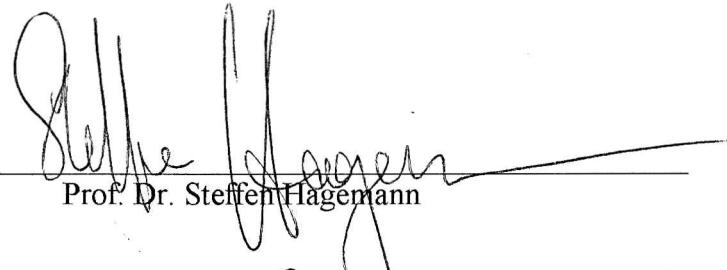

Prof. Dr. Steffen Hagemann

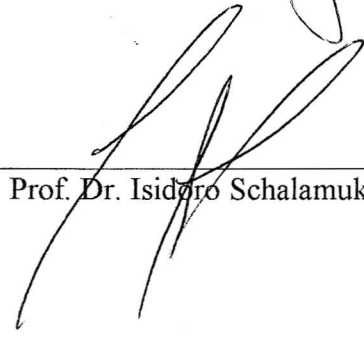

Prof. Dr. Isidoro Schalamuk

Participação através de teleconferência

Prof. Dr. João Orestes Schneider Santos

Dedico este trabalho a meu marido Glauber Fullana de Assis,
por seu companheirismo, amor e incentivo em todos os momentos.

AGRADECIMENTOS

Agradeço imensamente à minha orientadora e amiga, Profa. Dra. Lydia Maria Lobato, pelos ensinamentos, amizade, inúmeras discussões, dias e dias dispensados em sua casa dedicados a nosso trabalho, sempre tão animada e disposta a passar adiante seus conhecimentos;

Ao orientador Prof. Steffen Hagemann, pela ajuda e dedicação, principalmente durante o período na Austrália, por seu incentivo e esforço para que as análises fossem realizadas em laboratórios conceituados, e por seu entusiasmo durante as diversas discussões e correções dos *papers*;

Ao co-orientador Carlos Alberto Rosière, um dos maiores especialistas em minério de ferro no mundo, agradeço toda a colaboração e ensinamentos;

À Vale, pelo apoio financeiro e logístico, acesso e disponibilização dos furos de sondagem, mapas e seções geológicas dos depósitos da Serra Norte, em especial à equipe da Gerência de Planejamento de Mina e Geologia - GALPF (ex-GAJAN) pelo imenso apoio em Carajás, representada pelos geólogos Aroni Monteiro, Sérgio Guedes, Paulo Matias, Roberta Monteiro, Ivan Andrade, Celso Henning, Gilberto da Silva, engenheiros Flávio Ferreira e Júlio, e técnico Roberto Carvalho; agradeço ainda a mais recente colaboração dos geólogos Henry Galbiati, Antônio Seabra e Luciano da Gerência de Exploração Mineral de Ferrosos – DIPF;

Aos técnicos da Geoservice e Geoexplore, pelo apoio em Carajás durante amostragem;

À CAPES (Cordenação de Aperfeiçoamento de Pessoal de Nível Superior), pela bolsa de doutorado e apoio através do Programa de Estágio de Doutorando no Exterior (Processo 1222/05-8);

Ao Centro de Pesquisa Manoel Teixeira da Costa – CPMTC do Instituto de Geociências da UFMG, em especial ao laminador Fernando Soares de Souza, e à secretária da Pós-graduação Maria Paula Borges;

Ao Center for Exploration Targeting - CET da University of Western Australia - UWA, pela acolhida e acesso às facilidades, em especial ao colega de sala Warren Thorne, ao diretor Campbell McCuaig, geólogo Neil Macnaughton, funcionária Charmaine Lobo, e diretor da School of Earth and Environmental Victor Badenko;

Ao Centre for Microscopy, Characterisation and Analysis - CMCA, em especial Dra. Janet Muhling pela paciência e ajuda durante uso dos equipamentos;

Ao Prof. Dr. David Banks da School of Earth and Environmental, University of Leeds (Inglaterra), pela colaboração e auxílio durante a realização das análises LA-ICPMS e cromatrografia iônica em inclusões fluidas;

Aos Drs. Garry Davidson e Leonid Danyushevsky, e geólogos Sarah Gilbert e Keith Harris, do ARC Centre of Excellence in Ore Deposits da University of Tasmania - UTAS (Austrália), pela ajuda na realização das análises de isótopos de enxofre, carbono e oxigênio, e LA-ICPMS em óxidos;

Ao Prof. Dr. Torsten Venemann, do Stable Isotope Laboratory, Institute of Mineralogy and Geochemistry, Universitie de Lausanne - UNIL (Suíça), pela colaboração e auxílio na execução das análises de isótopos de oxigênio, e Dr. Tjerk Heijboer pela ajuda nas análises de isótopos de hidrogênio;

À colega Zsófia Wáczek, doutoranda da UNIL, pela imensa ajuda e acolhida durante o período em Lausanne;

Ao geólogo Franciscus Jacobus Baars, pelas excelentes discussões e desenhos fantásticos;

Aos demais membros da equipe do Projeto Ferro-Carajás, convênio UFMG-Vale: Francisco Javier Rios, José Carlos Seoane, Rodolfo Pacheco (*in memoriam*), Giubráz Mendes, Leonardo Lopes, Roberto Moreno, João Orestes Santos, e em especial à geóloga Ana Luísa Maciel e à estudante de Geologia Mariana Leite pela importante ajuda na parte final da tese;

Ao colega Luis Garcia do Laboratório de Microanálises da UFMG;

Aos geólogos Orivaldo Baltazar, Gabriel Berni e Kerley Andrade, pela ajuda na confecção dos mapas e seções geológicas;

Ao querido amigo e colega de doutorado Javier Eduardo Becerra Becerra, pela amizade e companheirismo durante esses quatro anos;

Aos demais colegas de doutorado, Sérgio Martins Pereira e Marcus Fernandes, mestrandos e colegas de sala Luis Carlos Silva, Rodrigo Pinho, Luiz Cláudio Lima, Roberto Moreno e Leandro Costa;

Aos queridos amigos que fiz na Austrália, Raimunda, Roger, Daniel e Rolland, Phill Winkler, Neils Perol, Warren Thorne, Estefânia Hagemann e Lukas, Klaus Petersen, Érica e filhas; sem eles esse período difícil longe de casa, não teria sido tão agradável e feliz;

À minha querida amiga e *housemate* Dra. Márcia Zucchetti, agradeço por tudo, paciência, amizade e companheirismo durante todo o doutorado, e principalmente nos doze meses de convivência na Austrália e Europa;

Agradeço imensamente à minha família, meus pais Regina Maria e João Manoel, minhas irmãs Jacqueline e Regiane, meus queridos sobrinhos João Gabriel e Paula, meu cunhado Bráulio, e meu avô Ciro (*in memoriam*), o incentivo, o carinho e a tolerância nos meus muitos momentos de ausência durante viagens e fase final de escrita da tese. Obrigada!

AO MEU MARIDO GLAUBER, AGRADEÇO TODO AMOR, CARINHO, INCENTIVO E APOIO CONSTANTE EM TODOS OS SENTIDOS;

A todos que de alguma maneira me apoiaram e fizeram parte desta etapa, muito obrigada!

‘Assim, nesse simples pouso na Serra Arqueada, na manhã do dia 31 de julho de 1967, foi revelada a razão da existência das clareiras: canga de minério de ferro. Entretanto, apesar da hipótese, de que as outras clareiras também fossem devidas à canga, fosse imediata, era assustadora demais pelo seu potencial. Devido à falta de disponibilidade de helicóptero, foi feito um reconhecimento com monomotor, a baixa altura, das clareiras da Serra Norte, confirmando a hipótese inicial. Houve imediata comunicação ao Tolbert, a partir de telefonema de Belém. Não houve interresse imediato pelo ferro, só despertado após a descoberta do manganês de Buritirama.....’

Geólogo Breno Augusto dos Santos
(trecho do texto sobre a descoberta dos depósitos de ferro em Carajás)

SUMÁRIO

ANEXOS

LISTA DE FIGURAS

ANEXO 1

crossed polars (200X). F. Anhedral hematite portions of high-grade hematite ore, N5E deposit. Note that holes made by laser ICP-MS analyses are shown. Reflected light, under crossed polars (100X). G. Anhedral hematite crystals with lobate borders in high-grade hematite ore, N5E deposit. Reflected light, under crossed polars (200X). H. Tabular hematite vein in brecciated N5E hematite ore. Reflected light, under crossed polars (200X). I. Paragenetic sequence of oxides. Mineral abbreviations: Mag = magnetite; Mt = martite; MpHem = microplaty hematite; AHem = anhedral hematite; THem = tabular hematite.

magnetite; B. martite; C. martite and microplaty hematite; D. anhedral hematite; E. platy hematite and martite from hydrothermally altered (chlorite-hematite) mafic wallrock; and F. tabular hematite.

LISTA DE TABELAS

RESUMO

A presente tese trata da evolução e gênese do minério de ferro hidrotermal dos gigantes depósitos N1, N4E, N4W, N5E e N5S da Serra Norte, localizados na Província Mineral de Carajás, Pará. O objetivo principal consiste no entendimento e estabelecimento de um modelo genético hidrotermal para formação do minério tipo compacto nos depósitos de ferro da Serra Norte, com base em amostras de jaspilitos mineralizados com diferentes graus de alteração, e variados tipos de minério compacto. Diversas técnicas analíticas são utilizadas, sendo a maior parte inédita para os depósitos estudados, como: (i) estudos de química mineral baseado em análises *in situ* de óxidos de ferro (magnetita e hematitas) através de *laser ablation ICP-MS*; (ii) estudos de inclusões fluidas (P, T, composição, fonte) em quartzo e carbonato de veios e brechas por microtermometria, cromatrografia iônica e *laser ablation ICP-MS;* (iii) estudos isotópicos que incluem isótopos radiogênicos de estrôncio em carbonatos (calcita, dolomita), isótopo estável de oxigênio em magnetita, variados tipos de hematita, jaspilitos e quartzo, isótopo estável de enxofre em sulfetos (pirita e calcopirita) e isótopo estável de hidrogênio em inclusões fluidas aprisionadas em quartzo de diferentes tipos de veio-brechas. Os resultados obtidos, aliados à mineralogia detalhada e estudos de paragêneses minerais, são utilizados para estalecer os processos e fontes de fluidos que proporcionaram o enriquecimento do jaspilito para formar minério duro de alto teor (> 64% Fe). Três zonas de alteração hidrotermal são estabelecidas, distal, intermediária e proximal, com base nos estudos petrográficos e geoquímicos. O modelo hidrotermal de mineralização magmático-meteórico proposto para formação do minério hipogênico a partir do protominério jaspilítico é substancialmente diferente de modelos de formação de minérios de ferro da Província de Hamersley na Austrália ou do Quadrilátero Ferrífero, mas tem uma provável associação genética com os inúmeros depósitos de Cu-Au magmático-hidrotermais proterozóicos na Província Mineral Carajás. O novo modelo hidrotermal tem ainda significante implicação para a exploração de minérios de ferro cobertos por outras sequências e/ou para a exploração de extensões profundas de corpos de minérios rasos, já existentes. A distinção de zonas de alteração hidrotermal, inclusive nas rochas máficas encaixantes, assim como a identificação de minerais- e elementos-guia, como REE, Ca, Na, Fe e S, também são parâmetros de exploração de suma importância nesses depósitos.

Palavras chave: minério de ferro duro; Carajás; hipogênico; alteração hidrotermal.

ABSTRACT

This thesis presents the hydrothermal evolution and genesis of the hard high-grade iron ore of the giants N1, N4E, N4W, N5E and N5S deposits in the Serra Norte, Carajás Mineral Province, Pará. In order to better constrain and understand the hydrothermal processes that lead to the modification of jaspilite to form hard, high-grade iron ores in the Serra Norte deposits, this thesis provide the investigation of the composition of hydrothermal fluids from vein-breccia types located in the different hydrothermal alteration zones, using two main research approaches: fluid inclusions and stable isotopes. Several different techniques are applied to fluid inclusions, such as microthermometry, bulk method of crush-leach extraction followed by ion-chromatography, and laser ablation coupled to ICP-MS. Regarding isotope analyses, stable carbon and oxygen and radiogenic strontium isotope analyses were performed on carbonates (calcite, dolomite); sulfur isotopes on sulfides (pyrite and chalcopyrite); oxygen isotopes on magnetite, different hematite types and quartz veins; hydrogen isotopes on fluid inclusions trapped in quartz from different vein-breccia types. The results of these methods paired with detailed mineralogy and paragenetic studies are used to constrain the processes and fluid sources that were integral to the enrichment of jaspilite to hard high-grade (> 64 wt % Fe) iron ore. Varying degrees of hydrothermal alteration have affected jaspilites to form hypogene hard iron ores, and three hydrothermal alteration zones established, distal, intermediate and proximal. The proposed magmatic-meteoric hydrothermal mineralization model for the Carajás hard ores is substantially different to models for the Hamersley or Iron Quadrangle iron ores, but may have a genetic link to the numerous Proterozoic magmatic hydrothermal deposits in the Carajás Mineral Province. The new hydrothermal model has also significant implication for iron ore exploration under cover other sequences and/or the exploration for deep extensions of existing shallow orebodies. The distinction of widespread hydrothermal alteration zones, including mafic wallrocks, as well as identification of related pathfinder minerals and chemical pathfinder elements such as REE, Ca, Na, Fe and S, are also very important exploration parameters in these deposits.

Keywords: hard iron ore; Carajás; hypogene; hydrothermal alteration.

CAPÍTULO 1 - INTRODUÇÃO

A Província Mineral de Carajás possui reservas de aproximadamente 16 bilhões de toneladas de minério de ferro de alto teor, sendo que as minas da Serra Norte representam um papel importante no cenário econômico brasileiro e mundial. O volume de minério de ferro produzido em Carajás atingiu em 2007 a marca histórica de um bilhão de toneladas desde o início de suas operações, em 1985, demonstrando a suma importância desse bem mineral.

Os depósitos de ferro N1, N4 e N5, alvos do presente trabalho, fazem parte da Serra Norte, onde mais seis corpos são constatados (N2, N3, N6, N7, N8 e N9) e têm Parauapebas como município referente (Figura 1A). Estes depósitos estão enquadrados na sequência metavulcanossedimentar do Grupo Grão Pará, onde predominam rochas máficas vulcânicas sobre- e sotopostas a jaspilitos, ambos metamorfizados em fácies xisto verde baixo, e corpos descontínuos de minério de ferro de alto teor (> 64% Fe) da Formação Carajás. A mina N4E foi a primeira a entrar em operação em 1985. Atualmente, as minas N4W, N4E, N5W e N5E estão em atividade (Figura 1B), e N5S entrará em breve em atividade de lavra.

A origem hipogênica para formação do minério de ferro duro do tipo HD (hoje denominado HC-hematita compacta pela Vale) nos depósitos da Serra Norte em Carajás foi sugerida desde o ínicio da década de 70 (Tolbert *et al*. 1971, Rezende & Barbosa 1972, Beisiegel *et al.* 1973), poucos anos após estes terem sido descobertos. No entanto, desde então poucos trabalhos tiveram como foco principal o estudo deste tipo de minério de ferro. A partir de meados da década de 90, observações de Guedes (publicadas em Guedes 2000, Guedes *et al.* 2002, Dalstra & Guedes 2004) deram início a uma série de estudos tanto no que diz respeito à classificação petrográfica e geoquímica das rochas (jaspilitos, minérios e rocha máfica encaixante) quanto no âmbito do processo hidrotermal mineralizador a ferro nos depósitos da Serra Norte (Figueiredo e Silva 2004, Figueiredo e Silva *et al.* 2004, 2007a, b, 2008a, b, Lobato *et al.* 2004, 2005a, b, 2007, 2008, Gutzmer *et al.* 2006, Clout & Simonson 2005). Na presente tese, diversas técnicas analíticas foram aplicadas com o intuito de aprofundar o entendimento acerca do fluido hidrotermal que interagiu com protominério jaspilítico formando corpos de minério de ferro hipogênico.

Atualmente, o modelo mais aceito para origem e deposição de ferro e sílica na gênese de formações ferríferas (FFs) baseia-se em processos hidrotermais vulcanogênicos de fundo oceânico (Klein & Beukes 1989, Klein 2005). Já em relação à gênese do minério de ferro tipo compacto, modelos hipogênicos vêm sendo estudados em diversos depósitos no mundo, como por exemplo, Hamersley, Austrália (Barley *et al.* 1999, Hagemann *et al.* 1999, Taylor *et al*. 2001, Thorne *et al.* 2004, 2008, Dalstra & Guedes 2004); Thabazimbi, África do Sul (Beukes *et al.* 2002, Netshiozwi 2002); Simandou Range, oeste da África (Cope *et al.* 2008); Noamundi, Índia (Beukes *et al.* 2008);

Quadrilátero Ferrífero, Brasil (Varajão 2002, Cabral *et al.* 2003, Spier *et al.* 2003, Rosière & Rios 2004).

A tese de doutorado tem como principal objetivo evoluir no entendimento acerca das características do fluido hidrotermal mineralizador a ferro nos depósitos da Serra Norte, para formação dos minérios de ferro tipo compacto. Um modelo genético hidrotermal para formação do minério tipo compacto nos depósitos de ferro da Serra Norte é estabelecido com base nos seguintes trabalhos realizados em amostras de jaspilitos mineralizados e variados tipos de minério compacto: (i) caracterização petrográfica, (ii) química mineral, (iii) geoquímica de rocha total, (iv) estudos de inclusões fluidas (P, T, composição, fonte), (v) geologia isotópica. Os estudos de química mineral incluem análises *in situ* de óxidos de ferro (magnetita e hematitas) através de *laser ablation ICP-MS*. Estudos de inclusões fluidas em quartzo e carbonato de veios e brechas englobam: (i) microtermometria; (ii) cromatrografia iônica; (iii) *laser ablation ICP-MS*. Os estudos isotópicos incluem: (i) isótopos estáveis de carbono e oxigênio e radiogênicos de estrôncio em carbonatos (calcita, dolomita); (ii) isótopo estável de oxigênio em magnetita, variados tipos de hematita, jaspilitos e quartzo; (iii) isótopo estável de enxofre em sulfetos (pirita e calcopirita); (iv) isótopo estável de hidrogênio em inclusões fluidas aprisionadas em quartzo de diferentes tipos de veio-brechas.

A tese faz parte do Programa de Pós-graduação em Geologia do Instituto de Geociências da Universidade Federal de Minas Gerais, e tem orientação da Profa. Dra. Lydia Maria Lobato, co-orientação do Prof. Dr. Carlos Alberto Rosière e do Prof. Dr. Steffen Hagemann do Center for Exploration Targeting-CET, University of Western Austrália. A pesquisa insere-se em projeto de pesquisa intitulado: “Os minérios de ferro de Carajás: tipologia, controle estrutural, gênese, implicações metalogenéticas e exploratórias e relação com as associações cobre-ouro”, com suporte financeiro da Vale, em convênio com a UFMG.

A estudante participou do programa de estágio de doutorando da CAPES Processo 1222/05-8, de agosto de 2005 a agosto de 2006, no Center for Exploration Targeting-CET, da University of Western Austrália, sob supervisão do Prof. Steffen Hagemann, onde foram realizadas as análises microtermométricas de inclusões fluidas, microssonda eletrônica e microscopia eletrônica de varredura-MEV. Demais análises foram realizadas em colaboração com pesquisadores de centros de pesquisa em universidades na Tasmânia, Melbourne, Leeds e Lausanne.

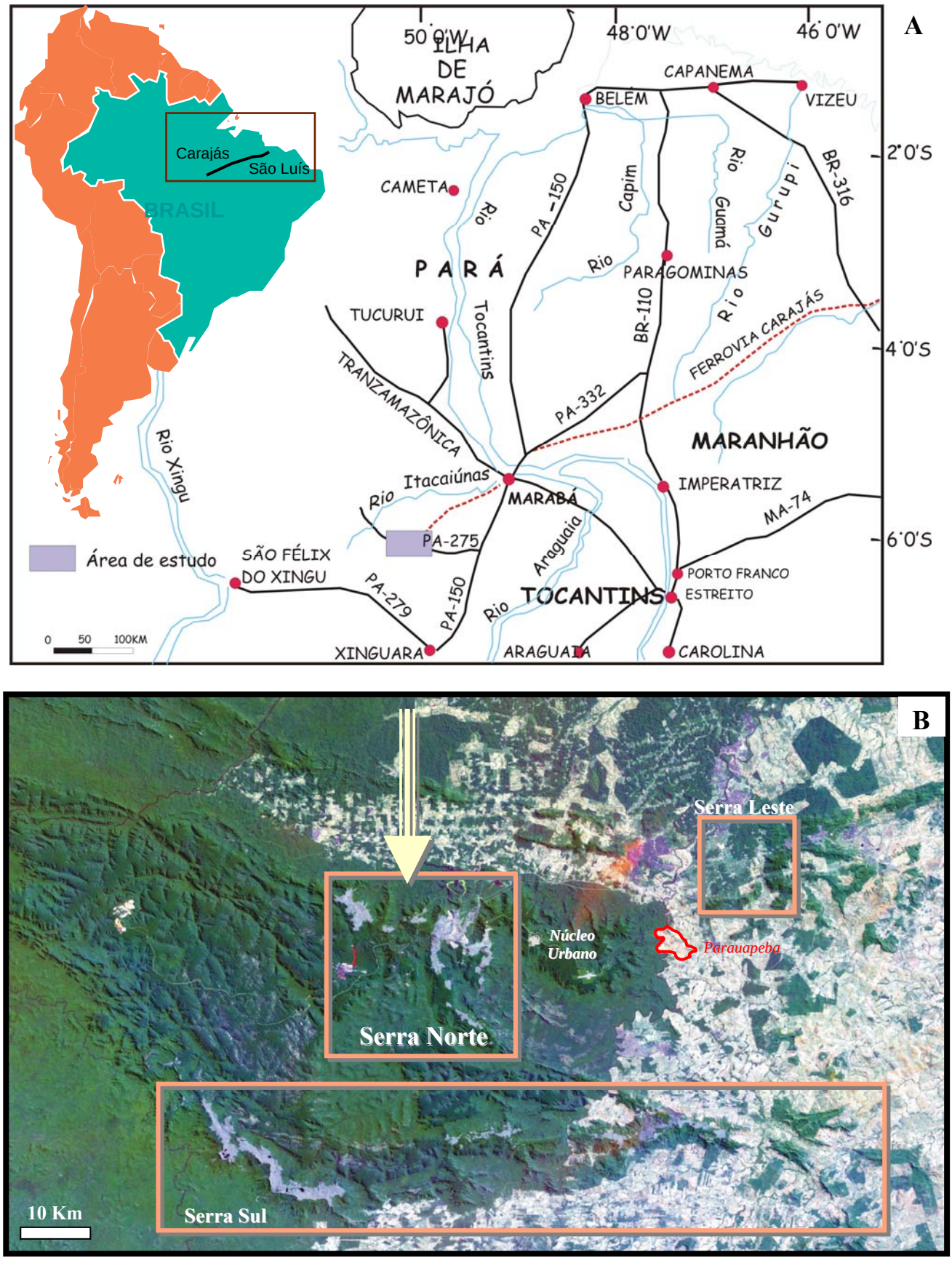

Figura 1 - A. Mapa de localização da Província Mineral Carajás, com as principais vias de acesso (modificado de Macambira 2003). B. Imagem de satélite com localização da área de trabalho, depósitos da Serra Norte (indicada por seta), Núcleo urbano de Carajás e município de Parauapebas. Os depósitos das Serras Sul e Leste também são apresentados.

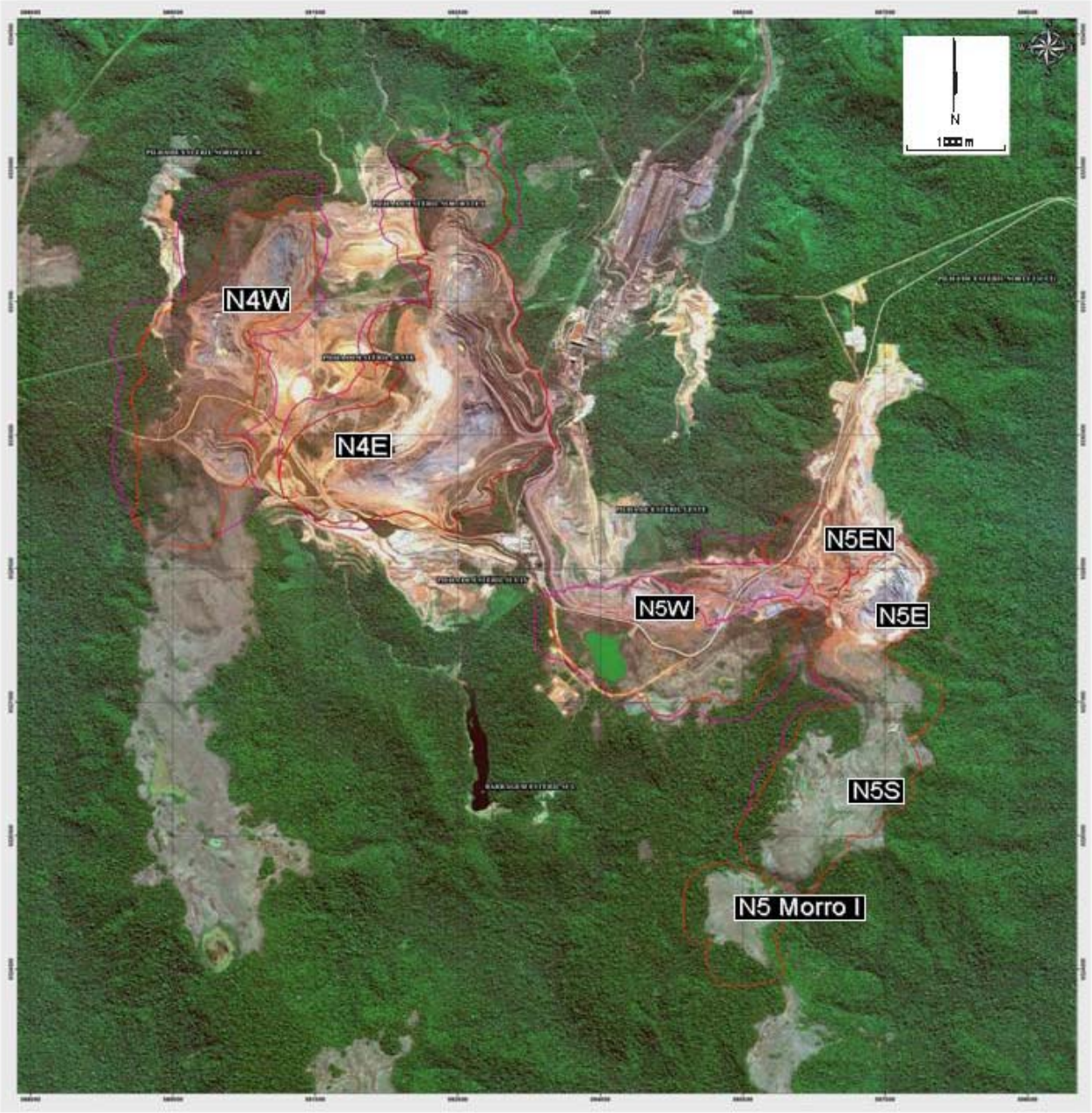

Figura 2 - Imagem de satélite mostrando os depósitos de ferro N4 e N5 da Serra Norte (fonte Vale).

CAPÍTULO 2 – APRESENTAÇÃO DA TESE

O volume final dessa tese de doutorado foi preparado, em parte, na forma de artigos científicos internacionais, detalhados a seguir. Em função disso, o texto de algumas tabelas e figuras acha-se no idioma inglês.

1) O primeiro artigo, entitulado "**A hydrothermal origin for the jaspilite-hosted, giant Serra Norte iron ore deposits in the Carajás Mineral Province, Pará State, Brazil",** está reproduzido no Anexo 1. O trabalho apresenta principalmente a geologia dos depósitos de ferro estudados, os estudos petrográficos e geoquímicos de rocha total e, de forma resumida, os dados de inclusões fluidas e isótopos estáveis. Este artigo foi publicado na Reviews of Economic Geology, volume 15, em maio de 2008.

2) O segundo artigo entitula-se **"Hydrothermal Fluid Process and Evolution of the Giant Serra Norte Jaspilite-Hosted Iron Ore Deposits in the Carajás Mineral Province, Pará State, Brazil"** e deverá ser submetido à Economic Geology nos próximos meses. O trabalho foca o zonamento hidrotermal associado à mineralização de ferro, com duas linhas principais de pesquisa: inclusões fluidas e isótopos estáveis. Além dos estudos de microtermometria tradicional em inclusões fluidas, foram realizadas análises de cromatografia iônica e *laser ablation* acoplado ao ICP-MS.

3) Um resumo expandido é apresentado no Anexo 3, entitulado "**Laser-ablation ICP-MS analyses of oxides and whole rock geochemistry of protore and ore, Giant Serra Norte Jaspilite-Hosted Iron Ore Deposits in the Carajás Mineral Province, Pará State, Brazil",** trabalho apresentado no 10th Biennial Meeting of the SGA em Townsville, Austrália. Um terceiro artigo completo deverá ser submetido à revista Ore Geology Reviews, focando a química mineral dos óxidos de ferro, com ênfase em análises *in situ laser ablation* ICP-MS, parcialmente apresentadas no resumo.

Além desses artigos, a publicação de Lobato et al. (2008; **Hypogene Alteration Associated with High-Grade BIF-related Iron Ore**), da qual a doutoranda é a primeira co-autora, apresenta em detalhe a sequência de alteração hidrotermal. A separata do artigo encontra-se reproduzida no Anexo 4.

Diversos dados são ainda parcialmente discutidos em resumos expandidos aceitos para apresentação oral no encontro da European Current Research of Fluid Inclusions (ECROFI), realizado em julho de 2007 em Bern (Figueiredo e Silva *et al.* 2007a), da Society for Geology Applied to Mineral Deposits-SGA, em agosto de 2007 em Dublin (Figueiredo e Silva *et al.* 2007b), e no pôster apresentado na reunião bienal da SEG, em julho de 2008 (Figueiredo e Silva *et al.* 2008b) na cidade de Johannesburgo.

Os temas abordados nos capítulos a seguir são em parte cobertos nos artigos dos anexos 1 e 2, e resumo expandido do Anexo 3, no entanto, informações adicionais relevantes dos mesmos acham-se apresentadas no texto em português a seguir.

Em relação às técnicas analíticas utilizadas, estas também estão apresentadas nos capítulos seguintes conforme o tema, e informações detalhadas encontram-se nos artigos dos anexos 1 e 2. A relação de amostras por depósito e os procedimentos analíticos aplicados para cada uma delas é apresentada no Anexo 5.

CAPÍTULO 3 – AMOSTRAGEM

Três etapas de campo, com cerca de quinze dias cada, foram realizadas em Carajás para reconhecimento-mapeamento e amostragem. A primeira delas ocorreu em maio de 2005, objetivando o reconhecimento e mapeamento das zonas de alteração hidrotermal, classificação dos diferentes tipos de veios-brechas, em furos de sondagem selecionados principalmente no depósito N5S.

Em abril de 2007, uma nova etapa de campo fez-se necessária para reconhecimento e amostragem de furos de sondagem com minério de ferro tipo compacto, objetivando a realização de análise geoquímica de rocha total e posterior seleção-separação de óxidos de ferro para análise isotópica de oxigênio (realizada em Julho de 2007 pela estudante).

Em uma última oportunidade, em julho de 2008, diversos furos de sondagem dos depósitos N5E, N5S e N5W foram amostrados visando detalhamento dos contatos entre: minério tipo duro (HD)-rocha máfica; minério friável (HM)-minério duro (HD); jaspilito-minério friável. As abreviações utilizadas ao longo do trabalho estão apresentadas a seguir.

A Tabela 1 e a listagem do Anexo 5 apresentam a relação de amostras investigadas, oriundas de quarenta furos de sondagem dos depósitos N1, N4 e N5, com fotografias mostrando as principais feições observadas. Vale ressaltar que também foram utilizadas amostras coletadas entre 2002 e 2004, durante o desenvolvimento da dissertação de mestrado da presente estudante.

Lista de abreviações:

Jp – jaspilito

HD – minério duro

HM – minério mole

FFB – formação ferrífera bandada

Qtz – quartzo;

Carb – carbonato;

Cal – calcita;

Kut – kutnahorita;

Dol – dolomita;

Py – pirita;

Cpy – calcopirita;

MiHem – hematita microcristalina;

Mag – magnetita;

Mt – martita;

MpHem – hematita microlamelar;

AHem – hematita anédrica;

THem – hematita tabular;

V1a – veios e brechas a quartzo ± sulfeto;

V1b – veios e brechas a carbonato(quartzo) ± magnetita ±sulfeto;

V2a – veios a quartzo ± hematita discordantes ao bandamento do jaspilito;

V2b – veios a quartzo + hematita *vuggy-textured* discordantes ao bandamento;

V3 – veios a hematita ± quartzo discordantes e/ou ao longo do bandamento;

V4 – veios e brechas a carbonato (poeira Fe) ± quartzo;

V5 – brecha a quartzo ± hematita microlamelar.

Tabela 1. Lista de furos selecionados para amostragem dos depósitos N1, N4 e N5.

Depósito	Furo	Rocha	Principais feições
N5Sul	686	Jp com veios (A) e porções de magnetita (Mag) em B.	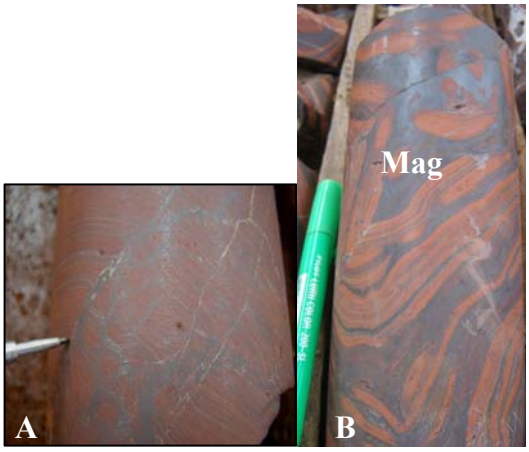
	700, 760	Jp passando a HM (veios V2b); lentes de HD bandado venulado	
	771	HD bandado; HD brechado e poroso; Jp cortado por veios de hematita V3 (8 amostras)	
	782	HM com fragmentos de HD e HM "consolidado", bandado, poroso e fragmentado (A) com veios de quartzo V1a (B)	
	817	FFB a magnetita; Jp intensamente venulado (veios V1, V2b em A, V3 em B) (29 amostras)	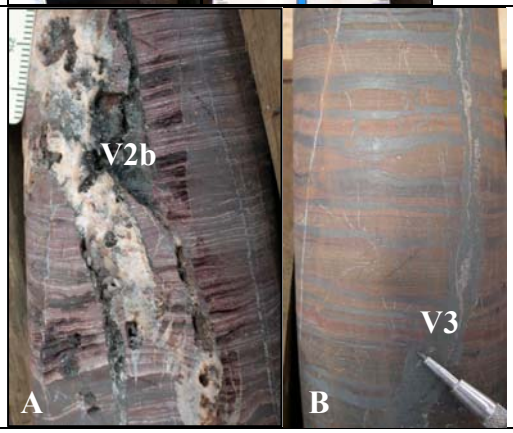

	825	Jp passando a HM (A); Jp com veios V1a, V1b, V2b em B; brecha a Qtz - rocha máfica (19 amostras)	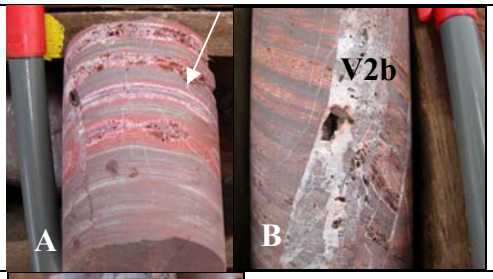
	834, 836, 837	Jp venulado (V2b em A, V3); HD poroso; Jp passando a HM (B)	
	907	HM-Jp fragmentado microbandado; contato HM-Jp poroso com veios de Qtz (V2a)-HM-HD bandado-máfica alterada-máfica hematitizada	
	897, 904, 910	HD bandado poroso; HD maciço (A); Jp mineralizado (B)	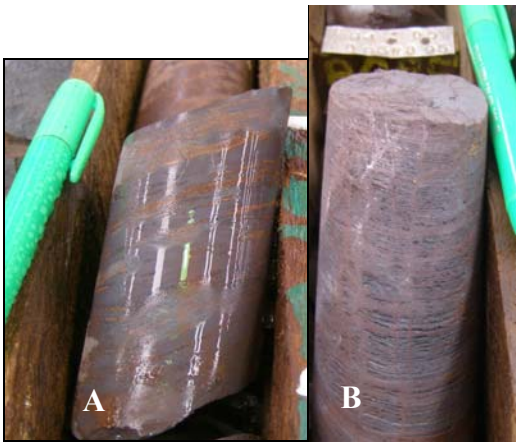
N5W	556	Contatos HM-HD-HM-Jp-HM; Jp (1 amostra)	
	968	HM-Jp fragmentado poroso com veios Qtz (V1a)-contato gabro cloritizado	

N5E	40, 274	HD c/ vênulas de hematita microlamelar e tabular	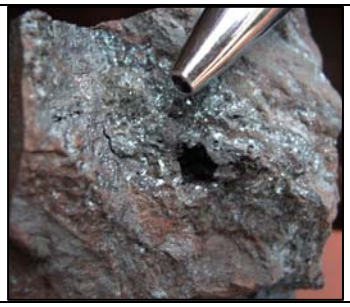
	439, 440	HD brechado (veios V4-V5) – contato máfica mineralizada com veios de hematita (Foto)	
	529, 577	HD brechado cimentado por Carb (veio-brecha V4); HD brechado no contato com rocha máfica (Foto)	
	947, 949, 950, 951	Contato gabro-HD c/ vênulas de hematita (Foto)-gabro	
N4E	181	HD bandado-brechado; vênulas de hematita microlamelar (2 amostras)	
	603	HD brechado, cimentado por carbonato (veio discordante e intrabanda V4 em A); HD brechado e/ou bandado (veio-brecha V5 em B)	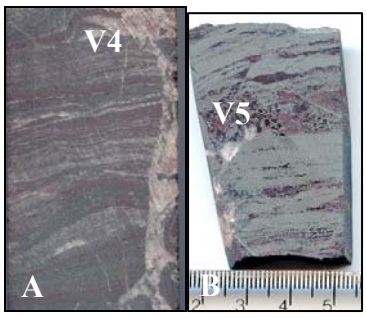
	703	Jp com intensa venulação de Mag-Cal-Qtz-sulfetos (V1b)	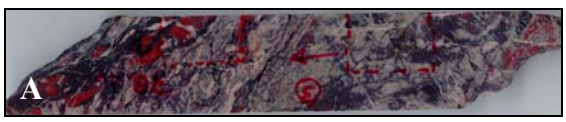

			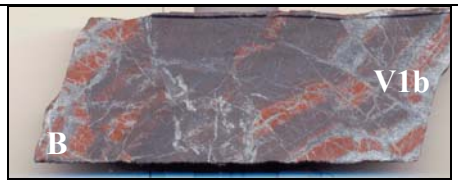
N4W	692, 693	Jaspilito mineralizado; veios V2b	
	1332	Jp no contato com basalto – veios de Mag-Carb-Qtz (V1b)	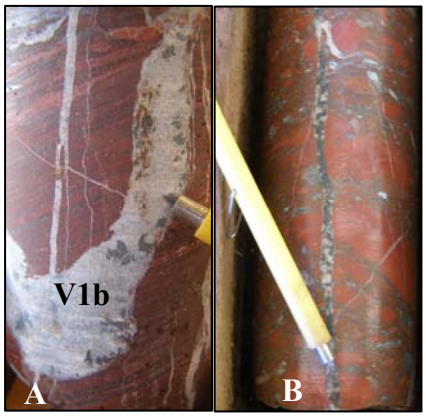
N1	Furos 08, 14 e 36	Lentes de HD magnético, compacto ou laminado em meio a rocha máfica ou em meio a HM	
	Furo 108	Lentes de HD magnético em meio a HM	

CAPÍTULO 4 – GEOLOGIA REGIONAL E A ESTRUTURA DA PROVÍNCIA CARAJÁS

A região da Província Mineral Carajás é considerada como a área limitada a leste pelos rios Araguaia-Tocantins, a oeste pelo rio Xingu, a norte pela serra do Bacajá, e a sul pela Serra dos Gradaús (DOCEGEO 1988). Sua designação como província deve-se à sua enorme riqueza mineral, incluindo os depósitos de ferro das serras Norte (N1 a N9), Sul (S1 a S45) e Leste (Fig. 1B); os depósitos da classe óxidos de Fe-Cu-Au, Salobo, Pojuca, Alemão, Igarapé Bahia, Cristalino, Sossego, Alvo 118, Gameleira; Manganês Azul; e de níquel Vermelho. A área coberta por esses depósitos constitui rochas metavulcanossedimentares, tida como uma bacia neoarqueana, sobreposta a um embasamento meso- a neoarqueano, e contém rochas de complexos ígneos e metamórficos (Tassinari *et al.* 2000).

Terrenos granito-gnáissicos tipo tonalito-trondhjemito-granodiorito (TTG) são tidos como pertencentes ao Complexo Xingu (Silva *et al.* 1974) e considerados por grande parte dos autores como embasamento, sendo sotopostos às sequências metavulcanossedimentares. Este complexo vem sendo subdividido em unidades geológicas independentes, em função de maior detalhamento da cartografia geológica. A cartografia geológica mais atual é parte do sistema de informações geográficas (SIG) de Bizzi *et al.* (2001) em escala 1:2.500.000, além de detalhamento da geologia da região em Santos (2003).

Na parte sul da região encontra-se o *greenstone belt* Rio Maria (3,2 a 2,9 Ga; Figura 3) (Huhn *et al.* 1988) que contém importantes mineralizações auríferas. DOCEGEO (1988) propõe o termo Supergrupo Andorinhas para nomear todas as sequências tipo *greenstone* da região da Província Mineral Carajás. A unidade é composta por rochas vulcânicas máficas a ultramáficas (incluindo komatiítos), intercaladas com rochas sedimentares (pelitos, formações ferríferas bandadas, *chert*) na base (Grupo Babaçu), gradando para rochas vulcânicas intermediárias a félsicas associadas com folhelho, grauvaca e FFB, no topo (Grupo Lagoa Seca). O resultado da datação, pelo método U-Pb em zircão de rochas vulcânicas félsicas do Grupo Lagoa Seca (Supergrupo Andorinhas) da região de Rio Maria, indica idades de 2,9 Ga (Macambira 1992) e 3,0 Ga (Pimentel & Machado 1994).

Vários corpos graníticos arqueanos também cortam a região, como os granitos e dioritos da Suíte Plaquê (aproximadamente 2,74 Ga, Huhn *et al.* 1999), e os álcali-granitos foliados Planalto (2,75 Ga - Huhn *et al.* 1999; 2.736±24 Ma - Avelar *et al.* 1999). Os complexos ígneos estão sendo individualizados geológica- e geocronologicamente, identificando-se então outras suítes neoarqueanas pertencentes ao embasamento (Lobato *et al.* 2005b). Nessa região, dados geocronológicos e relações de campo têm mostrado que plútons granitóides são mais novos que as sequências *greenstone belt*. A exceção é o tonalito Arco Verde, que é contemporâneo com as sequências tipo *greenstone belt* (idades de 2,9 Ga, segundo Althoff *et al.* 1991).

Segundo Araújo *et al.* (1988), a parte norte da Província é constituída pelo chamado Cinturão Itacaiúnas (Figura 3), com rochas mais antigas pertencentes ao Complexo Pium ou ao Complexo

Xingu. Segundo Araújo & Maia (1991), as rochas granulíticas do Complexo Pium (3,0 Ga, Rodrigues *et al.* 1992) ocorrem como numerosos corpos alongados (comprimento máximo de 35 km), subparalelos à foliação regional E-W. São interpretados como fragmentos de crosta inferior, colocados ao longo de zonas de cisalhamento (Araújo *et al.* 1988) ao sul da bacia.

A Serra dos Carajás, propriamente dita, é constituída de dois conjuntos rochosos maiores, sendo um conjunto metavulcanossedimentar e outro metassedimentar, que compõem o Supergrupo Itacaiúnas (DOCEGEO 1988). O mesmo inclui sequências litoestratigraficamente contemporâneas ou pene-contemporâneas, previamente descritas e agrupadas como os grupos Igarapé Bahia, Aquiri e Grão Pará na porção sul, em fácies metamórfica xisto verde, e grupos Igarapé Salobo e Igarapé Pojuca em fácies metamórfica anfibolito na porção norte da Província. Estes grupos foram assim caracterizados em função da posição geográfica dos depósitos homônimos, descritas em igarapés que cortam a região. DOCEGEO (1988) engloba ainda o Grupo Buritirama no Supergrupo Itacaiúnas.

O Complexo Pium

O Complexo Pium compreende rochas metamórficas de alto grau de origem magmática e vulcanossedimentar, cujo protólito mais antigo está datado em 3,0 Ga, pelo menos, com registro metamórfico de 2,85 Ga (Pidgeon *et al.* 2000). Embora este último dado seja proveniente de amostra de origem incerta, nota-se que é coincidente com as idades dos cinturões de rochas verdes localizados ao sul da Província Carajás, tais como os grupos Rio Maria e Andorinhas.

As Sequências Metavulcanossedimentares

O Grupo Grão Pará (Beisiegel *et al.* 1973), de idade 2,76 Ga (Santos 2003), compreende rochas metavulcânicas máficas e félsicas associadas a metasedimentos e lentes de formação ferrífera bandada, incluindo jaspilitos. Macambira *et al.* (1990) enquadraram as rochas metavulcânicas superiores aos jaspilitos do Grupo Grão Pará como uma unidade independente denominada Formação Igarapé Cigarra. O grau metamórfico é de fácies xisto verde muito baixo a baixo. As rochas ígneas foram consideradas co-originárias de vulcanismo marinho toleiítico, embora Meirelles & Dardenne (1991) as tenham interpretado como shoshonitos de um arco magmático. Zucchetti *et al.* (2007) concluíram a partir de estudos geoquímicos que estas rochas correspondem a basaltos de arco vulcânico, com afinidade calcio-alcalina, e contaminação crustal. Os grupos Igarapé Salobo e Igarapé Pojuca são sequências metavulcanossedimentares semelhantes que têm sido comparadas ao Grão Pará por diversos autores (*e.g.*, Hutchinson 1979, Lindenmayer & Fyfe 1992). Santos (2003) elaborou um sumário de dados geocronológicos que indicam que o Grupo Igarapé Pojuca é aproximadamente 30 Ma mais jovem que os grupos Grão Pará e Igarapé Salobo. Lobato *et al.* (2005b) concluem que, embora uma rigorosa correlação estratigráfica entre

estas unidades não seja ainda clara, as mesmas devem ter tido, provavelmente, seu desenvolvimento em um único sistema de arco magmático em evolução. Cada uma das idades de deposição vulcanossedimentar está diretamente associada à plutonismo máfico e granitogênese de idades correspondentes, refletindo prováveis períodos da evolução do arco. O Grupo Rio Novo (Figura 3) compreende uma sequência supracrustal de natureza vulcanossedimentar, metamorfisada em fácies xisto-verde, contendo formações ferríferas, xistos, anfibolitos, rochas máficas e ultramáficas (Costa 2007).

Uma sequência de sedimentos psamo-pelíticos, com grauvacas e arenitos, siltitos e conglomerados, cobre discordantemente o Grupo Grão Pará. Silva *et al.* (1974) denominaram-na Formação Rio Fresco, enquanto que Araújo & Maia (1991) a renomearam como Formação Águas Claras, pertencentes ao Grupo Grão Pará. Zircões detríticos da camada superior dessa unidade forneceram uma idade de 2,68 Ga (Trendall *et al.* 1998). Os mesmos foram interpretados como produto de vulcanismo sin-sedimentar relacionado a diques máficos de idade 2,64 Ga que cortam toda a sequência.

As Formações Ferríferas do Grupo Grã Pará

Na Serra Norte, as formações ferríferas do Grupo Grão Pará são principalmente jaspilitos. Estas rochas apresentam composição variável com 17,11-43,30% Fe e 35,10-60,85% SiO_2 (Tolbert *et al.* 1971, Beisiegel *et al.* 1973), apresentando típica intercalação de bandas claras e escuras, de espessura centimétrica (mesobandas), e microbandamento com lâminas milimétricas de óxido de ferro intercaladas com lâminas vermelho brilhante a claras, constituídas de SiO_2 microcristalina (jaspe e *chert*) com inclusões de hematita microcristalina. As mesobandas escuras são constituídas por óxidos de ferro apresentando uma variedade de texturas, sendo as fases dominantes hematita fina a microcristalina e magnetita martitisada. Localmente, desenvolvem-se cristais mais grossos de quartzo apresentando típica textura granoblástica. Figueiredo e Silva (2004), Figueiredo e Silva *et al.* (2004) e Figueiredo e Silva *et al.* (2005) descrevem em detalhe texturas sedimentares e hidrotermais preservadas no minério e nas encaixantes nos depósitos ao Serra Norte.

Amostras de jaspilitos, detalhadas em Lindenmayer *et al.* (2001), foram analisadas pelo método Sm-Nd e produziram uma isócrona que indica a idade de 2593 ± 260 Ma (Lobato *et al.* 2005b), com valor de $\varepsilon_{Nd}(T)$ de –4,2 e *MSWD* = 2,3, que indica a idade de formação dos jaspilitos. Levando em consideração a elevada incerteza analítica inerente ao método Sm-Nd, a idade obtida é comparável com os resultados U-Pb em zircão (Trendall *et al.* 1998), que estabelece idade mínima para a Formação Carajás, obtida em amostra de *sill* máfico a 2740 ± 8 Ma. Considerando que os jaspilitos: são produto de exalações hidrotermais submarinas, o valor negativo do parâmetro $e_{Nd}(T)$ é

indicativo de contaminação com crosta continental mais antiga. Krymsky *et al.* (2002) obtiveram idades U-Pb de 2751± 4 Ma em zircões de rochas vulcânicas da Formação Carajás.

Corpos de formação ferrífera são lenticulares, descontínuos, sendo melhor conhecidos e caracterizados nas zonas de ocorrência de corpos de minério de alto teor (Fe> 64%). A presença de formações ferríferas, minérios de alto teor e outros corpos monominerálicos de óxido de ferro de origem hidrotermal, tais como magnetititos, é comum na região, embora tais corpos não sejam obrigatoriamente de mesma idade ou sequer correlacionáves, temporal ou espacialmente entre si (Lobato *et al.* 2005b). Corpos maciços de óxidos de ferro estão também associados a corpos mineralizados em Fe-Cu-Au, Au e Cu em áreas distintas, tais como Igarapé-Bahia-Alemão, Cristalino, Serra do Rabo, Serra Pelada, Serra do Salobo e Sossego.

Complexos Máficos-Ultramáficos

Na Serra dos Carajás ainda ocorrem complexos máficos-ultramáficos, como os de Luanga (2763 ± 6 Ma; Machado *et al.* 1991), Serra das Onças, Vermelho e Santa Inês, intrusivos nas sequências metavulcanossedimentares.

O Complexo Granítico Estrela

O complexo Granítico Estrela (Barros 1997), que inclui granitos, monzonito miarolítico, sienito e diorito, é sinorogênico e intrusivo nas rochas metavulcanossedimentares do Supergrupo Itacaiúnas, ao longo de eixo de alongamento E-W, em 2,76 Ga (Barros *et al.* 2001), produzindo uma espessa auréola de metamorfismo de contato. A deformação foi predominantemente por achatamento, com desenvolvimento de xistosidade de orientação E-W, e milonitização local nas margens do plúton e nas encaixantes que incluem rochas metavulcânicas máficas, xistos de composição ultrabásica, formações ferríferas bandadas, quartzitos e rochas cálcio-silicáticas. Relações de campo e os trabalhos de petrografia metamórfica (Barros 1997) indicam que as rochas do Complexo Estrela, ou Suíte Estrela, intrudiram em ambiente crustal raso e tectonicamente ativo, interpretado em Lobato *et al.* (2005b) como associado ao fechamento das bacias do tipo retro-arco ou intra-arco, onde foram depositadas as sequências vulcanossedimentares. Esse representa o principal evento de deformação registrada na Província Carajás ao fim do Arqueano.

Dados geocronológicos de 2,56 Ga, para a cristalização do Granito Estrela, podem ser interpretados como representativos de uma idade mínima Pb-Pb. Entretanto, uma idade semelhante foi encontrada para o Granito Pojuca (Souza & Dall'Agnol 1996). Machado *et al.* (1991) determinaram idade de 2,57 Ga para o Granito Salobro Velho. Esta idade de plutonismo e/ou hidrotermalismo parece estar baseada em determinações de idade mínima Pb-Pb, necessitando consequentemente melhor definição (Lobato *et al.* 2005b).

A Suíte Granítica Plaquê

A suíte granítica cálcio-alcalina Plaquê compreende corpos intrusivos graníticos do tipo I, e de monzonito, alongados segundo a orientação E-W, incluindo variedades de trama variável entre equigranular e oftálmica, que intrudem as encaixantes principalmente a sul e leste da Província Carajás. Uma idade Pb-Pb de 2,74 Ga foi sugerida por Avelar *et al.* (1999) como a de intrusão. Os granitos Planato e Serra do Rabo, assim como o Diorito Cristalino, que hospedam parcialmente a mineralização Cu-Au, têm características semelhantes (Santos 2003). As relações de campo para essa suíte de rochas indicam uma intrusão sin-tectônica, semelhante ao Granito Estrela. As diferenças texturais são interpretadas em Lobato *et al.* (2005b) como diferenças de nível crustal e de erosão.

O Granito Serra dos Carajás e Suítes Granitóides Associadas

Os granitóides Serra dos Carajás, Musa, Cigano, Pojuca e suítes similares compreendem corpos plutônicos de granitos, álcali-granitos, granodioritos e dioritos de idade 1880 ± 2 Ma (Machado *et al*. 1991). Estas rochas são onipresentes no Craton Amazônico, a leste do arco magmático do Tapajós (Santos *et al.* 2002, Santos 2003). Os plútons não apresentam orientação preferencial e não mostram indícios de terem experimentado metamorfismo. Segundo Dall'Agnol *et al.* (2005), correspondem a suítes graníticas rapakivi tipo-A com idades modelo T_{DM} arqueanas e valores ε_{Nd} fortemente negativos (–12 to –8 em 1880 Ma), indicando derivação de crosta arqueana. Os granitos são alcalinos a cálcio-alcalinos, de modo que alguns autores os classificaram como anorogênicos (*e.g*., Dall'Agnol *et al.* 1999). Lobato *et al.* (2005b) sugerem, como alternativa, que tais granitóides sejam as manifestações intracontinentais de colisão continental distal ao arco magmático propriamente dito, estes representados por ambiente crustal tectônico distensivo, com possível herança radiogênica da placa subductada rasa e da litosfera associada. Recentemente, uma idade U–Pb SHRIMP de 1866 ± 4 Ma (Orestes S. Santos, comunicação verbal) foi obtida para o Granito Serra dos Carajás.

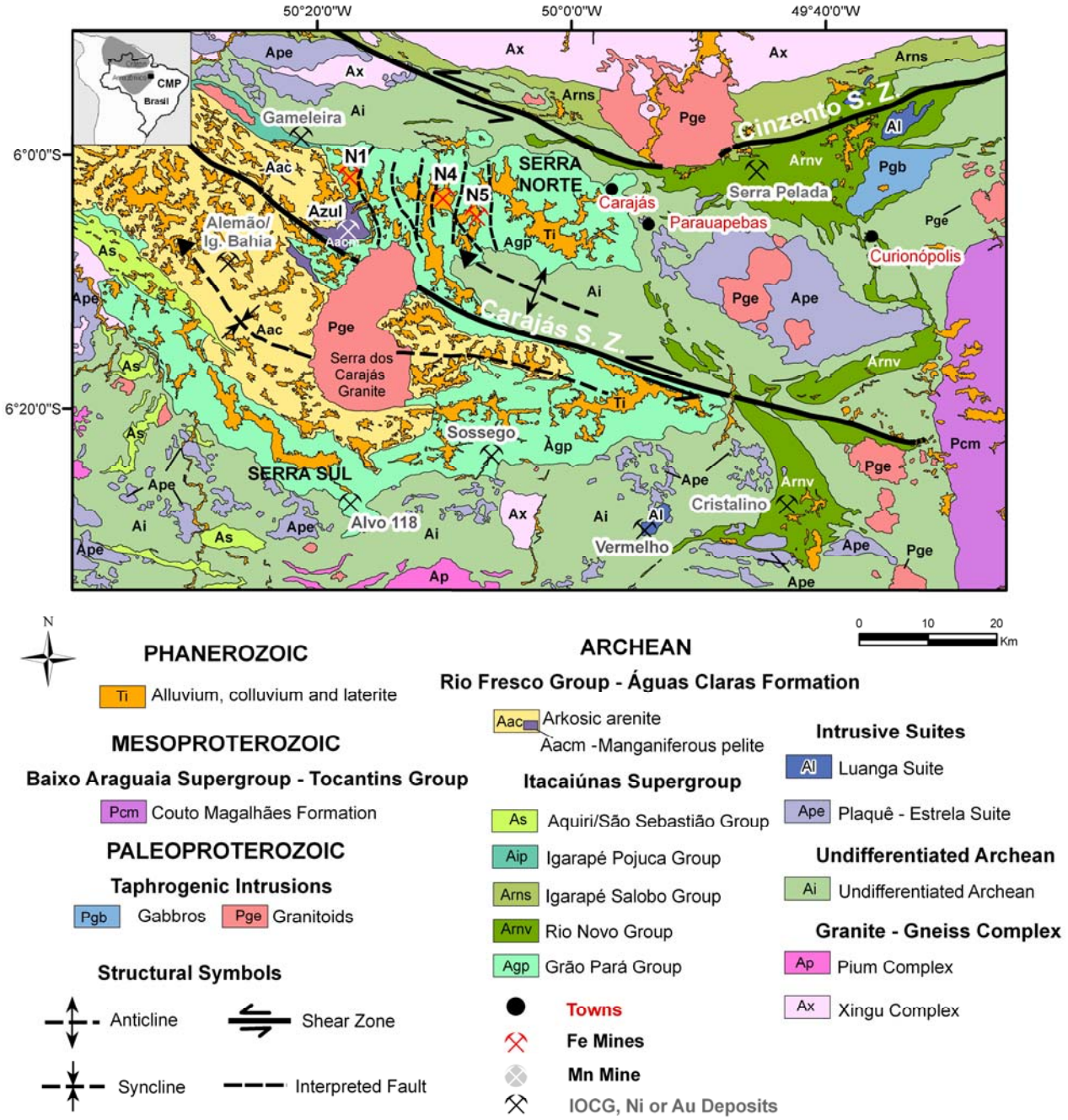

Figura 3 – Mapa geológico da região da Província Mineral Carajás (modificado de Rosiere *et al.* 2006, e Costa 2007) mostrando os principais recursos minerais, incluindo os depósitos de minério de ferro N1, N4 e N5 (Serra Norte), Serra Sul e Serra Leste; alguns depósitos *IOCG* (Alemão/Igarapé Bahia, Sossego, e Cristalino), sendo alguns Cu–Au (W-Bi-Sn) como os depósitos Gameleira e Alvo 118; o depósito Au-Pt-Pd de Serra Pelada; o depósito Mn Azul; e o depósito de Ni Vermelho. A classificação litoestratigráfica é adaptada a partir de dados de campo de Costa (2007) e interpretações de Seoane *et al.* (2004), baseadas em imagens Landsat ETM7 RGB 321, 752 e PC1-52.

A estrutura dominante da Serra dos Carajás é definida por Beisiegel *et al.* (1973) como um sinclinório de aproximadamente 1.000 km de comprimento e 100 km de largura, com eixo WNW-ESE. Araújo & Maia (1991) definiram o Cinturão de Cisalhamento Itacaiúnas, de orientação E-W, formado na porção norte pelos sistemas transcorrentes Carajás e Cinzento (Figura 3). O primeiro representa a descontinuidade mais destacada, com cerca de 130 km de comprimento (Pinheiro & Holdsworth 2000), e indicação cinemática predominantemente sinistral. Segundo Holdsworth & Pinheiro (2000), as deformações associadas à falha Carajás ocorreram em níveis crustais relativamente rasos (< 5 km), mas suas orientações seriam fortemente controladas por um *trend* de trama dúctil pré-existente nas rochas do embasamento (Pinheiro & Holdsworth 1997).

O domínio setentrional da falha contém corpos de minério de ferro dobrados, falhados e rotacionados, denominados N1 a N9 (na Serra Norte), além de corpos de minério na Serra Leste. Várias ramificações lístricas do tipo *splay,* de orientação N-S, controlam o posicionamento desses corpos. O domínio meridional inclui corpos de minério da Serra Sul, denominados S1 a S45, mergulhando para norte. Estes compõem um flanco sul da estrutura, sem aparente basculamento ou rotação de blocos.

Entretanto, a análise das estruturas em macro- e meso-escalas (Rosière *et al.* 2004, 2006) indica uma superposição de eventos. Esses podem ser interpretados de forma errônea, em função da complexidade geológica, da escassez de afloramentos, em grande parte das áreas, e do pequeno volume de informação detalhada e de domínio público (Lobato *et al* 2005b).

De acordo com Lobato *et al.* 2005b e Rosière *et al.* 2006, a continuidade regional das diferentes sequências vulcanossedimentares na Província Carajás apresenta uma estruturação aproximadamente NE-SW, dobrada com o desenvolvimento de um sistema de eixo com caimento moderado, aproximadamente para WNW, intersectado por diversas falhas de orientação geral E-W, subparalelas ao plano axial. A Serra Sul corresponde consequentemente ao flanco sul de um par sinforme-antiforme em forma de "S", denominado dobra de Carajás. A zona de charneira desta estrutura sinformal é angulosa e corresponde ao Platô da Água Boa. A Serra Norte corresponde ao antiformal conjugado, cujos flancos foram estirados, sendo a zona de charneira desmembrada em diversos blocos, alguns rotacionados (Rosière *et al.* 2006).

Uma análise estrutural detalhada da região é apresentada em Lobato *et al.* (2005b), utilizando como base **(i)** o geoprocessamento e interpretação lito-estrutural dos dados espectrais Landsat ETM7, **(ii)** modelo digital de terreno SRTM (NASA/JPL 2005, Seoane *et al.* 2004) e Imagem da Banda C de radar (NASDA/MITI 1998). Os mapas litológicos produzidos foram integrados nos mapas existentes (Rezende & Barbosa 1972, Araújo & Maia 1991, Faraco *et al.* 1996, Bizzi *et al.* 2001).

CAPÍTULO 5 – OS DEPÓSITOS DE FERRO

Os depósitos de ferro da Província Mineral Carajás distribuem-se ao longo da Dobra Carajás (Lobato *et al* 2005b, Rosière *et al.* 2006), contendo jaspilitos e minérios a hematita friável e compacta, contornados por rochas máficas vulcânicas predominantemente.

O minério hematítico ocorre como corpos friáveis de formato tabular a lenticular e irregular que envolvem lentes de corpos de minério duro, ambos inclusos em jaspilito (Jp). Na Serra Norte, correspondem a nove corpos (N1 a N9) com espessura aproximada de 250 a 300 metros e comprimento variando de centenas de metros a dezenas de quilômetros. Diques e *sills* de rocha máfica (diabásio) são comuns, com espessura de até algumas dezenas de centímetros, intercalados no minério (CVRD 1996).

Os minérios de alto teor podem ser do tipo hematita mole-macia (HM) e do tipo duro e compacto (HD). Os corpos de minério HD têm forma tabular e lenticular com espessura de até 50 m, em contatos abruptos e gradacionais. Acham-se, preferencialmente, em contato com rocha máfica da base. Têm cor cinza azulada e brilho metálico, sendo bastante densos com baixa porosidade. Podem ser bandados, caracterizados por um bandamento original do jaspilito preservado, definido por níveis compactos alternados por níveis porosos ou brechados (Rosière & Chemale Jr. 2000), apresentando fragmentos de rocha. Esses minérios também podem ser maciços, com trama original totalmente destruída, compostos por agregados de cristais de hematita. O teor deste tipo de minério é maior que 64% de ferro.

Os minérios acham-se localmente contaminados, com enriquecimento em: manganês, na região de contato entre o corpo de minério e a rocha máfica inferior; alumina e fósforo, no contato entre minério e rocha máfica superior; sílica, em profundidade; manganês, e fósforo em faixas de cisalhamento (CVRD 1996).

Os minérios de alto teor do tipo mole-macio-HM são comumente bandados, localmente exibindo planos de laminação primária. Podem alcançar até 350 m de espessura e conter os seguintes contaminantes: alumínio, manganês e fósforo. Consistem em material hematítico friável de cor cinza e brilho metálico, com alta porosidade; podem ser pulverulentos e se desagregam em pequenos fragmentos (placóides ou não). Caracterizam-se por teor médio de 64%.

O minério classificado como de baixo teor-MBT apresenta uma alta contaminação, com valores de silício> 1%, fósforo> 0,07%, alumínio> 1,2%, óxido de manganês> 1% e valores de ferro entre 50 e 60% (Lopes 1997).

Minérios de ferro e rocha máfica decomposta são recobertos por canga, material limonítico pobre em fragmentos detríticos, formado nas camadas mais superficiais dos depósitos.

A descrição detalhada dos depósitos estudados encontra-se no item **Iron Ore Deposits** - *Geological setting of the N1, N4 and N5 deposits,* página 70 no artigo do Anexo 1.

As figuras 4 e 5 apresentam os mapas dos depósitos N4E e N5E, baseados em dados fornecidos pela Vale, onde encontra-se a maior parte dos minérios estudados. Também são apresentadas seções geológicas esquemáticas com base em dados de furos de sondagem.

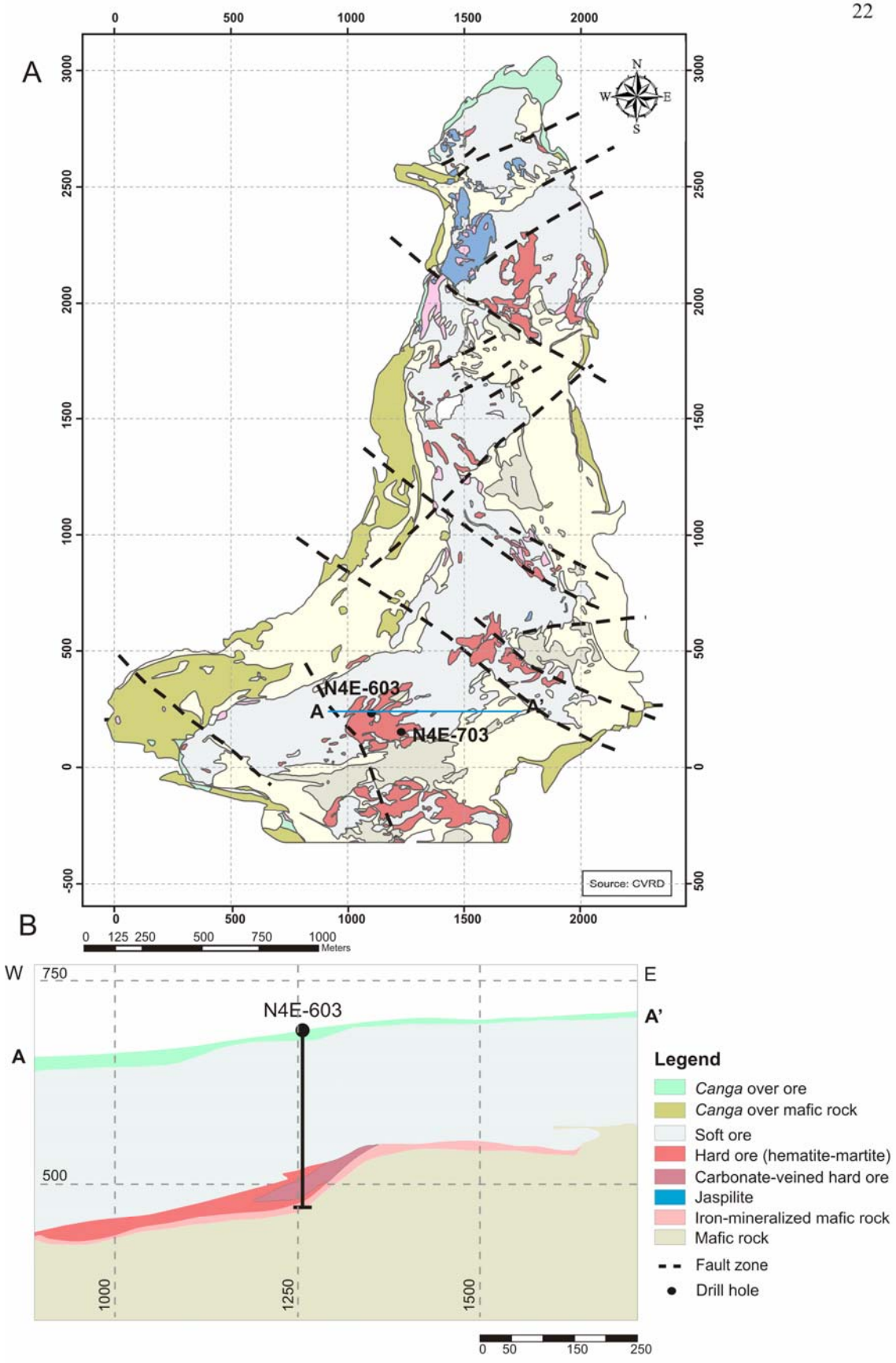

Figura 4 – A. Mapa litoquímico do depósito N4E com localização de furos de sondagem amostrados. B. Seção geológica esquemática.

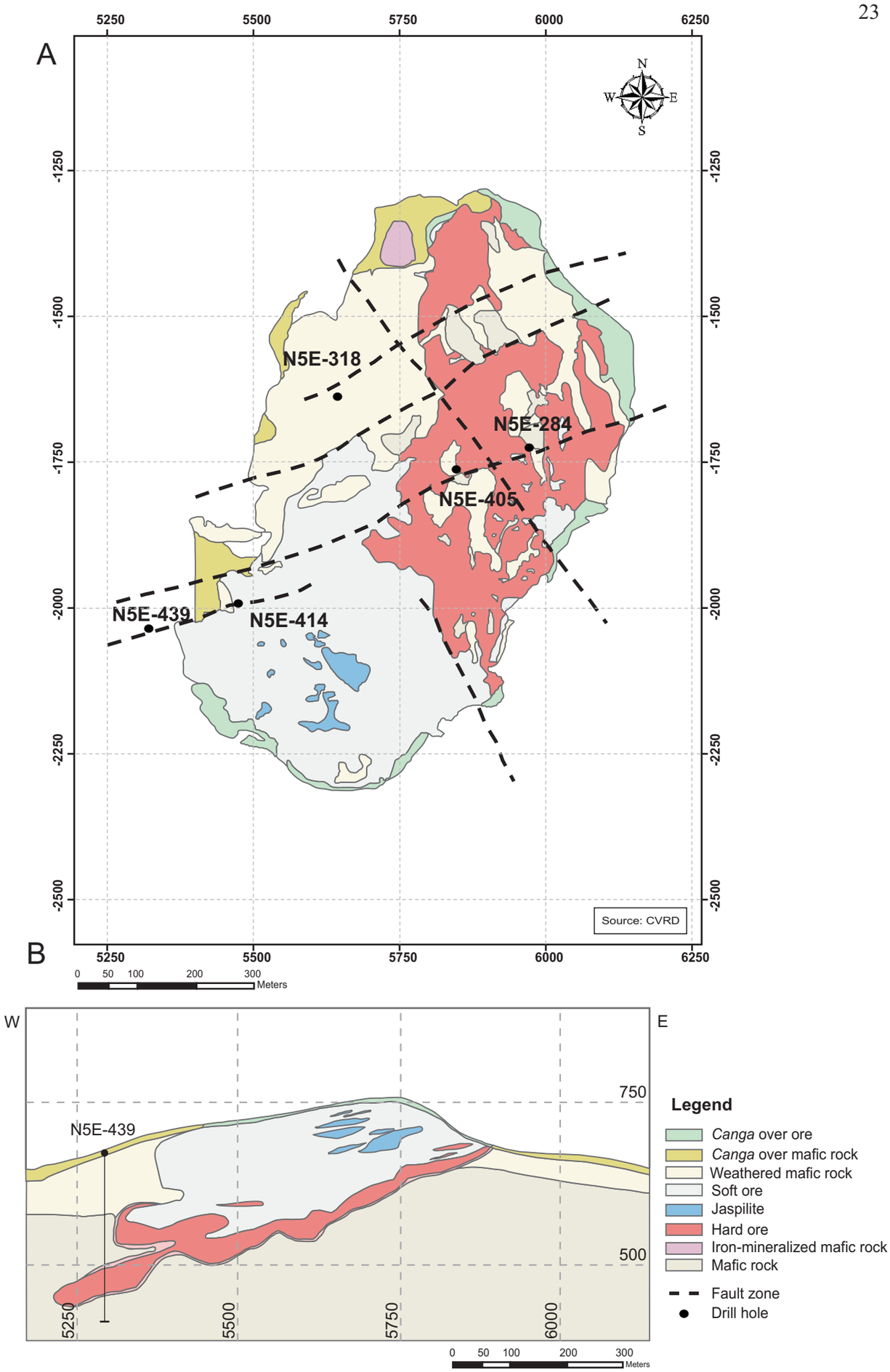

Figura 5 – A. Mapa litoquímico do depósito N5E com localização de furos de sondagem amostrados. B. Seção geológica.

CAPÍTULO 6 – ESTUDOS PETROGRÁFICOS

Jaspilitos com variados graus de alteração hidrotermal e diferentes tipos de minério tipo HD são os tipos petrográficos estudados, provenientes dos depósitos N4E, N4W, N5E, N5S e N1. Os jaspilitos correspondem ao protominério e são caracterizados essencialmente pela intercalação de bandas de jaspe e *chert* (e/ou carbonato) com bandas de minerais opacos (hematita microcristalina principalmente). Os minérios são classificados conforme a composição mineralógica em associações à hematita ± martita; martita-hematita venulada; hematita e carbonato.

Diversos trabalhos anteriores tratam igualmente das características petrográficas de jaspilitos da Formação Carajás (Meirelles 1986, Silva 1994, Lopes 1997, Pereira 1999, Guedes 2000, Lindenmayer *et al*. 2001, Macambira 2003), mas poucos discutem a petrografia dos minérios de ferro (Figueiredo e Silva 2004, Figueiredo e Silva *et al.* 2004, Lobato *et al.* 2004, 2005a, Dalstra & Guedes 2004).

Os resultados dos estudos petrográficos, incluindo a classificação mineralógica dos óxidos de ferro, estão apresentados nos itens **Iron Ore Deposits -** *Mesoscopic classification of ore types*, página 69 e **Petrography of Jaspilite and Hard Ore,** página 76 do texto do Anexo 1. As principais características dos minérios estão apresentadas na Table 2, página 78 do mesmo anexo.

6.1 – Classificação dos veios-brechas

Inicialmente foram detalhados cerca de 20 furos de sondagem dos depósitos N4 e N5 com descrição petrográfica e textural de veios e brechas. Com base nessa avaliação, foi sugerida uma classificação na tentativa de estabelecer a cronologia dos veios em relação à mineralização de ferro.

Uma nova classificação, baseada também no estudo de inclusões fluidas, é adotada no presente trabalho, e difere-se da classificação original apresentada no resumo do SGA (Figueiredo e Silva *et al.* 2007a). Por exemplo, verifica-se que os veios e brechas têm distribuição irregular, não sendo muito clara na maioria das vezes a relação temporal entre eles. A distinção mais geral no conjunto de veios é a presença ou não de hematita. A classificação mais detalhada, juntamente com as zonas de alteração hidrotermal está apresentada nos itens **Hydrothermal Alteration** (página 80) e **Serra Norte Iron Ore Deposits: Geological Setting and Hydrothermal Alteration Zonation** (página 135) nos artigos dos anexos 1 e 2, respectivamente.

A partir dos estudos petrográficos, e da definição das zonas de alteração hidrotermal, a sequência de formação dos óxidos de ferro hidrotermais foi estabelecida, conforme esquema da Figura 6.

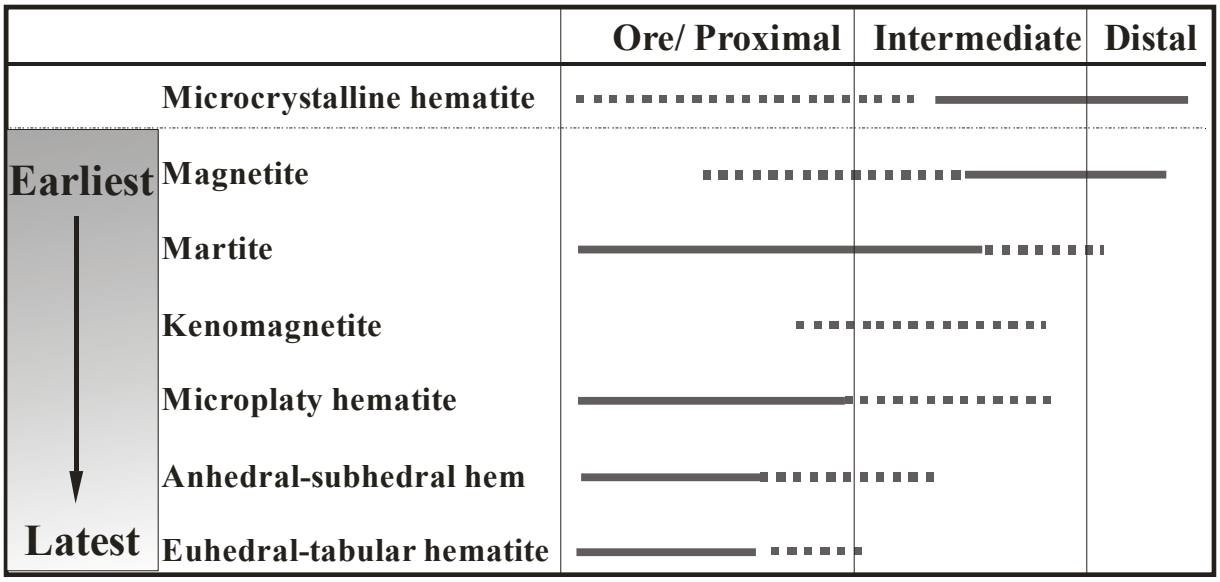

Figura 6 – Proposta geral de sequência de formação de óxidos de ferro hidrotermais em amostras de jaspilito mineralizado e minérios de ferro nas zonas de alteração distal, intermediária e proximal.

CAPÍTULO 7 – QUÍMICA MINERAL

As análises de química mineral foram realizadas pela doutoranda durante a permanência na Austrália e incluem análises quantitativas *WDS* (*wavelength dispersive spectroscopy*) em variados tipos de carbonato de veios e brechas, em jaspilitos e minérios, além de análises *in situ* nos diferentes tipos de óxido de ferro conforme sequência mineralógica estabelecida (Figura 6). Imagens de elétrons retroespalhados e análises qualitativas *EDS (energy dispersive spectroscopy)* foram realizadas com o objetivo de confirmar a presença de cristais de monazita, principalmente em amostras de minério de ferro. Estas análises foram realizadas pelo Dr. Luis Garcia no Laboratório de Microanálises do Departamento de Física da UFMG. As informações acerca do método utilizado para cada um dos tipos de análises, número de amostras, objetivos e resultados parciais são apresentados nos itens 7.1 e 7.2 a seguir.

7.1 – Microssonda eletrônica e MEV em carbonatos e óxidos de ferro

Análises químicas quantitativas foram realizadas em carbonato por microssonda eletrônica e imagens de variados tipos de óxidos de ferro por MEV - micróscopio eletrônico de varredura, no Centro de Microscopia e Microanálises na University of Western Australia, sob coordenação da Dra. Janet Muhling.

As análises em microssonda eletrônica JEOL, modelo JXA 8900RL, objetivaram a determinação da composição de carbonato (Tabela 2) em veios e brechas de jaspilito e minério de ferro, para posterior análise isotópica. As imagens adquiridas por MEV em óxidos de ferro (magnetita, variados tipos de hematita) visaram a identificação de zonamento nestes minerais, bem como a identificação de inclusões de monazita (ou xenotima), como auxílio na seleção de áreas analisadas no ICP-MS através de ablação a laser.

Tabela 2. Composição de cristais de carbonato analisados em microssonda.

Amostras	Carbonato	Ocorrência	Média composição %			
			MgO	FeO	MnO	CaO
N4E2A2B(C) – Jaspilito	Calcita	Vênulas e porções	0.38	0.34	3.67	50.63
N4E3A – Jaspilito	Calcita	Vênulas e porções c/ *chert*	0.23	0.04	4.36	53.11
N5SF825P235,25	Kutnahorita	Veio c/ Qtz (V1a)	9.81	13.37	5.63	28.00
N5SF825P276,40	Kutnahorita	Brecha (V1a) Contato JP-máfica	11.47	12.74	8.56	32.56
N4EF703P77,60	Calcita	Veios (V1b)	0.20	0.42	1.50	55.00
N4EF703P77,60B	Calcita	Veios (V1b)				
N4EF703P98,35	Calcite	Veios (V1b)	0.20	0.40	1.00	54.00
	Dolomita		15.00	8.50	2.00	29.00
N4EF703P123,90	Kutnahorita	Veio (V1b)	15.60	6.84	4.91	29.75
N4EF603P43,40 HD brechado	Kutnahorita	Veio-brecha (V4)	17.5	1.31	3.71	31.15
N4EF603P53,50 HD brechado	Kutnahorita	Intrabandamento (V5)	16.33	1.82	4.53	30.39
N5E439P247 HD brechado	Dolomita	Veios ao longo do bandamento (V5)	20.18	0.86	1.70	30.08

7.2 – *Laser ablation ICP-MS* em óxidos de ferro

Análises minerais *in situ* por espectroscopia *laser* (New Wave UP-213 Nd:YAG Q-switched Laser Ablation System) de massa com plasma acoplado (HP4500 Quadrapole ICP-MS) - *laser inductively coupled plasma-mass spectrometry – ICP-MS* – foram realizadas nos óxidos de ferro (cerca de 500 análises em cristais de hematita-magnetita). Os baixos limites de detecção dessas análises permitiram a determinação de enriquecimento em certos elementos traços em diferentes tipos de hematita, magnetita, sulfetos e carbonato. Este estudo foi realizado em duas etapas, dezembro de 2005 e março de 2006, no Centre for Ore Deposit Research - CODES na University of Tasmania, Austrália, em colaboração com o geólogo Dr. Leonid Danyushevsky e sob orientação da geóloga Sarah Gilbert. O equipamento foi manuseado pela própria estudante, após explanação técnica sobre o método e programa utilizado. Do mesmo modo, os cálculos também foram realizados pela estudante para obtenção das concentrações em PPM em cada ponto analisado.

Um total de 32 elementos (Mg, Al, Ti, V, Mn, Co, Ni, Cu, Zn, As, Sr, Y, Zr, Nb, Mo, Ba, La, Ce, Nd, Sm, Eu, Gd, Dy, Er, Yb, Lu, W, Au, Pb, Th, U) foram analisados em 25 amostras (de 15 a 20 pontos em cada), incluindo óxidos de jaspilitos mineralizados e minérios de ferro de alto teor (Tabela 3). As amostras de rocha foram preparadas em epoxy com diâmetro de 1 polegada e polidas. Os óxidos de interesse são previamente mapeados e identificados em microscópio ótico, e as áreas são circuladas e fotografadas para identificação. A ablação das amostras é feita em uma atmosfera de He de alta pureza que flui na câmara de amostras. Fora da câmara, He é misturado com Ar para transportar o material abladado, antes de seguir em direção ao ICP-MS. O tamanho da abertura do laser (*laser spot size*) varia de acordo com a granulação do mineral analisado, desde 8 até 110 μm, e a energia utilizada é entre 10-14Hz. Análises de padrões são realizadas a cada 2 horas para corrigir possíveis *shifts* do instrumento durante o dia. O padrão STDGL2b-2 é utilizado para análises de óxidos (Danyushevsky et al. 2003, 2004). O detector do ICP-MS mede o número de 'tiros' de uma simples massa iônica sobre um determinado período de tempo, convertendo-os para contagens por segundo (cps). Uma ablação a baixos pulsos (1-2 Hz) deve ser realizada por alguns segundos para remoção de qualquer contaminação na superfície da amostra antes da análise. Cálculos são realizados no programa excel para eliminar picos de interferência nos espectros obtidos.

Os dados obtidos estão parcialmente apresentados no resumo expandido do Anexo 3, página 220.

Tabela 3. Amostras de jaspilitos e minérios de alto teor analisadas pelo método *laser ablation* ICP-MS.

Amostra	Rocha	Minerais
N4EF703P89,85(8)	Jp	Magnetita, sulfeto & Carb
N4EF703P98,35 (10A)	Jp	
N4EF703P123,65(12)	Jp	
N1F082P107,70	BIF	
N4WF693P103	Jp	Martita c/ kenomagnetita
N4EF603P38,60	HD	Martita & Carb
N4EF603P53,50(B)	HD	
N4EF603P43,40	HD brechado	
N5EF439P247,00	HD	Hematita anédrica & Carb
N4EF621P55,40	Máfica mineralizada	Hematita lamelar
N5EF284P32,65	HD	Hematita microlamelar
N4EF621P50,15	HD	
N5SF817P111,10	FFB c/ magnetita	Magnetita
N5SF825P235,25	Jp c/ sulfeto em veio V1a	
S11DF130P132,25	FFB c/ blastos de magnetita	
N5WF556P121,90	Jp	Martita
N5EF040P251,80	HD c/ veios de hematita	Martita & Hem
N1F08P54,30	HD	Martita (Kmag & Goe)
N1F08P61	HD	Martita & Hem
N4EF603P55,50	HD c/ veios de Qtz V5	Martita
N5SF771P182,25	Jp c/ veios de Hem	Sub-AHem & THem
N5EF440P96,00	HD brechado	AHem-SubHem & THem
N5EF439P249,80	HD brechado	AHem
N5EF414P257,00	HD brechado	AHem & MpHem

Abreviações: Carb – carbonato; AHem, MpHem, SubHem, THem – hematita anédrica, microlamelar, subédrica, tabular; Goe – goethita; HD – minério duro; Jp – jaspilito; FFB – formação ferrífera bandada; Kmag – kenomagnetita; Qtz – quartzo

CAPÍTULO 8 – GEOQUIMICA DE ROCHA TOTAL

A concentração de elementos maiores, traços e terras raras em rocha total foi obtida em cinquenta amostras, a maior parte de minério de ferro tipo HD, pelos métodos ICP-ES e ICP-MS, no laboratório ACME Analytical Laboratories Ltd., em Vancouver, Canadá. Os resultados estão apresentados no diagrama da Figura 7 a seguir, além de descrições no item **Geochemistry -** *Whole-rock geochemistry* (página 87) e Discussion - *From jaspilite to ore: the REE fingerprint* (página 102) do texto do Anexo 1.

Vale ressaltar que parte dos dados (cerca de trinta e duas amostras incluindo jaspilitos, e minérios de ferro tipo HD com ou sem carbonato) apresentados no artigo do Anexo 1 foi extraída da dissertação de mestrado da estudante (Figueiredo e Silva 2004), a título de comparação com as análises do presente trabalho.

A Figura 7 apresenta o padrão de distribuição de elementos terras raras em 32 amostras que incluem minérios tipo compacto dos depósitos N5S e N5E, minérios brechados com carbonato do depósito N5E, e amostras de jaspilito do depósito N5S (Tabela 4). Estes dados foram obtidos em março deste ano e por esse motivo não puderam ser incluídos no artigo do Anexo 1.

Há um acentuado aumento na concentração dos elementos terras raras (principalmente leves) de amostras de minério a hematita de N5S (Figura 7B), quando comparados aos jaspilitos (Figura 7A) do mesmo depósito. No entanto, nota-se que a anomalia positiva de európio é mantida em todas as amostras de minério, sugerindo que este pode corresponder ao jaspilito mineralizado, mantendo, portanto, o padrão similar ao dos jaspilitos analisados. Já minérios a hematita do depósito N5E (Figura 7C), exibem discreta a ausente anomalia de európio e padrão quase horizontal, com notável aumento de elementos terras raras pesados. Os minérios de N4E que contem carbonato (Figura 7D), exibem as mais baixas concentrações de ETR, com exceção de uma amostra, como já anteriormente descrito para este tipo de minério (Anexo 1).

Tabela 4. Concentrações de elementos maiores, traços e terras raras em amostras de minérios a hematita tipo HD do depósito N5E, jaspilito mineralizado e minérios de ferro do depósito N5S.

	N5E hematite ores													
Drill Core	**F561**	**F571**	**F571**	**EF571**	**F577**	**F577**	**F577**	**F577**	**F577**	**F572**	**F572**	**F529**	**F529**	**F529**
Depth	**P156,75**	**P84,00**	**P90,55**	**P214,30**	**P222,25**	**P242,25**	**P257,86**	**P261,55**	**P445,40**	**P267,90**	**P382,85**	**P91,30***	**P100,40***	**P120,70***
SiO_2(%)	1.17	0.56	0.43	3.35	1.52	0.39	0.62	0.67	0.70	1.76	1.83	2.30	1.50	1.99
Al_2O_3(%)	0.35	0.30	0.18	2.49	1.09	0.09	0.31	0.27	0.65	1.25	1.51	0.11	0.11	0.20
Fe_2O_3(%)	98.77	99.10	99.55	93.64	96.74	100.18	99.26	99.03	98.60	96.60	95.06	100.36	96.75	52.55
MgO(%)	–	–	–	–	–	–	–	–	–	–	–	0.51	1.49	1.10
CaO(%)	0.01	0.02	0.02	0.03	–	0.01	–	0.02	–	–	0.01	0.93	2.89	23.93
Ba	29.0	16.0	11.0	63.0	58.0	36.0	14.0	49.0	33.0	17.0	23.0	6.0	2.0	8.0
Co	1.9	0.2	0.7	4.7	0.9	–	0.3	1.7	3.7	1.7	2.0	3.3	4.4	2.3
Cs	0.1	0.2	–	0.2	0.4	0.3	0.2	0.2	–	–	–	–	–	–
Ga	1.0	–	–	1.2	1.2	–	0.5	0.6	1.3	1.5	2.3	1.3	1.5	1.8
Hf	–	–	–	–	–	–	–	–	–	–	–	–	–	–
Nb	0.7	0.2	0.2	0.6	–	–	0.1	–	0.6	–	0.4	–	–	–
Rb	0.5	0.4	–	0.4	2.4	1.8	0.9	1.0	–	–	–	0.2	0.1	–
Sn	–	–	–	–	–	–	–	–	4	–	6	2	3	–
Sr	2.4	2.2	3.2	2.2	4.0	2.3	1.9	2.4	4.8	3.4	3.1	1.8	2.2	186.5
Th	0.3	0.3	–	0.2	–	–	–	–	–	–	–	–	–	–
U	38.9	2.0	3.1	7.1	5.0	7.4	6.2	3.1	31.7	6.3	85.4	1.0	1.2	1.0
V	578.0	43.0	34.0	94.0	70.0	45.0	73.0	72.0	1505.0	171.0	2140.0	45.0	14.0	94.0
W	1.8	–	–	0.7	–	–	0.5	–	3.8	0.6	2.2	–	–	1.6
Zr	1.8	0.7	–	0.5	–	–	–	–	0.3	–	–	–	–	–
Y	4.2	3.0	2.3	2.8	3.7	4.1	5.9	4.7	3.9	6.9	7.6	1.2	3.0	13.9
Mo	0.7	0.5	1.7	0.6	0.5	0.5	0.4	0.4	0.3	0.5	0.4	1.1	1.1	0.7
Cu	47.1	7.0	9.6	81.1	7.0	4.9	9.5	9.9	14.1	27.2	20.9	28.5	17.1	14.6
Pb	7.1	5.8	3.0	6.5	6.4	4.4	4.4	6.0	5.9	7.6	4.3	3.7	3.6	5.5
Zn	13.0	6.0	56.0	12.0	6.0	5.0	7.0	23.0	7.0	19.0	12.0	9.0	6.0	16.0
Ni	5.0	3.0	4.0	7.3	3.1	2.9	3.5	2.9	3.8	3.8	4.1	10.9	11.9	3.2
As	0.8	0.7	0.7	0.9	–	–	–	–	–	–	–	3.5	3.3	1.2
Sb	0.5	0.4	0.4	0.4	0.2	0.4	0.4	0.3	0.3	0.3	0.2	1.6	1.8	0.3
Bi	0.4	–	0.2	0.1	0.1	0.1	0.1	0.1	0.3	0.4	0.1	0.2	0.3	0.9
Au	5.4	0.9	3.8	2.2	1.1	1.8	0.6	0.6	1.3	4.9	1.5	1.8	1.5	0.5
La	3.6	3.6	3.0	3.4	3.5	7.5	5.5	6.1	4.8	3.6	7.5	2.1	2.4	10.4

Ce	6.4	4.3	4.4	3.9	5.8	9.7	5.4	4.0	5.3	6.6	10.8	2.7	3.7	16.6
Nd	2.9	1.8	2.8	1.8	3.3	6.9	6.1	8.2	3.6	4.5	5.0	1.5	1.8	8.0
Sm	0.69	0.34	0.64	0.41	0.75	1.33	1.39	1.71	0.71	1.22	0.84	0.26	0.48	1.99
Eu	0.31	0.20	0.23	0.21	0.28	0.49	0.57	0.58	0.25	0.50	0.32	0.11	0.19	0.73
Gd	0.75	0.37	0.50	0.45	0.83	1.15	1.51	1.43	0.78	1.44	1.28	0.25	0.52	2.43
Tb	0.14	0.07	0.09	0.09	0.13	0.17	0.21	0.21	0.13	0.22	0.19	0.05	0.10	0.33
Dy	0.71	0.38	0.39	0.43	0.81	0.88	1.18	0.95	0.61	1.18	1.22	0.15	0.43	1.58
Ho	0.12	0.06	0.07	0.07	0.12	0.12	0.17	0.15	0.12	0.19	0.25	0.03	0.08	0.30
Er	0.31	0.16	0.15	0.16	0.31	0.34	0.40	0.32	0.28	0.49	0.62	0.10	0.20	0.74
Tm	0.06	0.04	0.03	0.05	0.06	0.05	0.06	0.05	0.04	0.08	0.09	0.02	0.04	0.10
Yb	0.24	0.11	0.10	0.16	0.27	0.23	0.33	0.26	0.25	0.31	0.38	0.06	0.14	0.64
Lu	0.04	0.03	0.02	0.03	0.05	0.04	0.05	0.03	0.04	0.05	0.07	0.01	0.03	0.11

* carbonate-bearing ore samples

	N5S hematite ores																
Drill Core	**F897**	**F836**	**F817**	**F836**	**F817**	**F897**	**F897**	**F910**	**F910**	**F904**	**F904**	**700**	**F686**	**F686**	**686**	**F686**	**F686**	**F686**
Depth	**183,20**	**232,45**	**278,20***	**234,80**	**349,83**	**132,20**	**252,50**	**253,35**	**263,35**	**107,40**	**134,85**	**279,60**	**136,60**	**143,10***	**152,65***	**163,15***	**163,40**	**169,90**
SiO_2(%)	32.66	1.81	55.40	1.79	1.37	0.59	4.59	7.28	2.85	1.96	1.01	3.71	2.27	29.46	34.12	13.74	2.12	15.70
Al_2O_3(%)	0.73	0.91	0.25	0.67	0.73	0.28	0.07	0.15	0.07	0.15	0.27	2.22	1.08	0.34	0.37	0.19	0.70	1.43
Fe_2O_3(%)	67.43	97.17	55.05	97.58	98.73	100.00	95.19	90.95	96.89	98.96	98.32	93.14	94.93	71.01	65.08	86.92	97.02	82.04
MnO(%)	0.07	0.19	0.21	0.05	0.16	0.19	0.43	0.77	0.75	0.13	0.10	0.27	0.24	0.10	0.09	0.08	0.23	0.11
Ba	10.0	5.0	14.0	14.0	100.0	44.0	37.0	58.0	80.0	21.0	24.0	18.0	9.0	9.0	17.0	18.0	57.0	14.0
Co	1.2	3.2	10.2	1.0	1.1	0.9	2.5	7.5	4.0	0.5	0.6	3.2	5.9	2.8	5.3	3.0	1.2	4.4
Cs	–	0.1	–	0.3	0.2	0.2	0.3	0.4	0.4	0.2	0.4	–	–	–	0.2	–	0.1	–
Ga	0.8	1.7	2.3	1.0	1.4	–	0.8	1.3	0.8	0.6	0.6	4.9	3.2	1.0	1.5	0.9	1.1	2.6
Hf	–	–	–	0.1	0.1	–	–	0.1	–	–	–	–	–	–	0.1	–	–	0.2
Nb	1.0	–	1.1	0.7	0.7	0.4	0.9	1.9	0.2	0.4	0.5	0.7	1.3	0.7	1.5	1.1	–	2.2
Rb	0.2	0.3	0.6	0.6	0.9	0.6	0.7	1.4	1.4	1.1	0.8	0.7	0.8	0.3	2.0	0.5	0.7	0.5
Sr	2.2	1.3	4.2	2.1	2.9	18.3	9.6	16.6	8.7	10.3	5.1	4.0	–	1.6	2.6	1.3	1.7	1.4
Th	–	0.9	–	1.2	0.7	0.3	0.2	0.4	–	0.3	–	–	–	–	0.4	0.5	–	1.3
U	3.6	1.8	0.9	1.6	3.9	3.1	1.1	1.2	1.3	1.0	1.1	0.3	1.0	0.2	0.9	0.7	11.5	4.9
V	122	183	18	96	138	75	33	27	24	55	17	252	329	66	26	38	1128	214
W	1.6	0.6	0.7	0.6	0.5	1.5	0.6	1.2	–	0.9	–	1.0	1.1	2.2	0.9	1.5	1.2	3.0
Zr	–	0.6	2.2	3.5	5.3	2.5	3.0	4.5	1.9	3.4	1.8	2.0	0.8	0.5	4.6	1.7	0.1	2.9
Y	2.1	3.7	1.6	2.8	4.1	5.3	7.3	10.6	7.0	6.5	2.2	3.6	2.8	3.2	1.6	4.7	2.9	3.6
Mo	0.6	0.7	1.2	0.5	0.7	1.8	1.2	0.7	0.7	0.3	0.5	1.4	0.2	0.4	0.2	0.4	0.6	0.3

Cu	8.5	451.1	58.7	219.3	140.2	17.9	4.4	19.9	15.9	6.5	7.6	119.0	275.5	33.9	57.7	29.0	61.5	31.5
Pb	5.2	9.1	4.1	5.8	7.0	3.5	4.3	3.2	3.9	3.1	3.2	5.6	5.8	3.7	7.3	7.2	11.2	7.4
Zn	7.0	44.0	9.0	17.0	19.0	7.0	6.0	6.0	16.0	4.0	3.0	16.0	39.0	13.0	22.0	12.0	41.0	39.0
Ni	4.8	5.1	14.1	4.1	6.5	3.0	5.5	5.3	12.2	2.7	4.3	7.5	5.9	4.4	4.2	6.0	3.1	3.1
As	–	0.8	4.4	0.7	1.7	0.6	0.7	0.6	1.3	0.5	0.8	0.9	1.3	–	0.6	–	–	–
Sb	0.6	0.5	2.4	0.5	0.5	0.4	0.5	0.2	0.5	0.5	0.4	0.5	0.3	0.4	0.3	0.6	0.3	0.2
Bi	0.2	1.5	0.1	0.8	0.2	0.1	–	–	0.1	–	–	–	0.7	–	0.2	0.1	0.2	0.2
Ag	–	1.8	0.5	0.3	–	–	–	0.3	0.1	–	–	–	0.1	–	–	–	–	–
Au	1.6	2.8	2.1	1.2	1.8	4.9	0.7	1.8	2.5	1.1	1.9	1.0	4.3	8.5	1.6	1.9	25.7	1.6
La	3.8	3.7	2.2	3.9	3.1	70.9	22.5	6.5	6.6	15.0	3.9	3.2	2.2	2.8	3.6	5.6	4.1	3.7
Ce	6.8	6.2	2.0	5.5	4.8	104.4	33.7	8.5	8.5	18.3	6.2	4.8	8.1	4.2	2.7	8.4	6.9	4.6
Pr	0.73	0.77	0.32	0.66	0.50	11.48	3.98	1.18	1.12	3.67	0.91	0.74	0.49	0.54	0.30	0.86	0.56	0.66
Nd	3.20	2.40	1.10	2.20	1.40	35.60	14.50	4.30	3.80	16.70	3.80	2.60	1.50	2.00	0.70	2.60	1.50	2.50
Sm	0.54	0.59	0.24	0.56	0.34	4.01	2.64	1.24	1.05	3.86	0.82	0.69	0.45	0.54	0.18	0.47	0.26	0.39
Eu	0.28	0.39	0.13	0.24	0.23	1.09	0.95	0.63	0.52	1.84	0.41	0.23	0.15	0.25	0.10	0.45	0.32	0.26
Gd	0.54	0.57	0.31	0.62	0.37	2.00	2.35	1.68	1.33	3.68	0.88	0.77	0.46	0.55	0.17	0.43	0.29	0.36
Tb	0.09	0.10	0.05	0.11	0.07	0.24	0.34	0.32	0.25	0.47	0.12	0.14	0.10	0.10	0.04	0.08	0.05	0.07
Dy	0.48	0.47	0.20	0.59	0.36	0.96	1.47	1.67	1.28	1.79	0.50	0.57	0.54	0.46	0.20	0.38	0.26	0.39
Ho	0.08	0.09	0.05	0.10	0.09	0.18	0.21	0.28	0.20	0.24	0.07	0.08	0.10	0.07	0.06	0.08	0.04	0.08
Er	0.16	0.23	0.09	0.22	0.25	0.38	0.48	0.67	0.51	0.45	0.12	0.22	0.28	0.22	0.13	0.24	0.16	0.24
Tm	0.02	0.03	0.02	0.04	0.05	0.06	0.08	0.10	0.08	0.07	0.03	0.04	0.06	0.04	0.03	0.05	0.03	0.05
Yb	0.14	0.18	0.08	0.21	0.24	0.31	0.35	0.52	0.39	0.34	0.12	0.21	0.30	0.14	0.14	0.23	0.15	0.27
Lu	0.03	0.04	0.02	0.04	0.05	0.05	0.06	0.08	0.06	0.05	0.03	0.04	0.05	0.03	0.03	0.05	0.03	0.06

* altered jaspilites

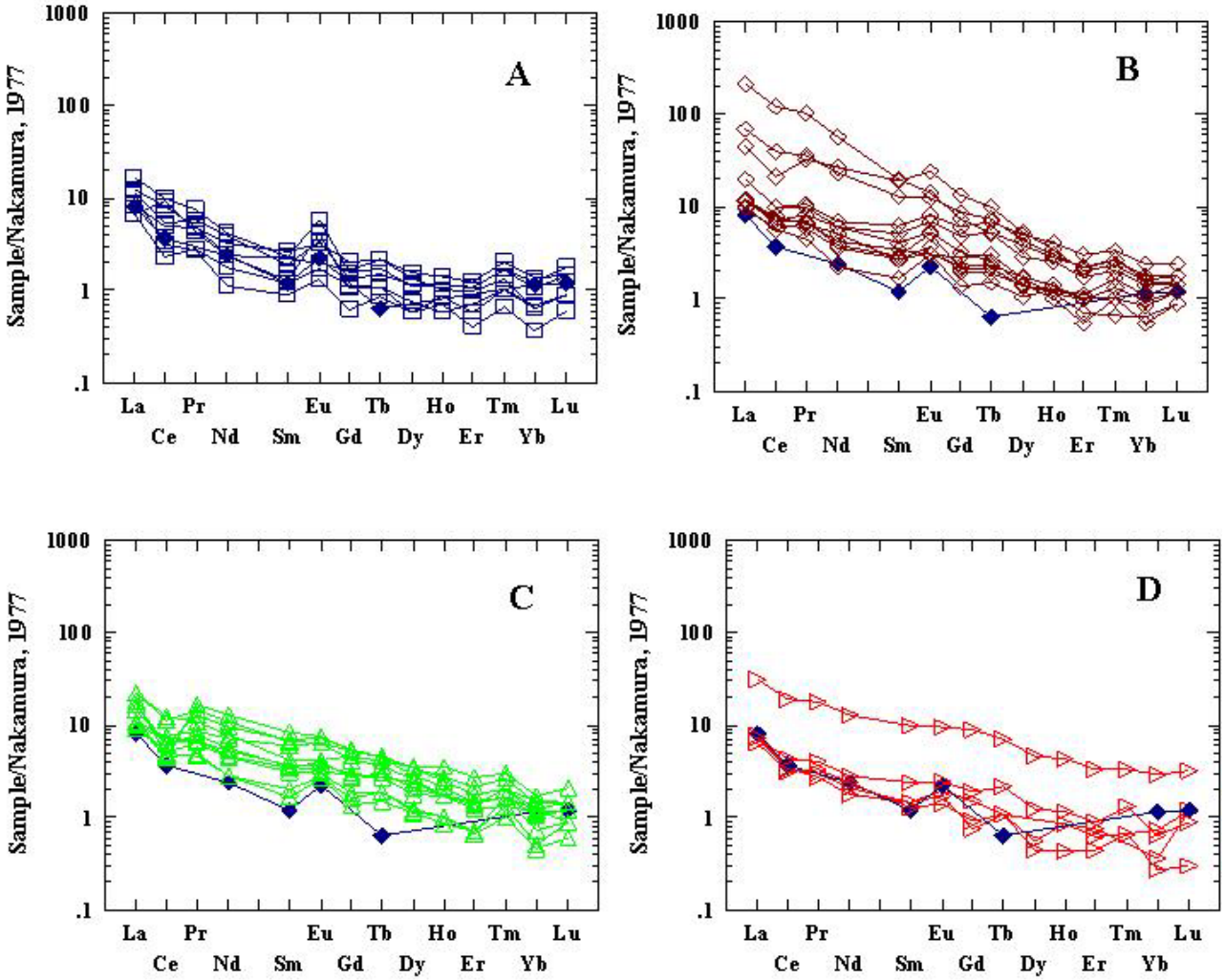

Figura 7 – Diagrama de distribuição de elementos terras raras, normalizados por condrito (Nakamura 1974), obitidos em: A. Jaspilitos alterados hidrotermalmente do depósito N5S; B. Minérios a hematita do depósito N5S; C. Minérios a hematita do depósito N5E; D. Minérios brechados com carbonato – depósitos N4E e N5E. Média de formação ferrífera bandado a quartzo-magnetita Isua (Dymek & Klein 1988) está apresentada em losangos azuis.

CAPÍTULO 9 – ESTUDOS DE INCLUSÕES FLUIDAS

Todos os estudos de inclusões fluidas foram realizados pela doutoranda na Austrália e na Inglaterra. As informações acerca do método utilizado para cada um dos tipos de análises, seleção de amostras, e resultados são apresentados no item **Fluid Inclusion Studies**, página 147 no artigo do Anexo 2.

A petrografia baseada nos tipos de incluões é apresentada de acordo com o tempo relativo e composição das inclusões. Em temperatura ambiente (~20 ºC), a maioria das inclusões são aquosas bifásicas com alta razão de preenchimento (80-90% liquido e 20-10% vapor).

Inclusões fluidas primárias-P e pseudosecondárias-PS ocorrem como grupos-aglomerados de inclusões ou dispostas em trilhas internas que terminam nas bordas do cristal. Têm formas irregulares e tamanhos entre 5 até 25 μm e, menos comumente, 75 μm. Raras inclusões ricas em vapor (20% líquido e 80% vapor) são documentadas, e algumas trifásicas (líquido-vapor-sólido).

Análises de espectroscopia Raman foram realizadas no laboratório de Metalurgia da Faculdade de Engenharia da UFMG, com auxílio da engenheira Maria Silvia, na tentativa de constatar a presença de fases gasosas (CO_2, CH_4, etc) em algumas inclusões que apresentaram temperaturas iniciais de fusão do gelo positiva (indicativo de clatrato). No entanto, não foi constatada a presença de CO_2, fazendo-se necessário um estudo posterior detalhado.

9.1 - Microtermometria

Análises microtermométricas (experimentos de resfriamento e aquecimento) em inclusões fluidas em cristais de quartzo e carbonato foram realizadas no Centre for Exploration Targeting na University of Western Australia (UWA) em Perth, sob orientação do professor Steffen Hagemann.

Cerca de 25 lâminas bipolidas de amostras de veios de quartzo e carbonato foram previamente mapeadas em microscópio ótico, e destas, treze foram selecionadas para análises microtermométricas em cristais de quartzo e sete em cristais de carbonato. Os estudos de microtermometria foram realizados em platina Linkam THMSG 600 de resfriamento (até cerca de –150ºC) e aquecimento das inclusões fluidas (até cerca de 500ºC), objetivando a obtenção de temperatura das mudanças de fases (T eutético-Te, T final de fusão do gelo-Tm_{ice}, T homogenização-Th_{tot}). Uma calibração foi realizada entre –56.6° e 374.1°C com inclusões fluidas sintéticas padrões (H_2O pura, mistura H_2O-CO_2). A precisão das medidas de resfriamento é de cerca de ±0.1°C e para aquecimento ±1°C entre 200-500 ºC. Salinidades aparentes são reportadas em peso percentual equivalente de NaCl e $CaCl_2$, baseado na equação de solubilidade da halita para inclusões saturadas e na fusão final do gelo para inclusões subsaturadas (Bodnar & Vityk 1994). Os cálculos de salinidade e densidade foram realizados com uso do programa MacFlinCor (Brown & Hagemann 1995).

Os resultados obtidos estão descritos nos subitens *Microthermometry results* (página 151) e *Quantitative estimation of fluid inclusions composition* (página 158) no artigo do Anexo 2, e de forma resumida no subitem *Fluid inclusions* (página 92) do artigo do Anexo 1.

9.2 – Cromatrografia iônica

Análises de cromatografia iônica (F^-, Cl^-, Br^-, SO_4^{2-}) também foram realizadas no laboratório citado acima. As inclusões fluidas foram extraídas dos minerais de quartzo, carbonato e óxidos de ferro pelo método *crush-leaching* (Banks & Yardley 1992, Banks *et al.* 2000). As concentrações dos cátions Na, K e Li foram obtidas por absorção atômica. Os dados estão apresentados no subitem *Ion chromatography* na página 162, do artigo do Anexo 2.

9.3 – *Laser ablation ICP-MS* em inclusões fluidas

Análises dos elementos Ca, K, Mg, Na, Li, Fe, Cu, Ba, Rb, Sr, Mn, Zn, Pb por ablação a *laser* em inclusões fluidas em cristais de quartzo e carbonato foram realizadas no Institute of Geological Sciences da Universidade de Leeds, Inglaterra em colaboração com o Dr. David Banks.

Estas análises objetivam quantificar a concentração de elementos traços e, principalmente, Fe em veios de quartzo e brechas para discriminar diferentes gerações de veios em relação à capacidade de carrear ferro juntamente com outros cátions.

Cerca de 500 inclusões fluidas foram bombardeadas pelo *laser* desde a superfície da amostra aumentando 1 μm a cada 10 tiros. A solução aquosalina liberada na ablação é então carreada em gás hélio até o espectrometro de massa quadrupolo Agilent 7500. O sistema de reação octopólo é utilizado para análise dos elementos Ca e Fe.

Os resultados obtidos estão descritos no subitem *In situ laser ICP-MS analysis of fluid compositions* (página 167) do artigo do Anexo 2.

CAPÍTULO 10 – ESTUDOS ISOTÓPICOS

As informações acerca do método utilizado para cada um dos tipos de análises, amostras selecionadas, e resultados são apresentados no item **Stable and Radiogenic Isotopes** (páginas 177 a 197) no artigo do Anexo 2, e de forma resumida no subitem *Stable and radiogenic isotope* (página 96) do Anexo 1.

A separação manual de cristais de carbonato para análises de isótopos de ^{13}C, ^{18}O e $^{87}Sr/^{86}Sr$ foi realizada pela estudante, com posterior moagem-trituração dos cristais pelo método convencional por técnicos da University of Tasmânia, e da Universidade de Monash em Melbourne ($^{87}Sr/^{86}Sr$).

Para o estudo de isótopos de oxigênio, cristais de quartzo de veios e óxidos de ferro (magnetita e hematita) foram separados de amostras de rocha total para obtenção de fração mineral com aproximadamente 90% de pureza. Foi realizada uma cuidadosa separação manual e limpeza de cristais de quartzo com auxílio de micróscopio binocular. As amostras foram primeiramente colocadas em solução HCl 5% para eliminação do carbonato quando presente. Para separação dos óxidos de ferro, as amostras passaram pelo separador magnético Frantz.

Os primeiros estudos geocronológicos, para investigar a idade da mineralização de ferro, foram realizados em colaboração com o Prof. Márcio Pimentel da Universidade de Brasília; os mesmos acham-se publicados em Lobato *et al.* (2005b). Mais recentemente, novos estudos vêm sendo desenvolvidos em colaboração com o Dr. João Orestes Santos, utilizando o método SHRIMP na Curtin University, Austrália. Algumas amostras de jaspilito mineralizado do depósito N4E foram utilizadas na tentativa de se obter a idade da mineralização a partir de cristais de monazita em equilíbrio com hematita em veios de carbonato, quartzo e sulfetos. No entanto, devido ao baixo conteúdo de urânio (da ordem de poucos ppm) dos cristais de monazita, não foi possível a obtenção de isócora.

10.1 – $\delta^{18}O$ em óxidos de ferro e quartzo

Isótopo de oxigênio foi analisado em um total de 40 amostras, incluindo jaspilitos, magnetita e hematitas, e em 16 amostras de quartzo de veios.

A composição dos isótopos de oxigênio (^{16}O, ^{17}O, ^{18}O) foi medida no Laboratório de Isótopos Estáveis na University of Lausanne, utilizando o método similar ao descrito por Sharp (1990) e Rumble & Hoering (1994), e ainda mais detalhado em Kasemann *et al.* (2001). São colocados aproximadamente 2 miligramas de amostra de óxido de ferro ou rocha total, e cerca de 0,5 miligrama de quartzo, em um pequeno porta amostra de Pt, e em seguida estes são bombeados no vácuo a cerca de 10^{-6} mbar. Após pré-fluorinação *overnight* da câmara de amostra, as amostras são aquecidas com um *laser* CO_2 em 50 mbars de puro F_2. O excesso de F_2 é separado do O_2 producido por conversão a Cl_2 utilizando KCl mantido a 150°C. O O_2 extraído é coletado em uma peneira

molecular (5A) e subsequentemente expandido dentro de um espectrômetro de massa Finnigan MAT 253. Composições isotópicas de oxigênio são dadas na notação padrão δ, expressa em relação ao VSMOW em permil (‰). Análises replicatas de isótopo de oxigênio dos padrões são usadas (NBS-28 quartzo e UWG-2 granada; Valley *et al.* (1995)) geralmente com uma média de precisão de ± 0,1‰ para $\delta^{18}O$. A acuracidade dos valores de $\delta^{18}O$ é comumente melhor que 0,2‰ comparado aos valores $\delta^{18}O$ aceitos para NBS-28 de 9,64‰ e UWG-2 de 5,8‰.

Os resultados obtidos e as interpretações são apresentados em detalhe no subitem *Oxygen isotope analysis in oxides* (página 177) no artigo do Anexo 2.

10.2 – $\delta^{34}S$ em sulfetos

Análises de isótopos de enxofre em cristais de pirita e calcopirita foram realizadas utilizando o *laser ablation* ICP-MS (Nd:YAG Laser System) no Central Science Laboratory na University of Tasmânia, em colaboração com o Dr. Garry Davidson e sob orientação do geólogo Keith Harris.

Os dados são apresentados no subitem *Sulfur isotope analysis* (página 182) no artigo do Anexo 2. Também são exibidos resultados obtidos em sulfetos de veios hidrotermais localizados na rocha máfica encaixante (Zucchetti 2007).

10.3 – δH em inclusões fluidas de quartzo

Análises de isótopos de hidrogênio em inclusões fluidas de cristais de quartzo foram realizadas na University of Lausanne na Suíça, sob orientação do Dr. Torsten Veneman e ajuda do Dr. Tjerk Heijboer.

Aproximadamente 0,5 gramas de quartzo são colocadas no recipiente com um pedaço de lã, para evitar que os cristais saltem para fora da linha de extração, e aquecida de 100 a 500^{o}C para que as inclusões sejam liberadas. A solução aquosa liberada é coletada em um tubo de vidro contendo 200 mg de zinco. Ambos são aquecidos para que o hidrogênio seja convertido em gás e posteriormente analisado no espectrômetro de massa. Se o tubo de vidro ficar escuro, significa que alguma matéria orgânica está presente. O tubo de vidro deve ser quebrado, permitindo que o gás hidrogênio seja expandido dentro do espectrômetro. Cerca de quatro amostras podem ser analisadas em até uma hora é liberado Os dados estão apresentados e discutidos no item *Hydroxygen isotope analyses* (página 187) no artigo do Anexo 2.

10.4 – $\delta^{13}C$ & $\delta^{18}O$ em carbonatos

Amostras de carbonato foram analisadas no Laboratório de Geologia Isotópica na Universidade da Tasmânia, pelo método de extração convencional. Os resultados estão dispostos no subitem *Carbon and Oxygen isotope analyses* (página 189) no artigo do Anexo 2, onde também encontram-se resultados de Lobato *et al.* (2005b), em um total de vinte e três determinações. Estas últimas

incluem: duas de calcita extraída de uma amostra de jaspilito do Depósito N4E, quatro em minérios ricos em dolomita do Depósito N5E e treze análises em minérios brechados com dolomita do Depósito N4E. Os dados de carbono estão calculados segundo o padrão PDB, Belemnitella Americana, formação Peedee do Cretáceo da Carolina do Sul. Os dados de isótopos de oxigênio acham-se calculados segundo o padrão SMOW, *Standard Mid Ocean Water*.

10.5 – $^{87}Sr/^{86}Sr$ em carbonatos

Um total de 15 amostras de carbonato (calcita, kutnahorita-dolomita) foram analisadas para obtenção das razões $^{87}Sr/^{86}Sr$ na Universidade de Monash, em Melbourne, pela Dra. Janet Hergdt. Os resultados encontram-se no subitem *Strontium isotope analyses* (página 197) no artigo do Anexo 2. Também foram analisadas quatro amostras de rocha total, incluindo uma amostra de basalto pouco alterado hidrotermalmente do depósito N5S, um gabro do mesmo depósito, e duas amostras de granito (Serra dos Carajás).

Os valores obtidos nos carbonatos são altamente radiogênicos, com razões isotópicas $^{87}Sr/^{86}Sr$ variando de 0,7115 (kutnahorita) a 0,7460 (calcita).

Veizer *et al.* (1982 *in* Faure & Mensing 2005) demonstraram que razões $^{87}Sr/^{86}Sr$ de carbonatos (calcita e dolomita) arqueanos marinhos são baixas e semelhantes à daquelas de rochas manto-derivadas (aproximadamento 0,7020; complexos metavulcanossedimenates, Austrália). Carbonatos de rochas sedimentares associadas a sequências tipo *greenstone belt* no Canadá e Zimbabwe (2,8 ± 0,2 Ga) também exibem baixas razões iniciais de Sr (0,7025 ± 0,0015). Quando comparados aos dados obtidos em carbonato de veios hidrotermais associados à mineralização de ferro do presente estudo (0.7115 to 0.7460), estes dados indicam que fluido mineralizador a ferro não deve ter sido originado da sequência metavulcanossedimentar arqueana do Grupo Grão Pará.

CAPÍTULO 11 – MODELO HIDROTERMAL

Com base nas observações de campo e nos resultados analíticos obtidos em amostras de jaspilito e minérios de ferro, um modelo de alteração hidrotermal foi estabelecido, conforme estágios descritos a seguir. O modelo está detalhado no subitem *Constraints on the evolution of the Serra Norte iron ore deposits* (página 105) do Anexo 1, e item **Paleohydrothermal Model for Iron Ore Formation at the Serra Norte Deposits** (páginas 198 a 206) no artigo do Anexo 2.

Três zonas de alteração hidrotermal são reconhecidas. A zona distal é representada pelo estágio cedo-hidrotermal de infiltração do fluido em jaspilitos, caracterizado por lixiviação de sílica acompanhada por precipitação de veios-brechas V1 quartzo-sulfetos e carbonato-magnetita-sulfetos. Magnetita corresponde ao óxido cedo-hidrotermal formada a partir de bandas de hematita microcristalina do jaspilito, e precipitada em veios-brechas com carbonato e algum sulfeto. Inclusões fluidas aprisionadas em quartzo e carbonato têm salinidade média a alta, e são ricas em cálcio. Valores isotópicos ($\delta^{18}O$ em magnetita, $\delta^{13}C$ e $\delta^{18}O$ em carbonatos, $\delta^{87}Sr/^{86}Sr$ em carbonatos, $\delta^{34}S$ em sulfetos, $\delta^{18}O$ em quartzo) em conjunto com dados de inclusões fluidas obtidos em minerais cedo-hidrotermais são compatíveis com fonte de fluido magmática para este estágio.

A zona intermediária é representada pelos veios de quartzo-hematita V2 e V3, caracterizados por inclusões fluidas com baixa a média salinidade, e salinas ricas em Na-K-Mg, aprisionadas em uma mesma faixa de temperatura (220 a 325^{o}C). Hematita microlamelar está presente em veios e espaços abertos em bandas de jaspilito. Considerando os valores de salinidade mais baixos em relação à zona distal e condições relativamente oxidantes do fluido (formação expressiva de hematita), sugere-se mistura de águas meteóricas no estágio intermediário de alteração.

A zona de alteração proximal é representada pelo estágio avançado de alteração hidrotermal, e caracteriza-se pelos veios e brechas a carbonato V4 e quartzo-hematita V5. Carbonato de brechas V4 contém inclusões fluidas de alta salinidade, ricas em Ca, aprisionadas entre 240 to 295^{o}C, e quartzo de veios-brechas V5 contém inclusões de baixa salinidade aprisionadas aproximadamente na mesma faixa de temperatura. Os óxidos de ferro desta zona de alteração são representados principalmente por agregados de hematita anédrica-AHem (formada pela progressiva martitização e recristalização) e hematita tabular-THem (que representa o estágio mais tardio). Esta última precipitada ao longo de veios discordantes, com ausência de quartzo. O estágio avançado de alteração mostra evidências de influxo de ambos fluidos magmáticos e meteóricos. A interação de agues meteóricas é indicada pela presence de fases dominantemente oxididadas (e.g., MpHem, AHem, e THem), inclusões fluidas pouco salinas ricas em Na, e ainda diminuição de valores isotópicos de oxigênio em direção aos estágios mais tardios de hematita.

CAPÍTULO 12 – CONSIDERAÇÕES FINAIS

► A evolução do fluido hidrotermal mineralizador a ferro que interagiu com jaspilitos formando minério de ferro compacto de alto teor nos depósitos da Serra Norte é aqui sugerida. O modelo genético hidrotermal para formação do minério foi estabelecido com base em estudos petrográficos e geoquímicos de detalhe em amostras de jaspilito e minérios (tipo HD) em diferentes estágios-zonas de alteração.

► Os estudos petrográficos indicam que as modificações mineralógicas em jaspilitos e minérios dos depósitos estudados envolveram: (i) Formação de cristais de magnetita-Mg, à custa de hematita microcristalina-Hm, nos jaspilitos; (ii) Recristalização de *chert* e jaspe, com expulsão de Hm do jaspe resultando na sua "limpeza" com formação de quartzo granoblástico fino; (iii) Lixiviação progressiva de *chert* (jaspe) ou quartzo, restando hematita microcristalina e inúmeros espaços vazios; formação de brechas; (iv) Preenchimento parcial de vazios por precipitação de hematita microlamelar; esta também parece se formar à custa de martita; (v) Aumento de martitização da Mg; recristalização de martita-Mt com desenvolvimento de aglomerados de cristais de hematita anédricos; (vi) Preenchimento continuado e avançado dos espaços vazios por hematita microlamelar, anédrica e euédrica-tabular, inclusive da matriz de brechas. Linhas de crescimento (geminação) observadas nestes tipos de hematita indicam precipitação direta do fluido (*open-space filling*).

► Os principais carbonatos nos minérios de N4E e jaspilitos de N5S são kutnahorita, dolomita rica em manganês, enquanto dolomita predomina em minérios de N5E. A forma de ocorrência predominante é em veios-vênulas (discordantes e intrabanda) e em cimento de brecha. Calcita ocorre em veios V1 com magnetita e sulfetos discordantes a bandamento de jaspilitos de N4E. A carbonatação é interpretada como fase desde sin a tardi-pós-mineralização, e parece ser restrita a minérios em profundidades >200 metros em N5E, e em N4E, ao contato com rocha máfica.

► Com base em análises *in situ* LA-ICP-MS, nos diferentes tipos de óxidos, verifica-se que: (i) cristais de magnetita têm conteúdos maiores que 100 ppm de Ni, Co, Cu, Pb e baixos conteúdos totais de elementos terras raras (até 10 ppm); (ii) kenomagnetita apresenta em sua composição os elementos traços Zn (até 200 ppm), Pb (até 20 ppm), Ba e Sr (menor que 10 ppm), também com baixos conteúdos de REE, concentrados em leves; (iii) martita contêm Mo > Zn > Pb > V, e conteúdos totais de REE entre 3,2 to 9,2 ppm; (iv) hematita lamelar exibe conteúdos entre 5 e 25 ppm em Mo, Y, Sc, As, V, W, Cr, Co, Nb, Ni, Zr, Sr, Zn, Pb; (iv) hematita do tipo anédrica e tabular têm concentrações de W e Pb menores que 50 ppm e conteúdos totais de REE entre 5 e 40 ppm. É notável o aumento progressivo de ETR da magnetita para a hematita tabular, com padrão de distribuição dos elementos mais regular.

► Estudos geoquímicos de rocha total mostram que há uma mudança no padrão de elementos terras raras em jaspilitos para o padrão em minérios de alto teor, com aumento do conteúdo total de ETR, principamente elementos leves, e padrão horizontal de ETRP em minérios. Nestes minérios com padrão horizontal há predomínio de hematita do tipo anédrica, tabular indicando que a fixação de ETRP de fluido residual se deu em estágio hidrotermal avançado.

► Baseado no estudo de inclusões fluidas, verifica-se que:

- Veios-brechas V1a compostos predominantemente por quartzo e V1b com predomínio de carbonato têm inclusões fluidas de alta salinidade, contendo Ca, além de Na, K e Mg, com temperaturas de aprisionamento na faixa de 220-320^{o}C. Inclusões fluidas em quartzo exibem ampla variação nas razões Cl/Br, e valores isotópicos de hidrogênio entre –14 e –50‰.
- Em veios V2 de quartzo (*vug-textured* ou não) com hematita e veios V3 a hematita-quartzo, inclusões fluidas em quartzo têm valores desde baixa (ricas em Na-Fe-Mg) a alta (ricas em Ca-Mg-Fe) salinidade e temperaturas de aprisionamento entre 180 a 320^{o}C. A maioria dos valores isotópicos de hidrogênio varia entre –20 e –43‰.
- Inclusões primárias em cristais de quartzo de brechas V4 a carbonato-quartzo, onde cristais de carbonato são manchados por poeira de ferro, também apresentam desde baixa a alta salinidade (Ttrap entre 260 e 290^{o}C). Carbonatos dos mesmos veios têm inclusões de alta salinidade, ricas em Ca.
- Inclusões em quartzo de veio V5 em equilíbrio com hematita microlamelar em minérios de alto teor exibem valores de baixa (ricos em Na) e alta salinidade (ricos em Ca), entre 240 e 290^{o}C.

► Dados de isótopos de carbono e oxigênio em carbonatos de veios V1, discordantes ao bandamento de jaspilitos, mostram mais ampla faixa de valores $\delta^{13}C$, de –5,46 a –2,35‰$_{PDB}$, enquanto valores $\delta^{18}O$ têm faixa relativamente estreita, entre +9,28 e +11,62‰$_{SMOW}$. Já carbonatos de veios-brechas V4 em minérios, apresentam maior variação de valores $\delta^{18}O$ (+15 a +20‰) e faixa mais restrita de $\delta^{13}C$, de –4,98 a –3,86, em relação aos jaspilitos. Nos depósitos tipo *IOCG* de Carajás (por exemplo, depósito Estrela – Lindenmayer *et al.* 2005) também domina estreita faixa de valores negativos de $\delta^{13}C_{PDB}$ em calcita (–3,15 e –4,82), e os autores interpretam estes resultados como fonte magmática para o carbono, como também sugerido em Lobato *et al.* (2005b) para os carbonatos de Carajás.

► Razões $^{87}Sr/^{86}Sr$ de 0,7115 a 0,7460 obtidas em carbonato de veios e brechas V1 e V4 de jaspilitos e minérios de Carajás se assemelham a composição do granito proterozóico Serra dos Carajás (Dall'Agnol *et al.* 1994), que contém $^{87}Sr/^{86}Sr$ de (0.7158). Assinaturas de Sr altamente radiogênicas também são descritas para alguns depósitos Fe-oxide Cu-Au de Carajás, como razões $^{87}Sr/^{86}Sr$ de 0,73924 a 0,75576, obtidos em calcita, e de 0,71209 a 0,71992 em turmalinas

hidrotermais do depósito Salobo (Tassinari *et al.* 2003). Os dados de Salobo são comparados com razões (0,73963 a 0,75961) encontradas em rochas do complexo gnáissico Xingu; os autores assumem que os fluidos evoluíram em ambiente continental. Carbonatos (calcita e siderita) do depósito Igarapé Bahia (Tallarico *et al.* 2005) exibem ampla variação das razões radiogênicas $^{87}Sr/^{86}Sr$ (0,714 to 0,755). Os autores sugerem uma derivação de múltiplas fontes crustais, consistentes com origem epigenética magmática-hidrotermal. Esses valores obtidos nas amostras dos depósitos de ferro aqui estudadas e nos depósitos tipo *IOCG* citados (Igarapé Bahia e Salobo), são inconsistentes com a composição isotópica da água do mar a ~2,575 Ga (Veizer & Compston 1976) e com razões iniciais $^{87}Sr/^{86}Sr$ de rochas metavulcânicas do Grão Pará (0,7057 ± 0,0010), determinadas por Gibbs *et al.* (1986). Segundo Faure & Powell (1976), rochas formadas por fusão, metassomatismo ou que assimilaram material crustal têm razões iniciais maiores que rochas manto derivadas não contaminadas.

► Os valores de $\delta^{34}S$ próximos de 0‰, obtidos em amostras de pirita e calcopirita oriundas de veios hidrotermais V1b com carbonato e magnetita, e de veios-brechas localizados na rocha máfica encaixante hidrotermalizada, indicam uma origem magmática para o enxofre, de acordo com dados de reservatórios em Hoefs (2007). Dados de sulfetos em veios do Alvo Estrela (Cu-Au) (Lindenmayer *et al.* 2005) e de sulfetos ($\delta^{34}S$ de 0 a +2‰) de diferentes tipos de minério do depósito de Cu (Au, W, Mo, Sn) Breves (Botelho *et al.* 2005), também indicam fonte magmática para o enxofre, com valores de $\delta^{34}S$ igualmente próximos de 0‰. No entanto, a ampla variação nos valores isotópicos de enxofre (até cerca de + 10‰) obtidos no presente estudo, não é conclusiva no estabelecimento de uma origem magmática hidrotermal para o fluido. A combinação de dados de inclusões fluidas, isótopos de enxofre e outros dados isotópicos aqui apresentados apontam para fluido magmático inicial com interação de água meteórica.

► Dados de isótopos de oxigênio em jaspilitos (rocha total) constituem os mais pesados valores de ^{18}O, seguidos por magnetita e diferentes tipos de hematita. Há uma clara diminuição progressiva no conteúdo de ^{18}O da magnetita em direção à hematita do tipo tabular, que corresponde ao estágio hidrotermal mais avançado e maior razão fluido/rocha. Valores calculados para o fluido hematita-água (de 0 a +8‰), a temperaturas entre 250º e 275º, indicam contribuição de fluido magmático, de acordo com os campos de Taylor (1974), e de Hoefs (2007) para rochas graníticas.

► Com base em todos estes dados, interpreta-se que: (i) o estágio cedo hidrotermal parece ter sido dominado por fluidos magmáticos; (ii) no estágio hidrotermal intermediário houve mistura de águas meteóricas; (iii) o estágio avançado de alteração é dominado por fluido meteórico, com formação dos tipos mais tardios de hematita. Segundo estudos de Rios *et al.* (2004) e Lobato *et al.* (2005b), inclusões fluidas nessas hematitas (por exemplo, tipo lamelar) têm baixa salinidade (< 4 % em peso

NaCl) e temperaturas mínimas de formação entre 240 e 290^{o}C.

► As figuras 8 e 9 apresentam bloco diagramas esquemáticos com proposta de ambiente tectônico da bacia de deposição de jaspilitos no Arqueano, e detalhe da área da Serra Norte com disposição das rochas e estruturas - Dobra Carajás e *splays* associados à falha Carajás – no final do Arqueano e início do Paleoproterozóico. Sugere-se uma associação da mineralização de ferro nos depósitos estudados com a granitogênese paleoproterozóica, como provável fonte de fluidos para mineralização de ferro. Estes fluidos possivelmente aproveitaram estruturas arqueanas reativadas, interagindo com as rochas, principalmente ao longo do contato jaspilito-rocha máfica encaixante. No entanto, faz-se necessário um estudo detalhado desses granitos, em *melt inclusions,* por exemplo, além de estudo geocronológico aprofundado da mineralização de ferro, para confirmação da hipótese levantada.

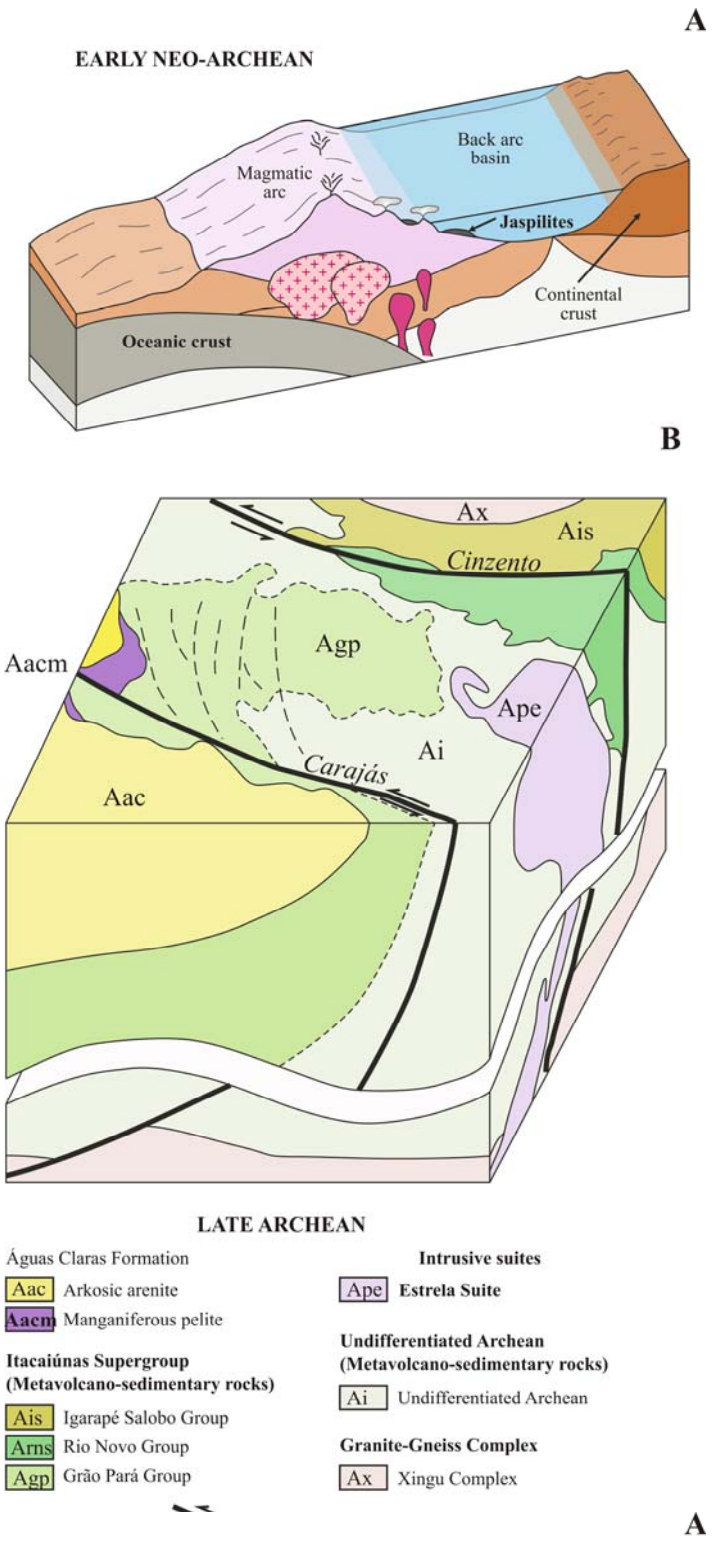

Figura 8 – Bloco diagramas esquemáticos mostrando em A. provável ambiente tectônico da bacia de deposição de jaspilitos no Arqueano, e em B. Detalhe da área da Serra Norte (mapa em planta extraído do mapa geólogico da Figura 3) com disposição das rochas e estruturas - Dobra Carajás e *splays* associados à falha Carajás – no final do Arqueano.

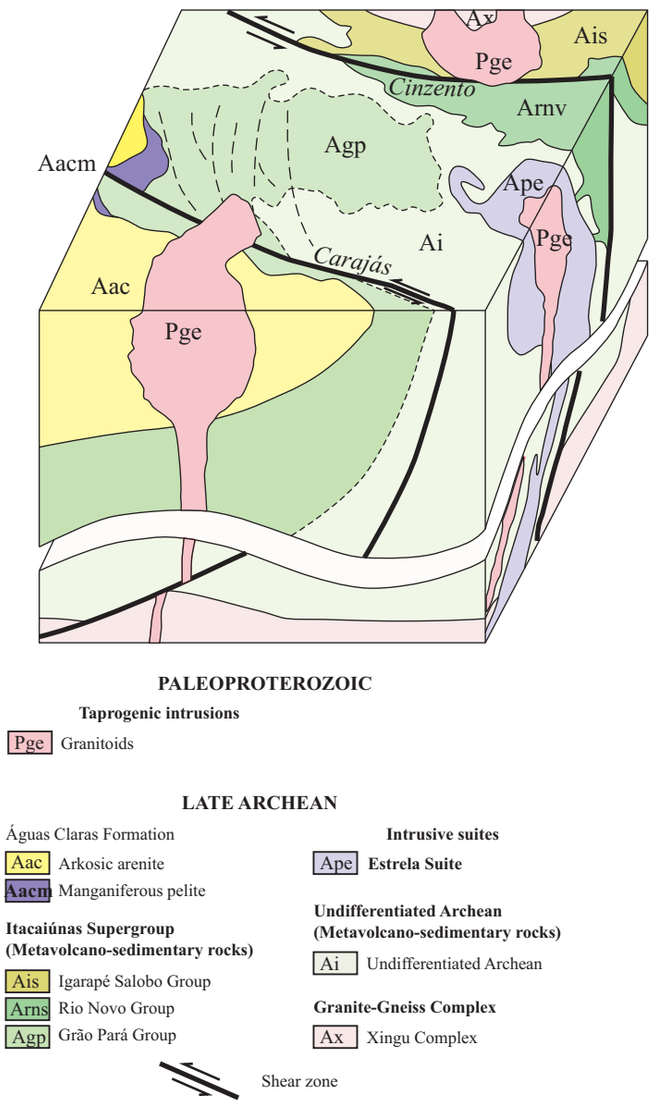

Figura 9 – Bloco diagramas esquemáticos mostrando em A. provável ambiente tectônico da bacia de deposição de jaspilitos no Arqueano, e em B. Detalhe da área da Serra Norte (mapa em planta extraído do mapa geólogico da Figura 3) com disposição das rochas e estruturas - Dobra Carajás e *splays* associados à falha Carajás – no final do Arqueano.

REFERÊNCIAS BIBLIOGRÁFICAS

Althoff A.M.R., Dall´Agnol R., Souza Z.S. 1991. Região de Marajoara - SE do Pará: Prolongamento dos terrenos arqueanos de Rio Maria ou retrabalhamento? *In*: Simpósio de Geologia da Amazônia, Belém, Anais, **3**: 130-141.

Araújo O.J.B., Maia R.G.N. 1991. Programa levantamentos geológicos básicos do Brasil. Projeto especial mapas de recursos minerais, de solos e de vegetação para a área do Programa Grande Carajás. Subprojeto Recursos Minerais. Serra dos Carajás, Folha SB.22-Z-A. Brasília: DNPM/ Companhia de Pesquisa e Recursos Minerais-CPRM, 152p.

Araújo O.J.B., Maia R.G.N., João X.S.J., Costa J.B.S. 1988. A megaestruturação arqueana da folha Serra dos Carajás. *In*: Congresso Latino-Americano de Geologia, 7, Belém, Anais, **1**: 324-328.

Avelar V.G., Lafon J.M., Correa Jr F.C., Macambira, E.M.B. 1999. O magmatismo arqueano da região de Tucumã, Província Mineral Carajás, Amazônia Oriental, Brasil: novos dados geocronológicos. Revista Brasileira de Geociências, **29**: 453-460.

Banks D.A., Yardley B.W.D. 1992. Crush-leach analysis of fluid inclusions in small natural and synthetic samples: Geochimica Cosmochimica Acta, **56:**245-248.

Banks D.A., Green R., Cliff R.A., Yardley B.W.D. 2000. Chlorine isotopes in fluid inclusions: Determination of the origins of salinity in magmatic fluids: Geochimica et Cosmochimica Acta, **64**:1785-1789.

Barley M.E., Pickard A.L., Hagemann S.G., Folkert S.L. 1999. Hydrothermal origin for the 2 billion year old giant iron ore deposit, Hamersley Province, Western Australia. Mineralium Deposita, **34**: 784-789.

Barros C.E.M. 1997. Pétrologie et structure du Complexe Granitique Estrela (2.5 Ga) et de son encaissant métavolcano-sédimentaire (Province Métallifère de Carajás, Brésil). Tese de Doutorado, Université Henri Poincaré, Nancy I, Nancy, France.

Barros C.E.M., Macambira M.J.B., Barbey P. 2001. Idade de zircão do Complexo Granítico Estrela: Relações entre magmatismo, deformação e metamorfismo na Província Metalogenética Carajás. *In*: Proceedings Simpósio de Geologia da Amazônia 7, p 17-20.

Beisiegel V.R., Bernardelli A.L., Drummond N.F., Ruff A.W., Tremaine J.W. 1973. Geologia e recursos minerais da Serra dos Carajás. Revista Brasileira de Geociências, **3**(4): 215- 242.

Beukes N.J., Gutzmer J., and Mukhopadhyay J. 2002: The geology and genesis of high-grade hematite iron ore deposits. Iron Ore Conference, Perth. Pp. 23-29.

Beukes N.J., Mukhopadhyay, J., and Gutzmer, J., 2008, Genesis of High-Grade Iron Ores of the Archean Iron Ore Group around Noamundi, India: Economic Geology, v. 103, p. 365-386.

Bizzi L.A., Schobbenhaus C., Gonçalves J.H., Baars F.J., Delgado I.M., Abram M.B., Leão Neto R., de Matos G.M.M., Santos J.O.S. 2001. Geologia, Tectônica e Recursos Minerais do Brasil: Sistema de Informações Geográficas–SIG e Mapas na Escala 1:2 500 000. 4ª Edição, 4 CD-rom. Companhia de Pesquisa e Recursos Minerais-CPRM.

Bodnar R.J., Vityk M.O. 1994. Interpretation of microthermometric data for H_2O-NaCl fluid inclusions. *In*: De Vivo B, Frezzotti ML (eds) Fluid inclusions in minerals: methods and applications. VPI Press, Blacksburg, Virginia, pp 117–130.

Botelho N.F., Moura M.A., Teixeira L.M., Olivo G.R., Cunha L.M., Santana M.U. 2005. Caracterização geológica e metalogenética do depósito de Cu (Au, W, Mo, Sn) Breves, Carajás. *In*: Marini OJ, Queiroz ET de & Ramos BW (eds), Caracterização de depósitos minerais em distritos mineiros da Amazônia. DNPM/CT-Mineral/FINEP/ADIMB, Brasília, pp 340-389.

Brown P.E., Hagemann S.G. 1995. MacFlinCor and its application to fluids in Archaean lode-gold deposits: Geochimica et Cosmochimica Acta, **59:**3943–3952.

Cabral A.R., Rocha Filho O.G., Jones R.D. 2003. Hydrothermal origin of soft hematite ore in the Quadrilátero Ferrífero of Minas Gerais, Brazil. Petrographic evidence from the Gongo Soco iron ore deposit. Applied Earth Science, **112**: 279-286.

Clout J.M.F., Simonson B.M. 2005. Precambrian iron formations and iron formation-hosted iron ore deposits: Economic Geology, 100th Anniversary Volume, p. 643-679.

Cope I. L, Wilkinson J. J., Boyce A. J., Chapman J. B., Herrington R. J., D Harris C. J. 2008. Genesis of the Pic de Fon Iron Oxide Deposit, Simandou Range, Republic of Guinea, West Africa. *In*: Hagemann, S.G., Rosière, C.A., Gutzmer, J., and Beukes, N.J. (eds.), BIF-Related High-Grade Iron Mineralization: Reviews in Economic Geology, **15**:339–360.

Costa L.P. 2007. Caracterização das sequências metavulcanossedimentares da porção leste da Província Mineral Carajás, Pará. Dissertação de Mestrado, Departamento de Geologia, Universidade Federal de Minas Gerais, 113p.

CVRD. 1996. Resumo dos aspectos geológicos da Província Mineral Carajás. Guia de excursão, DIGEB/DEPAB/GIMB/SUMIC, 392-403.

CVRD. 2004. Atualização dos recursos e reservas provadas e prováveis das minas de N4 e N5, Relatório de pesquisa para o Departamento Nacional de Produção Mineral-DNPM, vol. I, 197p.

Dall'agnol R., Lafon J.M., Macambira M.J.B. 1994. Proterozoic anorogenic magmatism in the Central Amazonian Province, Amazonian Craton: geochronological, petrological and geochemical aspects: Mineralogy and Petrology**, 50**: 113-138.

Dall´Agnol R., Rämö O.T., Magalhães M.S., Macambira, M.J.B. 1999. Petrology of anorogenic, oxidised Jamon and Musa granites, Amazonian Craton: implications for the genesis of Proterozoic A-type granites. Lithos, **46**: 431-462.

Dall'Agnol R., Teixeira N.P, Rämö O.T., Moura A.V., Macambira M.J.B., Oliveira D.C. 2005. Petrogenesis of the Paleoproterozoic rapakivi A-type granites of the Archean Carajás metallogenic province, Brazil. Lithos, **80**:101– 129.

Dalstra H., Guedes S. 2004. Giant hydrothermal hematite deposits with Mg-Fe metasomatism: a comparison of the Carajás, Hamersley, and other iron ores. Economic Geology, **99**: 1793-1800.

Danyushevsky L., Robinson P., McGoldrick P., Large R., Gilbert S. 2003. LA-ICPMS of sulphides: Evaluation of an XRF glass disc standard for analysis of different sulphide matrixes, 2003. Goldscmidt

Conference, Japan, Geochimica Et Cosmochimica Acta, **67**(18): A73 Suppl.

Danyushevsky L., Robinson P., McGoldrick P., Large R., Gilbert S. 2004. Quantitative multi-element analysis of sulphide minerals by laser ablation ICPMS, 17th AGC, Hobart, p. 260.

DOCEGEO. 1988. Revisão litoestratigráfica da Província Mineral Carajás. *In*: Congresso Brasileiro de Geologia, 35, Belém, Anexo aos anais, 11-54.

Dymek R.F., Klein C. 1988. Chemistry, petrology, and origin of banded iron formation litholoties from the 3800 Ma Isua supracrustal belt, West Greenland. Precambrian Research, **39**: 241-302.

Faraco M.T.L., Carvalho J.M.A., Klein E.L. 1996. A carta metalogenética da Província Carajás/Sul do Pará–Folha Araguaia (SB.22). Congresso Brasileiro de Geologia, 39, Salvador, Anais, **3**: 248-250.

Faure G., Powell J.L. 1972. Strontium isotope geology. *In*: Minerals, rocks and inorganic materials: Monograph Series of Theoretical and Experimental Studies 5, New York, Springer-Verlag, 188 p.

Faure G., Mensing T.M. 2005 Isotopes principles and applications (3rd ed). Wiley, New Jersey, USA, 928 p.

Figueiredo e Silva R.C. 2004. Caracterização petrográfica e geoquímica de jaspilitos e minérios de ferro, Província Mineral Carajás, Pará: implicações para a mineralização de ferro. Dissertação de Mestrado, Departamento de Geologia, Universidade Federal de Minas Gerais, 151p.

Figueiredo e Silva R.C.F., Lobato L.M., Rosière C.A., Guedes S.C., Monteiro A.M., Meireles H., Matias P.H. 2004. Estudos petrográficos microscópicos e geoquímicos em jaspilitos e minérios de ferro dos depósitos N1, N4E, N4W e N5E, Província Mineral Carajás, Pará. *In*: Simpósio Brasileiro Exploração Mineral, maio 2004, Ouro Preto, CD rom, ADIMB.

Figueiredo e Silva R.C., Lobato L.M., Rosière C.A. 2005. Petrografia e geoquímica em jaspilitos e minérios hidrotermais de ferro dos depósitos da serra norte (N1, N4E, N4W e N5E), Província Mineral Carajás, Pará. *In*: SBG, I Simpósio de Metalogenia, Gramado, CD rom.

Figueiredo e Silva R.C., Hagemann S.C., Lobato L.M., Banks D. 2007a. Hydrothermal fluid characteristics and evolution for the giant Carajás North Range iron deposits, Brazil [abs]: Biennial Conference European Current Research of Fluid Inclusion (ECROFI) 19th. University of Bern, Switzerland, p 98.

Figueiredo e Silva R.C., Hagemann S.G., Lobato L.M., Rosière C.A., Vennemann T. 2007b. Iron oxide paragenesis, quartz vein chronology and hydrothermal fluid evolution at the giant North Range Carajás iron deposits in Brazil. [ext. abs.]: Biennial Meeting of the Society for Geology Applied to Mineral Deposits 9th. Proceedings, **SGA,** Dublin, Ireland**, 2**:1223-1226.

Figueiredo e Silva R.C., Lobato L.M., Rosière C.A., Hagemann S., Zucchetti M., Baars F.J., Morais R., Andrade I. 2008a. Hydrothermal origin for the jaspilite-hosted, giant Serra Norte iron ore deposits in the Carajás mineral province, Para State, Brazil. *In:* Hagemann, S.G., Rosière, C.A., Gutzmer, J., and Beukes, N.J. (eds.), BIF-Related High-Grade Iron Mineralization: Reviews in Economic Geology, **15**: 255-290.

Figueiredo e Silva R.C., Lobato L.M., Rosière C.A., Hagemann S.G. 2008b. The Giant Serra Norte Iron Ore Deposits, Carajás: Hydrothermal imprint from jaspilites to iron ores [ext. abs.]: SEG-GSSA Conference, Johannesburg, CD rom.

Gibbs A.K., Wirth K.R., Hirata W.K., Olszewski Jr. W.J. 1986. Age and composition of the Grão Pará Group volcanics, Serra dos Carajás. Revista Brasileira de Geociências, **16**(2): 201-211.

Guedes S.G. 2000. Evidências de alteração hidrotermal na formação ferrífera bandada e minérios de ferro de N4, N5 e Serra Leste, Serra dos Carajás-Pará, Brasil. Seminário de Qualificação, Departamento de Geologia, Universidade Federal de Minas Gerais, 61p

Guedes S.C., Rosière C.A., Barley M., Lobato L.M. 2002. The importance of carbonate alteration associated with the Carajás high-grade hematite deposits, Brazil. Iron Ore 2002, The Australasian Institute of Mining and Metallurgy, Publication Series No. **7**:63-66.

Gutzmer J., Mukhopadhyay J., Beukes N. J., Pack A., Hayashi K., Sharp Z.D. 2006. Oxygen isotope composition of hematite and genesis of high-grade BIF-hosted iron ores: Memoirs- Geological Society of America, **198**:257-268.

Hagemann S.G., Barley M.E., Folkert S.L., Yardley B.W., Banks D.A. 1999. A hydrothermal origin for the giant Tom Price iron ore deposit. *In*: Hughes F.E. (ed.), Mineral Deposits, Process to Processing. Balkema, p. 41-44.

Hoefs J., 2007, Stable isotope geochemistry, (5th ed). Springer-Verlag, New York, USA, 244 p.

Holdsworth R.E., Pinheiro R.V.L. 2000. The anatomy of shallow-crustal transpressional structures: insights from the Archaean Carajás fault zone, Amazon, Brazil. Journal of Structural Geology, **22**:1105-1123.

Huhn S.R.B., Santos A.B.S., Amaral A.F., Ledsham E.J., Gouveia J.L., Martins L.P.B., Montalvão R.M.G., Costa V.C. 1988. O terreno granito-greenstone da região de Rio Maria – Sul do Pará. Congresso Brasileiro de Geologia, Anais, Sociedade Brasileira de Geologia, **35**:1438-1452.

Huhn S.R.B., Souza C.I.J., Alburquerque M.C., Leal E.D., Brustolin V. 1999. Descoberta do Depósito Cu(Au) Cristalino: Geologia e Mineralização Associada-Região de Serra do Rabo – Carajás – PA. *In*: Simpósio de Geologia da Amazônia, Manaus, Anais, **6**:140-143.

Hutchinson R.W. 1979. Report on DOCEGEO copper Projects MM1, Salobo and Regional Geological Relationships, Pará, Brazil. Internal Report, Companhia Vale do Rio Doce.

Kasemann S., Meixner A., Rocholl A., Vennemann T., Schmitt A., and Wiedenbeck M. 2001. Boron and oxygen isotope composition of certified reference materials NIST SRM 610/612, and reference materials JB-2G and JR-2G. Geostandards Newsletter, **25:**405-416.

Klein C. 2005. Some Precambrian banded iron-formations (BIFs) from around the world: Their age, geologic setting, mineralogy, metamorphism, geochemistry, and origin. American Mineralogist, **90**:1473-1499.

Klein C., Ladeira E.A. 2000. Petrography and geochemistry of the least altered banded iron-formation of the Archean Carajás Formation, northern Brazil. Economic Geology, **97**:643-651.

Klein C., Beukes N.J. 1989. Geochemistry and sedimentology of a facies transition from limestone to iron formation deposition in the Early Proterozoic Transvaal Supergroup, South Africa: Economic Geology, **84**:1733–1774.

Krymsky R.Sh., Macambira J.B., Macambira M.B.J. 2002. Geocronologia U-Pb em zircão de rochas vulcânicas da Formação Carajás, Estado do Pará. *In*: Simpósio sobre vulcanismo e ambientes associados, 2, Belém, Resumos, SBG-NO. p.41.

Lindenmayer Z.G., Fleck A., Gomes C.H., Santos A.B.Z., Caron R., Paula F.C., Laux J.H., Pimentel M.M., Sardinha A.S. 2005. Caracterização geológica do Alvo Estrela (Cu-Au), Serra dos Carajás, Pará. 2005. *In*:

Marini OJ, Queiroz ET de & Ramos BW (eds), Caracterização de depósitos minerais em distritos mineiros da Amazônia. DNPM/CT-Mineral/FINEP/ADIMB, Brasília, pp 157-226.

Lindenmayer Z.G., Fyfe W.S. 1992. Comparação preliminar entre os metabasaltos dos grupos Parauapebas e Salobo da bacia Carajás, PA. Anais Congresso Brasileiro de Geologia, **2**:33-34.

Lindenmayer Z.G., Laux J.H., Teixeira J.B.G. 2001. Considerações sobre a origem das formações ferríferas da formação Carajás, Serra dos Carajás. Revista Brasileira de Geociências, **31**(1):21-28.

Lobato L.M., Figueiredo e Silva R.C., Hagemann S., Thorne W., Zucchetti M. 2008. Hypogene Alteration Associated with High-Grade BIF-related Iron Ore. *In*: Hagemann, S.G., Rosière, C.A., Gutzmer, J., and Beukes, N.J. (eds.), BIF-Related High-Grade Iron Mineralization: Reviews in Economic Geology: **15:**107-128.

Lobato L.M., Figueiredo e Silva R.C., Hagemann S.G., Thorne W. 2007. Mineralizing fluid evolution and REE patterns for the hydrothermal Carajás iron ores, Brazil, and for selected Hamersley iron deposits, Australia. 9th SGA Meeting, Dublin (ago/2007), In press.

Lobato L.M., Figueiredo e Silva R.C., Rosière C.A., Zucchetti M., Baars F.J., Seoane J. C.S., Rios F.J., Monteiro A.M. 2005a. Hydrothermal origin for the iron mineralisation, Carajás Province, Pará State, Brazil. *In*: Proceedings Iron Ore 2005, The Australasian Institute of Mining and Metallurgy, Publication Series No. **8**:99-110.

Lobato L. M., Rosière C. A. , Figueiredo e Silva R. C., Zucchetti M., Baars F. J., Seoane J. C. S., Rios F. J., Pimentel M., Mendes G. E., Monteiro A. M. 2005b. A mineralização hidrotermal de ferro da Província Mineral Carajás - Controle es-trutural e contexto na evolução metalogenética da província. In: Marini OJ, Queiroz ET de & Ramos BW (eds), Caracterização de depósitos minerais em distritos mineiros da Amazônia. DNPM/CT-Mineral/FINEP/ADIMB, Brasília, pp 25-92.

Lobato L.M., Rosière C.A., Baars F.J., Figueiredo e Silva R.C., Zucchetti M., Rios F.J., Seoane J.C.S., Pimentel M., Lindenmayer Z.G., Mendes G.E., Maciel A.L. 2004. Timing of hydrothermal iron mineralisation, Carajás province, PA. *In*: Simpósio Brasileiro Exploração Mineral, maio 2004, Ouro Preto, CD rom, ADIMB.

Lopes P.M.S. 1997. Mineralogia dos minérios de ferro da jazida N4E, Carajás-PA. Trabalho de Graduação, Centro de Geociências, Universidade Federal do Pará, 66p.

Macambira J.B. 2003. O ambiente deposicional da Formação Carajás e uma proposta de modelo evolutivo para a Bacia Grão Pará. Tese de Doutorado, Instituto de Geociências, Universidade Estadual de Campinas, 217p.

Macambira M.J.B. 1992. Chronologic U-Pb, Rb-Sr, K-Ar et croissance de la croute continentale dans I'amazonie du sud-est; Exemple de Ia region de Rio Maria, Province de Carajás, Brésil. Tese de Doutorado, Montpellier, Université de Montpellier H., 212p.

Macambira M.J.B., Ramos J.F.F., Assis J.F.P., Figueiras A.J.M. 1990. Projeto Serra Norte e Projeto Pojuca. Convênio SEPLAN/DOCEGEO/UFPA/DNPM. Relatório final, 150 p.

Machado N., Lindenmayer Z., Krogh T.E., Lindenmayer D. 1991. U-Pb geochronology of Archean magmatism and basement reactivation in the Carajás área, Amazon shield, Brazil. Precambrian Research, **49**:329-354.

Meirelles M.R. 1986. Geoquímica e petrologia dos jaspilitos e rochas vulcânicas associadas, Grupo Grão-Pará, Serra dos Carajás, Pará. Dissertação de Mestrado, Instituto de Geociências, Universidade de Brasília, 171p.

Meirelles M.R., Dardenne M.A. 1991. Vulcanismo basáltico de afinidade shonshonítica em ambiente de arco arqueano, Grupo Grão Pará, Serra dos Carajás, Pará. Resumos Expandidos dos Anais Congresso Brasileiro de Geoquímica, **4**:131-132.

Nakamura N. 1974. Determination of REE, Ba, Fe, Mg, Na and K in carbonaceous and ordinary chondrites. Geochimica Cosmochimica Acta, **38**:757-775.

NASA/JPL North American Space Agency, Jet Propulsion Laboratory, 2005. http://www2.jpl.nasa.gov/srtm.

Netshiozwi S. T. 2002. Origin of High-Grade Hematite Ores at Thabazimbi Mine, Limpopo Province, South Africa. Msc Dissertation, Faculty of Science at the Rand Afrikaans University, 135 p.

Pereira A.B. 1999. Minerografia dos jaspilitos da Formação Carajás. Trabalho de Graduação, Centro de Geociências, Universidade Federal do Pará, 40p.

Pidgeon R., Macambira M.J.B., Lafon J.M. 2000. Th-U-Pb isotopic systems and internal structures from an enderbite from the Pium Complex, Carajás Province, Brazil: evidence for the ages of granulite facies metamorphism and the protolith of the enderbite. Chemical Geology, **166**:159-171.

Pimentel M.M., Machado N. 1994. Geocronologia U-Pb dos terrenos granito-greenstone de Rio Maria, Pará. Congresso Brasileiro de Geologia, 38, Camburiú, Anais, **1**:390-391.

Pinheiro R.V.L., Holdsworth R.E. 1997. The structure of the Carajás N-4 ironstone deposit and associated rocks: relationship to Archaean strike-slip tectonics and basement reactivation in the Amazon region, Brazil. Journal of South American Earth Sciences, **10**(3-4):305-319.

Pinheiro R.V.L., Holdsworth R.E. 2000. The Anatomy of shallow – crustal transpressional structures: insights from the Archaean Carajás fault zone, Amazon, Brazil. Journal of Structural Geology, **22**:1105-1123.

Pinheiro R.V.L., Nezio J.A., Guedes S.C. 2001. A falha Carajás e a estruturação tectônica dos depósitos de ferro da Serra Norte, Carajás (PA). Simpósio de Geologia da Amazônia, 7, Belém. Resumos Expandidos. Sessão Temática IX – Geologia Estrutural/Geotectônica, 11-14, CD ROM

Rezende N.P., Barbosa A.L.M. 1972. Relatório de Pesquisa – Distrito Ferrífero Sera dos Carajás, Estado do Pará. Volume II – Mapas e Seções. Relatório em 5 volumes para o Departamento Nacional de Produção Mineral – DNPM & Companhia Vale do Rio Doce, 119p.

Rios F.J., Lobato L.M., Rosière C.A., Silva R.C.F., Souza A.S. 2004. Resultados preliminares do estudo metalogenético do minério hematítico de alto teor do depósito de ferro N5 – Carajás, utilizando microscopia e microtermometria de infravermelho, PA. *In*: Simpósio Brasileiro de Exploração Mineral, Ouro Preto, Maio 2004, Anais.

Rosière C.A., Chemale Jr. F. 2000. Brazilian formations and their geological setting. Revista Brasileira de Geociências, **30**(2):274-278.

Rosière C.A., Rios F.J. 2004. The origin of hematite in high-grade iron ores based in infrared microscopy and fluid inclusion studies: the example of the Conceição Deposit, Quadrilátero Ferrífero, Brazil. Economic Geology, **99**:611-624.

Rosière C.A., Seoane J.C.S., Baars F.J., Lobato L.M. 2004. Estruturação da Província Carajás e sua influência na mineralização de ferro, PA. *In*: Simpósio Brasileiro de Exploração Mineral, Ouro Preto, Maio 2004, Anais.

Rosière C.A., Baars F.J., Seoane J.C.S., Lobato L.M., da Silva L.L., de Souza S.R.C., Mendes GE.. 2006. Structure and iron mineralisation of the Carajás Province. Applied Earth Science (Trans. Inst. Min. Metall. B) 115(4):126-136.

Rumble D. III., Hoering T.C. 1994. Analysis of oxygen and sulfur isotope ratios in oxide and sulfide minerals by spot heating with a carbon dioxide laser in a fluorine atmosphrere. Accounts of Chemical Research, 27, 237-241.

Santos J.O.S. 2003. Geotectônica dos Escudos das Guianas e Brasil-Central. *In*: Geologia, Tectônica e Recursos Minerais do Brasil, Bizzi L.A., Schobbenhaus C., Vidotti R.M., Gonçalves J.H. (eds.), Companhia de Pesquisa e Recursos Minerais–CPRM, Cap. IV, p 169-226.

Santos J.O.S., Hartmann L.A.**,** McNaughton N.J., Fletcher I.R. 2002. Timing of mafic magmatism in the Tapajós Province (Brazil) and implications for the evolution of the Amazon Craton - Evidence from baddeleyite and zircon U-Pb SHRIMP geochronology. Journal of South American Earth Sciences, **15**:409-429.

Seoane J.C.S., Rosière C.A., Baars F.J., Lobato L.M. 2004. Mapeamento litoestrutural 3-D do Grupo Grão Pará, Província Mineral Carajás, PA. *In*: Simpósio Brasileiro Exploração Mineral, maio 2004, Ouro Preto, CD rom, ADIMB.

Sharp Z. D. 1990. A laser-based microanalytical method for the in-situ determination of oxygen isotope ratios of silicates and oxides: Geochimica et Cosmochimica Acta, **54**:1353-1357.

Silva G.G., Lima M.I.C., Andrade A.R.F., Issler R.S., Guimaraes G. 1974. Geologia das folhas SB-22 Araguaia e parte da SC-22 Tocantins. *In*: Levantamento de Recursos Minerais, Projeto Radam (Departamento Nacional da Produção Mineral–DNPM e Companhia de Pesquisa e Recursos Minerais–CPRM).

Silva V.F. 1994. Caracterização petrológica, mineralógica e química da formação ferrífera na Mina N4E Carajás-PA. Trabalho de Graduação, Centro de Geociências, Universidade Federal do Pará, 38 p.

Souza Z.S., Dall'Agnol R. 1996. Vulcanismo dacítico cálcio-alcalino Mesoarqueano no¨greenstone belt¨ Identidade, sudeste do Pará, Brasil. Geochimica Brasilienses, **10**:225-240.

Spier C.A., Barros de Oliveira S.M., Rosière C.A. 2003. Geology and geochemistry of the Águas Claras and Pico Iron Mines, Quadrilátero Ferrífero, Minas Gerais, Brazil. Mineralium Deposita, **38**:751-774.

Tallarico F.H.B., Figueiredo B.R., Groves D.I., Kositcin N., McNaughton N.J., Fletcher I.R., Rego J.L. 2005. Geology and SHRIMP U-Pb Geochronology of the Igarapé Bahia deposit, Carajás copper-gold belt, Brazil: an Archean (2.57 Ga) example of iron-oxide Cu-Au-(U-REE) mineralization. Economic Geology, **100**:7-28.

Tassinari C.C.G., Bettencourt J.S., Geraldes M.C., Macambira M.J.C., Lafon J.M. 2000. The Amazonian Craton. *In*: Cordani U.G., Milani E.J., Thomaz-Filho A., Campos D.A. (eds.), Tectonic Evolution of South America. Internat. Geological Congress, Rio de Janeiro, Brasil, 41-99.

Tassinari C. C. G., Mellito K. M., Babinski M. 2003. Age and origin of the Cu (Au-Mo-Ag) Salobo 3A ore deposit, Carajás Mineral Province, Amazonian Craton, northern Brazil. Episodes, **26**:1, p. 2:9.

Taylor H.P.Jr. 1968. The oxygen isotope geochemistry of igneous rocks: Contributions to Mineralogical Petrology, **19:**1-71.

Taylor H.P.Jr. 1974. The application of oxygen and hydrogen isotope studies to problems of hydrothermal alteration and ore deposition: Economic Geology, **69**:843–883.

Taylor D., Dalstra H.J., Harding A.E., Broadbent G.C., Barley, M.E. 2001. Genesis of high-grade hematite orebodies of the Hamersley Province, Western Australia. Economic Geology, **96**:837-873.

Thorne W.S., Hagemann S.G., Barley M.E. 2004. Petrographic and geochemical evidence for hydrothermal evolution of the North deposit, Mt Tom Price, Western Australia. Mineralium Deposita, **39**:766-783.

Tolbert G.E., Tremaine J.W., Melcher G.C., Gomes C.B. 1971. The recently discovered Serra dos Carajás iron deposits, Northen Brazil. Economic Geology, **7**:985-994.

Trendall A.F., Basei M.A.S., Laeter J.R., Nelson D.R. 1998. Shrimp zircon U-Pb constraints on the age of the Carajás Formation, Grão Pará Group, Amazon Craton. Journal of South American Earth Sciences, **11**(3):265-277.

Valley J.W., Kitchen, N., Kohn, M.J., Niendorf, C.R., Spicuzza, M.J. 1995. UWG-2, a garnet standard for oxygen isotope ratios: strategies for high precision and accuracy with laser heating. Geochimica et Cosmochimica Acta, V. 59, p. 5223-5231.

Varajão C.A.C., Bruand A., Ramanaidou E.R., Gilkes R. 2002. Microporosity of BIF hosted hematite ore, Iron Quadrangle, Brazil. Anais da Academia Brasileira de Ciências, **74**(1):113-126.

Veizer J., and Compston W. 1976. $^{87}Sr/^{86}Sr$ in Precambrian carbonates as an index of crustal evolution: Geochimica et Cosmochimica Acta, **40**:905–914.

Zucchetti M. 2007. Rochas máficas do Supergrupo Grão Pará e sua relação com a mineralização de ferro dos depósitos N4 e N5, Carajás, (PA): Unpublished Ph.D. thesis, Belo Horizonte, Brazil, Universidade Federal de Minas Gerais, Departamento de Geologia, 125p.

Zucchetti M., Lobato L.M., Hagemann S.G. 2007. Hydrothermal alteration of basalts host to the giant Northern Range Carajás iron deposits, Brazil. 9th SGA Meeting, Dublin (ago/2007), In press.

ANEXO 1

A hydrothermal origin for the jaspilite-hosted, giant Serra Norte iron ore deposits in the Carajás Mineral Province, Pará State, Brazil

Artigo publicado na Reviews of Economic Geology em Junho de 2008

A hydrothermal origin for the jaspilite-hosted, giant Serra Norte iron ore deposits in the Carajás Mineral Province, Pará State, Brazil

[1†]ROSALINE CRISTINA FIGUEIREDO E SILVA

rosalinecris@yahoo.com.br,

[1]LYDIA MARIA LOBATO, [1]CARLOS ALBERTO ROSIÈRE

[1]*Universidade Federal de Minas Gerais, Centro de Pesquisas Prof. Manoel Teixeira da Costa-Instituto de Geociências. Av. Antônio Carlos 6627, Campus Pampulha, Belo Horizonte, MG, 31270.901, Brazil*

[2]STEFFEN HAGEMANN

[2]*Centre for Exploration Targeting, School of Earth and Geographical Sciences, University of Western Australia, Australia, Crawley, Western Australia 6009*

[3]MÁRCIA ZUCCHETTI

[3]*Companhia de Pesquisas e Recursos Minerais-CPRM, Serviço Geológico do Brasil, Av. Brasil 1731, Funcionários, Belo Horizonte, MG, 30140.002, Brazil*

[4]FRANCISCUS JACOBUS BAARS,

[4]*Consulting Geologist, Av. Afonso Pena 4343/402, Mangabeiras, Belo Horizonte, MG, 30130.008, Brazil*

[5]ROBERTA MORAIS, IVAN ANDRADE

[5]*Vale, Estrada Raymundo Mascarenhas s/no, 66516.000, Serra dos Carajás, Parauapebas, Pará, Brazil*

Abstract

The Carajás iron ore deposits located in the southern part of the state of Pará in Brazil were discovered in 1967 and have produced about 70 million tons of iron ore annually. The deposits are hosted by the Neo - Archean metavolcano-sedimentary sequence of the Grão Pará Group, Itacaiúnas Supergroup. The protoliths to iron mineralization are jaspilites, whith are under- and overlain by basalts, both greenschist facies metamorphosed. The major Serra Norte N1, N4E, N4W, N5E and N5S iron ore deposits of the Carajás Mineral Province are distributed along, and structurally controlled by, the northern flank of the Carajás fold. High-grade iron mineralization (> 65 % Fe) is made up of hard and soft ores. The hard ores can be banded, massive and/or brecciated and are characterized by hematite-martite and hematite types. The soft ores are very porous, discontinuous and tabular, friable and banded. The basal contact of high-grade iron ore is defined by a hydrothermally altered basaltic rock mainly composed of chlorite and microplaty hematite.

Varying degrees of hydrothermal alteration have affected jaspilites to form iron ores. The study of variably altered jaspilites and hard ores indicates that the distal alteration zone represents an early alteration stage. It is mainly characterized by the recrystallization of jasper with the removal of its iron, and formation of magnetite (commonly martitized), overgrowing original microcrystalline and hematite associated with quartz and calcite veins. Two vein-breccia types characterize the distal alteration zone: V1a (quartz ± sulfide breccias) and V1b (carbonate ± sulfide breccia-veins). Sulfides are pyrite and chalcopyrite. The intermediate alteration zone, synchronous with the main iron-ore forming event, is characterized by: (i) progressive leaching of chert and quartz, leaving oxides and vugs; (ii) presence of martite as the dominant oxide along altered jaspilite layers; and (iii) partial filling of open spaces with microplaty/platy hematite. The intermediate alteration zone also contains the V2a (quartz ± hematite bedding-discordant veins), V2b (vug-textured quartz + hematite discordant vertical veins), and V3 (hematite ± quartz veins crosscutting and/or parallel to the jaspilite bedding). The proximal alteration zone, also synchronous with the iron-ore forming event, represents an advanced alteration stage (i.e., the high-grade iron ore) and is characterized by progressive martitization, forming anhedral hematite, continued space filling by comb-textured euhedral and tabular hematite in veinlets and along banding. The proximal alteration zone contains intense carbonate alteration associated with the high-grade ores resulting in the formation of ore breccias cemented by dolomite. Vein-breccias are classified as V4 – carbonate(iron cloud)-quartz breccia, and V5 (quartz ± microplaty hematite breccia) both located in high-grade ore.

The distribution of the rare-earth elements (REE) in variably altered jaspilites and hard ores follows two main distinctive patterns. Jaspilites from the N4W, N5E and N5S deposits, and hard ores from N1 and N4E have a low ∑REE content, are enriched in light REE and exhibit positive europium anomalies (Eu/Eu*> 1), which is typical of Archean banded iron formations. The REE

pattern defined by N5E ores is nearly flat and displays an increase in ∑REE and absence of the positive Eu anomaly. The increase in LREE was accentuated during the formation of magnetite and microplaty hematite, and the advance of martitization to form anhedral hematite. This may have favored the relative increase of HREE in the residual fluid, resulting in an increase in HREE in advanced-stage precipitates and almost flat REE patterns associated with the advanced stage of mineralization. It is during this hydrothermal stage that euhedral and tabular hematite are dominant. The REE increase in N4E and N5E ore samples further suggests the presence of significant amounts of Fe in the mineralizing fluid.

The first evidence for hydrothermal fluids that infiltrated the jaspilites is the vein-breccia type 1, which contains Ca-Fe-rich, high-salinity (up to 29.3 eq. wt % $CaCl_2$) fluid inclusions in quartz and carbonate with trapping temperatures-T_{trap} of 209 to 285°C. The next stage of hydrothermal fluid infiltration is characterized by vein type 2, which contains medium- to high-salinity Na-Fe-Mg-rich (13.6 to 21.2 eq. wt % $CaCl_2$) and Ca-rich fluid inclusions (6.8 to 18.4 eq. wt % $CaCl_2$) with T_{trap} of 225 to 275 °C and 190 to 295°C, respectively. Vein type V3 is characterized by low- and medium-salinity Ca(Mg)-Fe-Na-rich inclusions (1.2 to 19.2 eq. wt % $CaCl_2$) with trapping temperatures of 195 to 255°C and medium-salinity Na-Mg-rich fluid inclusions (8.9 to 14.4 eq. wt % CaCl2) with trapping temperatures of 240 to 277°C. Brecciated vein types V4 and V5 have Ca-rich, medium- to high-salinity fluid inclusions in quartz and high-salinity inclusions in carbonate (9.7 to 24.5 and 19. 2 to 30.1 eq. wt % $CaCl_2$, respectively), both trapped at 237 to 314°C, and low-salinity Na-K-Mg fluid inclusions (0.2 to 7.3 eq. wt % NaCl) trapped at 245 to 316°C.

Oxygen isotope analyses on quartz from V1 to V3 veins range from +10 to +18 per mil, respectively, and –1.0 per mil on martite to –10.0 per mil for the paragenetically latest euhedral-tabular hematite in the high-grade ores. This shift in $\delta^{18}O$ values of oxides may reflect influx of meteoric water during the advanced hydrothermal alteration stage and/or represents a result of intense fluid fluxes (i.e., high fluid/rock ratios). Sulfur isotope analyses of pyrite within distal V1 veins display a range of $\delta^{34}S$ from +2.5 to +10.8 per mil, with lighter $\delta^{34}S$ values (–5 to +5 per mil) in sulfides from the intermediate alteration zone of the wallrock basalts; these latter values are compatible with juvenile magmatic fluids. Carbon and oxygen isotopes on carbonates (i.e., calcite, kutnahorite and dolomite) from V1 and V4 vein types revealed a restricted range of $\delta^{13}C$ from –6.0 to –2.0 per mil and a wider range of $\delta^{18}O$ from +8.0 to +20.0 per mil, suggesting variable oxygen sources due to interaction with more than one fluid type, or significant changes in fluid-rock ratios during interaction with a heavy $\delta^{18}O$ fluid possibly magmatic. Strontium isotope ($^{87}Sr/^{86}Sr$) ratios of calcite±kutnahorite (V1 vein type) in equilibrium with magnetite, and kutnahorite-dolomite (V4 vein type) range from 0.712 to 0.750. The extremely radiogenic $^{87}Sr/^{86}Sr$ values from V1 vein type carbonates are probably only compatible with a granitic source. The mineralogical, geochemical

and isotopic changes from jaspilites to high-grade iron ores suggests a hydrothermal origin for hard ore via interaction with an early-stage medium to high-salinity Ca-rich and Ca-Fe-rich, relatively reduced magmatic fluid, which leached silica and formed magnetite. This fluid evolved to more oxidizing conditions, with the advance of martitization, increase in the REE concentration and microplaty hematite precipitation in veins and martite borders. Low $\delta^{18}O$ values of oxides suggest mixing with meteoric water during this intermediate hydrothermal alteration stage. The predominance of oxidized phases such as anhedral and euhedral/tabular hematites, low-salinity Na-rich fluid inclusions, and decreasing oxygen isotopic values towards late hematite types, indicate that the advanced-alteration stage is dominated by the meteoric fluids.

The proposed magmatic-meteoric hydrothermal mineralization model for the Carajás hard ores is substantially different to models for the Hamersley or Iron Quadrangle iron ores, but may have a genetic link to the numerous Proterozoic magmatic hydrothermal deposits in the Carajás Mineral Province. The new hydrothermal model has also significant implication for iron ore exploration under cover sequences and/or the exploration for deep extensions of existing shallow orebodies. New exploration parameters include the distinct structural control of ore zones by faults and folds, widespread hydrothermal alteration zones and related pathfinder minerals and chemical pathfinder elements such as REE, Ca, Na, Fe and S.

Introduction

The Carajás Mineral Province is located in the eastern part of the Amazon craton, east-southeastern Pará State, Brazil (Fig.1), and is considered one of most important mineral provinces of the world, with production and growing potential for Fe, Mn, Cu, Au, Ni, U, Ag, Pd, Pt, Os, Zn and W. The iron ores are hosted by the Carajás Iron Formation, which is interbedded with mafic volcanic rocks of the Grão Pará Group of the Neo-Archean Itacaiúnas Supergroup (Fig. 1). The Grão Pará Group outcrops along the northern and southern flanks of a synclinal structure, known as the Carajás fold, with a major shear zone known as the Carajás shear zone along the axis of the fold. Iron ore deposits developed along the northern flank of the fold, known as the Serra Norte (Northern Range) deposits and along the southern flank known as the Serra Sul (Southern Range) deposits (Fig. 1). At present, only some of the Serra Norte deposits are mined with extensive exploration taking place in some of the Serra Sul deposits. There are nine deposits in the Serra Norte, numbered N1 – N9 (Figs. 1 and 2), with strike lengths from hundreds of meters to tens of kilometers and some of them comprise two or more orebodies. The combined resources of the nine deposits are 17.3 Bt at 66 wt. percent Fe (CVRD, 2007), with orebody thicknesses varying from approximately 250 to 300 meters. Production from five orebodies (N4E, N4W, N5E, N5W and N5EN), mined presently in open pits (Figs. 2A and B), reached 85 million tons in 2006 (CVRD 2007), which made Carajás the second-largest Brazilian producer of iron following the Quadrilátero Ferrífero (Iron Quadrangle) region of Minas Gerais State (Rosière et al., 2008). Production, reserves and ore grades for the Carajás Serra Norte iron ore deposits are presented in Table 1.

Jaspilites constitute the protore in many iron ore deposits of the Carajás region (Meirelles, 1986). The term jaspilite was first applied in the Lake Superior area to name oxide-facies iron-formation in which silica is present as jasper (UNESCO, 1973), and in the Lake Superior-type iron ore deposits in Australia (Liddy, 1968). In Carajás, the term jaspilite was first used by Suszczynski (1972) to describe the banded iron formations (BIFs) in the Serra Norte deposits (Fig. 1). This type of BIF consists of bands of chert with hematite dust (i.e., jasper) intercalated with iron oxides. In this paper, and other recent contributions to the Carajás iron ore mineralization (e.g., Lobato et al., 2004; 2005a, b; 2008; Figueiredo e Silva, 2004; Hagemann et al., 2006; Figueiredo e Silva et al., 2007a; b; in preparation; Zucchetti, 2007; Zucchetti et al., 2007), we use the term jaspilite as the BIF type described in the Serra Norte mines and surroundings. This BIF type is clearly different from BIF found in other parts of the Carajás area. A volcanogenic origin for these jaspilites is indicated by Meirelles (1986), Dardenne and Schobbehaus (2001, and references therein) and Klein and Ladeira (2002) based on the Grupo Grão Pará tectonic environment and/or the geochemical characteristics of the jaspilites. However, we use jaspilite as a descriptive term with no genetic connotation.

The Carajás Range iron ore occurrences were discovered in August 1967 by Companhia Meridional de Mineração, the pilot area being the current N1 deposit (Beisegel et al., 1973). In 1969, 18 mineral exploration license areas were claimed by Companhia Meridional de Mineração and Companhia Vale do Rio Doce (CVRD – now named Vale) encompassing some 160 000 ha area. From 1970 to 1972, an intensive exploration program was executed (Beisegel et al., 1973). Open pit mining of the N4E deposit started in 1984, followed by the N4WC (central northwestern 4 orebody) in 1994, the N4WN (north northwestern 4 orebody) in 1996, and the N5W and N5E deposits in 1998 (Huhn et al., 2000). Presently, all iron ore deposits belong entirely to Vale, the world's largest producer of iron ore (CVRD 2007). At the moment, the S11 orebody in the Serra Sul is the subject of an intensive exploration campaign

Similar to other BIF iron ore districts in Brazil, such as the itabirites in the Iron Quadrangle in Minas Gerais State, jaspilites hosts soft (i.e., high porosity) and hard (i.e., low porosity) high-grade ores. Both supergene and hypogene genetic models explaining the formation of iron ores have been suggested (Morris, 1985). During the past 10 years, many research groups have studied iron ore deposits in Australia (Barley et al., 1999; Hagemann et al., 1999; Taylor et al., 2001; Thorne et al., 2004), South Africa (Beukes et al., 2002; Netshiozwi, 2002; Gutzmer et al., 2006) and Brazil (Varajão et al., 2002; Cabral et al., 2003; Spier et al., 2003; Rosière and Rios, 2004; Rosière et al., 2008,). Although these deposits contain hypogene iron mineralization, with silica leaching, with or without iron addition, most authors agree that supergene fluids are involved in the iron ore forming process as well. Recent studies have proposed a hydrothermal origin for the Carajás hard iron ores, with hydrothermal introduction of e.g., hematite, carbonate and sulfide (Guedes, 2000; Guedes et al., 2002; Figueiredo e Silva, 2004; Figueiredo e Silva et al., 2004; Figueiredo e Silva et al., 2005; Dalstra and Guedes, 2004; Lobato et al. 2004, 2005a, b). There is significant evidence, based on constraints of the paragenetic sequence and textural features, for the contemporaneous emplacement of veins and hydrothermal alteration in the jaspilite and also in the mafic wall rocks, which caused the transformation of jaspilites to high-grade ores, i.e., the mineralization process(es). This paper is only concerned with the formation of hard ores considered to be of hypogene origin and provides: (1) a reevaluation of the regional setting of the Carajás Mineral Province, (2) descriptions of the main iron ore deposits, (3) the petrography and geochemistry of the protore and hard iron ores, (4) hydrothermal alteration zonation including vein classification, (5) preliminary fluid chemistry data with regards to veins and hydrothermal alteration minerals that formed during the transformation of jaspilite to hard ores, (6) an assessment of previous models, and (7) a preliminary genetic model.

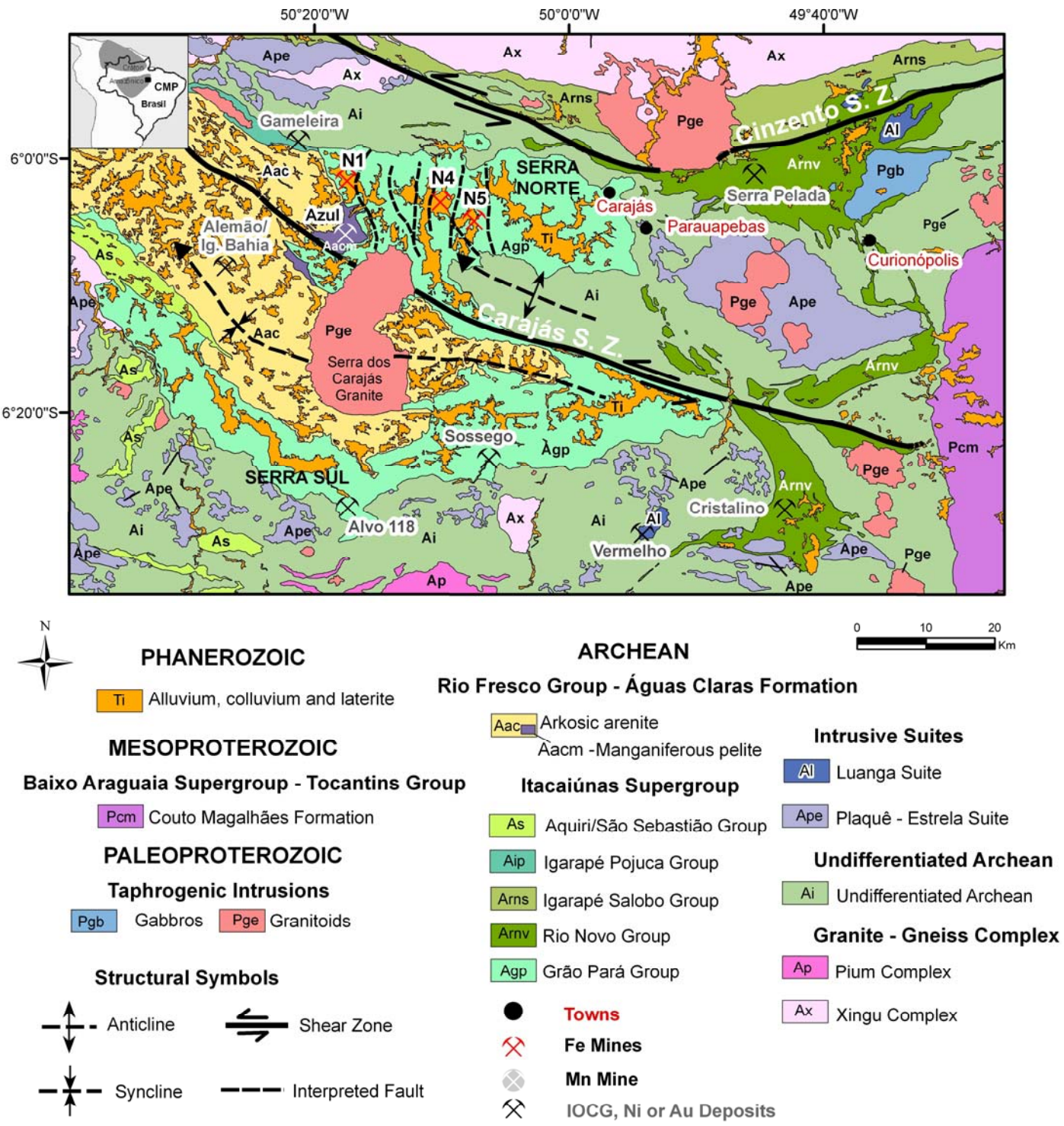

FIG. 1. Geological map of the Itacaiúnas Shear Belt, Carajás Mineral Province (modified after Rosière et al., 2006) showing major mineral resources including iron ore deposits N1, N4 and N5 (Serra Norte), Serra Sul and Serra Leste; some IOCG deposits (Alemão/Igarapé Bahia, Sossego, Cristalino); some Cu-Au (W-Bi-Sn) Gameleira and Alvo 118 deposits; the Serra Pelada gold-palladium deposit; the Azul manganese deposit, and the Vermelho nickel deposit. Lithostratigraphic classification is adapted with field data from Costa (2007) and interpretation by Seoane et al. (2004), based on Landsat ETM7 RGB 321, 752 and PC1-52 images.

Geological Setting of the Carajás Mineral Province

The Carajás Mineral Province is divided into two Archean tectonic blocks, the southern Rio Maria granite-greenstone terraine (Huhn et al., 1988) and the northern Itacaiúnas Shear Belt (Araújo et al., 1988). The Carajás Mineral Province is characterized by: (1) the giant iron ore deposits of the Serras Norte (N1 to N9), Sul (S1 to S45) and Leste , (2) the iron oxide-copper-gold (IOCG) deposits of Salobo, Pojuca, Alemão-Igarapé Bahia, Cristalino, Sossego, and the Cu-Au (W-Bi-Sn) deposits Alvo 118 and Gameleira(Grainger et al., 2008); (3) the gold-palladium deposit at Serra Pelada, (4) the manganese deposits at Azul and Sereno; and (5) the nickel deposit at Vermelho (Fig.1). The area covered by these deposits is characterized by metavolcano-sedimentary rocks, and Meso- to Neo-Archean basement, which consist of igneous suites and metamorphic complexes (Santos, 2003; Tassinari et al., 2000).

In the northern Itacaiúnas Shear Belt, granite-gneissic terrains, such as the tonalite-trondhjemite-granodiorite Xingu Complex (Silva et al., 1974), form the basement underlying the volcano-sedimentary sequence. Many Archean granitoids intrude the basement and cover volcano-sedimentary sequences, such as the granites and diorites of the 2.74 Ga Plaquê Suite (Fig. 1) (Huhn et al., 1999), and the foliated 2736 ± 24 Ma Planalto alkali granite (Avelar et al., 1999; Huhn et al., 1999). Mafic-ultramafic intrusive rocks are represented by the 2763 ± 6 Ma Luanga suite (Machado et al., 1991).

The Serra dos Carajás (the S-shaped mountain belt that contains the major iron ore deposits) itself is composed of metavolcano-sedimentary and metasedimentary rock units of the Itacaiúnas Supergroup (Fig. 1). In the southern part of the Serra dos Carajás, the Itacaiúnas Supergroup includes greenschist-facies metavolcano-sedimentary and metasedimentary sequences of the Igarapé Bahia (2745 ± 1 and 2747 ± 1 Ma; Galarza and Macambira, 2002), Aquiri, Grão Pará (Santos, 2003) and Rio Novo (e.g., Costa, 2007) Groups. In the north it includes the amphibolite-facies Igarapé Salobo and Igarapé Pojuca Groups (e.g., Lindenmayer, 1990). Despite their tectono-metamorphic overprint, these rocks commonly exhibit low-strain features, and original structures and textures may be preserved. Igneous or sedimentary terminology is widely used for these rocks and the prefix ‘meta’ is implicit but omitted for ease of reading in this manuscript.

The Grão Pará Group (Fig. 1) is a typical greenstone-belt succession composed of volcanic and sedimentary rocks with ages between 2.8 and 2.7 Ga (Gibbs et al., 1986; Wirth et al., 1986; Olszewsky, 1989; Macambira et al., 1996b; Trendall et al., 1998) with interbeds of BIF. The lower unit of this Group, the Parauapebas Formation (Meirelles et al., 1984), consists mainly of basalts and basaltic andesites, and minor basic to intermediate pyroclastic rocks. An amygdaloidal facies is found closer to the top of the unit (Meirelles et al., 1984) with BIF and basic tuff intercalations. In the basal portions, rhyolite layers are found together with fluvial conglomerates and arenite. The rocks

were subjected to regional greenschist metamorphism and hydrothermal alteration that caused iron enrichment (Figueiredo e Silva et al., 2007; Lobato et al., 2007). The pyroclastic or volcanoclastic rocks preserve ocean-floor hydrothermal minerals, and this suggests very low-grade metamorphism (Zucchetti and Lobato, 2004; Zucchetti, 2007). Parauapebas Formation metabasalts that are devoid of hydrothermal alteration are composed of actinolite, chlorite, epidote, quartz, and calcite, compatible with greenschist facies metamorphism (Meirelles, 1986; Macambira et al., 1990; Teixeira and Eggler, 1994; Teixeira et al., 1997).

The middle part of the Grão Pará Group is formed by the BIFs of the Carajás Formation (2751 ± 4 Ma; Krymsky et al., 2002), which host the giant iron ore deposits (Tolbert et al., 1971, 1973; Gibbs and Wirth, 1990). The Carajás Formation was defined in 1972 (DOCEGEO, 1988). It contains layers and discontinuous lens-shaped bodies, or lenses, of jaspilites and iron ores, intruded by mafic sills and dikes. The mafic sills and dikes at the N4E deposit vary from centimeters to tens of meters in width (Macambira and Silva, 1995). Jaspilites display typical intercalation of centimeter-thick, light and dark layers, or mesolayers (about 5 cm), and microlayers with iron-oxide layers intercalated with reddish to light-colored layers comprised of jasper and chert, respectively. Primary structures and textures in the jaspilites such as syn-sedimentary microfaults and spherulites (jasper or chert ringed by hematite) are still observed, despite the greenschist grade of metamorphism (Meirelles, 1986). Dolomite-bearing iron formations consist of layers of dolomite and chert in varying proportions, alternating with dark iron-oxide layers (Macambira and Schrank, 2002; Dalstra and Guedes, 2004). The dolomite-bearing iron formations are approximately 50 meters thick extending for about 400 m along strike.

In the central part of the Serra dos Carajás, the volcano-sedimentary rocks are covered by sedimentary psammo-pelitic rocks (e. g., arenites, calcarenites, siltites and conglomerates) of the Águas Claras Formation (Fig. 1), which yielded zircon U-Pb ages of 2708 ± 37 Ma (Mougeot, 1996) and 2645 ± 12 Ma (Dias et al., 1996).

Paleoproterozoic A-type, alkaline to subalkaline granites such as the Serra dos Carajás granite (Fig. 1) intrude the Itacaiúnas Supergroup and have an age of about 1880 ± 2 Ma (Machado et al., 1991). Dall'Agnoll and de Oliveira (2007) have classified these as oxidized, magnetite-series, rapakivi-type granites.

A Paleoproterozoic age for the iron mineralization has been constrained by whole-rock Sm-Nd data on hematitized mafic volcanic (basalt) wall rocks, along the contact with the high-grade iron ore (Lobato et al., 2005b). This age is well correlated to A-type granites in the Carajás region (e.g., Serra dos Carajás granite at 1880 ± 2 Ma; Machado et al., 1991). Moreover, a preliminary Pb-Pb SHRIMP age of 1866 ± 7 Ma has recently been obtained for hydrothermal brookite crystals (João Orestes S. Santos, verbal communication), formed after ilmenite in hematitized mafic volcanic

(basalt) wall rocks.

Tectonic and Structural Setting

Several interpretations have been presented for the tectonic evolution of the Itacaiúnas Supergroup volcano-sedimentary sequence in the Carajás region. Dardenne et al. (1988) suggest a rift-related subduction zone to account for the basin responsible for the Grão Pará Group's evolution, which would have developed on continental crust adjacent to rift zones (Olszewsky et al., 1989). Other authors point out that the volcano-sedimentary sequence is related to intracratonic basins (Gibbs et al., 1986; Machado et al., 1991; Lindenmayer and Fyfe, 1992; Santos, 2003; Grainger et al., 2007), or that such sequences formed in an arc environment of an evolving subduction zone (Meirelles and Dardenne, 1991; Teixeira, 1994; Lobato et al., 2005b; Rosière et al., 2006).

According to Zucchetti (2007) and Zucchetti et al. (2007), the Grão Pará Group basalts have a calc-alkaline magmatic affinity, and Nb-negative and Th-positive anomalies that are consistent with a subduction zone signature. Trace-element enrichment (e.g., high Zr/Y and Nb/Yb ratios) suggests that they formed in a continental-arc environment (Olszewsky et al., 1989; Zucchetti, 2007). Basalts and jaspilites with negative ε_{Nd} values (Lobato et al., 2005b) indicate crustal contamination of the Grão Pará sequence. Thus, the trace-element geochemistry characteristics suggest a back-arc-related tectonic setting on an attenuated continental crust (Zucchetti, 2007; Zucchetti et al., 2007). These authors also suggested that the Grão Para Group is a greenstone-belt-type sequence as previously indicated by Hirata et al. (1982), Meireles et al. (1984), Araújo and Maia (1991) and Faraco et al. (1996).

The structural setting of the Carajás Mineral Province is extensively discussed in the literature (Beisegel et al., 1973; Silva et al., 1974; Araújo and Maia, 1991; Holdsworth and Pinheiro, 2000; Pinheiro and Holdsworth, 1997; 2000) despite a distinct lack of detailed field data. A recent summary of the structural framework was provided by Rosière et al. (2006) who proposed that the dominant structure is a flattened flexural fold system with axes moderately plunging ESE to WNW, intersected by several strike-slip faults that trend sub-parallel to the fold plane of the fold system. This interpretation is based on structural data taken from several iron ore deposits (N1 to N5), regional mapping and satellite image analyses. Further to the southeast (N6 to N8), other Serra Norte deposits are currently being investigated in order to better define the regional structural setting including the anticlines and synclines.

The Serra dos Carajás itself is a S-shaped syncline-anticline pair, named the Carajás fold, and is partially disrupted by the Carajás shear zone. The latter divides the entire structure into blocks that subsequently were named the Serra Norte and Serra Sul (Fig. 1). The approximately WNW-ESE-

trending sinistral Carajás and Cinzento shear zones (Fig. 1) represent major structural discontinuities sub-parallel to the axial plane of several minor regional folds. The shear zones were likely developed to accommodate progressive flattening of the Carajás fold by lateral escape (Rosière et al., 2006). Another major event that influenced the structural setting of the area, particularly in the eastern part of the Carajás Mineral Province, was the intrusion of shallow-level (Barros et al., 2001), syntectonic calc-alkaline granite intrusions (named intrusive suites in Fig. 1), such as the Estrela Complex (Barros and Barbey, 1998, 2000), into the metamorphosed volcano-sedimentary sequences of the Itacaiúnas Supergroup.

The Carajás and Cinzento shear zones (Fig. 1) played a decisive role in the iron mineralization processes by preparing the terrane (i.e., increased the porosity) during the Archean and creating pathways for hydrothermal fluids to percolate in the Proterozoic when these shear zones were reactivated, resulting in roughly north-south splays along the Serra Norte iron ore deposits.

The high-grade Serra Norte orebodies developed in zones of greatly enhanced rock permeability at the regional hinge zone of the anticlinal Carajás fold (Rosière et al., 2006), which has been subsequently disrupted and rotated by faults and related splays. Hard orebodies surrounded by soft ore are preferentially concentrated in the hinge zone of large folds such as in the N5 deposit (Lobato et al., 2005a). The Serra Sul deposits are located within large (i.e., hundreds of meters to kilometer wavelength) second-order folds (Lobato et al, 2005b), but the detailed structural framework and relative timing relationships are presently not well constrained.

According to Rosière et al. (2006) and Lobato et al. (2005b), the formation of the Carajás iron orebodies postdated regional metamorphism and all Archean deformation events documented in the Carajás Mineral Province. Regional metamorphic grade is very low in rocks of the Grão Pará Group (e.g., Beisiegel et al., 1973; Gibbs et al., 1986). In the province, medium- to high-temperature minerals and tectonic fabrics in both ore and country rocks are found exclusively in the shear-zone domains, where high hydrothermal fluid-to-rock ratios control the mineral assemblages, or at the contact metamorphic zones near granitic bodies. Most of the granites in the Carajás Mineral Province and near the iron ore deposits are of Proterozoic age (e.g., Machado et al., 1991). High-grade iron ores also display a distinct hydrothermal texture, such as comb-textured hematite veins and breccias, which overprints the jaspilite fabric.

Table 1. Production and reserves (proven and probable) of N4 and N5 mines, based on database 31/12/2006 (CVRD, 2007).

Deposits	***Beginning of Operations***	***Expected Life of deposits***	***Production****		***Grade (wt % Fe)***	***Proven and probable reserves****	
			2005	**2006**		**2005**	**2006**
N4E	1984	2017	27.2	27.2	66.7	413.1	438.8
N4W	1994	2020	21.9	34.3	66.4	562.7	601.2
N5E	1998	2017	12.7	12.7	67.2	43.1	55.7
N5E-N	2003	2016	2.4	2.4	65.9	25.5	28.2
N5W	1998	2023	8.4	8.4	66.3	308.8	325.4
N5S	-	-	-	-	67.5	607.0	607.0
TOTAL			72.6	85		1960.2	2056.3

*million metric tons; - not in operation

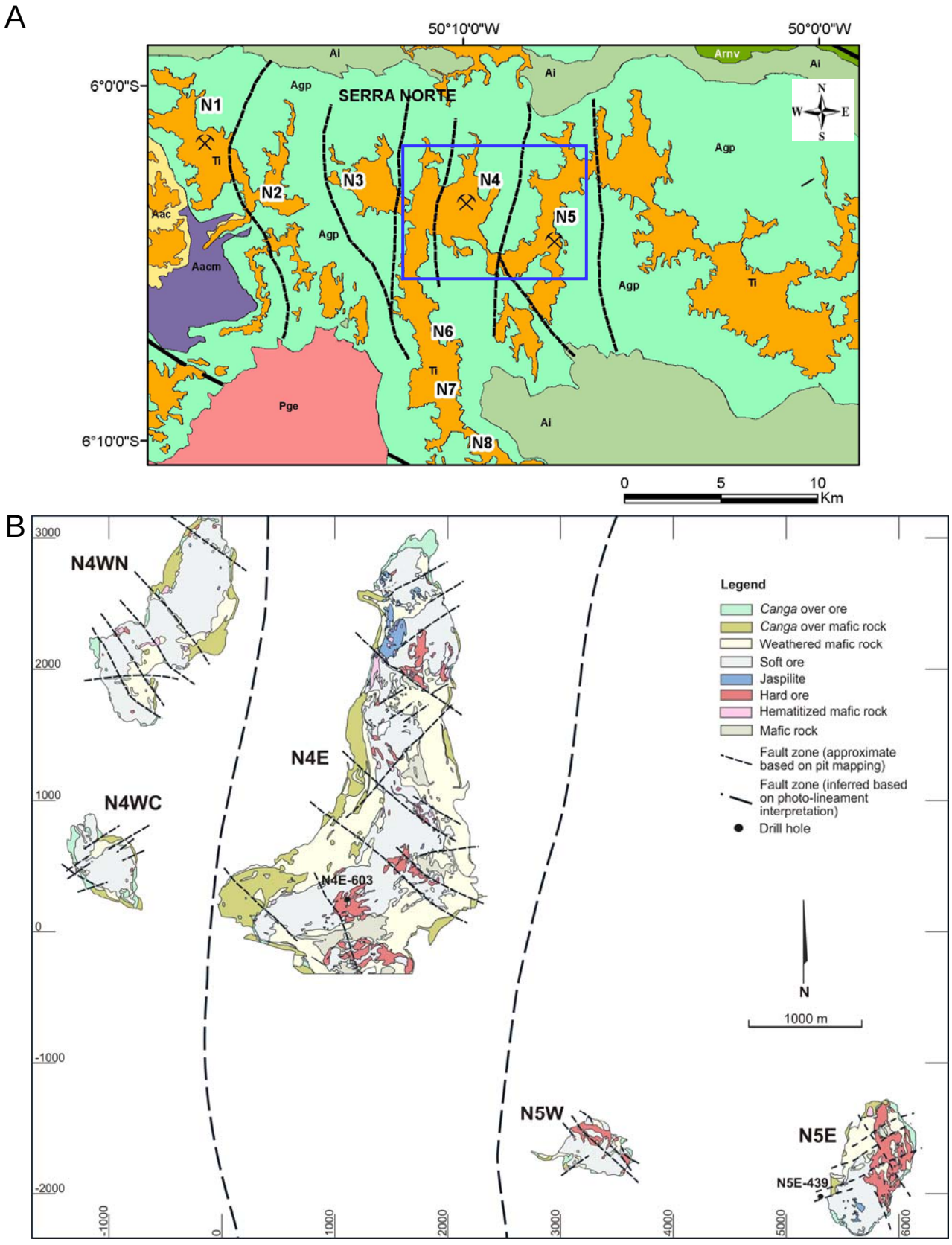

FIG. 2. A. Location of Serra Norte N1 to N8 deposits. Blue square represents area detailed in B (Refer to figure 1 for legend). B. Schematic geological map obtained from drill core and open pit mapping of the N4WN, N4WC, N4E, N5W and N5E deposits.

Iron Ore Deposits

Mesoscopic classification of ore types

The protore at the Serra Norte iron ore deposits is defined as: (1) jaspilite, which may contain bedding-parallel quartz veins, and (2) early-stage hydrothermally altered, so-called, least-altered jaspilite. Iron ore is defined as advanced stage hydrothermally altered and mineralized jaspilite and consists of hard- and porous hard-ore. Hard ore also includes variable amounts of quartz +/– hematite vein types. Soft ores can be the direct product of jaspilite and hypogene ores via supergene enrichment (see for example Tolbert, 1971), but these are not described here. The transition from the jaspilite to the hydrothermal hard ore encompasses the development of varying porosity stages that may locally characterize a high-grade soft ore type (Lobato et al., 2005a; 2008). This type of hypogene soft ore is typical of the N4E deposit.

High-grade ores can be both soft and hard, and are classified in terms of their physical hardness into hard to medium-hard, friable, soft and powdery and dusty ore (Clout and Simonson, 2005). Hard to medium-hard ores have a low porosity with an interlocking texture between martite and hematite, or martite-microplaty hematite grains. Friable ores are easily disintegrated by hand, and are more porous than medium-hard ore. They commonly break into centimeter-size prisms/plates, defined by joint planes and fissile beds. Soft (0.05-1.0 mm particles) ores are those that can be dug in situ by hand or with a shovel; they are very porous, but typically not powdery. Soft orebodies are discontinuous and tabular, friable and banded, and locally contain massive hard ore lenses.

The friable ore displays primary lamination and contains 64 to 67 wt per cent Fe. It consists of friable hematitic material with gray color, metallic luster and a high porosity. High-grade hard ores may be massive, and/or compact, brecciated and banded where the layers can be compact and/or porous (Rosière and Chemale Jr., 2000). Locally, the brecciated ores exhibit fragments of disilicified jaspilite layers, with the original fabric completely destroyed in places (Figueiredo e Silva, 2004). Compact hard ores, commonly gray blue, contain 67 wt percent Fe, have a metallic luster and low porosity. Massive hard ores are mainly observed along the contact between jaspilites and lower basaltic wall rocks as small lenses and tabular bodies (first described by Tolbert et. al., 1971), and also as lenses surrounded by basaltic rock.

Basalts in the N4 and N5 deposits display hydrothermal alteration minerals, with both intense chloritization and hematitization along the contact with the orebody (Figueiredo e Silva, 2004; Lobato et al., 2005b; Zucchetti, 2007).

Iron ores and weathered basaltic rocks are covered by ferricrete (*canga*), which formed in the superficial portions of deposits as a supergene product. It consists of cemented goethitic/limonitic material, with colloform, vuggy textures, and a high porosity. Where *canga* is located directly over

iron ore, it consists of hematite blocks that are cemented by hydrated iron oxides (Lopes, 1997). The classification and description of the supergene ores are provided in Rezende and Barbosa (1972), Beisiegel et al. (1973), Beisiegel (1982), and Ladeira and Cordeiro (1988).

Iron ore may be contaminated with: (i) manganese, particularly where in contact with lower basaltic wall rocks; (ii) aluminum and phosphorous where in contact with *canga*; and (iii) silica, which generally increases with depth (CVRD, 1996). The cut-off grade for iron ore is 60 wt % Fe, 2 wt % Mn, 2-2.5 wt % Si and Al, and 0.2 wt % P.

Geological setting of the N1, N4 and N5 deposits

N1 deposit: At the N1 deposit, the dip of the rocks of the Carajás Formation varies from 45^{o} to subvertical and outcrops are characterized by soft friable ore, soft lateritic hematite ore and *canga* cover. Hard ore is subordinate to soft ore and is found as either discordant (northeastern part of the N1 deposit) vein-controlled or - concordant (southeastern part of the deposit) lenses to the soft ore. Hard ore may contain hematite veinlets.

N4 deposit: The N4 deposit comprises two main orebodies, namely N4E and N4W that are interpreted to be separated by a N-S oriented fault (Fig. 2B). The N4W orebody (Fig. 2B) is presently the most important in the Carajás iron district, with total reserves in excess of 0.5 billion tons (Table 1), and consists mainly of soft ore and only minor hard ore. Bodies of hard ore are frequently close to NE-SW and NW-SE trending faults (Domingos, 2005). Jaspilites (Fig. 3A) have an average thickness of 220 meters (Borges, 1994) and crop out in the northern portion of the N4E deposit as well as smaller, < 40 meters thick lenses contained within the orebodies. Phosphorous, aluminum and manganese contents increase close to the ferricrete cover, and along contacts with mafic volcanic wall rock and dikes (CVRD, 2004).

The N4E open pit displays an approximate J shape structure in plan-view (Fig. 2B), with a N-S extension of 5 km, width of about 500 m and an average orebody thickness of 350 m. The deposit is divided into a northern and southern domain. In the northern domain, the lithological units strike mainly N-S and dip to the W. According to Ladeira and Cordeiro (1988), hard hematite orebodies and jaspilites are distributed discontinuously along a N30W trend in the northern domain of the N4E deposit, which is also the trend of the axial trace of early-stage folds (F1). The second-generation F2 folds plunge 4° toward N25-50W. Laminated soft ore predominates in the northern domain, containing many irregular and partially preserved jaspilite lenses. Lenses of hard ore are in the middle of soft ore (Figs. 2B, 4A) that is in contact with jaspilite. The jaspilites contain concordant and discordant quartz veins, as well as hematite veinlets with quartz nuclei. The soft ore contains hematite veinlets and is locally brecciated at the basal contact with basaltic rocks.

In the southern domain, bedding planes strike NE-SW and dip to the NW, giving the J shape of this deposit (Pinheiro et al., 2001). Soft ore also predominates in the southern domain, enclosing lenses of dolomite-bearing and manganiferous jaspilites and, banded hard ore that contains dolomitic carbonate veins (Fig. 3B). Hydrothermally altered, hematitized basaltic rocks are found in the eastern portion of this domain at the lower contact of jaspilite with the ore sequence. Near the contact with the iron ore, the basalts are totally replaced by chlorite and hematite (up to ~ 80 vol % of chlorite and 15-20 vol % of hematite) and minor quartz, calcite, and white mica. Hard hematite orebodies (>66 wt % Fe) occur mainly near the contact with the underlying mafic metavolcanic rocks. They are typically surrounded by a hydrothermal aureole, which may contain hydraulic breccias; vugs filled with carbonate, quartz, kaolinite, microplaty hematite, quartz-hematite veins (Fig. 3C), and fibrous chlorite aggregates (Guedes, 2000). Carbonate-sulfide veins are known to be present along the jaspilite-basaltic lower contact (Figueiredo e Silva et al., 2007b) in the southeastern portion of the N4E deposit.

At the N4W deposit, soft ore predominates and hard ore is scarce. The soft ore consists mainly of friable and porous hematite-martite material. The open pit is approximately 7 km long, 200 to 500 m wide (CVRD, 1996) and presentely reachs approximately 120m deep. The bedding of jaspilites and ores strike NW-SE with variable dips from subvertical to 40^{o}-50^{o} to the SW in the central part of the open pit. In the northern part of the open pit bedding strikes N20-30E, and dips 40^{o}-50^{o} to the NW (Pinheiro et al., 2001). Poles of these structures indicate major mine-scale folds with their axes plunging shallowly (< 30^{o}) to the NW (Pinheiro et al., 2001). A gradational soft ore and jaspilite contact is often observed in many of these mine benches (Fig. 3D). Quartz breccias (hematite-free), as well as bedding-discordant quartz veins, are commonly observed.

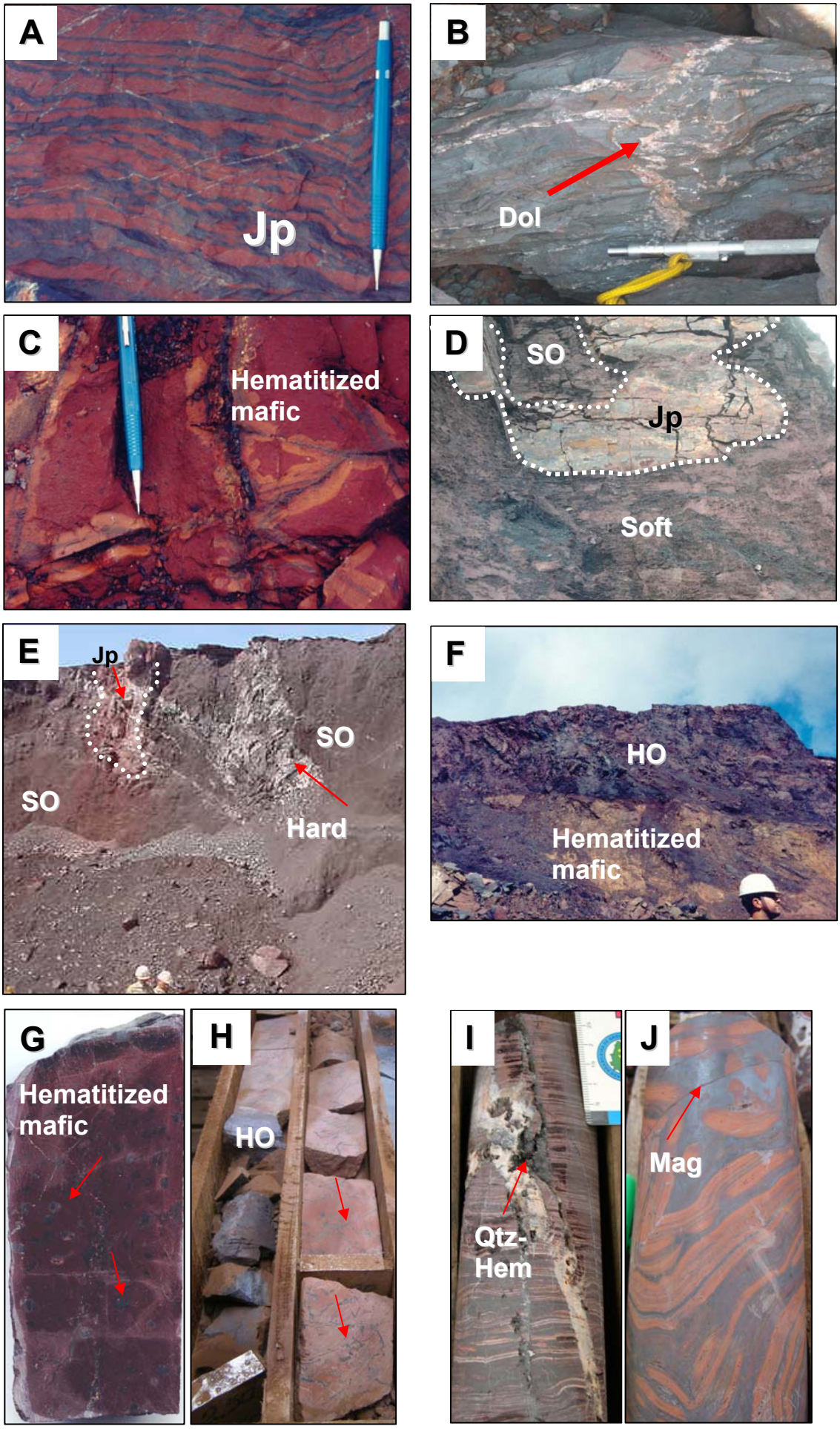
A
Jp
B
Dol
C
Hematitized
mafic
D
SO
Jp
Soft
E
Jp
SO
SO
Hard
F
HO
Hematitized
mafic
G
Hematitized
mafic
H
HO
I
Qtz-
Hem
J
Mag

FIG. 3. A. Jaspilite (Jp) in the N4E northern domain. Microbanding is defined by alternating jasper and iron oxides bands. B. High-grade massive ore with carbonate veins discordant to (arrow) and along bedding in the N4E southern domain. C. Mafic rock partially hematitized with hematite veinlets, N4E deposit. D. Gradational contact between jaspilite and soft high-grade ore (SO) in N4W deposit. E. Hematite hard ore stock-work veins crosscutting soft ore and also jaspilite lens, N5E deposit. F. Hematitized basaltic rock in contact with hard orebody, N5E deposit. G. Core sample of incipiently disilicified hematitized basaltic rock where amygdales are replaced by hematite (arrows), N5E deposit. H. Core samples showing contact between hard ore and basalt replaced by chlorite and hematite, with hematite veinlets (arrow), N5E deposit. I. Core sample of incipientily disilicified banded jaspilite from the N5S deposit showing quartz-hematite vuggy veins (arrow) cutting across the bedding in the jaspilite. J. Core sample of jaspilite from N5S deposit showing magnetite veins (arrow) cross-cutting the jaspilite. Abbreviations: Jp = jaspilite; SO = soft ore; HO = hard ore; Dol = dolomite; Qtz = quartz; Hem = hematite; Mag = magnetite.

N5 deposit: The N5 deposit (Figs. 2, 4B) displays geological characteristics, such as the dominance of massive hard ore overlying soft ore that are distinct from those at the N4 deposit. The N5E orebody is presently pod shaped, with jaspilites and high-grade ore, mainly hematite, surrounded by mafic rocks, which are locally hematitized where in contact with hard ore (Figs. 4B, 5). The jaspilites and basaltic rocks have a predominantly N40W to N80W strike and dip 50^{o}-60^{o} to the SW (Pinheiro et al., 2001). Numerous, metallic gray hematite, stockwork veins may constitute hard ore and locally crosscut both the soft ores and jaspilites (Fig. 3E). “Christmas-tree” veinlets are also observed (Guedes et al., 2002), similar to those described by Taylor et al. (2001) and Thorne et al. (2004). Evidence of dolomitic ore has only been noted in drillcore where dolomite veinlets crosscut and/or are parallel to beds, locally forming a carbonate-rich breccia fill (Figueiredo e Silva, 2004; Figueiredo e Silva et al., 2007a). The contacts between basaltic rock and hard ore, and jaspilite and porous hard ore, are gradational with clear lateral bedding continuity. The soft ore is enriched in silica near jaspilite lenses. Phosphorous contamination increases toward the ferricrete cover, whereas aluminum and silica increase towards the base of the orebody (CVRD, 2004). Discordant quartz veins are rarely associated with the hard ore. Zucchetti (2007) reported basaltic rocks that are completely replaced by chlorite and hematite where in contact with the iron orebodies (Figs. 3F-G). Late-stage hematite veins crosscut the chlorite-hematite rocks (Fig. 3H). At the N5S deposit, incipiently disilicified jaspilites are crosscut by vuggy quartz-hematite, and hematite-only veins that are either discordant or parallel to the jaspilite beds (Fig. 3I). Soft ore predominates and silica contamination is common. The most common hard ore in the N5S deposit constitutes meter-scale banded, silica-contaminated ore. This ore differs from the typical hard ores (which are scarce in N5S) in other deposits because it contains remnants of strongly desilicified (Fig. 3I) and hematitized jaspilite-like bands. Hard magnetite-rich lenses (approximately 2-m thick) are unique in the Serra Norte iron ore deposits, and are found locally at the jaspilite-ore contacts. Magnetite is also found as veins that are discordant or parallel to jaspilite beds (Fig. 3J).

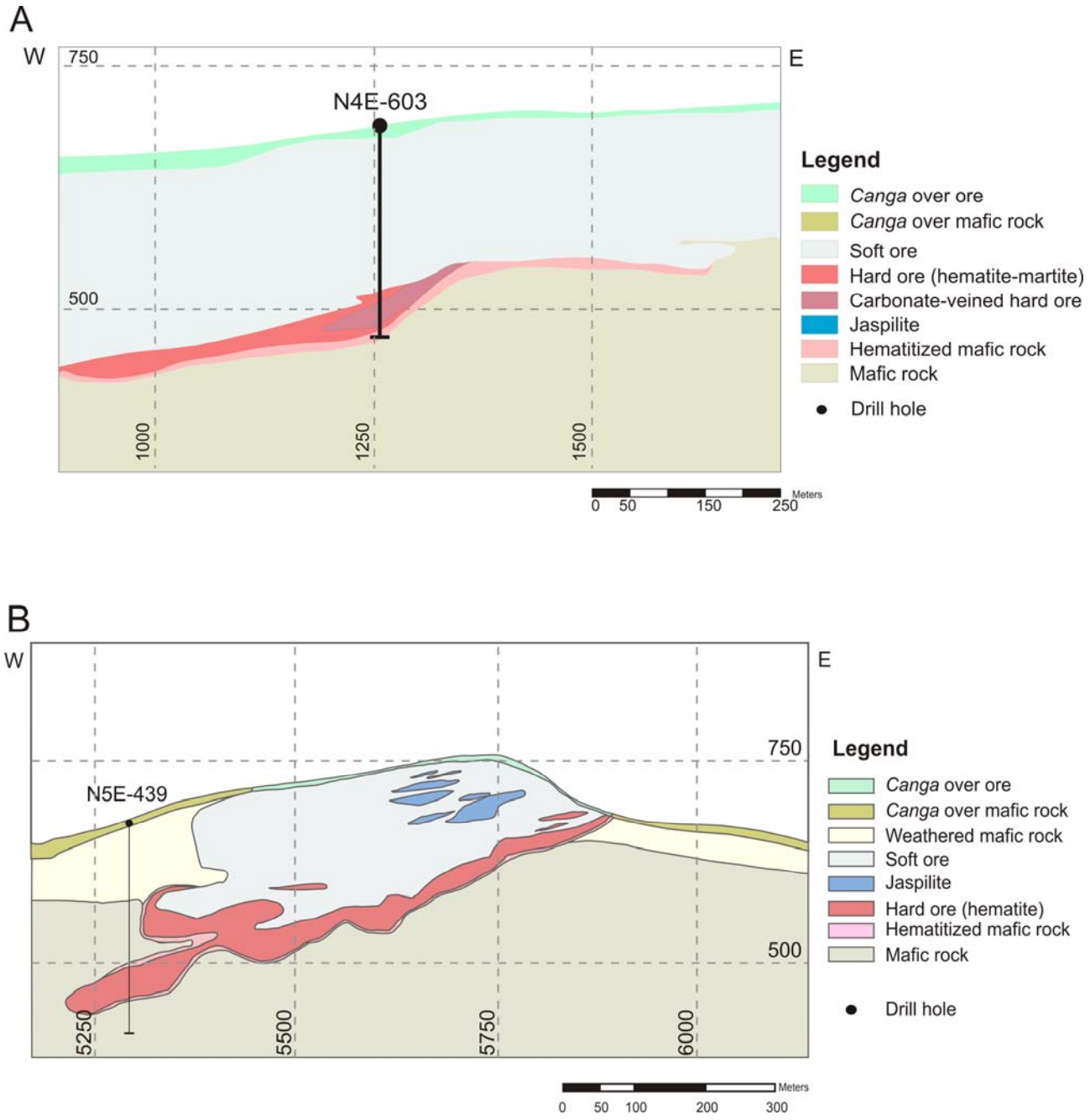

FIG. 4. A. Cross-section of the N4E orebody. B. Cross-section of the N5E orebody. Note the presence of a lens of hard ore along the contact with hematitized mafic rock. Source Vale (local mine grid). For location of drill cores refer to figure 2B.

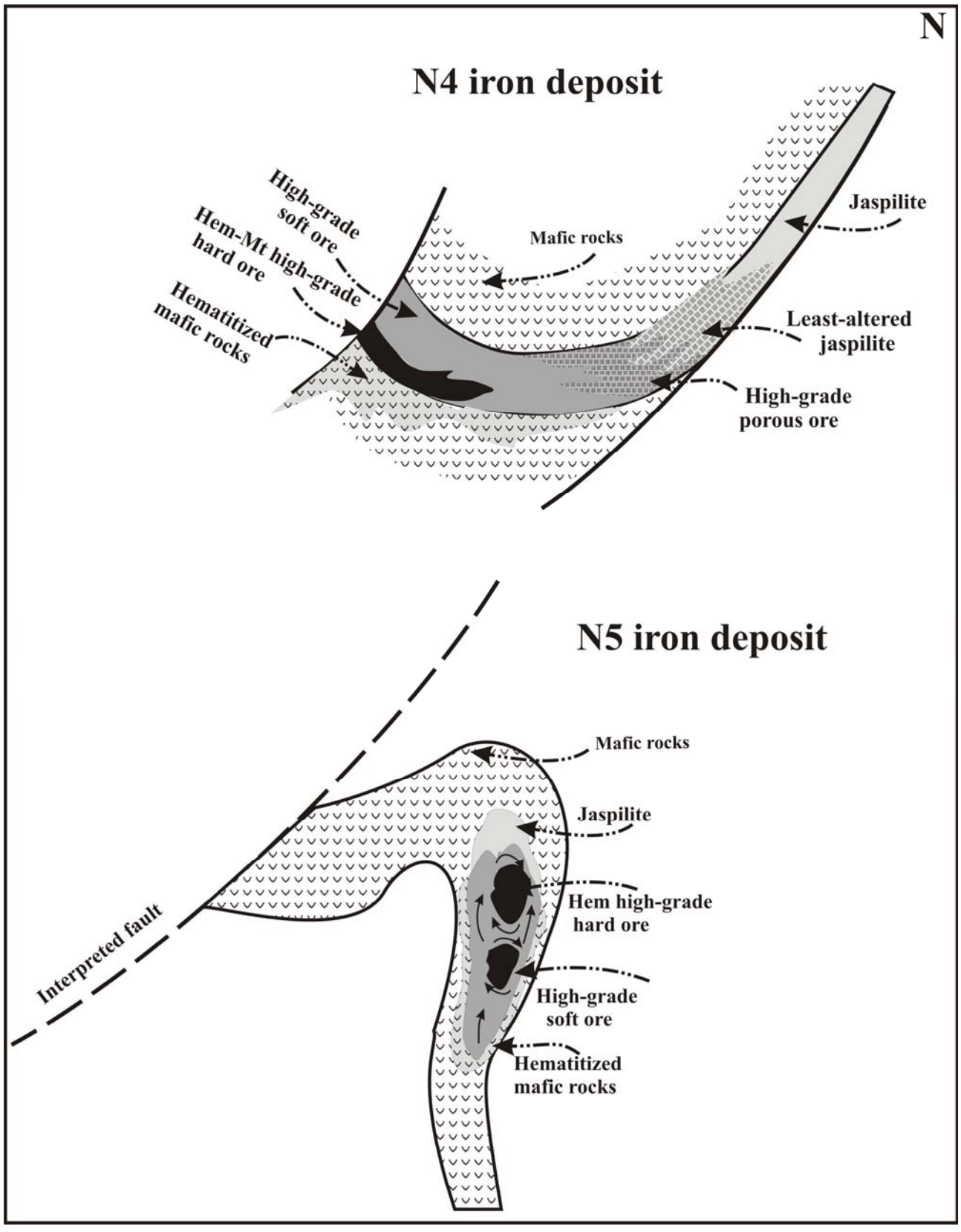

FIG. 5. Schematic illustration of the geological setting of the N4 and N5 deposits (Modified after Lobato et al. 2005a). The upper diagram represents the Serra Norte N4 deposit, which contains a large amount of the porous, high-grade soft hematite-type ore with lenses of hard ore. They are in contact with least-altered jaspilites and hematitized mafic rocks. The lower scheme depicts the N5 ore deposit, where the high-grade hard hematite-type ore is abundant. Mineral abbreviations: Hem: hematite; Mt: martite; Mag magnetite.

Petrography of Jaspilite and Hard Ore

Jaspilite and least-altered jaspilite

Jaspilite is characterized by alternating micro- to mesolayers (2 to 40 mm) of jasper and microcrystalline hematite (MiHem). The jasper layers (Fig. 6A) contain chert and dusty hematite, which is defined as <0.004 mm hematite particles. Locally the jasper layers contain chalcedony spherulites (0.01 to 0.1 mm in diameter). The MiHem layers (Fig. 6B) are composed of dense concentrations of very fine-grained, <0.004 mm, hematite crystals that represent the original oxide species of the jaspilite bands.

Least-altered jaspilite contains portions of hematite-free, recrystallized chert in equilibrium with magnetite, interpreted as the early stage of hydrothermal alteration. Variably altered jaspilites may be brecciated, containing various amounts of hematite types (e.g. microplaty and anhedral), and vein-associated quartz, carbonate and sulfide minerals.

Iron Ores

Iron ores are classified based on the oxide paragenetic sequence and detailed texture and mineralogy of oxides and gangue minerals such as quartz and carbonate (Table 2 and Fig. 7). Two main ore types are recognized: (i) hematite-martite (Figs. 7A, B and C), and (ii) hematite ores (Figs. 7D and E). Locally, the major ore types may develop certain variations (Table 2). Ores from the N4E deposit, for example, are characterized by a combination of different hematite types and martite, and may preserve layering (Fig. 7A) inherited from the jaspilitic protore; such ores may exhibit a continuous transition from a typical hard to a porous hard ore. The martite-hematite hard ore with quartz veins (Figs. 7C and H) has only minor amounts of carbonate. In contrast, carbonate and hematite-martite ores (Figs. 7B and G) contain significant amounts (up to 70 vol %) of carbonate (Figs. 7B and G). The ores of the N5E deposit differ from those of other deposits because they are brecciated and comprised almost entirely of hematite, i. e., massive or porous hard ore (Figs. 7D and J), representing those hard ores where the original layers were almost obliterated (Figs. 7 I, J and K).

Hematite-martite ore type: This ore type is typical of the N4E and N1 deposits. Hematite-martite ore is mainly composed of microcrystalline (+/– microplaty) hematite and disperse euhedral martite crystals with or without MpHem. Most of these ores still preserve the original jaspilite texture. Euhedral martite crystals are about 100 to 300 μm in size (Fig. 6D) and overgrow the massive MiHem and/or MpHem. Locally, kenomagnetite relics are present. Microplaty (or lamellar) hematite is made up of platy crystals, commonly with diamond-shaped sections of approximately 4-8 μm, locally up to 100 to 200 μm in length. The MpHem generally occupies vein walls (Fig. 6E), grows at the expense of martite (Fig. 7F), and less commonly is found in the center of martite

crystals. Anhedral hematite (AnHem) forms eye-shaped agglomerates of lobate crystals in the oxide layers and also in veins. The crystals are ~ 20 μm in size and where located in veins, they display growth lamellae (Fig. 6F). Euhedral and bladed-tabular (EHem-THem) hematite occurs in veins, is fine- to medium-grained (200 to 300 μm) and forms internal selvages to veins (Fig. 6G). Microcrystalline hematite is recrystallized, where in contact with these EHem-THem hematite veins.

Table 2. Hard ore types characteristics.

	Ore types				
Main types	**Hematite-martite**			**Hematite**	
	Hematite-martite (Hard Ore - HO**)**	Martite-hematite (brecciated HO)	Carbonate and hematite-martite (banded and brecciated HO)	Veined hematite (banded and/or brecciated HO)	Hematite and carbonate (brecciated HO)
Deposits	N1 and N4E	N4E	N4E	N5E	N5E
Mineralogy oxides	MiHem, Mt (KenoMag), MpHem (±THem)	Mt (KenoMag), MiHem, MpHem, AHem-THem	Mt, MpHem, MiHem	MiHem, Sub-AHem, EHem-THem MpHem	AHem-EHem-THem, MpHem (filling porous), MiHem.
sulfides	absent	absent	absent	Ccp	absent
Veins-Veinlets	(i)Qtz-Chalc, (ii)Qtz-Kut, (MpHem), (iii) MpHem + AHem, aside from AHem + THem*, (iv)Qtz-Talc-PlatyHem, (v)LamellarHem	Qtz-Kut-MpHem	Kut-Qtz; Carb-Qtz-MpHem	Qtz; MpHem-THem*; AHem-EHem	Dol
Others	Some samples are essentially composed by MpHem and Mt (Kmag), where MpHem is (i) fine-grained (< 5 μm) and (ii) coaser-grained (140 μm)	Pyramidal Qtz (up to 4 mm); AHem-THem overprint massive aspect.	Kut (cal) can constitute up to 70 %; Kut zoning is defined by fine hematite dust in triangular and rhombohedral forms.	Rare Au particle included in hematite; Coarser-grained (300 μm) AHem with growth lamellae.	Original banding is the most obliterated, together with veined-hematite association.

Hematite ore type: These ores are typical of the N5E deposit and are essentially composed of hematite, mainly microcrystalline (<0.004 mm), besides AHem, MpHem, EHem (+/– 0.3 mm) and THem (0.2-0.3 mm) (refer to Table 2 for explanation of abbreviations). These ores are generally brecciated, but locally preserve the original micro- to meso-layers that, if present, are defined by the intercalation of continuous and/or discontinuous layers of fine-grained (+/–0.03 mm) AHem aggregates with MiHem. The latter hematite can be recrystallized at the contact with MpHem-THem veins. Anhedral hematite mesobands are locally discontinuous and interspersed with vugs that may contain MpHem. The EHem-THem is commonly comb textured, may exhibit growth lines, and partially fill open spaces or vugs.

Hematitized wall rock: It consists of hydrothermally altered basalt, which are found only at the contact between the mineralized jaspilite and the underlying basaltic wallrock. In the N4E deposit, they are composed of talc, kutnahorite, quartz and rare chlorite (locally in veinlets) together with

MpHem (up to 0.4 mm) (Fig. 6H), with subordinate anhedral crystals of martite. The EHem-THem veinlets crosscut these rocks and exhibit growth lamellae. At the N5E deposit, the hydrothermally altered basalts are composed of chorite (60%), with rare white mica, and MpHem (+/–35%) and martite (+/–5%). Rare kenomagnetite relics are present and locally also platy hematite with crystals up to 0.2 mm in length.

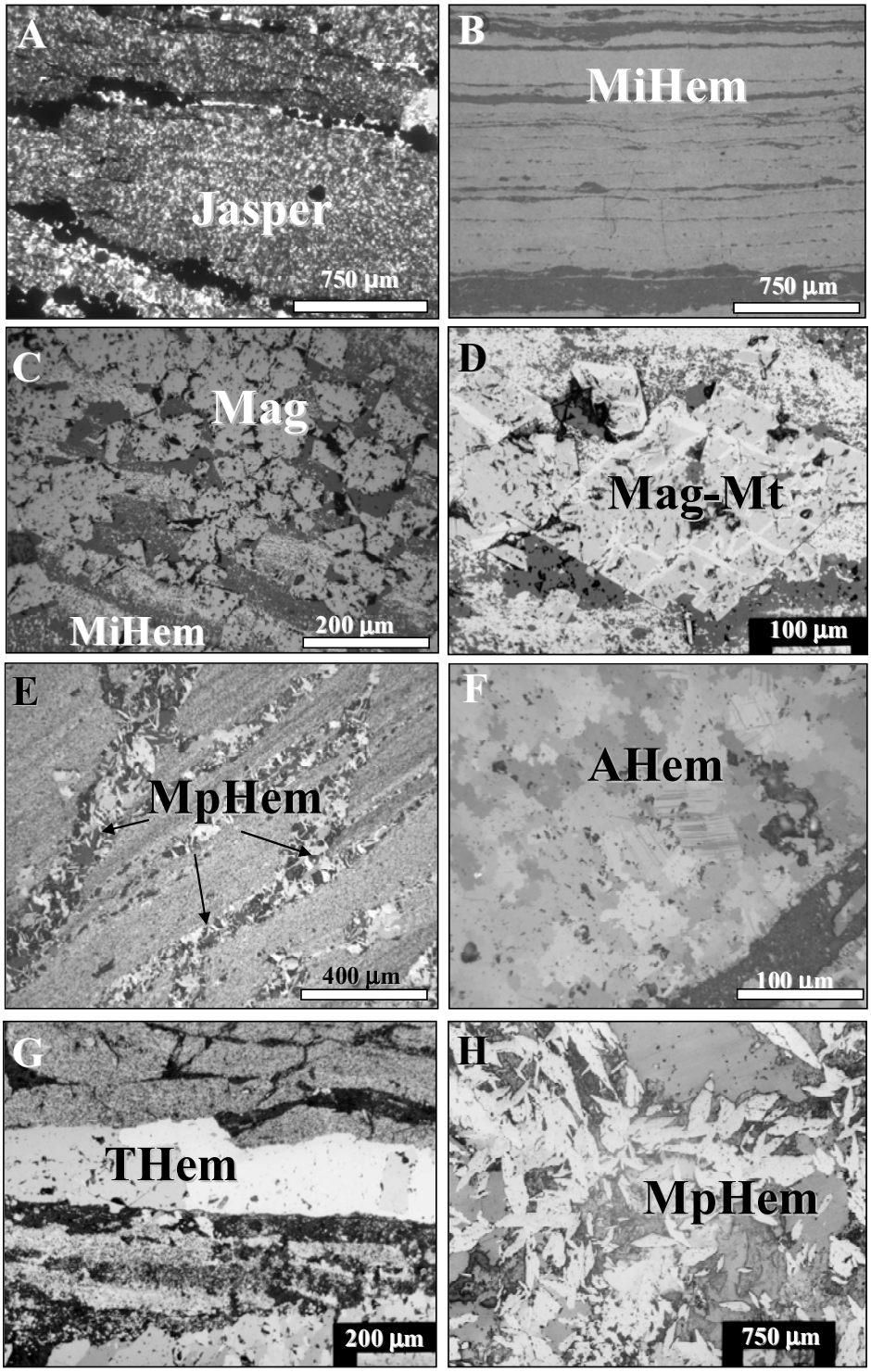

FIG. 6. Photomicrographs of jaspilite and ore. A. Jasper bands, rich in microcrystalline (or dusty) hematite, and recrystallized quartz in altered jaspilite, N4W deposit. Transmitted light, under crossed polars (25X). B. Bands of microcrystalline hematite in jaspilite, N4E. Reflected light (25X). C. Bands of microcrystalline hematite that is overgrown by magnetite, N4E deposit. Reflected light (100X).D. Magnetite partially oxidized to martite, N4W deposit. Reflected light (200X).E. Microplaty hematite developed along cavity/veinlets in brecciated hard ore, N5E deposit. Reflected light (50X). F. Anhedral hematite crystals with lobate borders in high-grade hematite ore, N5E deposit. Reflected light, under crossed polars (200X). G. Tabular hematite vein in brecciated N5E hematite ore. Reflected light, under crossed polars (100X). H. Microplaty hematite crystals in choritititized and hematitized mafic rock. Reflected light, under crossed polars (25X). Mineral abbreviations: MiHem = microcrystalline hematite; Mag = magnetite; MpHem = microplaty hematite; Mt = martite; AHem = anhedral hematite; THem = tabular hematite.

Hydrothermal Alteration

Hydrothermal alteration of jaspilite

Varying degrees of hydrothermal alteration have affected jaspilites. It caused the transformation of jaspilite to iron ore and is defined by a distinct paragenetic sequence of iron-oxide minerals with concomitant removal of silica and formation of a specific suite of veins that may contain quartz, carbonate, hematite, sulfide, monazite, and rare gold (e.g. Fig. 2 of Lobato et al., 2008).

The distal alteration zone represents an early alteration stage, whereas the intermediate and proximal alteration stages are synchronous with the main iron ore forming event. The proximal alteration stage also represents the advanced alteration stage, i.e., the high-grade ore itself. The distal alteration zone (up to ~ 80 m wide in the N4E deposit and ~ 100 m in the N4W deposit, measured vertically) in jaspilite is mainly characterized by the recrystallization of jasper and the removal of its iron, and the associated formation of magnetite (Fig. 8A). Magnetite crystals are euhedral to anhedral and form: (i) overgrowths on MiHem layers (Fig. 6C), (ii) grains in the nuclei of recrystallized chert invariably associated with crosscutting quartz veins, or (iii) grains in equilibrium with vein calcite and quartz. Magnetite is commonly replaced by hematite (martitization), leaving kenomagnetite relics (confirmed by Mössbauer analyses according to Figueiredo e Silva, 2004), which is a deficient Fe^{+2} magnetite phase (Kullerud et al., 1969). Sulfides such as pyrite, chalcopyrite (Figs. 8C and D) may be associated with the hydrothermal alteration, but it should be noted that relatively rare, syngenetic pyrite (N4W) and calcite (N4E) crystals also occur in parallel laminae of jaspilite (Fig. 8B). The veins formed in this alteration zone lack hematite.

The intermediate alteration zone is about 200 m in width (e.g., in the N5S deposit) and is characterized by martite, with or without kenomagnetite. Quartz-hematite and hematite-quartz veins are common (Fig. 8E) and contain MpHem and subordinate sulfides. The porosity increase in the altered jaspilites is significant, and affects the original jasper layers.

FIG. 7. Main features and characteristics of the different hard ore types. Core samples from A to E and photomicrograph from F to K. A. Hematite-martite ore type from the N4E deposit. B. Carbonate and hematite-martite (banded and brecciated) hard ore from the N4E deposit. C. Martite-hematite (brecciated and quartz veins) hard ore from the N4E deposit. D. Veined hematite (banded and/or brecciated) hard ore from the N5E deposit. E. Hematite and carbonate (brecciated) hard ore from the N5E deposit. F. Martite and MpHem crystals in hematite-martite type, N4E deposit. Note that MpHem grows along martite borders. Reflected light, under crossed polars (50X). G. Carbonate (kutnahorite) veins crosscutting MiHem and Mt bands of carbonate and hematite-martite ore, N4E deposit. Reflected light (50X). H. Mt crystals over MiHem bands in hematite-martite ore association, N4E deposit. Reflected light (50X). I. Anhedral-subhedral hematite portion characterizing brecciated hematite ore, N5E deposit. Reflected light, under crossed polars (50X). J. AHem and MpHem portions in brecciated hematite ore, N5E deposit. Reflected light (50X). K. Platy hematite (PHem)-quartz vein in brecciated ore, N5E deposit. Reflected light (50X). Mineral abbreviations: MiHem = microcrystalline hematite; MpHem = microplaty hematite; Mt = martite; AHem = anhedral hematite.

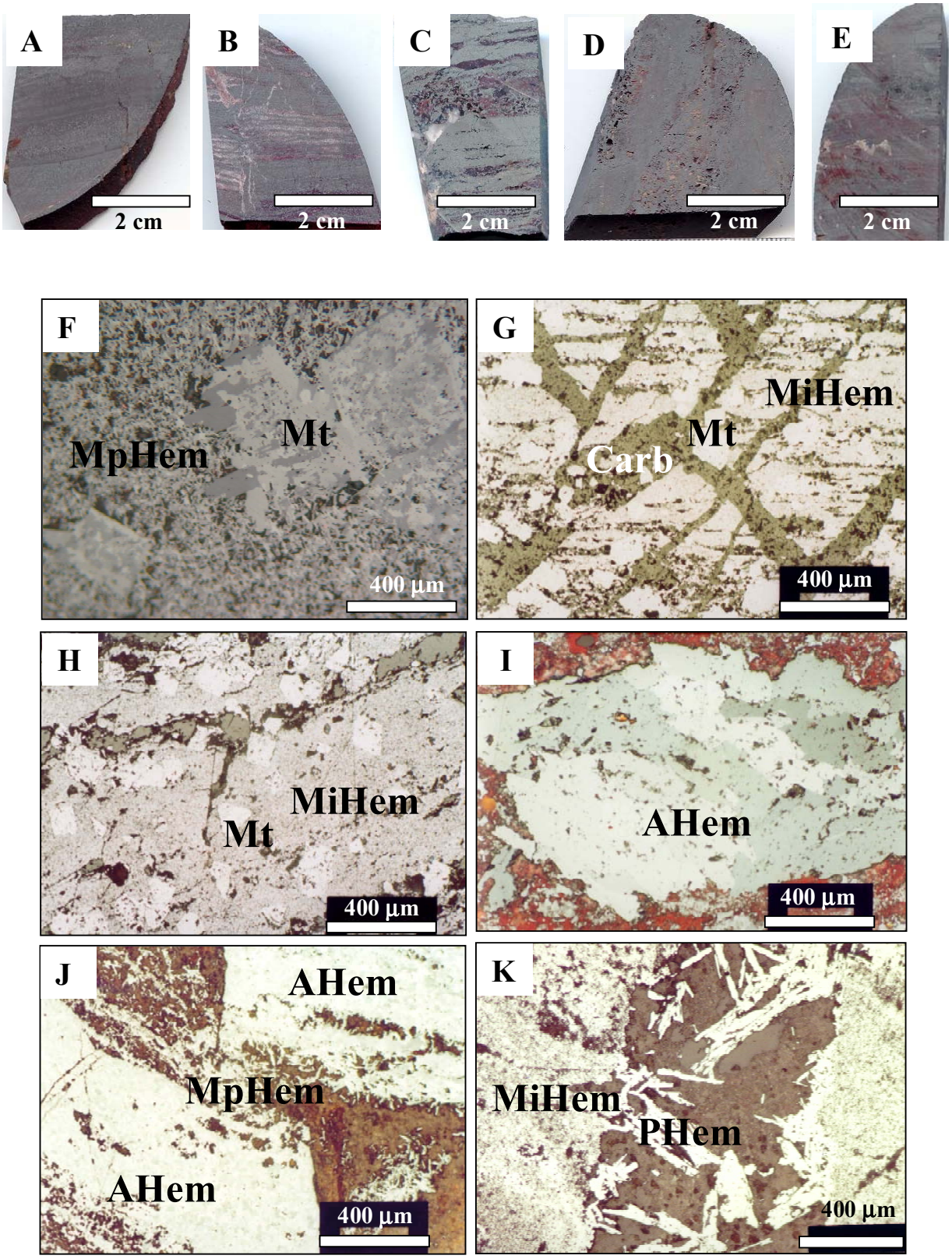
A
2 cm
B
2 cm
C
2 cm
D
2 cm
E
2 cm
F
MpHem
Mt
400 µm
G
MiHem
Mt
Carb
400 µm
H
MiHem
Mt
400 µm
I
AHem
400 µm
J
AHem
MpHem
AHem
400 µm
K
MiHem
PHem
400 µm

The proximal alteration zone, represented by hard and hard porous ores, is about 20 to 50 m in width. The original shape of martitic magnetite "blasts" is destroyed by the progressive martitization, forming Ahem (Table 2) in abundant eye-shaped agglomerates of lobate crystals. Intense carbonate alteration associated with the high-grade ores results in the formation of ore breccias cemented by dolomite. Examples are locally observed in the N5 deposit, and as kutnahorite cemented breccias in the N4 deposit. Hard ore with predominance of late-stage anhedral and tabular hematite lack quartz and carbonate veins. The presence of carbonate is mostly restricted to ores at depths >200 meters in the N5E deposit, and along the jaspilite-basaltic contact in the N4E deposit.

Microcrystaline hematite is stable even in the more advanced hydrothermal alteration stages. Stockwork-type veins contain tabular hematite. These zones are also characterized by discontinuous quartz ± carbonate veins with intergrown MpHem, which may be included in the hematite-martite ore type. The MpHem intergrown with quartz forms the matrix of hydrothermal breccias in the proximal alteration zone (Figure 8F).

Hydrothermal alteration of basaltic wallrock

Hydrothermal alteration of basaltic wallrock has also been subdivided into intermediate and proximal alteration zones (Zucchetti, 2007), but these do not correspond exactly to the alteration zones of jaspilites. The hydrothermal zones are characterized by chlorite and chlorite-hematite replacement of the igneous minerals, respectively. The intermediate alteration zone has abundant chlorite, calcite, quartz, hematite, white mica, albite, titanite, magnetite, and subordinate sulfide minerals. Chlorite and MpHem from the proximal alteration zone occur along veins, or replace amygdales (Figs. 8G and H). Quartz, white mica, albite, titanite, and calcite are subordinate. The intermediate zone can locally extend up to about 30 m, whereas the proximal zone is approximately 60 m wide relative to non-altered basaltic rock (Fig. 5C).

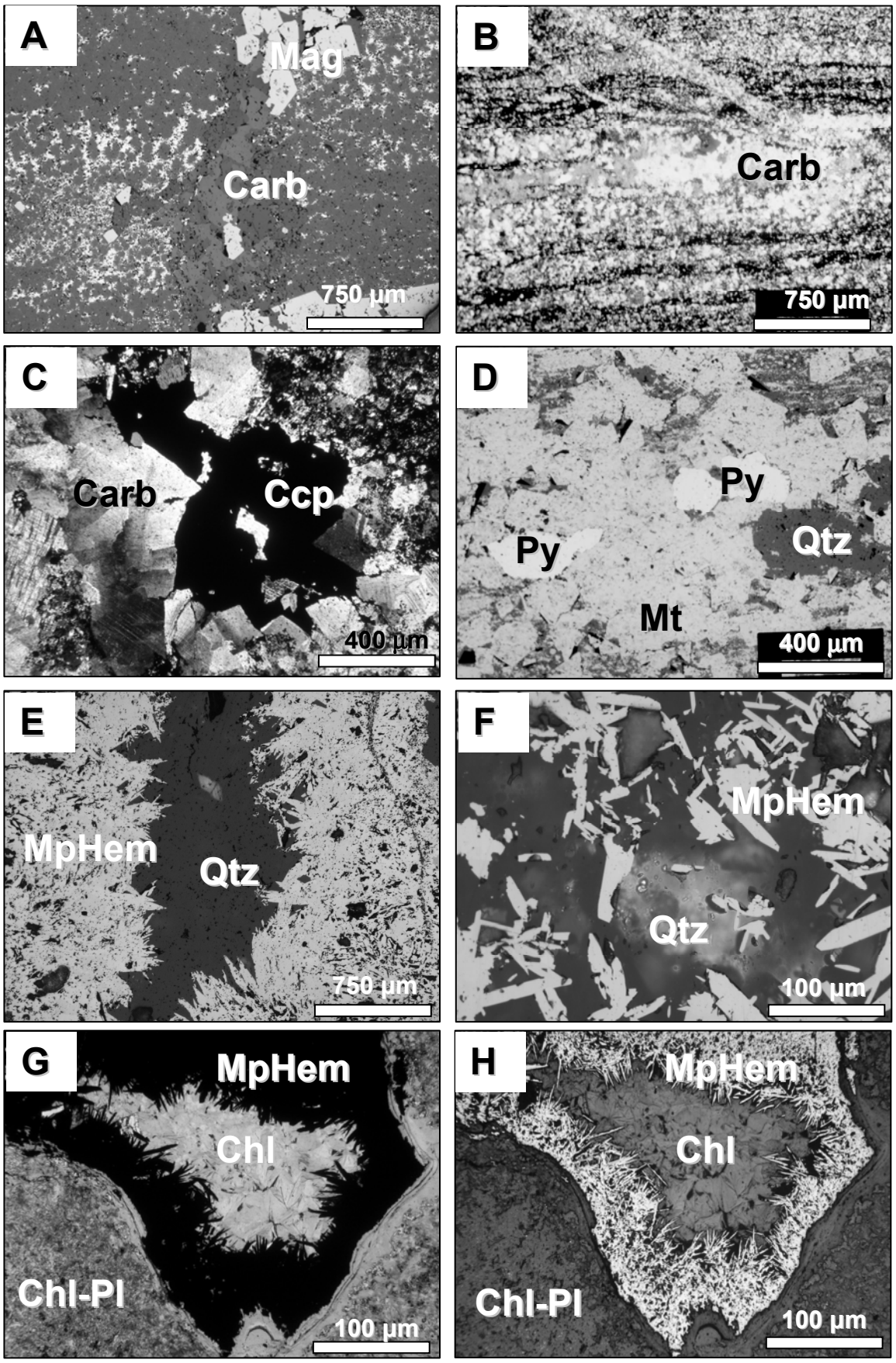
A
Mag
Carb
750 µm
B
Carb
750 µm
C
Carb
Ccp
400 µm
D
Py
Py
Qtz
Mt
400 µm
E
MpHem
Qtz
750 µm
F
MpHem
Qtz
100 µm
G
MpHem
Chl
Chl-Pl
100 µm
H
MpHem
Chl
Chl-Pl
100 µm

FIG. 8. Photomicrographs displaying some hydrothermal alteration features. A. Magnetite-carbonate (calcite) vein-breccia in altered jaspilite, N4E deposit. Reflected light (25X). B. Carbonate (calcite) vein-veinlets discordant and along jaspilite banding, N4E deposit. Transmitted light, under crossed polars (25X). C. Carbonate (calcite-kutnahorite) and chalcopyrite crystals in brecciated altered jaspilite, N4E deposit. Transmitted light, under crossed polars (50X). D. Pyrite crystals intergrown with martite in altered jaspilite. Reflected light (50X). E. Quartz-microplaty hematite vein, N5S deposit. Reflected light (25X). F. Microplaty hematite intergrown in matrix quartz of hydrothermal breccia from the proximal alteration zone, N4E deposit. Reflected light (200X). G. Chlorite and microplaty hematite replacing amygdale in hydrothermally altered basalt composed by chlorite and plagioclase. Transmitted light, under crossed polars (200X). H. Microplaty hematite replacing amygdale. Reflected light (200X). Mineral abbreviations: Mag= magnetite; Carb= carbonate; Ccp= chalcopyrite; Qtz = quartz; Chl = chlorite; Pl = plagioclase, MpHem = microplaty hematite.

Veins and breccias

Detailed logging of about 20 diamond-drill cores, through the N4 and N5 deposits, and petrographic and textural descriptions of veins and breccias were used to establish a vein classification with respect to their location in specific hydrothermal alteration zones and associated iron mineralization and the iron oxide paragenesis (Fig. 9). It must be emphasized that the vein types from the distal alteration zone do not contain hematite, and represent an early mineralization stage. In contrast, hematite is intergrown with quartz, carbonate and sulfides (where present) in veins from the intermediate and proximal alteration zones.

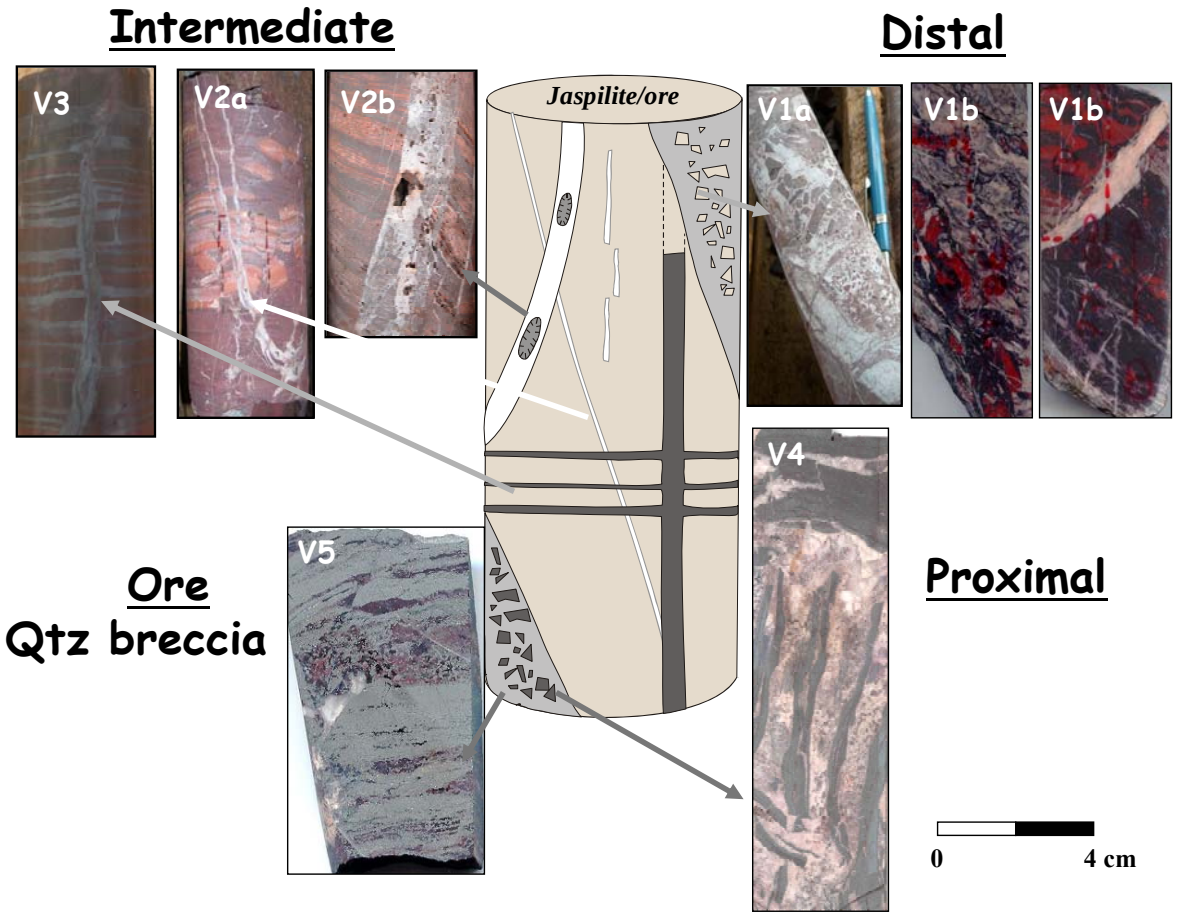

FIG. 9. Schematic diagram illustrating the classification of veins and breccias. Also shown are photographs of examples from core samples. Two vein-breccia types characterize the distal alteration zone in jaspilite: V1a - quartz ± sulfide breccia and V1b - carbonate ± sulfide breccia-veins. The intermediate alteration zone is represented by the following vein types: V2a - quartz ± hematite bedding discordant veins; V2b - vug-textured quartz + hematite discordant vertical veins; V3 - hematite ± quartz veins crosscut and/or along the jaspilite bedding. The proximal alteration zone is characterized by V4 - carbonate (iron cloud)-quartz breccia, and V5 - quartz ± microplaty hematite breccia, both are located in high-grade ore.

Two vein-breccia types characterize the distal alteration zone in jaspilite: V1a (quartz ± sulfide breccias, and V1b) carbonate ± sulfide breccia-veins. The intermediate alteration zone is represented by the following vein types: V2a (quartz ± hematite bedding discordant veins); V2b (vug-textured quartz + hematite discordant vertical veins); V3 (hematite ± quartz veins crosscut and/or parallel to the jaspilite bedding). The proximal alteration zone is characterized by vein filling in breccia classified as V4 (carbonate-quartz breccia) and V5 (quartz ± microplaty hematite breccia), both are located in high-grade ore.

Quartz is present principally as (i) micro- to cryptocrystalline crystal aggregates of mosaic texture, probably the product of recrystallization of chalcedony and amorphous quartz (Lovering, 1972), (ii) comb-textured crystals observed in V2 and V3 veinlets and veins, and oriented perpendicular to

magnetite crystal faces, and (iii) fine to very coarse (8 mm), pyramidal crystals that occur along polygonal grain boundaries in V1, V2 and V5 veins.

Carbonate crystals occur in V1 type breccia veins, cement V4 type ore breccias; carbonate is locally present along the relict jaspilite bedding. The anhedral to euhedral carbonate crystals are generally fine grained, but locally coarse grained (>10 mm). Zoned crystals display a dusty hematite pigment. They are classified as manganese-rich dolomite (i. e., kutnahorite), dolomite and calcite (Figueiredo e Silva, 2004). Calcite is only associated with V1 veins that are concordant and discordant to bedding in jaspilite.

Sulfide minerals: Pyrite is present as fine grained (0.1 to 0.2 mm), subhedral and anhedral crystals or grains, and occurs in veins with associated magnetite-calcite or along the jaspilite bands. In places, pyrite overgrows kenomagnetite or is intergrown (less commonly included) in martitized magnetite crystals (Fig. 8D). Chalcopyrite crystals are subhedral to euhedral, mainly in textural equilibrium with carbonate (Fig. 8C) or dispersed in anhedral quartz aggregates in V1 veins. Rare chalcopyrite crystals are included in kenomagnetite and locally in jasper bands. Rare covellite is associated with goethite, fine-grained hematite, chalcopyrite, and is found within quartz-rich martite crystals. Locally, veins of native copper and fine-grained gold are observed in jaspilite and martite aggregate, respectively.

Rare very fine monazite crystals were identified using scanning electron microscopy. They are associated with V1 veins.

Geochemistry

Whole-rock geochemistry

Major, trace and rare-earth element (REE) analyses of 50 samples from the N1, N4E, N4W, N5E, and N5S deposits include protore jaspilite, hydrothermally altered jaspilite and high-grade iron ore (Appendix 2) (Figueiredo e Silva, 2004; Lobato et al., 2007; Figueiredo e Silva et al., in preparation). Analytical procedures, instruments and standards can be found in the Appendix 1. The major-element diagram Fe_2O_3 versus SiO_2 for the N4W and N5E jaspilites exhibits a negative correlation characterized by the progressive decrease in Fe_2O_3 as SiO_2 increases (Fig 10A). The Fe_2O_{3Total} contents vary between 48.7 and 63.2 wt percent (34.2 wt % to 44.2 wt % Fe), and SiO_2 contents between 35 and 50 wt percent. Two hydrothermally altered jaspilite samples from the N4W deposit exhibit elevated Fe_2O_3 content of ~ 80 wt percent (aprox. 60 wt % Fe) similar to the ore samples. The hard ores have a high iron concentration, with N1 samples exhibiting between 68.2 and 69.7 wt percent Fe, and those from N5E between 64 and 67.5 wt percent Fe, with very low SiO_2 contents (Fig. 10A). The Al_2O_3 contents are < 0.3 wt percent in the jaspilites, and < 2 wt

percent in the ores; values from 2.3 to 4 wt percent were obtained for high-grade ore samples at the contact with basaltic wall rocks.

Trace-element compositions in jaspilites and iron ores are normalized to chondrite (Taylor and McLennan, 1985) (Fig. 10B). The elements Ba, U, Nb and Y are enriched in all types of ores when compared to jaspilites (Fig. 10B). The ores display an enrichment of U on the order of 20 to 200 times compared to jaspilite (Fig. 10B). Ores from the N5E deposit have U values up to 1000 times that of chondrite. The Ba concentration reaches ~ 100 X that of chondrite and 10 X that of jaspilites. The Nb varies up to 10 X chondrite, except in N5E jaspilites where there is no Nb enrichment. The Y contents only exceed chondrite values in ores and hydrothermally altered basaltic rock. Jaspilites and ores from the N5E deposit display depletion of Rb, Pb and Zn (Fig. 10B), but V is enriched by ~ 20 X chondrite in ores (Appendix 2).

The REE data are normalized to chondrite (Nakamura, 1974). The sum of the REE_N in least-altered jaspilites varies in the N4W deposit from 5.6 to 23 ppm, in the N5E deposit from 4.5 to 13.8 ppm, and in the N5S deposit from 4.9 to 24.9 ppm. In contrast, for the ores this sum is more variable ranging from 6.5 to 14.8 ppm in the N1 deposit, except in two samples, in which ΣREE_N = 103 and 91 ppm, 8.1 to 44.2 ppm for the N4E deposit, and 14.6 to 97 ppm for the N5E deposit.

The REE patterns of least-altered jaspilite samples from the N4W, N5E and N5S deposits are shown in Figs. 11A, B and C. Samples from the different deposits exhibit similar fractionation patterns with light REE_N ($LREE_N$) enrichment $(La/Sm)_N$ = 9.53 to 13.69, small to moderated positive Eu anomalies (Eu/Eu* = 1.54 to 2.34), and relatively horizontal patterns for the heavy REE_N ($HREE_N$) that commonly exhibit low contents ($\Sigma HREE_N$ <1 ppm). Samples from N5S display a wider range of REE values, mainly HREE (Fig. 11C).

Ores from the N4E deposit display two different populations (Figs. 11E and F), with higher (14.8 to 44.2 ppm) and lower (8.3 and 8.1 ppm) ΣREE_N. The former displays a LREE enrichment and discrete negative Eu anomaly, whereas the latter, a kutnahorite-bearing ore (Fig. 11F), presents a weakly positive Eu anomaly (1.3 and 1.5).

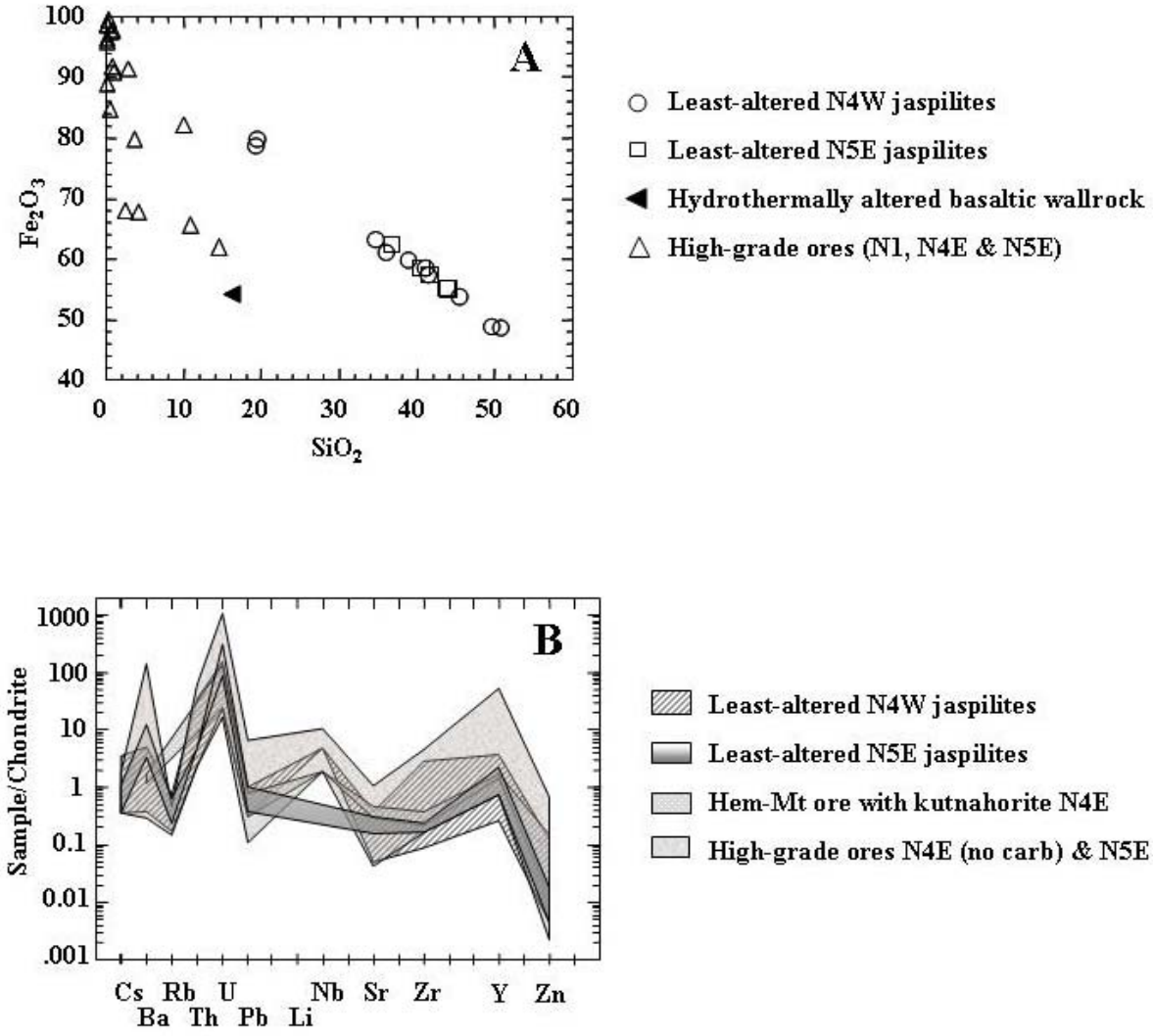

FIG. 10. A. Bivariate plot of Fe_2O_3 and SiO_2 compositions (in wt %) of least-altered jaspilite (here understood as variably altered jaspilite) and high-grade ores from the N4W, N4E and N5E deposits. Note negative correlation between Fe_2O_3 and SiO_2 compositional values. Note that two altered jaspilites from the N4W deposit have higher iron contents (~ 80% Fe_2O_3) than others. B. Trace element distribution in jaspilites and iron ores. Data are presented in Appendix 2 and normalized to chondrite (Taylor and McLennan, 1985).

The characteristic pattern in ores from the N1 deposit, with ΣREE = 11.7 to 14.8 ppm (Fig. 11D), is verry similar to that of the N4W jaspilites (Fig. 11A), except for higher Eu anomalies (2.1 to 2.9) and relative increase in HREE contents. In high-grade, hematite-martite N1 ores, oxides that formed due to the hydrothermal alteration are microplaty hematite-martite ± tabular hematite; however original MiHem is still preserved. The slightly higher total ΣREE contents of the N1 ores, when compared to N4W jaspilites, may be related to their lack of jasper bands, and also to the larger proportion of newly formed MpHem (see Table 2).

Two distinct chondrite-normalized REE patterns characterize ore samples from N5E deposit. The first (Fig. 11G) shows an almost flat pattern and is characterized by veined hematite ore, locally layered with MiHem, AHem, and THem and MpHem veinlets. The second is represented by two brecciated hematite ore samples and yields the highest ΣREE_N contents, respectively 85.54 and 97.52 ppm (Fig. 11H). They are predominantly comprised of the advanced-stage alteration oxides, with subhedral to AHem, and also contain tabular, lamellar and euhedral hematite veinlets. This REE pattern shows the most prominent LREE enrichment in comparison to the HREE, a slightly negative Eu anomaly (Eu/Eu* = 0.62 and 0.79), with the possible addition of iron. Michard (1989) related the increase in the concentration of REE, negative Eu anomaly and LREE enrichment to equilibration with low-pH fluids. The ubiquitous presence of newly formed MpHem in these ores suggests a greater incorporation of REE, favored by the same coordination in the structure and size of the ionic radii of REE (Khan et al., 1996), from 1.032 Å (La) to 0.861 Å (Lu) (Grossi Sad and Dutra, 1987).

In comparison to least-altered jaspilites (Figs. 11A, B and C), the N1, N4E and N5E ores yield REE compositional populations progressively enriched in REE, in that order. In general, there is closer similarity to the HREE than to the LREE chondrite concentrations (Fig. 11D). The $\Sigma LREE_N$ commonly yields higher concentrations, up to 88.2 ppm in N5E ores, and elements with greater standard deviations are represented by Ce, La and Nd, in jaspilites and ores.

Very fine-grained (< 0.01 mm) monazite inclusions in some anhedral hematite crystals from N5E deposit were identified under SEM. Their influence on the especially elevated LREE enrichment cannot be discarded.

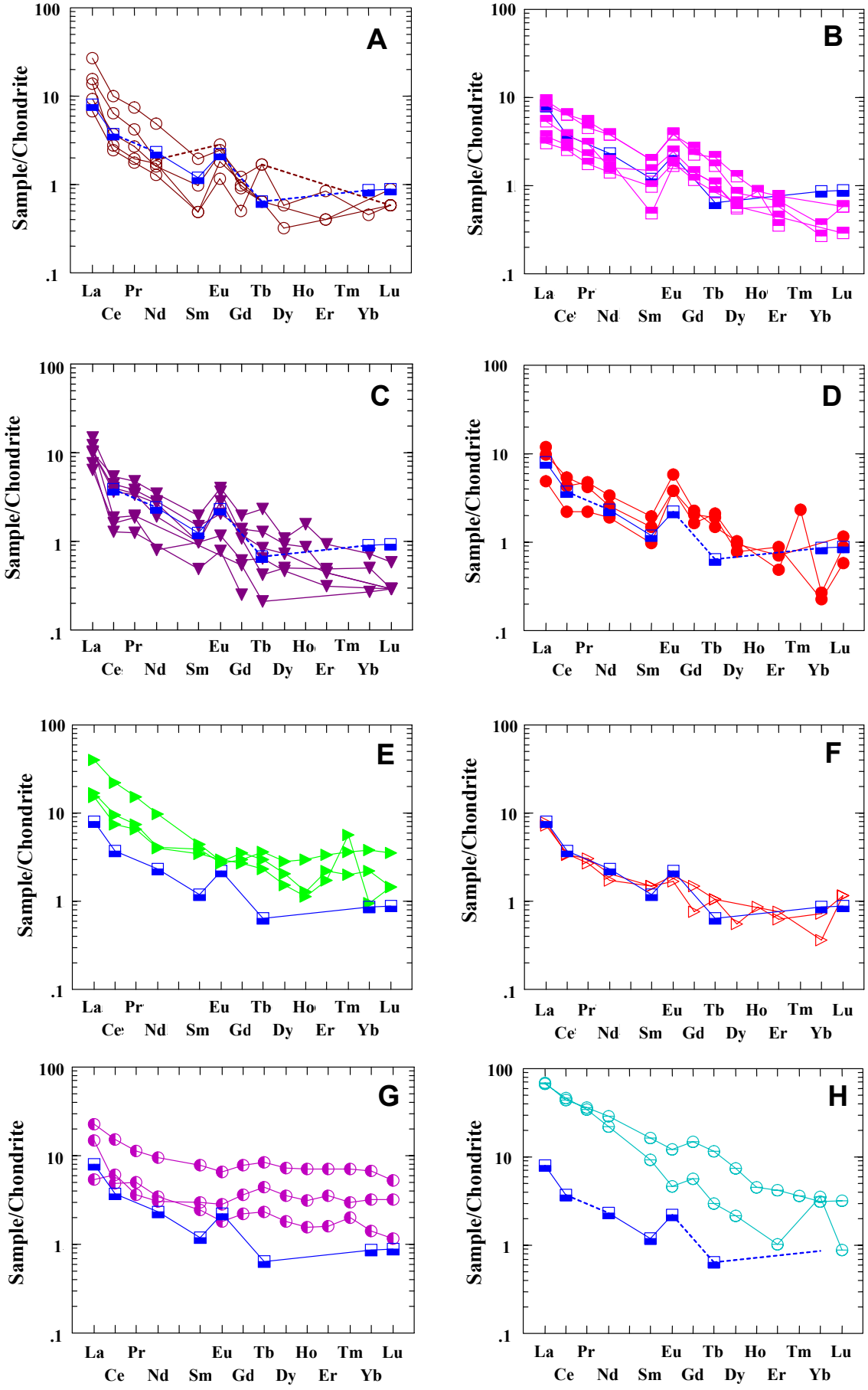
A
B
C
D
E
F
G
H
Sample/Chondrite
100
10
1
.1
La Ce Pr Nd Sm Eu Gd Tb Dy Ho Er Tm Yb Lu

FIG. 11. Chondrite-normalized rare-earth elements plots for the jaspilite and iron ore of the Serra dos Carajás deposit. A. Least- to variably altered jaspilites, N4W deposit (Samples F618P96.6, P113.9 and P 161A are not included). B. Least- to variably altered jaspilites, N5E deposit. C. Least- to variably altered jaspilites, N5S deposit. D. Hematite-martite ores, N1 deposit (Samples F36P25.55 and P 28.60 not included). E. Hematite-martite ores, N4E deposit. F. Carbonate (kutnahorite) and hematite-martite ores, N4E deposit. G. Veined hematite ores (locally banded), N5E deposit. H. Brecciated hematite ores with sub- to anhedral hematite, and euhedral-tabular and lamellar hematite veins, N5E deposit. Line with boxes corresponds to average of Isua quartz-magnetite banded iron formation, West Greenland (Dymek and Klein 1988). Data shown in Appendix 2 and normalized to chondrite (Nakamura 1974).

Fluid inclusions

Fluid inclusions trapped in quartz and carbonate from veins and breccias (Fig. 9) associated with the hydrothermal alteration system, that caused the transformation from jaspilites to high-grade iron ore, were analyzed by microthermometry (Figueiredo e Silva et al., 2007a; b; in prep). Analytical procedures, instruments and standards are shown in the Appendix 1. Fluid inclusions were examined from the: (i) early-mineralization stage V1 veins (Fig. 12A), (ii) syn-mineralization stage, intermediate alteration V2-V3 veins and breccias fillings in altered jaspilites (Fig. 12B), (iii) syn-mineralization stage and advanced alteration stages V4-V5 veins located in high-grade iron ores (Fig. 12 C), and, (iv) quartz and carbonate vein breccias located in the intermediate and proximal alteration zones of basaltic wall rocks (Fig. 12D).

At room temperature, primary and pseudosecondary (P/PS) inclusions are mostly aqueous, liquid rich (10 to 20 vol % vapor), with rare vapor-rich (70 to 80 vol % vapor) inclusions documented only locally. They occur as clusters or internal trails, have oval to irregular shapes and sizes ranging from <5 to 35 microns (rarely up to 75 μm).

Microthermometry results are summarized in Table 3 and Figure 12. Eutectic temperatures (Te) are variable from –63 to –17 ^{o}C (Table 3) suggesting that complex aqueous inclusions were trapped during hydrothermal fluid flow. Due to the lack of equation of states for complex water-salt systems the H_2O-$CaCl_2$ and H_2O-NaCl systems were used for inclusions with Te >21^{o}C and Te <21^{o}C, respectively to calculate equivalent salinities. Most inclusions are liquid rich and homogenize into the liquid phase, therefore the trapped fluid inclusions are not located at the solvus of an aqueous system and a pressure (temperature) correction must be applied in order to estimate the true trapping temperatures (Table 3). In combination, the absence of a pervasive foliation, preservation of igneous and sedimentary features, such as amygdales in basalts and spherulites in jaspilites, mineral equilibrium assemblage of chlorite, calcite, tremolite-actinolite and epidote representative of low-grade metamorphism prior to hydrothermal alteration (Zucchetti 2007) and high-grade iron ore formation, and some typical textures of epizonal conditions (e.g., comb-textured quartz and hematite) all suggest that structural and hydrothermal processes operated at a high crustal level in

the Serra Norte iron deposits during the time of high-grade iron ore formation. Assuming a pressure of approximately 1.3 kbars, which is compatible with the pressure estimate by Zucchetti (2007) based on isochore intersections with temperatures obtained by chlorite geothermometry (on alteration related chlorites), a pressure correction of 95 degrees is applied in the present study, resulting in trapping temperatures-T_{trap} for the majority of aqueous inclusions between 190 to 316^{o}C (Table 3).

Table 3. Summarized microthermometry results from fluid inclusions trapped in quartz and carbonate crystals from V1 to V5 vein types.

Relative Timing		Major chemical system	Microthermometry data (^{o}C)
	P/PS1	H_2O-$CaCl_2$-$FeCl_2$	Te = –63 to –36; Tm_{ice} = –46 to –17; $Th_{TOT(L)}$= 114 to 159; T_{trap} = 209 to 254; 19.9 to 29.3 eq. wt % $CaCl_2$ (n=14)
V1	P/PS2	H_2O-$CaCl_2$-solid*	Te= –60 to –50; Tm_{ice}= –12.7 to –7.1 (n=26) and –23.7 to –15 (n=10); $Th_{TOT(L)}$= 155 to 190;T_{trap}= 250 to 285; 18.4 to 23.6 eq. wt % $CaCl_2$
V2	P1	H_2O-NaCl-$FeCl_2$-$MgCl_2$	Te= –42 to –17; Tm_{ice}= –19 to –9.7; $Th_{TOT(L)}$= 130 to 180; T_{trap}= 225 to 275; 13.6 to 21.2 eq. wt % $CaCl_2$ (n=18)
	P/PS1	H_2O-$CaCl_2$	Te = –57 to –34; Tm_{ice}= –15 to –4.3; $Th_{TOT(L)}$= 95 to 200; T_{trap}= 190 to 295; 6.8 to 18.4 eq. wt % $CaCl_2$ (n=25)
	P1	H_2O-$CaCl_2$-$FeCl_2$-NaCl	Te= –56 to –37; Tm_{ice}= –11.1 to –0.6; $Th_{TOT(L)}$= 150 to 160; T_{trap}= 245 to 255; 1.2 to 15 eq. wt % $CaCl_2$ (n=9)
V3	P/PS1	H_2O-NaCl-$MgCl_2$-(KCl?)	Te= –38 to –17; Tm_{ice}= –10.4 to –5.8; $Th_{TOT(L)}$= 145 to 182; T_{trap}= 240 to 277; 8.9 to 14.4 eq. wt % $CaCl_2$ (n=21)
	P/PS2	H_2O-$MgCl_2$-$FeCl_2$-NaCl	Te= –38 to –17; Tm_{ice}= –16 to –0.6; $Th_{TOT(L)}$= 100 to 155; T_{trap}= 195 to 250; 1.2 to 19.2 eq. wt % $CaCl_2$ (n=16)
V4	P1	H_2O-$CaCl_2$	Qtz: Te= –62 to –49; Tm_{ice}= –22 to –6.4 (n=12) and –2.6 to –0.3 (n=18); $Th_{TOT(L)}$= 145 to 219; T_{trap}= 237 to 314; 9.7 to 22.3 and 0.7 to 4.4 eq. wt % $CaCl_2$ Carb: Te= –49; Tm_{ice} = –49 to –16; $Th_{TOT(L)}$= 142 to 190; T_{trap}= 237 to 285; 19.2 to 30.1 eq. wt % $CaCl_2$ (n=27)
V5	P1	H_2O-$CaCl_2$-$FeCl_2$	Te= –60 to –36; Tm_{ice}= –24 to –6; $Th_{TOT(L)}$= 142 to 200; T_{trap}= 237 to 295; 19.5 to 24.5 eq. wt % $CaCl_2$ (n=22)
	P/PS1	H_2O-NaCl-KCl-$MgCl_2$-$FeCl_2$	Te= –46 to –17; Tm_{ice}= –4.6 to –0; $Th_{TOT(L)}$=150 to 221; T_{trap}= 245 to 316; 0.2 to 7.3 eq. wt % NaCl (n=70)

Abbreviations: P– primary; P/PS– primary/pseudosecondary; Te– eutectic point temperatures; Tm_{ice}–final ice melting temperature; $Th_{TOT(L)}$– homogenization temperature into liquid; T_{trap}– trapping temperature. The cations differentiation is based on eutectic temperatures from microthermometry studies supported by laser ablation ICP-MS analyses on individual inclusions. Temperatures in ^{o}C.

Figure 12 displays total homogenization temperatures versus salinities for primary and pseudosecondary fluid inclusions trapped in different vein types. The following observations can be made: (i) homogenization temperatures of fluid inclusions for all vein types are mostly between 100 and 220^{o}C, except for veins in basalts (130 to 325^{o}C; Fig. 12D); (ii) salinities vary significantly from about <1 to 30 eq. wt % NaCl and $CaCl_2$, with fluid inclusions in all veins displaying a continous range from low to high salinities; (iii) fluid inclusions in veins from hydrothermally altered basalt display a large range in both homogenization temperatures (130 to 325^{o}C) and salinities <1 to 29 eq. wt % NaCl and $CaCl_2$); (iv) fluid inclusions trapped in carbonate from V4-V5 veins contain only high-salinity (19-30 eq. wt % $CaCl_2$) inclusions that homogenize between 140 and 190^{o}C. The large range in salinities, but restricted range in homogenization temperatures, in combination with apparent lack of pervasive fluid boiling, may be explained by mixing of magmatic fluids or basinal brines, expressed by the high-salinity inclusions, and heated meteoric water, expressed by the low-salinity fluid inclusions. In such a scenario, the fluid inclusions that display medium salinities maybe the result of mixing of the two fluid sources.

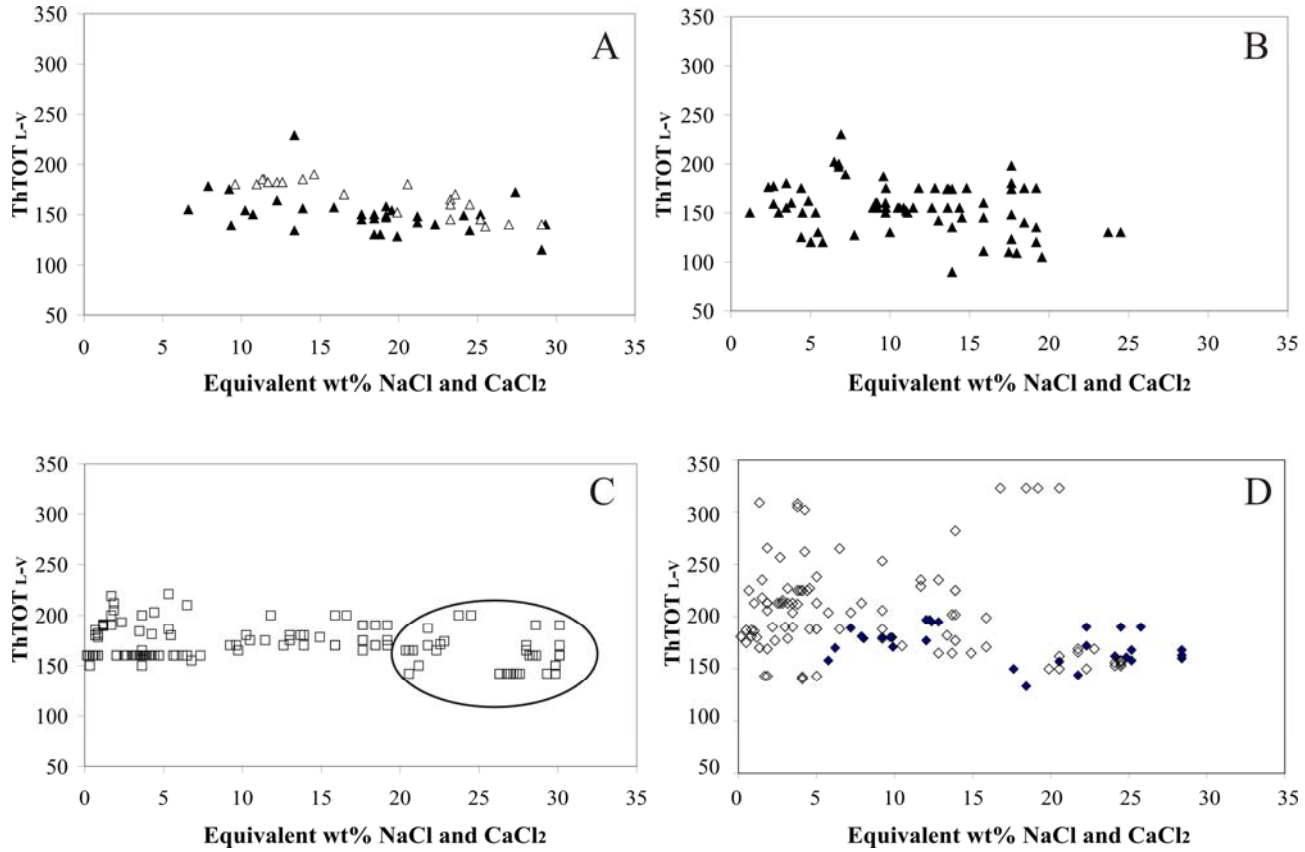

FIG. 12. Salinity versus homogenization temperature (Thtot) based on microthermometry analyses obtained from fluid inclusions trapped in quartz and carbonate from: A. Quartz (filled triangles) and carbonate (empty triangles) from V1 vein-breccia type located in altered jaspilite (distal alteration zone); B. V2 and V3 vein types located in altered jaspilites (intermediate alteration zone); C. V4 and V5 vein-breccias located in ores (proximal alteration zone). Circle – carbonate. D. Quartz and carbonate vein-breccias from intermediate (filled diamonds) to proximal (empty diamonds) alteration zones in hydrothermally altered basaltic wall rock. Data from basaltic wallrocks in Zucchetti (2007).

Stable and radiogenic isotopes

Stable and radiogenic isotopic data, information on analytical techniques, standards, precision and accuracy of analyses are listed in Appendix 1and data displayed in Appendix 3 (see also Figueiredo e Silva et al., 2007b; in prep.).

Oxygen isotope data: Oxygen isotope compositions were analyzed from: (i) all types of iron oxides (microcrystalline to tabular hematite and magnetite), (ii) quartz from V1, V2 and V3 vein-breccia fills, and, (iii) whole-rock least-altered jaspilite (jasper - magnetite±martite±microplaty hematite) samples.

The $\delta^{18}O$ values range from +15.2 per mil for the least-altered jaspilites (whole rock analyses) to –9.5 per mil for the paragenetically latest euhedral-tabular hematite in the high-grade iron ore (mineral analyses; Fig. 6). Note that magnetite, which is the first hydrothermal oxide to develop

after MiHem in least-altered jaspilite (Fig. 6C), has intermediate $\delta^{18}O$ values (0 to +4‰) between jaspilites and the different types of hematites (Fig. 13A). For quartz in V1 veins from the distal alteration zone and V2 and V3 veins from the intermediate alteration zone the $\delta^{18}O$ varies from +10.1 to +13.1 per mil, and +13.7 to +18.8 per mil (Fig. 13A), respectively.

Interpretation of oxygen isotope data: The $\delta^{18}O_{fluid}$ values were calculated based on fluid inclusion homogenization temperatures and the equations of state of Yapp (1990) for hematite, and Zheng (1991, 1995) for magnetite. As shown in Figure 13A, the $\delta^{18}O_{fluid}$ values for the different hematite types almost overlap with the measured data, whereas the average $\delta^{18}O_{fluid}$ value for magnetite increases by about 6 per mil when compared to the average measured values. The decrease of $\delta^{18}O$ values from the earliest to the latest hematite types may reflect influx of light, evolved meteoric water during the advanced hydrothermal alteration stage and iron mineralization. Alternatively, the shift in $\delta^{18}O$ could also be a result of intense fluid fluxes (i.e., high fluid/rock ratios; Figueiredo e Silva et al., 2007b). The $\delta^{18}O_{fluid}$ values of V1, V2 and V3 quartz vein types were calculated according to Matsuhisa et al. (1979) equation, using trapping temperature values from 245 to 265^{o}C and they overlap values typically of magmatic fluids (Taylor, 1997). The magmatic nature of at least some of these fluids is corroborated by the occurrence of high-salinity fluid inclusions in all vein types.

Sulfur isotope data: In situ laser ablation sulfur isotope analyses were obtained from: (i) pyrite associated with early stage hydrothermally altered jaspilite in discordant V1 veins (Figs. 8C and D), and (ii) pyrite and chalcopyrite located in veins in the intermediate alteration zone of hydrothermally altered basalts (Figueiredo e Silva et al., in preparation; Zucchetti et. al., in preparation).

The results (Fig. 13B) show two different populations of $\delta^{34}S$ values: (i) high $\delta^{34}S$ values from 7.4 to 10.8 per mil for pyrites in V1 veins from the early-stage alteration (with the exception of two data points that display $\delta^{34}S$ values of 2.5 and 3.0 per mil), and (ii) low $\delta^{34}S$ values from –5 to +5 per mil for pyrite and chalcopyrite from the intermediate alteration zone of hydrothermally altered basalts (Fig. 13B). The majority of the data points of the latter population are placed between –2.5 to +2.5 per mil but several data points display a shift of up to 2.5 per mil towards high $\delta^{34}S$ values (Fig. 13B).

Interpretation of sulfur isotope data: The source of sulfur for sulfides of the early stage alteration (V1 veins) in jaspilites is presently unknown. The $\delta^{34}S$ values for sulfides in hydrothermally altered basalt (Fig. 13B) that range between –2.5 and +2.5 per mil are compatible with juvenile magmatic sulfur (i.e., Hoefs, 2007). The slightly (up to 2.5 per mil) higher $\delta^{34}S$ values may be the result of exchange (mixing) reactions between the magmatic sulfur and an additional external sulfur source. Potentially heavy seawater sulfur, compatible with the high $\delta^{34}S$ values for pyrites from the early-

stage alteration in jaspilites (Fig. 14B), could have exchanged with the lighter magmatic sulfur resulting in the shift to higher $\delta^{34}S$ for some of the sulfides in the altered basalts (Fig.13B). However, relative and absolute timing relationships, as well as oxygen (Fig. 13A) and strontium isotope (Fig. 13D) values argue against seawater contribution during the geological and hydrothermal evolution of the iron orebodies at Carajás. In contrast, there is significant geochemical evidence for meteoric water infiltration into the iron orebodies in the advanced stages of hydrothermal alteration and mineralization process (e.g., Fig. 13A; Lobato et al., 2005b; Figueiredo e Silva et al., 2007a; b), which may have caused exchange reactions that resulted in the shift to slightly lower $\delta^{34}S$ values for some of the sulfides when compared to the typical magmatic sulfur isotope compositions of the majority of the sulfides in hydrothermally altered basalts (Fig. 13B).

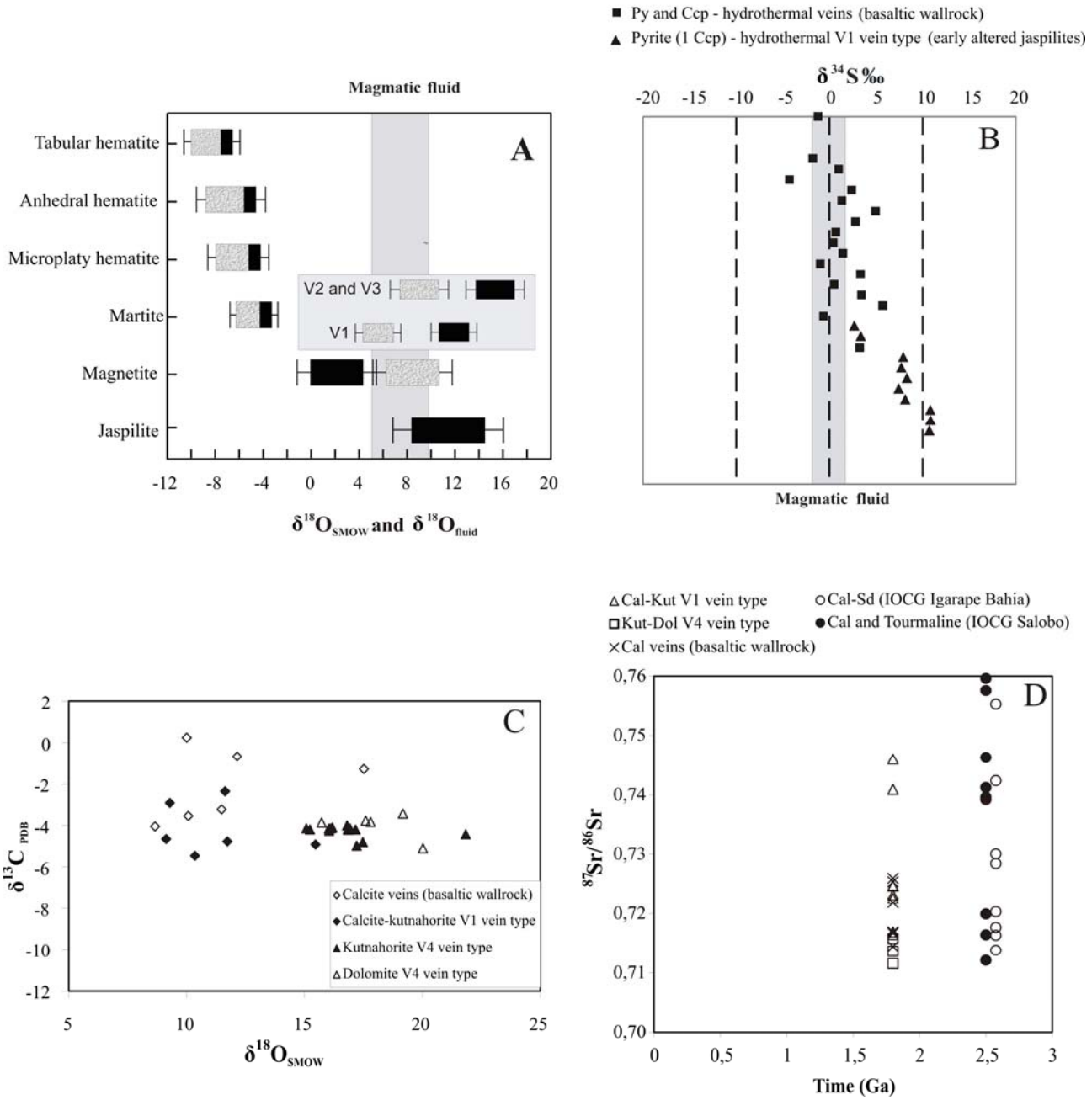

FIG. 13. Cross plots of stable and radiogenic isotope compositions. A. Oxygen isotope values of least-altered jaspilite, magnetite, different hematite types and quartz veins. Light gray boxes correspond to calculated fluid values according to the following equations: Yapp (1990) for hematite; Zheng (1991) for magnetite; Matsuhisa et al. (1979) for quartz. Magmatic reservoir box is shown in gray, according to Taylor (1997). B. Sulphur isotopes. Basaltic wallrock data from Zucchetti (2007). Magmatic box, shown in gray, is after values from Hoefs (2007). C. Carbon and oxygen isotopes composition of carbonates in veins. D. Strontium isotopes on carbonate samples from Carajás iron ore deposits (at age 1.8 Ga, see text); calcite-siderite veins from Igarapé Bahia deposit (Tallarico et al., 2005) and calcite-tourmaline from Salobo (Tassinari et al., 2003). Mineral abbreviations: Cal = calcite, Ccp = chalcopyrite, Dol = dolomite, Kut = kutnahorite, Py = pyrite, and Sd = siderite.

Carbon and oxygen isotope data on carbonate: Carbon and oxygen isotope analyses of carbonates were obtained from: (i) calcite of early-stage alteration V1 discordant veins in jaspilite, (ii) kutnahorite and dolomite of proximal alteration zone in V4 breccias in high-grade ore, and (iii) calcite of veins from the intermediate and proximal alteration zones in the basaltic wallrocks.

Two main groups are noticed (Fig. 13C): (i) V1 veins in jaspilite and calcite veins in hydrothermally altered basalt have the lowest $\delta^{18}O$ values with the latter one also the highest $\delta^{13}C$ values (Fig. 13C), and (ii) V4 veins exhibit the highest $\delta^{18}O$ values and a relatively well-constrained range of $\delta^{13}C$ values.

Interpretation of carbon and oxygen isotope data on carbonates: Calcite from the early-estage V1 vein type presents a relatively wide range of $\delta^{13}C$ values which may reflect isotopic disequilibrium. The restricted range of $\delta^{13}C$ values (Fig. 13C) for carbonates in hydrothermal proximal- alteration V4 veins suggest that all carbon was derived from the same carbon source, potentially magmatic (Faure, 1977; Rollinson, 1993; Faure and Mensing, 2005; Hoefs, 2007), as previously suggested by Lobato et al. (2005b). The wide range of $\delta^{18}O$ values in both V1 and V4 veins (Fig. 13C) suggests variable oxygen sources possibly due to interaction with more than one type of fluid or significant changes in fluid-rock ratios during interaction with a fluid that contained ^{18}O. The heavier $\delta^{18}O$ values in carbonate veins from ores, compared to veins in jaspilites, could be explained by interaction with a mantle-derived fluid (Faure and Mensing, 2005).

Analyses in carbonates from some IOCG deposits in the Carajás Mineral Province (e.g., the Igarapé Bahia and Gameleira deposits; Grainger et al., 2007 and Lindenmayer et al., 2005, respectively) also show a restricted range of $\delta^{13}C$ and larger range of $\delta^{18}O$ values when compared with carbon isotopes from the Serra Norte iron ore deposits (Fig. 13C). These authors suggest a magmatic fluid source for the carbonates from these deposits.

Strontium isotopes: Strontium isotope analyses from fifteen samples of hydrothermal carbonate minerals (e. g., calcite, kutnahorite and dolomite) were obtained from early-alteration V1 veins in jaspilites and proximal-alteration V4 veins and breccias in iron ores, and veins in the intermediate alteration zones in the altered basaltic wall rocks.

Figure 13D depicts the initial $^{87}Sr/^{86}Sr$ ratios at 1.8 Ga (preliminary age, João Orestes S. Santos, verbal communication), considered as the time of iron mineralization. The $^{87}Sr/^{86}Sr$ ratios of most carbonates range between 0.712 and 0.725 with two extremely radiogenic values of 0.74 and 0.75 (Fig. 13D) for early alteration V1 carbonates.

All $^{87}Sr/^{86}Sr$ values are extremely radiogenic and are probably only compatible with a granitic source (Faure and Powell, 1972). The highest values are those of carbonate from the early alteration (distal) zone, suggesting a possible different strontium source. In the Carajás district, similar extremely radiogenic $^{87}Sr/^{86}Sr$ isotope ratios were determined for hydrothermal calcite and

tourmaline crystals from Salobo (Tassinari et al., 2003) and calcite and siderite from Igarapé Bahia 2.5 Ga old IOCG deposit (Tallarico et al., 2005) (Fig. 13D). These authors suggest multiple crustal sources, consistent with an epigenetic magmatic-hydrothermal fluid as the main cause for the radiogenic isotope signature of the hydrothermal carbonates and tourmalines.

Discussion

Review of the genetic models proposed for the Carajás iron ore formation

A number of workers have proposed a hypogene genesis for the iron ore deposits at Carajás, which preceded supergene residual enrichment via leaching of silica (Tolbert et al., 1971; Rezende and Barbosa, 1972; Beisegel et al., 1973; Ladeira and Cordeiro, 1988; Macambira and Lopes, 1996a; Dardenne and Schobbenhaus, 2001; Lindenmayer et al., 2001; Beukes et al., 2002; Klein and Ladeira, 2002; Guedes et al., 2002; Dalstra and Guedes, 2004; Clout and Simonson, 2005). However, no systematic work, either in the public or private domains, existed regarding the hypogene ore, with the exception of a few generalized descriptions (e.g., Dalstra and Guedes, 2004). In addition, there was only restricted information available about the jaspilites at Carajás (e.g., Lindenmayer et al., 2001; Macambira, 2003).

At Carajás a volcanic origin for the so-called "primary iron ore", which contains magnetite, titano-magnetite and ilmenite, was first suggested by Suszczynski (1972), who also mentioned a close association between the hard ore and volcanic rocks. He further suggested that magnetite developed during a magmatic stage, whereas hematite was considered to be post-magmatic. Rezende and Barbosa (1972) and Beisiegel et al. (1973) also proposed a hypogene, metasomatic origin for the massive ore lenses within friable orebodies. Lenses of massive orebodies are associated with intrusive basic dikes, and are located along the hangingwall contact with these dikes, which also crosscut the soft orebodies. Based on these ideas, Melo et al. (1981) suggested that the dikes generated heat for the metasomatic process. The authors also indicated that in the Serra Leste deposits the distribution of the principal lenses of massive hematite ore is structurally controlled.

According to Tolbert et al. (1971), ore formation resulted from leaching of silica from the "iron formations" via weathering due to water percolation that generated residual enrichment of iron oxides and formation of the present orebodies.

Teixeira et al. (1997) first mentioned the occurrence of scarce dolomite lenses at the base of the "BIF". According to the authors, these lenses are relics of former limestone beds that underwent calcite leaching during hydrothermal alteration. These authors indicated that removal of these limestone might have enhanced the "BIF" permeability via fracturing and crack propagation. This would have been followed by silica leaching resulting in iron enrichment of the "BIF". Macambira

et al. (1999) pointed out that these carbonate lenses (~ 50 meters wide) represent a "carbonate-bearing jaspilite facies" and suggested that carbonate had been leached from those rocks in order to form hard ores.

Due to the local presence of finely laminated dolomite in the N4E deposit, Guedes et al. (2002) and Dalstra and Guedes (2004) defined carbonate-rich protores (45 wt % Fe), which they referred to as "dolomitic iron formation". According to these authors, chert was replaced by dolomite along the layering, accompanied by magnetite development. Dalstra and Guedes (2004) also pointed out that a second dolomitization stage was responsible for carbonate precipitation in veins and vugs, with the local development of breccias. The intense tropical weathering would have leached the carbonates from "dolomitic iron formation" resulting in the development of friable, soft ore.

Nevertheless, recent detailed documentation of the hydrothermal alteration stages (Figueiredo e Silva, 2004; Lobato et al., 2005a; Zucchetti, 2007) that are spatially and temporally associated with the formation of hard ore have shown that the majority of the carbonate (i.e., dolomite, kutnahorite and calcite) is in the form of discordant and concordant veins and breccias commonly in association with sulfides (e.g., chalcopyrite and pyrite), with or without subordinate magnetite and hematite. Carbonate alteration is only ubiquitous in the N4E and N5E deposits, and is lacking or less common in most other deposits. Moreover, replacement textures of chert or quartz by carbonate are only locally observed. As such, carbonate cannot be considered to be paramount to iron ore formation in the Serra Norte deposits.

From jaspilite to ore: the REE fingerprint

The crystals of magnetite in hydrothermally altered jaspilites are locally surrounded by recrystallized and "clean" jasper, and in equilibrium with fine (~ 0.01mm) vein quartz. In accordance with Taylor et al. (2001), the leaching of quartz in BIFs is principally a function of temperature, between 150 to 250º C (discussion in Hagemann et al., 2008). This may have been the case in the deposits studied here (Lobato et al., 2004; Rios et al., 2004; Figueiredo e Silva et al., in preparation). The leaching of quartz was accompanied by an increase in martitization of magnetite (Fig. 6D). Quartz and carbonate, therefore, precipitated prior to or synchronous to the formation of magnetite in the jaspilites (Fig. 8A). The leaching of quartz may have been responsible for the general increase in total REE contents, as only magnetite and MiHem remain (Fig. 6C). With the growth of magnetite and MpHem, and the progressive martitization to form AHem, the total REE concentration increased significantly (Figs. 11G and H). This is corroborated by the distribution coefficients K_D of magnetite, which favor the fixation of LREE (Schock, 1979; Li, 2000). This process may also have favored the relative increase in HREE in the residual hydrothermal fluid, explaining the increase in HREE and the flat REE patterns (Fig. 11) for some ore samples in

comparison to least-altered jaspilites. The change in the REE patterns of the ores in relation to jaspilites, encompassing a general REE enrichment with almost flat HREE patterns for some ore samples (Fig. 11G), indicates that the fluids responsible for the early-hydrothermal stage were significantly different or evolved to those of the advanced hydrothermal stage. Indeed, it is during the advanced hydrothermal stages that the EHem and THem generations dominate (Figs. 6F and G).

Hydrothermally altered jaspilites from the N4E, N5E and N5S deposits (Figs. 11A, B and C), ores from N1 and a specific group of samples from the N4E deposit (Figs. 11D to H) display positive Eu anomalies. Locally, N4E and N5E ores have a weakly negative Eu anomaly (Figs. 11E, G and H). According to Grossi and Dutra (1987), no mineral retains Eu^{2+} under accentuated oxidizing conditions, since the element would be unavailable at that oxidation state. However, under reducing conditions, Eu is isolated, potentially being incorporated in the Eu^{2+} state. The initial hydrothermal fluid that interacted with the Serra Norte rocks was relatively reducing (i.e., fO_2 in equilibrium with magnetite), probably causing Eu reduction, which may be corroborated by the formation of magnetite after original hematite. The Eu^{2+} was possibly fixed in the structure of minerals, such as dolomites. For example, in the case of the N4E ores, samples with carbonate do in fact display a positive anomaly (Fig. 11F). With the evolution of the hydrothermal fluids, fluids became relatively more oxidizing, with the remaining Eu^{2+} not incorporated in the rocks, resulting in REE patterns with a weakly negative Eu anomaly, for example in the high-grade ores (Figs. 11G and H).

Ore samples from selected Hamersley deposits show similar features, with less pronounced enrichment in LREE (Lobato et al., 2007). The overall higher REE contents of the Carajás samples compared to the Hamersley ore samples suggest that different fluid sources may have been involved in the origin of the deposits. For Carajás, a magmatic fluid source has been postulated (Lobato et al., 2005b; Figueiredo e Silva et al., 2007a), whereas, for example, Hagemann et al. (1999) and Thorne et al. (2004) suggest that basinal brines were involved in the origin of the Mt. Tom Price deposit.

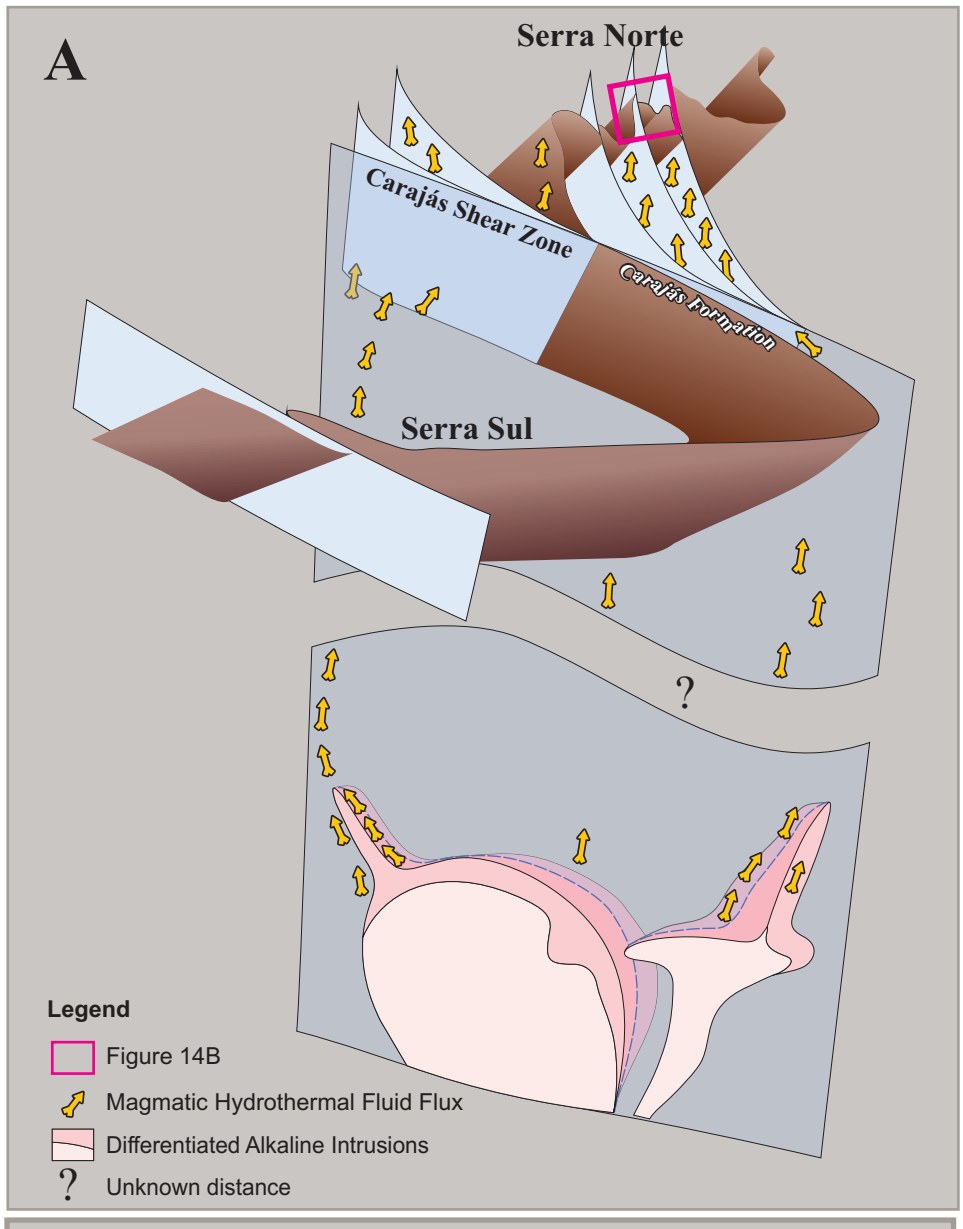
A
Serra Norte
Carajás Shear Zone
Carajás Formation
Serra Sul
?
Legend
Figure 14B
Magmatic Hydrothermal Fluid Flux
Differentiated Alkaline Intrusions
Unknown distance

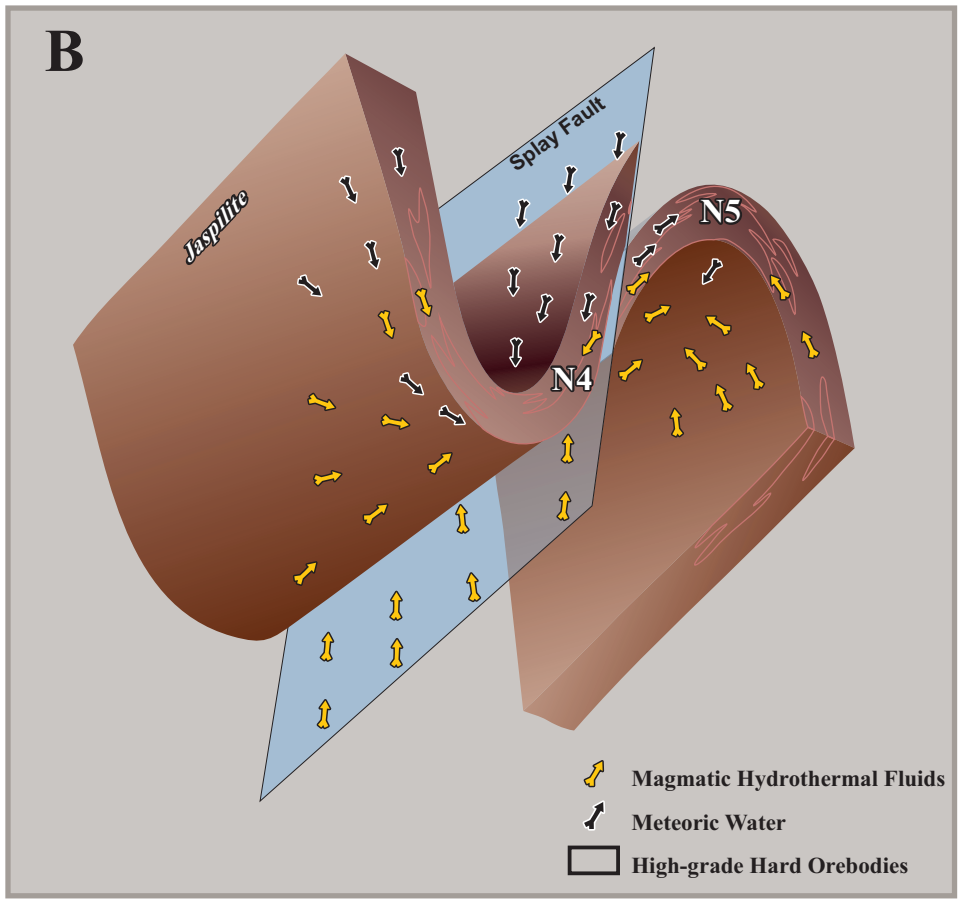
B
Splay Fault
Jaspilite
N5
N4
Magmatic Hydrothermal Fluids
Meteoric Water
High-grade Hard Orebodies

FIG. 14. Diagrammatic scheme for the regional and Serra Norte scale geological structural evolution. A. The figure displays the Archean structural framework, including the Carajás shear zone, which prepared the Grão Pará Group supracrustal rocks to receive massive fluid flow during the Paleoproterozoic. Note that the Carajás Formation (including jaspilites and ores) together with mafic rocks are clearly set within the Carajás S-fold, plunging steeply to the NW and WNW (Rosière et al., 2006). During hydrothermal iron mineralization in the Paleoproterozoic, steep dipping faults and splay faults of the Carajás shear zone served as channels for mineralizing early-stage fluids of magmatic origin. B. Inset of figure 15A showing the distribution of the Serra Norte N4 and N5 deposits. The figure reflects hydrothermal fluid interaction at the intermediate and advanced stages of mineralization, with participation of meteoric water. The splay faults of the Carajás shear zone resulted due to the disharmonic nature of the folds, which are best displayed at Serra Norte, and to the requirement of brittle-ductile conditions for spatial compensation. It is likely that other, similar, coeval structural systems exist along the Cinzento shear zone to the north (Fig. 1). Therefore a hypothetical major shear zone is inferred on figure 15A within or to the south of Serra Sul.

Constraints on the evolution of the Serra Norte iron ore deposits

During the last five years, our research group has advanced significantly in the knowledge of the hydrothermal alteration processes related to the formation of iron ore at Carajás, as summarized by Lobato et al. (2005b). To these authors, the iron mineralization took place in the Paleoproterozoic over exhumed rocks from the Archean metavolcano-sedimentary sequence. Large shear zones formed in the Archean were likely reactivated during Proterozoic times, thereby locally increasing permeability of the rocks and facilitating hydrothermal fluid flow that caused the upgrade of jaspilite to high-grade ore, with the development of different high-grade orebodies (Fig. 14A). Considering the nature of the regional structures (Rosière et al., 2006) and the textural characteristics, it is clear that the hydrothermal fluid must have interacted with the jaspilites and basalts along fluid flow channels under brittle-ductile and epizonal crustal conditions, in association with a relatively shallow igneous hydrothermal system. Lobato et al. (2005b) also inferred that the Carajás iron ore deposits may represent low temperature end-members of a hydrothermal system responsible for the iron oxide-copper-gold deposits (IOCG) for example in the Carajás Mineral Province (discussion in Lobato et al., 2008), envolving igneous as well as meteoric fluids.

During the Late Paleoproterozoic, at the time of mineralization, the deep-seated, mid- to upper-crustal shear zones, such as the Carajás shear zone, and their associated splay-fault arrays, were loci for intrusions and plumbing systems for the mineralizing hydrothermal magmatic fluids derived from strongly differentiated, probable alkaline igneous intrusions. Some of these are outcropping in the Carajás Mineral Province, and are directly associated with Cu-Au (W, Bi, Sn) (according to Grainger et al., 2008) ore systems

Iron-rich fluids were likely channeled preferentially into intensely folded, cleaved and dismembered fold closures and along the jaspilite-basalt contact, closely intercepted by splay faults (Rosière et al., 2006; Fig. 14B). These faults, commonly at high angles to the regional shear zones,

experienced multi-stage hydrothermal processes caused by the complex interaction of magmatic and meteoric hydrothermal fluid systems (Fig. 14B) outlined below.

Early-stage hydrothermal alteration and fluid flow: The early stage of hydrothermal fluid infiltration into the jaspilites is characterized by V1 vein-breccia, which contains medium to high-salinity Ca-rich and high salinity Ca-Fe-rich fluid inclusions in quatz and cabonate with trapping temperatures of 209 to 285^{o}C. Magnetite represents an early mineralization (alteration) stage dominated by relatively reduced fluids that caused the formation of magnetite from microcrystalline-MiHem. Magnetite is subsequently oxidized to form martite leaving kenomagnetite (Fig. 6D) relics. Fluid interaction caused silica leaching (and iron removal) from jasper bands accompanied by precipitation of vein quartz, which is first observed in the earliest hydrothermal stage (Fig. 6A). The high-salinity fluid inclusions, in conjunction with carbon, oxygen and strontium isotope ratios in carbonate minerals, and oxygen isotope ratios in magnetite, are compatible with a magmatic fluid source for the early-stage alteration (Fig. 13).

Intermediate stage hydrothermal alteration and fluid flow: The intermediate alteration stage, represented by V2 and V3 veins, is characterized by high-salinity Na-Fe-Mg-rich fluid inclusions (up to 21 eq. wt % $CaCl_2$) with trapping temperatures of 225 to 275^{o}C, and low- to medium-salinity Ca-Fe-rich fluid inclusions with trapping temperatures of 245 to 255^{o}C. The microplaty hematite-MpHem is commonly associated with martite borders (Fig. 7F) or in the martite nucleus representing the reaction of the remaining Fe^{+2} with the oxidizing fluid in the intermediate stage. The MpHem also precipitates in V2 and V3 veins and open spaces. Locally, platy hematite crystals contain magnetite relics or inclusions indicating that a relatively oxidizing fluid had interacted with the jaspilite sequence during the intermediate alteration stage. Considering the lower salinity values and the relatively oxidizing fluid nature of the intermediate hydrothermal alteration stage, fluid mixing with meteoric water is suggested (Fig. 14B).

Advanced stage hydrothermal alteration and fluid flow: In the advanced alteration stage, the progressive martitization generates aggregates of anhedral hematite-AHem crystals with lobate contacts (Fig. 6F). These aggregates may occur as eye-shaped portions in banded or brecciated ores. The latest stage tabular hematite-THem (Fig. 6G) precipitates mainly along discordant veins where quartz is absent. Brecciated V4 carbonate veins display Ca-rich, high-salinity fluid inclusions, trapped at about 237 to 285^{o}C, and brecciated V5 quartz veins display low-salinity Na-K-Mg fluid inclusions trapped at 245 to 316^{o}C.

The advanced stage hydrothermal alteration displays evidence for influx of both magmatic and meteoric fluids. The latter is indicated by predominance of oxidized phases (e.g., AnHem and THem), low-salinity Na-rich fluid inclusions, and also decreasing oxygen isotopic values towards

late hematite types (Fig. 13A). Infrared microthermometric investigations on fluid inclusions from these platy hematite grains display low-salinity inclusions (< 4 eq. wt % NaCl) with trapping temperatures of 255 to 295 ^{o}C (Rios et al., 2004; Lobato et al., 2005b).

As depicted in Figure 13A, each oxide type displays a unique range in $\delta^{18}O$ values, from higher (e.g., MiHem and altered jaspilite) to lower (e.g., EHem and THem) values, suggesting a depletion in ^{18}O content of the fluid with time. These variations in $\delta^{18}O$ values in the different hematite types would be expected if the hematites were formed from two different oxygen reservoirs (magmatic and meteoric fluids) with different isotopic signatures. However, magnetite crystals display a narrow range in $\delta^{18}O$ values (from 0 to 4‰) suggesting that they formed under the influence of a similar fluid source, which is interpreted to have been magmatic. These values are similar to magnetites from e.g., El Laco in Chile (Taylor, 1968; Chiba et al., 1989; Rhodes et al., 1999) that display $\delta^{18}O$ values between 3.5 and 5. 2 per mil and are also interpreted as magmatic in nature.

Since $\delta^{18}O$ values are low in hematite relative to magnetite (Zheng, 1991), lower $^{18}O/^{16}O$ ratios would be expected where euhedral-tabular hematites are typically precipitated. These zones may also represent the zones with the highest fluid/rock ratios. It is therefore reasonable to conclude that the decreasing isotopic values (Fig. 13A) also reflect variations in fluid/rock ratios during iron ore mineralization, under relatively shallow crustal conditions.

Conclusions

The giant Serra Norte Carajás iron ore deposits are hosted by the Neo-Achean metavolcano-sedimentary sequence of the Grão Pará Group, Itacaiúnas Supergroup, where the jaspilitic protore and high-grade iron ores (> 64 wt % Fe) are under- and overlain by low metamorphic grade basaltic rocks. The iron ore forming age is considered to be Paleoproterozoic age (Lobato et al., 2005b, 2008) and is well correlated with the A-type granites of the Carajás region (e.g., Serra dos Carajás Granite). Detailed mineralogical, geochemical and fluid chemistry investigations on the Serra Norte Carajás iron ore deposits revealed the following:

1. Considering the hydrothermal origin of iron ore forming event at the studied Serra Norte iron ore deposits (Guedes et al., 2002; Figueiredo e Silva, 2004; Lobato et al., 2005b), the sequential order of oxides that follows the original microcrystalline hematite-MiHem is interpreted as: magnetite → martite with or without associated kenomagnetite → microplaty hematite (MpHem) → anhedral hematite (AHem) → euhedral (EHem) and/or tabular hematite (THem). Other mineralogical modifications are: (i) recrystallization and cleansing of jasper with the formation of chert and fine quartz; (ii) progressive leaching of chert and quartz, leaving oxides and a significant volume of empty spaces as vugs; (iii) silicification and dolomitization with

associated sulfides and oxides in veins, breccias and along jaspilite bands; (iv) advanced martitization with the formation of AHem, partial MiHem recrystallization to AHem and partially filling spaces with microplaty/platy hematite; (v) continued space filling by comb-textured EHem and THem in veinlets and along bands.

2. The iron mineralization involved hydrothermal fluids probably under epizonal conditions. Comb textures defined by quartz, hematite and talc, as well as preserved primary amygdales in basaltic rocks (Zucchetti, 2007) and spherulites in jaspilites, are typical of deposits formed under epizonal conditions and preserved at shallow, low-temperature crustal conditions.

3. Two different populations of REE patterns are notable: (i) those characteristic of the jaspilites, ore samples from the N1 deposit and a group from the N4E deposit, which indicate a distinct LREE enrichment and positive Eu anomalies, similar to patterns displayed by Archean BIFs worldwide; and (ii) those of N5E ores that are almost flat, with relative enrichment in both LREE and HREE. Another group of N5E brecciated hematite ores display high total REE contents, principally LREE, which may reflect the fixation of these elements in hematite.

4. The REE enrichment in ores and the changes in the shapes of the REE patterns indicate a hydrothermal fluid evolution, where silica leaching may have resulted in a relative general REE increase during the early hydrothermal stage. The LREE increase was more accentuated during the formation of magnetite and MpHem, and the advance of martitization to AHem. This may have favored the relative increase of HREE in the residual fluid, resulting in an increase in HREE in advanced mineralization stage precipitates and almost flat REE patterns. It is during the advanced hydrothermal stages that the generation of euhedral and tabular hematite was dominant. The increase in REE concentrations in N4E and N5E ore samples further suggests the presence of significant amounts of Fe in the mineralizing fluid.

5. Vein types V1 to V5 contain iron mineralization related complex aqueous fluids, which were mostly trapped between 190 and 325^{o}C. These fluids display low to high salinities and are characterized by various cations such as Ca, Mg, Fe, Na and K. Stable (C-O-S) and radiogenic (Sr) isotope ratios of carbonates, quartz and sulfides in equilibrium with various oxide stages and the ore mineral hematite suggest that iron ore resulted from interaction of early magmatic hydrothermal fluids which in the advanced hydrothermal stage interacted with downwards penetrating meteoric water, thereby forming euhedral and tabular hematite with characteristic light $\delta^{18}O$ values.

6. The mineralogical, geochemical and isotopic changes of jaspilites and ores attest to a hydrothermal origin for the formation of the hypogene high-grade iron ores, via interaction with: (i) an early-stage, high-salinity, relatively reducing magmatic fluid, which leached silica, formed magnetite and precipitated quartz, carbonate and sulfides; (ii) an intermediate stage fluid

that evolved to more oxidizing conditions, with the advance of martitization, increase in the REE concentration and precipitation of hematite in quartz veins; (iii) a late hydrothermal fluid of both low and high salinities, associated with the development of euhedral- and/or tabular-hematite bearing veins. The main hydrothermal fluid flow was probably focused along the original jaspilite-basaltic contact (Lobato et al., 2005b) with intensive lateral fluid diffusion through the jaspilitic sequence and less intense diffusion through the basaltic rocks as these had a more isotropic fabric when compared to banded jaspilites (Lobato et al., 2005b). An inherited Archean structural framework prepared the terrane for the iron mineralizing hydrothermal fluids, as the hard orebodies formed mainly in the hinge zone (e.g., the. N5E deposit) of large folds, and associated with splays from existing shear zones (Lobato et al., 2005b; Rosière et al., 2006; Figs. 5 and 14).

7. A correlation may exist between the formation of these iron ore deposits and the formation history of the hydrothermal magmactic deposits, dominantly rich in Cu and Au (including IOCG type) that are distributed throughout the Carajás Mineral Province as previously suggested by Lobato et al. (2005b). Nevertheless, this tantalizing hypothesis requires extensive further investigation.

Exploration Significance and Criteria

This contribution and related studies by our group provides an alternative model for the formation of high-grade iron ore in the Carajás region. In contrast to the model in which Archean iron ore deposits formed due to chemical sedimentary deposition near volcanic centers, with subsequent supergene enrichment, we suggest here that they can form by hydrothermal alteration associated with fluids derived from possibly distal Paleoproterozoic alkaline magmatic intrusions (Lobato et al., 2005a, b) mixed with meteoric waters, with later supergene enrichment forming most types of soft ores.

Geological characteristics that support our model and have exploration significance include: (i) iron orebodies vary in composition according to geometry that does not follow the weathering profiles; (ii) contacts between ores and wall rocks as well as jaspilite and mafic rocks are not always concordant; (iii) soft ores that overlie non-weathered volcanic rocks are generally interpreted as supergene; some of the soft ore characteristics such as high porosity, however, are not exclusively supergene and have been shown to be the result of hydrothermal alteration (Lobato et al., 2005a and b); (iv) ore characteristics among different deposits vary as function of structural variations, indicating that post-sedimentary structures directly influenced the mineralogical and chemical ore composition; and (v) discordant stratigraphic contact between the jaspilitic sequence and iron

mineralization, confirmed by deep drilling (Guedes, 2000). Those geological characteristics can be translated in different exploration parameters. For example, subsiduary structures spatially related to large-scale shear zones or complex fault symmetries can be prospective for iron mineralization. Pathfinder minerals and pathfinder elements can be deduced from hydrothermal alteration zones, which can then be used as vectors towards high-grade ore zones. The economic consequences using the exploration criteria deduced from hydrothermal iron metallogeny are immediate and positive (Lobato et al., 2005b).

The identification and understanding of basaltic wall-rock alteration as well as the distribution of hypogene high-grade ore at this contact are very important parameters that can be used in exploration drilling.

Open Questions and Future Work

Since discovery of the Carajás iron ores in 1967, their origin has been the subject of much debate. The present studies have added significantly to the understanding of the hypogene genesis of these high-grade iron ore deposits. Most of these are related to detailed petrography and geochemistry of jaspilitic protore, basaltic wallrocks and hard ores from deposits in the Serra Norte district. However, some crucial points must still be addressed: (i) the extension of the jaspilite-type BIFs in other parts of the district, and how compositional BIF variation may or may not have affected iron ore quality and type; (ii) mineralogical and geochemical characterization of the different types of soft ores, also attempting to establish better criteria to separate hypogene from supergene ores; (iii) evaluation of some of possible contaminants such as sulfur, phosphorous, among others.

The fluids responsible for the hypogene ore formation were both magmatic and meteoric, although the source of the former remains largely unknown. Lobato et al. (2005b) suggest that the magmatic fluids were derived from the Paleoproterozoic alkaline granites. In that sense, the relationship (link) between the iron ore deposits and numerous hydrothermal magmatic deposits, dominantly rich in Cu and Au, in the Carajás Mineral Province (including IOCG deposits) pointed out by Lobato et al. (2005b) needs a special investigation, since the fluid, isotopic and geochemical dataset do in fact show similarities between these deposits types (Figueiredo e Silva et al., in preparation). One line of research to be pursued is that of melt inclusions on minerals from selected granitoid samples, in conjuction with results of Rios et al. (1992) who studied fluid inclusions trapped in quartz, calcite and fluorite from hydrothermal veins related to the Serra dos Carajás granite. Also, fluid inclusion studies on hematite (Rios et al., 2004; Lobato et al., 2005b) must be carried on in order to better constrain the meteoric water interaction in the advanced-hydrothermal stage.

At the Serra Sul deposits, in the Carajás Mineral Province, lack of detailed structural reconstruction and evidence of hypogene alteration transition between BIF and high-grade ore, limits the integration of these deposits with the Serra Norte deposits. Near the contact with the Serra dos Carajás granite, the S11Serra Sul BIFs are locally recrystallized and display a complex mineralogical composition, including aegirine-type pyroxene, iron-rich biotite and large amount of magnetite (Lobato et al., 2005a).

Acknowledgments

The authors wish to acknowledge Vale (previously called CVRD) for their technical, logistic and financial support during our research. Our special thanks to all technicians, helpers and geologists who throughout the years made this work possible, especially to Dr. Flávio Ferreira. A great deal of the analytical data presented here were financed by Vale, jointly with Financiadora de Estudos e Projetos (FINEP) during the period 2001-2005 under the coordination of Agência para o Desenvolvimento Tecnológico da Indústria Mineral Brasileira (ADIMB). Thanks are due to the research staff at the Centre for Exploration Targeting, University of Western Australia and at the Centro de Pesquisas Prof. Manoel Teixeira da Costa, Universidade Federal de Minas Gerais. We also wish to thank the support in the various isotopic laboratories, namely from technicians and geologists, especially Garry Davidson, David Banks, Torsten Venemann and Zsofia Waczek. The geological map of Carajás results from literature, field and image interpretation, for which we are indebted to Prof. José C. S. Sícoli and geologist MSc Leandro Costa. We also appreciate the help of geologists Gabriel Berni, Orivaldo Baltazar and Bruno Daconti for putting together the final digital version of this map. E. Crocco and V. de Oliveira drafted the remaining figures of the manuscript. RCFS and MZ were recipients of scholarships from Coordenação de Aperfeiçoamento de Pessoal de Nível Superior (CAPES) as part of their PhD degrees. LML and CAR acknowledge their grants from the Conselho Nacional de Desenvolvimento Científico e Tecnológico (CNPq). Finally we would like to express our appreciation to the reviewers Joydip Mukhopadhyay and Hennie Theart and the editorial staff especially Nic Beukes and Steve Kesler for constructive criticism of an earlier version of this manuscript.

References

Araújo, O.J.B., and Maia R.G.N., 1991, Programa levantamentos geológicos básicos do Brasil. Projeto especial mapas de recursos minerais, de solos e de vegetação para a área do Programa Grande Carajás: Subprojeto Recursos Minerais, Serra dos Carajás, Folha SB.22-Z-A. Brasília, DNPM/Companhia de Pesquisa e Recursos Minerais-CPRM, 152 p.

Araújo, O.J.B., Maia, R.G.N., João, X.S.J., and Costa, J.B.S., 1988, A megaestruturação arqueana da folha Serra dos Carajás: Congresso Latino-Americano de Geologia, 7th, Belém, Anais, 1, p. 324-328.

Avelar, V.G., Lafon, J.M., Correa Jr., F.C., and Macambira, E.M.B., 1999, O magmatismo arqueano da região de Tucumã, Província Mineral Carajás, Amazônia Oriental, Brasil: novos dados geocronológicos: Revista Brasileira de Geociências, v. 29, p. 453-460.

Barley, M.E., Pickard, A.L., Hagemann, S.G., and Folkert, S.L., 1999, Hydrothermal origin for the 2 billion year old giant iron ore deposit, Hamersley Province, Western Australia: Mineralium Deposita, v. 34, p. 784-789.

Barros, C.E.M., and Barbey, P., 1998, A importância da granitogênese tardi-arqueana na evolução tectono-metamórfica da Província Mineral de Carajás: Revista Brasileira de Geologia, v. 28, p. 513-522.

Barros, C.E.M., and Barbey, P., 2000, Significance of garnet-bearing metamorphic rocks in the Archean supracrustal series of the Carajás Mining Province, Northern Brazil: Revista Brasileira de Geologia, v. 30(3), p. 367-370.

Barros, C.E.M., Barbey, P., and Boullier, A.M., 2001, Role of magma pressure, tectonic stress and crystallization progress in the emplacement of syntectonic granites. The A-type Estrela Granite Complex (Carajás Mineral Province, Brazil): Tectonophysics, v. 343, p. 93-109.

Beisiegel, V.R., Bernardelli, A.L., Drummond, N.F., Ruff, A.W., and Tremaine, J.W., 1973, Geologia e recursos minerais da Serra dos Carajás: Revista Brasileira de Geociências, v. 3(4), p. 215-242.

Beisiegel, V.R., 1982, Distrito ferrífero da Serra dos Carajás: Simpósio de Geologia da Amazônia, Belém, Anais, v. 1, p. 21-46.

Beukes, N.J., Gutzmer, J., and Mukhopadhyay, J., 2002, The geology and genesis of high-grade hematite iron ore deposits: Australasian Institute of Mining and Metallurgy, Publication Series 7, p. 23-29.

Bizzi, L.A., Schobbenhaus, C., Gonçalves, J.H., Baars, F.J., Delgado, I.M., Abram, M.B., Leão Neto, R., de Matos, G.M.M., and Santos, J.O.S., 2001, Geologia, Tectônica e Recursos Minerais do Brasil: Sistema de Informações Geográficas–SIG e Mapas na Escala 1:2 500 000. 4ª Edição, 4 CD-rom. Companhia de Pesquisa e Recursos Minerais-CPRM.

Borges, A.W.G., 1994, Geologia da porção Norte da Jazida de Ferro N4, Carajás-Pará: Trabalho de Conclusão de Curso, Universidade Federal do Pará, 60 p.

Cabral, A.R., Rocha Filho, O.G., and Jones, R.D., 2003, Hydrothermal origin of soft hematite ore in the Quadrilátero Ferrífero of Minas Gerais, Brazil. Petrographic evidence from the Gongo Soco iron ore deposit: Applied Earth Science, v. 112, p. 279-286.

Chiba, H., Chacko, T., Clayton, R.N., and Goldsmith, J.R., 1989, Oxygen isotope fractionations involving diopside, forsterite, magnetite, and calcite: Application to geothermometry: Geochimica et Cosmochimica Acta, v. 53, p. 2985-2995.

Clout, J.M.F., and Simonson, B.M., 2005, Precambrian iron formations and iron formation-hosted iron ore deposits: Economic Geology, 100th Anniversary Volume, p. 643-679.

Costa, L.P., 2007, Caracterização das seqüências metavulcanossedimentares da porção leste da Província Mineral Carajás, Pará: Unpublished M.Sc. dissertation, Belo Horizonte, Brazil, Universidade Federal de Minas Gerais, Departamento de Geologia, 113 p.

CVRD, 1996. Resumo dos aspectos geológicos da Província Mineral Carajás, in Guia de excursão: DIGEB/DEPAB/ GIMB/SUMIC, p. 392-403.

CVRD, 2004. Atualização dos recursos e reservas provadas e prováveis das minas de N4 e N5, in Relatório de pesquisa: Departamento Nacional de Produção Mineral-DNPM, v. I, 197 p.

CVRD, 2007, 20 Form annual report pursuant to section 13 or 15(d) of the securities exchange act of 1934, United States Securities and Exchange Commission.

Dall'Agnoll, R., and de Oliveira, D.C., 2007, Oxidized, magnetite-series, rapakivi-type granites of Carajás, Brazil: Implications for classification and petrogenesis of A-type granites: Lithos, v. 93(3-4), p. 215-233.

Dalstra, H.J., and Guedes, S., 2004, Giant hydrothermal hematite deposits with Mg-Fe metasomatism: a comparison of the Carajás, Hamersley, and other iron ores: Economic Geology, v. 99, p. 1793-1800.

Dardenne, M.A., Ferreira Filho, C.F., and Meirelles, M.R., 1988, The role of shoshonitic and calç-alkaline suites in the tectonic evolution of the Carajás district, Brazil: Journal of South Americam Earth Science, v. 1(4), p. 363-372.

Dardenne, M.A., Schobbenhaus, C. 2001, Metalogênese do Brasil, Editora Universidade de Brasília, 392 p.

Dias, G.S., Macambira, M.J.B., Dall'Agnol, R., Soares, A.D.V., and Barros, C.E.M., 1996, Datação de zircões de sill de metagabros: comprovação da idade arqueana da Formação Águas Claras, Carajás-Pará [ext. abs.]: Simpósio de Geologia da Amazônia, 5th, Belém, Brazil, p. 376-379.

DOCEGEO, 1988, Revisão litoestratigráfica da Província Mineral de Carajás: Proceedings of Congresso Brasileiro de Geologia 35th, Sociedade Brasileira de Geologia: Belém, Brazil, p. 11-54.

Domingos, F.H.G., 2005, Geometria, cinemática e história tectônica das rochas da Serra Norte, Carajás-PA: Unpublished M.Sc. dissertation, Belém, Brazil, Universidade Fereral do Pará, 119 p.

Dymek, R.F., and Klein C., 1988, Chemistry, petrology, and origin of banded iron formation lithologies from the 3800 Ma Isua supracrustal belt, West Greenland: Precambrian Research, v. 39, p. 241-302.

Faraco, M.T.L., Carvalho, J.M.A., and Klein, E.L., 1996, A carta metalogenética da Província Carajás/Sul do Pará–Folha Araguaia (SB.22): Congresso Brasileiro de Geologia, 39, Salvador, Anais, v. 3, p. 248-250.

Faure, G., 1977, Principles of isotope geology. John Wiley & Sons, New York, 464 p.

Faure, G., and Powell, J.L., 1972, Strontium isotope geology. In: Minerals, rocks and inorganic materials, Monograph Series of Theoretical and Experimental Studies 5, New York, Springer-Verlag, 188 p.

Faure, G., and Mensing, T.M., 2005, Isotopes principles and applications (3rd ed). Wiley, New Jersey, USA, 928 p.

Figueiredo e Silva, R.C., 2004, Caracterização petrográfica e geoquímica de jaspilitos e minérios de ferro, Província Mineral Carajás, Pará: implicações para a mineralização de ferro: Unpublished M.Sc. dissertation, Belo Horizonte, Brazil, Universidade Federal de Minas Gerais, Departamento de Geologia, 151 p.

Figueiredo e Silva, R.C., Lobato, L.M., Rosière, C.A., Guedes, S.C., Monteiro, A.M., Meireles, H., and Matias, P.H., 2004, Estudos petrográficos microscópicos e geoquímicos em jaspilitos e minérios de ferro dos depósitos N1, N4E, N4W e N5E, Província Mineral Carajás, Pará [abs.]: Simpósio Brasileiro de Exploração Mineral, 1st, Ouro Preto, Brazil, Agência para o Desenvolvimento Tecnológico da Indústria Mineral Brasileira (ADIMB), CD-ROM.

Figueiredo e Silva, R.C., Lobato, L.M., and Rosière, C.A., 2005, Petrografia e geoquímica em jaspilitos e minérios hidrotermais de ferro dos depósitos da serra norte (N1, N4E, N4W e N5E), Província Mineral Carajás, Pará [abs]: Simpósio de Metalogenia, 1st, Gramado, Brazil, SBG, CD ROM.

Figueiredo e Silva, R.C., Hagemann, S.C., Lobato, L.M., and Banks, D., 2007a, Hydrothermal fluid characteristics and evolution for the giant Carajás North Range iron deposits, Brazil [abs]: Biennial Conference European Current Research of Fluid Inclusion (ECROFI) 19th. University of Bern, Switzerland, p 98.

Figueiredo e Silva, R.C., Hagemann S.C., Lobato, L.M., and Venemann, T., 2007b, Iron oxide paragenesis, quartz vein chronology and hydrothermal fluid evolution at the giant North Range Carajás iron deposits in Brazil [ext. abs.]: Biennial Meeting of the Society for Geology Applied to Mineral Deposits 9th. Proceedings, SGA, Dublin, Ireland, v. 2, p. 1223-1226.

Galarza, M.A., and Macambira, M.J.B., 2002, Petrologia e geocronologia das rochas encaixantes do depósito de Cu-Au Igarapé Bahia, Província Mineral de Carajás, Pará, Brasil, in Klein, E.L., Vasquez, M.L., Rosa-Costa, L.T. (Eds.), Contribuições à Geologia da Amazônia 3, Belém, SBG, p. 153-168.

Gibbs A.K., and Wirth, K.R., 1990, Geologic setting of the Serra dos Carajás iron deposits, Brazil, in Chauvel, J.J., Yuqi, C., and El Shazly, E.M., eds., Ancient banded iron formations (regional presentations): Athens, Theophrastus, p. 83–102.

Gibbs, A.K., Wirth, K.R., Hirata, W.K., and Olszewski Jr., W.J., 1986, Age and composition of the Grão Pará Group volcanics, Serra dos Carajás: Revista Brasileira de Geociências, v. 16(2), p. 201-211.

Grainger, C.J., Grooves, D.I., Tallarico, F.B., Fletcher, I.R., 2008, Metallogenesis of the Carajás Mineral Province, Southern Amazon Craton, Brazil: Varying styles of Archean through Paleoproterozoic to Neoproterozoic base- and precious-metal mineralization: Ore Geology Reviews, V.33, p. 451-484.

Grossi Sad, J.M., and Dutra, C.V., 1987, Fracionamento dos elementos terras raras e suas aplicações em metalogênese. Parte I: Princípios gerais: Congresso Brasileiro de Geoquímica, 1st, Porto Alegre, 40 p.

Guedes, S.G., 2000, Evidências de alteração hidrotermal na formação ferrífera bandada e minérios de ferro de N4, N5 e Serra Leste, Serra dos Carajás-Pará, Brasil: Seminário de Qualificação, Belo Horizonte, Brazil, Universidade Federal de Minas Gerais, Departamento de Geologia, 61 p.

Guedes, S.G., Rosière, C.A., Barley, M., and Lobato, L.M., 2002, The importance of carbonate alteration associated with the Carajás high-grade hematite deposits, Brazil, in Iron Ore 2002 Proceedings, The

Australasian Institute of Mining and Metallurgy, Melbourne, Australia, Publication Series 7, p. 63-66.

Gutzmer, J. Mukhopadhyay, J. Beukes, N. J. Pack, A. Hayashi, K. and Sharp, Z. D., 2006, Oxygen isotope composition of hematite and genesis of high-grade BIF-hosted iron ores: Memoirs- Geological Society of America 2006, Issue 198, p. 257-268.

Hagemann, S.G., Barley, M.E., Folkert, S.L., Yardley, B.W., and Banks, D.A., 1999, A hydrothermal origin for the giant Tom Price iron ore deposit, in Stanley, C.J. et al., eds., Mineral deposits: Processes to processing: Rotterdam, Balkema, p. 41-44

Hagemann, S.G., Rosière, C.A., Lobato, L.M., Baars, F.J., Zucchetti, M., and Figueiredo e Silva, R.C., 2006, Controversy in genetic models for high-grade BIF related Fe deposits: Unifying or discrete model(s)?: Applied Earth Science, Transactions Institute of Mining and Metallurgy B, v. 115, p. 147-151.

Hirata, W.K., Rigon, J.C., Kadekaru, K., Cordeiro, A.A.C., and Meireles, E.M., 1982, Geologia Regional da Província Mineral de Carajás: Simpósio de Geologia da Amazônia, Belém, Anais, 1, p. 100-108.

Hoefs, J., 2007, Stable isotope geochemistry, (5th ed). Springer-Verlag, New York, USA, 244 p.

Holdsworth, R.E., and Pinheiro, R.V.L., 2000, The anatomy of shallow-crustal transpressional structures: insights from the Archean Carajás fault zone, Amazon, Brazil: Journal of Structural Geology, v. 22, p. 1105-1123.

Huhn, S.R.B., Santos, A.B.S., Amaral, A.F., Ledshan, E.J., Gouveia, J.L., Martins, L.P.B., Montalvão, R.G.M., and Costa, V.G., 1988, O terreno 'granito-greenstone' da região de Rio Maria – sul do Pará [ext. abs.]: Congresso Brasileiro de Geologia, 35th, Belém, p. 1438-1452.

Huhn, S.R.B., Souza, C.I.J., Alburquerque, M.C., Leal, E.D., Brustolin, V., 1999, Descoberta do Depósito Cu(Au) Cristalino: Geologia e Mineralização Associada-Região de Serra do Rabo – Carajás – PA: Simpósio de Geologia da Amazônia, 6th, Manaus, Brazil, p. 140-143.

Huhn, S.R.B.; Soares, A.D.V.; Medeiros Filho, C.A.; Magalhães, C.C.; Guedes, S.C.; Moura, L.G.B.; Rego, J.L.; and Cravo, C.H., 2000, Carajás Mineral Province, Pará state, north of Brazil: Field Trip Guide, International Geological Congress 31st, Rio de Janeiro, Brazil, 24 p.

Khan, R.M.K., Sharma, S.D., Patil, D.J., and Naqvi, S.M., 1996, Trace, rare-earth element, and oxygen isotopic systematics for the genesis of banded iron-formations: Evidence from Kushtagi schist belt, Archean Dharwar Craton, India: Geochimica et Cosmochimica Acta, v. 60, p. 3285-3294.

Klein, C., and Ladeira, E.A., 2002, Petrography and geochemistry of the least-altered banded iron-formation of the Archean Carajás Formation, northern Brazil: Economic Geology, v. 97, p. 643-651.

Krymsky, R.Sh., Macambira, J.B., and Macambira, M.B.J., 2002, Geocronologia U-Pb em zircão de rochas vulcânicas da Formação Carajás, Estado do Pará [abs.]: Simpósio sobre vulcanismo e ambientes associados, 2nd, Belém, p. 41.

Kullerud, G., Donnay, G., and Donnay, J.D.H., 1969, Omission solid solution in magnetite: kenotetrahedral magnetite: Zeitschrifft der Kristallographie, v. 128, p. 1-17.

Ladeira, E.A., and Cordeiro, J.R.C., 1988, Jazida N4E: Reavaliação dos corpos de hematita dura e jaspilitos: Proceedings of Congresso Brasileiro de Geologia 35th, Sociedade Brasileira de Geologia: Belém, Brazil, p. 103-120.Li, Yuan-Hui., 2000, A compendium of geochemistry: from solar nebula to the human brain:

Princeton University Press, 475 p.

Li, Yuan-Hui, 2000, A compendium of geochemistry: from solar nebula to the human brain. Princeton University Press, 475 p.

Liddy, J.C., 1968, The Jaspilite Iron Ores of Australia: Economic Geology, vol. 63, p. 815-821.

Lindenmayer, Z.G. 1990. Salobo Sequence, Carajás, Brazil: geology, geochemistry and metamorphism: Unpublished Ph.D. thesis, London, Canada, University of Western Ontario, Department of Earth Sciences, 406 p.

Lindenmayer, Z.G., and Fyfe W.S., 1992, Comparação preliminar entre os metabasaltos dos grupos Parauapebas e Salobo da bacia Carajás, PA: Anais Congresso Brasileiro de Geologia, v. 2, p. 33-34.

Lindenmayer, Z.G., Laux, J.H., Teixeira, J.B.G., 2001, Considerações sobre a origem das formações ferríferas da formação Carajás, Serra dos Carajás: Revista Brasileira de Geociências, v. 31(1), p. 21-28.

Lindenmayer, Z.G., Fleck, A., Gomes, C.H., Santos, A.B.Z., Caron, R., Paula, F.C., Laux, J.H., Pimentel, M.M., and Sardinha, A.S., 2005, Caracterização geológica do Alvo Estrela (Cu-Au), Serra dos Carajás, Pará. 2005, in Marini, O.J., Queiroz, E.T., and Ramos B.W. (eds), Caracterização de depósitos minerais em distritos mineiros da Amazônia. DNPM/CT-Mineral/FINEP/ADIMB, Brasília, p. 157-226.

Lobato, L.M., Rosière, C.A., Baars, F.J., Figueiredo e Silva, R.C., Zucchetti, M., Rios, F.J., Seoane, J.C.S., Pimentel, M., Lindenmayer, Z.G., Mendes, G.E., and Maciel, A.L., 2004, Timing of hydrothermal iron mineralization, Carajás Province, PA [abs.]: Simpósio Brasileiro Exploração Mineral, 1st, Ouro Preto, Brazil, Agência para o Desenvolvimento Tecnológico da Indústria Mineral Brasileira (ADIMB), CD-ROM.

Lobato, L.M., Figueiredo e Silva, R.C., Rosière, C.A., Zucchetti, M., Baars, F.J., Seoane, J.C.S., Rios, F.J., and Monteiro, A.M., 2005a, Hydrothermal origin for the iron mineralisation, Carajás Province, Pará State, Brazil: Iron Ore 2005 Proceedings, The Australasian Institute of Mining and Metallurgy, Perth, Australia, Publication Series 8, p. 99-110.

Lobato, L.M., Rosière, C.A., Figueiredo e Silva, R.C., Zucchetti, M., Baars, F.J., Seoane, J.C.S., Rios, F.J., Pimentel, M., Mendes, G.E., and Monteiro, A.M., 2005b, A mineralização hidrotermal de ferro da Província Mineral de Carajás - Controle estrutural e contexto na evolução metalogenética da província, in Marini, O.J., de Queiroz, E.T., and Ramos, B.W., eds., Caracterização de depósitos minerais em distritos mineiros da Amazônia. Departamento Nacional da Produção Mineral (DNPM)/Fundo Setorial Mineral (CT-Mineral/FINEP)/Agência para o Desenvolvimento Tecnológico da Indústria Mineral Brasileira (ADIMB), Brasília, Brazil, p. 25-92.

Lobato, L.M., Figueiredo e Silva, R.C., Hagemann, S., and Thorne, W., 2007, Mineralizing fluid evolution and REE patterns for the hydrothermal Carajás iron ores, Brazil, and for selected Hamersley iron deposits, Australia [ext. abs.]: Biennial Meeting of the Society for Geology Applied to Mineral Deposits 9. Proceedings, SGA, Dublin, v. 2, p. 1227-1230.

Lobato, L.M., Hagemann, S., Figueiredo e Silva, R.C., Thorne, W., Zucchetti, M., and Gutzmer, J., 2008, Hypogene hydrothermal alteration associated with BIF-related iron ore mineralization, in Hagemann, S.G., Rosière, C.A., Gutzmer, J., and Beukes, N.J., BIF-Related High-Grade Iron Mineralization: Reviews in Economic Geology, v. 15, p.

Lopes, P.M.S., 1997, Mineralogia dos minérios de ferro da jazida N4E, Carajás-PA: Trabalho de Graduação, Pará, Brazil, Universidade Federal do Pará, 66 p.

Lovering, T.G., 1972, Jasperoid in the United States- its characteristics, origin, and economic significance: U.S. Geological Survey Professional Paper 710, 164 p.

Macambira, J.B., and Silva,V.F., 1995, Estudo petrológico, mineralógico e caracterização das estruturas sedimentares e diagenéticas preservadas na Formação Carajás, Estado do Pará: Boletim Museu Para. Emílio Goeldi, Série Ciência da Terra, v. 7, p. 363-387.

Macambira, J.B., and Lopes, P.M.S, 1996a, Mineralogia dos minérios de ferro da jazida N4E – Carajás: Resultados preliminares [ext. abs.]: Congresso Brasileiro de Geologia, 39th, Salvador, p. 269-271.

Macambira, J.B., Macambira, M.J.B., Scheller, T., Gomes, A.C.B., 1996b. Geocronologia Pb/Pb e tipologia de zircões de rochas vulcânicas da Formação Carajás - Pará: Indicador da idade dos BIFs [ext. abs.]: Congresso Brasileiro de Geologia, 39th, Salvador, p. 516-518.

Macambira, J.B., Guedes, S., and Matias, P.H., 1999, *Bif* Carbonático na Formação Carajás: Alteração Hidrotermal ou uma Nova Fácies? [abs]: Simpósio de Geologia da Amazônia, 6th, Manaus, p. 563-565.

Macambira, J.B., and Schrank, A. 2002, Químio-estratigrafia e evolução dos jaspilitos da Formação Carajás (PA): Revista Brasileira de Geociências, v. 32(4), p. 567-578.

Macambira, J.B., 2003, O ambiente deposicional da Formação Carajás e uma proposta de modelo evolutivo para a Bacia Grão Pará: PhD Thesis, São Paulo, Brazil, Universidade Estadual de Campinas, 217 p.

Macambira, M.J.B., Ramos, J.F.F., Assis, J.F.P., and Figueiras, A.J.M., 1990, Projeto Serra Norte e Projeto Pojuca. Convênio SEPLAN/DOCEGEO/UFPA/DNPM: Relatório final, 150 p.

Machado, N., Lindenmayer, Z., Krogh, T.E., and Lindenmayer, D., 1991, U-Pb geochronology of Archean magmatism and basement reactivation in the Carajás área, Amazon shield, Brazil: Precambrian Research, v. 49, p. 329-354.

Matsuhisa, Y., Goldsmith, J.R., and Clayton, R.N., 1979, Oxygen isotopic fractionation in the system quartz-albite-anorthite-water: Geochimica et Cosmochimica Acta, v. 43(7), p. 1131-1140.

Meireles, E.M., Hirata, W.K., Amaral, A.F., Medeiros Filho, C.A., and Gato, W.C., 1984, Geologia das folhas Carajás e Rio Verde, Província Mineral de Carajás, Estado do Pará: Congresso Brasileiro de Geologia, 33, Rio de Janeiro, Anais, v. 5, p. 2164-2174.

Meirelles, M.R., 1986, Geoquímica e petrologia dos jaspilitos e rochas vulcânicas associadas, Grupo Grão-Pará, Serra dos Carajás, Pará: Unpublished M.Sc. dissertation, Brasília, Brazil, Universidade de Brasília, 171 p.

Meirelles, M.R., and Dardenne, M.A., 1991, Vulcanismo basáltico de afinidade shonshonítica em ambiente de arco arqueano, Grupo Grão Pará, Serra dos Carajás, Pará [ext. abs.]: Congresso Brasileiro de Geoquímica, 4th, p. 131-132.

Melo 1981, Jazida N4E, Geologia e Reservas, Distrito Ferrífero da Serra dos Carajás, Rio de Janeiro, Amazônia Mineração S/A, v.4, p.

Michard, A., 1989, Rare earth element systematics in hydrothermal fluids: Geochimica et Cosmochimica Acta, v. 53, p. 745-750.

Mougeot, R., 1996, Estude de la limite Archeen-Proterozoique et des mineralizations Au, +/_U associees. Exemples de la region de Jacobina (Etat de Bahia, Bresil) et de Carajás (Etat de Para, Bresil), Unpublished PhD thesis, University of Montpellier II, 301 p.

Morris, R.C., 1985, Genesis of iron ore in banded iron-formation by supergene and supergene-metamorphic - A conceptual model, in Wolff, K.H. (ed.), Handbook of Strata-bound and Stratiform Ore dep, Elsevier, v. 13, p. 73-235.

Nakamura, N., 1974, Determination of REE, Ba, Fe, Mg, Na and K in carbonaceous and ordinary chondrites: Geochimica Cosmochimica Acta, v. 38, p. 757-775.

Netshiozwi, S.T., 2002, Origin of High-Grade Hematite Ores at Thabazimbi Mine, Limpopo Province, South Africa: Msc Dissertation, Faculty of Science at the Rand Afrikaans University, 135 p.

Olszewski, W.J., Wirth, K.R., Gibbs, A.K., and Gaudette, H.E., 1989, The age, origin, and tectonics of the Grao Pará Group and associated rocks, Serra dos Carajás, Brazil: Archean Continental Volcanism and rifting: Precambrian Research, v. 42, p. 229-254.

Pinheiro, R.V.L., and Holdsworth, R.E., 1997, The structure of the Carajás N-4 ironstone deposit and associated rocks: relationship to Archean strike-slip tectonics and basement reactivation in the Amazon region, Brazil: Journal of South American Earth Sciences, v. 10(3-4), p. 305-319.

Pinheiro, R.V.L., and Holdsworth, R.E. 2000, The Anatomy of shallow – crustal transpressional structures: insights from the Archean Carajás fault zone, Amazon, Brazil: Journal of Structural Geology, v. 22, p. 1105-1123.

Pinheiro, R.V.L., Nezio, J.A., and Guedes, S.C, 2001, A falha Carajás e a estruturação tectônica dos depósitos de ferro da Serra Norte, Carajás (PA) [ext. abs]: Simpósio de Geologia da Amazônia, 7th, Belém, p. 11-14.

Rezende, N.P., and Barbosa, A.L.M., 1972, Relatório de Pesquisa – Distrito Ferrífero Serra dos Carajás, Estado do Pará. Mapas e Seções. Departamento Nacional de Produção Mineral – DNPM & Companhia Vale do Rio Doce, v. 2, 119 p.

Rios, F.J., and Villas, R.N.N., 1992, Granito Central da Serra dos Carajás, Pará: II. Minerais de alteração e correspondente ambiente deposicional [ext. abs]: Congresso Brasileiro de Geologia, 37th, São Paulo, p. 214-215.

Rios, F.J., Lobato, L.M., Rosière, C.A., Figueiredo e Silva, R.C., and Souza, A.S., 2004, Resultados preliminares do estudo metalogenético do minério hematítico de alto teor do depósito de ferro N5 – Carajás, utilizando microscopia e microtermometria de infravermelho, PA [abs.]: Simpósio Brasileiro de Exploração Mineral, 1st, Ouro Preto, Brazil, Agência para o Desenvolvimento Tecnológico da Indústria Mineral Brasileira (ADIMB), CD-ROM.

Rhodes, A. L., Oreskes, N., and Sheets, S. A., 1999, Geology and rare earth element geochemistry of magnetite deposits at El Laco, Chile, *in* Skinner, B. J., ed., Geology and ore deposits of the central Andes: Littleton, CO, Society of Economic Geologists, Special Publication no. 7, p. 299–332.

Rollinson, H.R., 1993, Using geochemical data: evaluation, presentation, interpretation. Singapore, Longman, 352 p.

Rosière, C.A., Chemale, Jr. F., 2000, Brazilian formations and their geological setting: Revista Brasileira de Geociências, v. 30(2), p. 274-278.

Rosière, C.A., and Rios, F.J., 2004, The origin of hematite in high-grade iron ores based in infrared microscopy and fluid inclusion studies: the example of the Conceição Deposit, Quadrilátero Ferrífero, Brazil: Economic Geology, v. 99, p. 611-624.

Rosière, C.A., Baars, F.J., Seoane, J.C.S., Lobato, L.M., da Silva, L.L., de Souza, S.R.C., and Mendes, G.E., 2006, Structure and iron mineralisation of the Carajás Province: Applied Earth Science, Transactions Institute of Mining and Metallurgy B, v. 115(4), p. 126-136.

Rosière, C.A., Spier, C.A., Rios, F.J., and Suckau, V.E., 2008, The Itabirites from the Quadrilátero Ferrífero and related High-grade Iron Ores: an overview, in Hagemann, S.G., Rosière, C.A., Gutzmer, J., and Beukes, N.J., BIF-Related High-Grade Iron Mineralization: Reviews in Economic Geology, v. 15, p

Santos, J.O.S., 2003, Geotectônica dos Escudos das Guianas e Brasil-Central, in Bizzi L.A., Schobbenhaus C., Vidotti R.M., Gonçalves J.H. (eds.), Geologia, Tectônica e Recursos Minerais do Brasil, Companhia de Pesquisa e Recursos Minerais–CPRM, p. 169-226.

Schock, H.H., 1979, Distribution of rare-earth and other trace elements in magnetites: Chemical Geology, v. 26, p. 119-133.

Seoane, J.C.S., Rosière, C.A., Baars, F.J., and Lobato, L.M., 2004, Mapeamento litoestrutural 3-D do Grupo Grão Pará, Província Mineral Carajás, PA [abs]: Simpósio Brasileiro Exploração Mineral, Simpósio Brasileiro de Exploração Mineral, 1st, Ouro Preto, Brazil, Agência para o Desenvolvimento Tecnológico da Indústria Mineral Brasileira (ADIMB), CD-ROM.

Silva, G.G., Lima, M.I.C., Andrade, A.R.F., Issler, R.S., and Guimarães, G., 1974, Geologia das folhas SB-22 Araguaia e parte da SC-22 Tocantins, in Levantamento de Recursos Minerais, Projeto Radam (Departamento Nacional da Produção Mineral–DNPM e Companhia de Pesquisa e Recursos Minerais–CPRM).

Spier, C.A., Barros de Oliveira, S.M., and Rosière, C.A., 2003, Geology and geochemistry of the Águas Claras and Pico Iron Mines, Quadrilátero Ferrífero, Minas Gerais, Brazil: Mineralium Deposita, v. 38, p. 751-774.

Suszczynski, E., 1972, A origem vulcânica do minério de ferro primário da Serra dos Carajás – Estado do Pará – Região Amazônica: Proceedings of Congresso Brasileiro de Geologia 26th, Sociedade Brasileira de Geologia: Belém, Brazil, p. 103-120.

Tallarico, F.H.B., Figueiredo, B.R., Groves, D.I., Kositcin, N., McNaughton, N.J., Fletcher, I.R., and Rego, J.L., 2005, Geology and SHRIMP U-Pb Geochronology of the Igarapé Bahia deposit, Carajás copper-gold belt, Brazil: an Archean (2.57 Ga) example of iron-oxide Cu-Au-(U-REE) mineralization: Economic Geology, v. 100, p. 7-28.

Tassinari, C.C.G., Bettencourt, J.S., Geraldes, M.C., Macambira, M.J.C., and Lafon, J.M., 2000, The Amazonian Craton, in Cordani, U.G., Milani, E.J., Thomaz-Filho, A., and Campos, D.A. (eds.), Tectonic Evolution of South America, International Geological Congress, Rio de Janeiro, Brasil, p. 41-99.

Tassinari, C.C.G., Mellito, K.M., and Babinski, M., 2003, Age and origin of the Cu (Au-Mo-Ag) Salobo 3A

ore deposit, Carajás Mineral Province, Amazonian Craton, northern Brazil: Episodes, v. 26(1), p. 2-9.

Taylor, D., Dalstra, H.J., Harding, A.E., Broadbent, G.C., and Barley, M.E. 2001, Genesis of high-grade hematite orebodies of the Hamersley Province, Western Australia: Economic Geology, v. 96, p. 837-873.

Taylor, H.P. Jr., 1968, The oxygen isotope geochemistry of igneous rocks: Contributions to Mineralogical Petrology, v. 19, p. 1-71.

Taylor, H.P. Jr., 1997, Oxygen and hydrogen isotope relantionships in hydrothermal mineral deposits, in Barnes, H.L. (ed.), 1997, Geochemistry of Hydrothermal Ore Deposits (3rd ed.), John Wiley & Sons, New York, 972 p.

Taylor, S.R., and McLennan, S.M., 1985, The continental crust: its composition and evolution, Blackwell, 312 p.

Teixeira, J.B.G., 1994, Geochemistry, petrology, and tectonic setting of Archean basaltic and dioritic rocks from the N4 Iron ore deposit, Serra dos Carajás, Pará, Brazil: Unpublished Ph.D. thesis, Departament of Geoscience, Penn State University, 161 p.

Teixeira, J.B.G., and Eggler, D.H., 1994, Petrology, geochemistry, and tectonic setting of Archean basaltic and dioritic rocks from the N4 iron ore deposit, Serra dos Carajás, Pará, Brazil: Acta Geológica Leopoldensia 40, v. 40, p.71-114.

Teixeira, J.B.G., Ohmoto, H., and Eggler, D.H., 1997, Elemental and oxygen isotope variations in Archean mafic rocks associated with the banded iron-formation at the N4 iron ore deposit, Carajás, Brazil, in: Costa, M.L., and Angélica, R.S. (coords.), Contribuições à Geologia da Amazônia, FINEP/SBG, Brazil, p. 161-203.

Thorne, W.S., Hagemann, S.G., and Barley, M.E., 2004, Petrographic and geochemical evidence for hydrothermal evolution of the North deposit, Mt Tom Price, Western Australia: Mineralium Deposita, v. 39, p. 766-783.

Tolbert, G.E., Tremaine, J.W., Melcher, G.C., and Gomes, C.B., 1971, The recently discovered Serra dos Carajás iron ore deposits, Northen Brazil: Economic Geology, v. 7, p. 985-994.

Tolbert, G.E., Tremaine, **J.**W., Melcher, G.C., and Gomes, C.B., 1973, Genesis of Precambrian iron and manganese deposits: in Proceedings of the Kiev Symposium, Earth sciences, 9, p. 271-280.

Trendall, A.F., Basei, M.A.S., Laeter, J.R., and Nelson, D.R., 1998, Shrimp zircon U-Pb constraints on the age of the Carajás Formation, Grão Pará Group, Amazon Craton: Journal of South American Earth Sciences, vol 11(3), p. 265-277.

UNESCO, 1973, Genesis of Precambrian iron and manganese deposits: Proceedings of the Kiev Symposium, Earth sciences, 9, 382 p.

Varajão, C.A.C., Bruand, A., Ramanaidou, E.R., and Gilkes, R. 2002, Microporosity of BIF hosted hematite ore, Iron Quadrangle, Brazil: Anais da Academia Brasileira de Ciências, v. 74(1): p. 113-126.

Wirth, K.R., Gibbs, A.K., and Olszewski, W.J., 1986, U-Pb ages of zircons from the Grão-Pará Group and Serra do Carajás Granite, Pará, Brazil: Revista Brasileira de Geociências, v. 16, p. 195-200.

Yapp, C.J., 1990, Oxygen isotopes in iron (III) oxides 1. Mineral-water fractionation factors: Chemical Geology, v. 85, p. 329-335.

Zheng, Y.-F., 1991, Calculation of oxygen isotope fractionation in metal oxides: Geochimica Cosmochimica. Acta, v. 55, p. 2299-2307.

Zheng, Y.-F., 1995, Oxygen isotope fractionation in magnetites: structural effect and oxygen inheritance: Geochimica Cosmochimica. Acta, v. 121, p. 309-316.

Zucchetti, M., 2007, Rochas máficas do Supergrupo Grão Pará e sua relação com a mineralização de ferro dos depósitos N4 e N5, Carajás, (PA): Unpublished Ph.D. thesis, Belo Horizonte, Brazil, Universidade Federal de Minas Gerais, Departamento de Geologia, 125 p.

Zucchetti, M., and Lobato, L.M., 2004, Alteração hidrotermal a hematita das rochas máficas associadas aos depósitos de ferro N4 e N5, Província Mineral de Carajás, PA [abs.]: Simpósio Brasileiro de Exploração Mineral, 1st, Ouro Preto, Brazil, Agência para o Desenvolvimento Tecnológico da Indústria Mineral Brasileira (ADIMB), CD-ROM.

Zucchetti, M., Lobato, L.M., and Hagemann, S.G., 2007, Hydrothermal alteration of basalts that host to the giant Northern Range Carajás iron ore deposits, Brazil [ext. abs.]: Meeting of the Society for Geology Applied to Mineral Deposits 9th, Proceedings, SGA, Dublin, Ireland, v. 2, p. 1231-1234.

Appendix 1. Laboratory procedures

Whole rock geochemical analyzes were performed by ACME Labs Analytical Laboratories Ltd. in Vancouver, Canada. Total abundances of the major oxides and trace elements, including rare earth elements, were determined by ICP mass spectrometry following a lithium metaborate/tetrabortate fusion and nitric acid digestion of a 0.1 g. Detection and upper limits (ppm) are shown in brackets respectively: Fe_2O_3 and SiO_2 (0.04 %; 1000%), Al_2O_3 (0.03 %; 100%), Ba, Nb, Zr and Sr (0.5; 50000); U, Cu, Ni, Cs, Th and Pb (0.1; 10000), Y (0.1; 50000), Zn (1; 10000), Co and Rb (0.5; 10000), V (5; 10000), La and Ce (0.5; 50000); Nd (0.4; 10000), Sm (0.1; 10000), Eu and Gd (0.05; 10000), Tb (0.01; 10000), Dr to Yb (0.05; 10000) and Lu (0.01; 10000).

Electron microanalyses were conducted using a JEOL 6400 Scanning Electron Microprobe (SEM) and Zeiss 1555 VPSEM at the Centre for Microscopy, Characterization and Analysis (CMCA), University of Western Australia. Major oxides were determined by Energy Dispersive Spectroscopy (EDS) using a Link Analytical Si(Li) detector and Multi-Channel Analyzer (MCA). The following analytical conditions were used: accelerating voltage, 15 kV; beam current, 5 nA; count time, 60 seconds; ZAF correction program. Secondary electron images were obtained with aperture size of 120 μm at a working distance between 16 and 25 mm. Detection limits for Ca, Mg, Fe, and Mn were 0.08, 0.01, 0.06, and 0.06 %, respectively.

Microthermometric measurements (heating and freezing experiments) were conducted at the Center for Exploration Targeting - University of Western Australia on double-polished thin sections using a full automated Linkham THMSG 600 heating and freezing stage. The stage was calibrated between -56.6° and 374.1°C with synthetic fluid inclusion standards (pure H_2O and mixed H_2O-CO_2). The accuracy of the freezing measurement runs is about ±0.1°C and for heating runs ±1°C between 200-500 ºC. Apparent salinities are reported in weight percent NaCl and $CaCl_2$ equivalent, based on the halite solubility equation (Bodnar and Vityk, 1994).

Ion chromatography analyses were performed at the School of Earth and Environment, University of Leeds. Fluid inclusions were analyzed after a bulk crush-leach method (Banks and Yardley, 1992; and Banks et al., 2000). Samples between 0.5 and 1 g were crushed to a grain size of 1 to 2 mm and cleaned in distilled water. The samples were finally cleaned by repeated boiling and rinsing in 18.2-MΩ milli Q water, dried, and crushed to a fine powder in an agate pestle and steel mortar. The powder was transferred to a sample container and approximately 5 ml of milli Q water was added to re-dissolve the dried salts. The solution was finally filtered through a 0.2-μm pore size nylon filter prior to analysis. The leachates were analyzed for Cl^-, Br^-, F^- and SO_4^{2-} using ion chromatography, and Na+, K+, and Li+ by atomic absorption. Detection limits for Cl, Br, SO_4, Na, K, and Li were 10, 0.2, 10, 30, 30, and 0.1 ppb, respectively (Wouter et al., 2004).

The oxygen isotope composition (^{16}O, ^{17}O, ^{18}O) of quartz and oxide samples were measured at the University of Lausanne, using a method similar to that described by Sharp (1990) and Rumble and Hoering (1994) and is described in detailed by Kasemann et al. (2001). Between 0.5 to 2 mg of sample was loaded onto a small Pt-sample holder and pumped out to a vacuum of about 10^{-6} mbar. After pre-flourination of the sample chamber overnight, the samples were heated with a CO_2-laser in 50 mbars of pure F_2. Excess F_2 is separated from the O_2 produced by conversion to Cl_2 using KCl held at 150°C. The extracted O_2 is collected

on a molecular sieve (5A) and subsequently expanded into the inlet of a Finnigan MAT 253 isotope ratio mass spectrometer. Oxygen isotope compositions are given in the standard δ-notation, expressed relative to VSMOW in permil (‰). Replicate oxygen isotope analyses of the standards used (NBS-28 quartz and UWG-2 garnet; Valley et. al., 1995) generally have an average precision of ± 0.1‰ for $\delta^{18}O$. The accuracy of $\delta^{18}O$ values is commonly better than 0.2‰ compared to accepted $\delta^{18}O$ values for NBS-28 of 9.64‰ and UWG-2 of 5.8‰.

Sulfur isotope analyzes were conducted using a laser ablation sulfur isotope microprobe at the Stable Isotope Laboratory of the Central Science Laboratory, University of Tasmania. The analytical procedure is described by Huston et al. (1995) with the dynamic collection technique employed for SO_2 extraction. The reported precision (2σ) for laser ablation sulfur isotope analyzes of pyrite at the University of Tasmania is ±0.41‰ (Huston et al., 1995). The following analytical conditions were used: pressure 256; current 38 to 40 amperes; hole size 150 to 300 μm; laser duration 1 shot x 2 seconds until 7 shots x 2 seconds (when small crystals).

Strontium analyses were runned on a Nu Plasma MC-ICPMS at the School of Earth Sciences of the University of Melbourne. All samples were digested using distilled HCl in screw-cap Savillex beakers on a hotplate. Strontium was purified by passing the solution over EICHROM Sr resin before analysed. $^{87}Sr/^{86}Sr$ values have been corrected for mass bias by normalising $^{88}Sr/^{86}Sr$ to 8.37521 and adjusted to a value for SRM 987 of 0.710230. Internal precision is better than ±0.000020 for all samples and external precision approximately twice this value.

Bodnar, R.J., and Vityk, M.O., 1994, Interpretation of microthermometric data for H_2O-NaCl fluid inclusions, in De Vivo, B., Frezzotti, M.L., Fluid inclusions in minerals: methods and applications: VPI Press, Blacksburg, Virginia, p 117:130.

Huston, D.L., Power, M., Gemmell, J.B., and Large, R.R., 1995, Design, calibration and geological application of the first operational Australian laser ablation sulphur isotope microprobe: Australian Journal of Earth Sciences, v. 42, p. 549-555.

Kasemann, S., Meixner, A., Rocholl, A., Vennemann, T., Schmitt, A., and Wiedenbeck, M., 2001, Boron and oxygen isotope composition of certified reference materials NIST SRM 610/612, and reference materials JB-2G and JR-2G: Geostandards Newsletter, v. 25, p. 405:416.

Rumble D. III., and Hoering, T.C., 1994, Analysis of oxygen and sulfur isotope ratios in oxide and sulfide minerals by spot heating with a carbon dioxide laser in a fluorine atmosphrere: Accounts of Chemical Research, v. 27, p. 237:241.

Sharp, Z.D., 1990, A laser-based microanalytical method for the in-situ determination of oxygen isotope ratios of silicates and oxides: Geochimica et Cosmochimica Acta, v. 54, p. 1353:1357.

Valley J.W., Kitchen, N., Kohn, M.J., Niendorf, C.R., and Spicuzza, M.J., 1995, UWG-2, a garnet standard for oxygen isotope ratios: strategies for high precision and accuracy with laser heating: Geochimica et Cosmochimica Acta, v. 59, p. 5223-5231.

Wouter, H., Philippe, M., Banks, D.A., Schneider, J., Kucha, H., and Keppens, E., 2004, Carbonate-Hosted Zn-Pb Deposits in Upper Silesia, Poland: Origin and Evolution of Mineralizing Fluids and Constraints on Genetic Models, Economic Geology, v. 98, p. 911:932.

Appendix 2. Major, trace and rare earth elements contents in least-altered jaspilites and hard ores from the Serra Norte iron deposits.

	N4W least-altered jaspilites										N4E hematite-martite hard ores					
Drill core	**F588**	**F613**	**F617**	**F618**	**F618**	**F618**	**F618**	**F618**	**F618**	**F660**	**F603**	**F603**	**F603**	**F603**	**F603**	**F621**
Depth	**P144.1**	**P168.7**	**P267.1**	**P96.6**	**P113.9**	**P161 (A)**	**P161 (B)**	**P166**	**P171**	**P176.45**	**P20.7**	**P21.7**	**P30**	**P53.5***	**P55.5***	**P50.15**
SiO_2	38.89	45.39	19.22	49.59	34.74	50.79	19.40	41.43	40.99	35.97	0.98	0.77	0.42	14.53	2.56	10.09
Fe_2O_3	59.70	53.85	78.66	48.86	63.24	48.68	79.76	57.34	58.60	61.20	90.92	91.88	84.62	61.95	67.94	82.09
Al_2O_3	0.04	0.06	0.26	0.10	0.07	0.11	0.12	0.05	0.03	0.03	1.56	1.56	1.27	0.13	1.17	0.08
Ba	5.40	6.10	13.40	9.40	4.40	6.60	4.40	1.30	3.10	4.00	17.70	194.20	8.00	4.10	5.80	4.30
Co	46.50	30.10	19.90	27.10	25.20	33.60	28.50	31.70	30.00	31.80	15.20	15.00	16.20	29.60	10.20	36.30
Cs	—	0.10	0.50	0.20	0.10	0.10	0.30	—	—	0.10	1.00	0.50	0.20	—	—	0.10
Nb	—	—	—	—	—	—	—	—	—	—	1.80	2.40	—	—	0.70	—
Rb	—	—	1.10	—	—	—	0.60	—	0.90	—	2.60	1.60	—	—	—	—
Sr	1.50	0.60	1.90	0.80	—	1.30	0.70	1.00	—	—	4.50	5.80	5.20	3.40	5.40	1.30
Th	0.10	0.10	0.40	0.30	0.10	—	0.20	0.10	—	0.10	1.50	2.60	0.10	—	—	0.40
U	—	—	—	—	—	—	0.30	—	—	—	1.90	1.70	5.80	0.30	1.60	2.70
V	—	—	—	—	—	—	—	—	—	—	22.00	31.00	71.00	107.00	137.00	10.00
Zr	0.80	1.20	4.40	1.60	—	0.50	3.10	—	0.60	0.50	16.20	24.80	1.50	2.10	1.20	2.00
Y	1.30	5.30	2.70	1.00	0.60	1.10	1.50	0.80	0.80	0.80	8.20	6.60	4.30	3.90	3.20	8.60
Cu	7.80	193.70	7.10	9.30	6.10	9.90	114.10	9.30	7.80	62.30	47.10	32.90	13.60	2.70	9.10	15.90
Pb	2.90	1.70	3.20	1.60	3.00	1.60	3.30	1.60	1.10	2.00	3.60	5.70	5.60	1.10	2.80	4.30
Zn	16.00	5.00	4.00	4.00	4.00	8.00	3.00	3.00	4.00	2.00	56.00	44.00	56.00	6.00	67.00	5.00
La	1.30	8.90	3.10	1.00	0.90	1.30	5.10	4.50	2.20	2.90	5.50	13.20	5.00	2.40	2.60	1.50
Ce	1.60	8.60	3.20	1.00	1.10	1.20	5.60	2.40	2.10	3.20	8.30	19.00	6.40	3.00	2.90	3.20
Pr	0.12	0.84	0.30	0.10	0.08	0.29	0.47	0.22	0.20	0.46	0.84	1.72	0.74	0.30	0.34	0.60
Nd	0.40	3.10	1.00	—	0.50	—	1.20	1.10	0.80	0.60	2.60	6.20	2.50	1.10	1.30	2.60
Sm	—	0.40	0.20	—	—	—	—	0.10	0.10	—	0.80	0.90	0.70	0.30	0.30	1.20
Eu	—	0.19	0.17	—	0.08	—	0.22	0.09	0.14	0.08	0.21	0.22	0.23	0.15	0.13	0.44
Gd	0.08	0.34	0.27	0.08	—	0.06	0.25	0.14	—	—	0.82	0.98	0.75	0.41	0.21	1.78
Tb	0.03	0.08	0.03	0.03	—	0.03	0.03	0.08	0.03	0.03	0.17	0.14	0.11	0.05	0.05	0.38
Dy	—	0.20	0.11	—	—	—	—	—	—	—	0.96	0.70	0.52	0.19	—	1.58
Ho	—	—	—	—	—	—	—	—	—	—	0.21	0.09	0.08	0.06	—	0.26
Er	0.05	0.19	0.09	—	—	0.07	0.09	—	—	—	0.75	0.50	0.39	0.14	0.17	0.60
Tm	—	—	—	—	—	—	—	—	—	—	0.11	0.06	0.17	—	—	0.07
Yb	—	0.10	—	—	—	—	—	—	—	—	0.83	0.49	0.21	0.16	0.08	0.54
Lu	0.02	0.02	0.02	0.01	—	0.01	0.03	0.02	—	—	0.12	0.05	0.05	0.04	0.04	0.10
Eu/Eu*	—	1.54	2.25	—	—	—	—	2.34	—	—	0.79	0.72	0.97	1.31	1.51	0.92
ΣETR	3.60	22.96	8.49	2.22	2.66	2.96	12.99	8.65	5.57	7.27	22.22	44.25	17.85	8.30	8.12	14.85

* kutnahorite-bearing ore samples

	N5E least-altered jaspilites					N5E hematite hard ores						N5S least-altered jaspilites						
Drill core	**F284**	**F284**	**F284**	**F405**	**F405**	**F318**	**F318**	**F414**	**F414**	**F414**	**F439**	**F817**	**F817**	**F817**	**F817**	**F825**	**F836**	**F837**
Depth	**P27**	**P29.15**	**P36.9**	**P19**	**P24**	**P160.7**	**P172.7**	**P246.1**	**P252**	**P257**	**P249.8**	**P271.40**	**P296.60**	**P308.57**	**P361.90**	**P88.95**	**P156.25**	
SiO_2	43.93	41.57	40.54	36.72	43.80	2.76	0.20	0.17		3.62	4.23	41.49	41.43	37.99	47.79	51.30	46.97	57.04
Fe_2O_3	55.06	57.47	58.42	62.28	55.32	91.30	96.51	95.86		79.87	67.84	57.71	53.93	61.48	51.51	47.69	51.08	42.27
Al_2O_3	0.06	0.03	0.03	0.05	0.03	2.30	0.07	0.12		3.32	2.87	0.10	0.15	0.20	0.04	0.07	0.03	0.05
Ba	11.20	28.30	40.70	40.80	33.30	478.60	26.80	132.20	25.20	76.90	38.10	—	—	—	—	—	—	—
Co	43.80	31.60	23.70	19.50	23.60	19.50	5.50	30.90	30.50	15.20	8.20	—	—	—	—	—	—	—
Cs	0.10	0.30	0.30	0.20	0.30	—	—	—	—	—	—	—	—	—	—	—	—	—
Nb	—	—	—	—	—	0.70	3.90	—	—	1.10	—	—	—	—	—	—	—	—
Rb	0.80	1.70	2.20	1.40	1.30	0.60	—	—	—	0.50	—	—	—	—	—	—	—	—
Sr	3.70	1.90	3.30	3.50	3.10	3.50	3.40	1.50	4.90	2.80	12.80	—	—	—	—	—	—	—
Th	0.20	0.20	—	—	—	0.30	—	0.30	0.40	0.70	0.20	—	—	—	—	—	—	—
U	3.70	2.70	1.90	1.80	1.10	8.30	7.40	1.40	13.00	5.60	3.40	—	—	—	—	—	—	—
V	15.00	10.00	8.00	13.00	5.00	56.00	24.00	408.00	1926.00	1396.00	1250.00	—	—	—	—	—	—	—
Zr	1.20	1.10	1.30	1.00	0.90	2.50	1.30	2.00	0.90	7.80	2.30	—	—	—	—	—	—	—
Y	5.00	1.70	2.20	4.00	3.30	14.20	5.50	17.60	8.20	3.40	13.80	—	—	—	—	—	—	—
Cu	5.30	2.80	2.50	8.00	5.30	38.10	7.20	46.40	15.60	7.00	12.00	—	—	—	—	—	—	—
Pb	3.10	1.40	1.70	3.70	2.00	14.20	4.20	2.00	2.00	3.70	24.00	—	—	—	—	—	—	—
Zn	8.00	3.00	2.00	3.00	3.00	36.00	19.00	53.00	310.00	87.00	87.00	—	—	—	—	—	—	—
La	2.70	1.20	1.00	3.10	1.80	7.40	6.10	1.80	4.90	22.20	22.90	3.40	7.60	3.30	3.40	2.10	4.00	4.90
Ce	5.50	2.50	2.20	5.60	3.20	13.30	8.10	5.30	4.20	40.00	38.60	3.50	8.80	4.70	3.10	1.40	1.60	3.80
Pr	0.51	0.25	0.20	0.61	0.33	1.26	1.44	0.41	0.56	3.81	4.08	0.39	1.13	0.53	0.38	0.21	0.22	0.43
Nd	2.40	1.20	0.90	2.40	1.00	6.00	8.70	1.90	2.20	13.80	18.40	1.20	4.00	2.20	1.70	0.50	—	1.80
Sm	0.40	0.10	0.20	0.40	0.30	1.60	1.60	0.60	0.50	1.90	3.30	0.20	0.90	0.40	0.20	0.20	—	0.30
Eu	0.30	0.13	0.14	0.29	0.19	0.50	0.87	0.22	0.14	0.36	0.94	0.22	0.31	0.31	0.28	0.09	—	0.16
Gd	0.63	0.39	0.32	0.75	0.39	2.13	1.43	1.00	0.61	1.56	4.07	0.30	0.64	0.54	0.33	0.17	0.15	0.38
Tb	0.10	0.05	0.04	0.08	0.05	0.40	0.18	0.21	0.11	0.14	0.54	0.02	0.11	0.11	0.04	0.03	0.01	0.06
Dy	0.44	0.20	0.22	0.28	0.19	2.51	0.81	1.22	0.62	0.74	2.53	0.17	0.65	0.37	0.25	0.16	—	0.32
Ho	0.06	—	0.06	—	—	0.49	0.10	0.22	0.11	—	0.32	—	0.13	0.11	—	—	—	0.06
Er	0.17	0.10	0.08	0.15	0.13	1.61	0.48	0.79	0.36	0.23	0.94	0.11	0.30	0.21	0.10	0.07	—	0.10
Tm	—	—	—	—	—	0.21	0.08	0.09	0.06	—	0.11	—	—	—	—	—	—	—
Yb	—	—	—	0.08	0.06	1.47	0.32	0.71	0.31	0.77	0.68	0.11	0.28	0.16	—	—	0.06	—
Lu	0.02	0.01	—	0.02	—	0.18	0.06	0.11	0.04	0.03	0.11	0.01	0.03	0.02	0.01	0.01	0.01	0.01
Eu/Eu*	1.83	1.77	1.70	1.61	1.71	0.83	1.73	0.87	0.78	0.62	0.79							
ΣETR	13.23	6.13	4.46	13.76	7.64	39.06	30.27	14.58	14.72	85.54	97.52	9.63	24.88	12.96	9.79	4.94	6.05	12.32

	N1 hard ores					
Drill core	**F08**	**F08**	**F08**	**F14**	**F36**	**F36**
Depth	**P54.3**	**P66.1**	**P61**	**P197.2**	**P25.55**	**P28.6**
SiO_2	0.74	0.59	0.10	0.14	0.22	0.06
Fe_2O_3	97.89	97.54	98.84	98.74	99.57	88.93
Al_2O_3	0.31	0.10	0.11	0.14	0.39	0.49
Ba	3.40	—	4.10	1.00	5.80	3.80
Co	16.30	15.50	13.90	15.50	10.20	16.50
Cs	—	0.20	—	—	—	—
Nb	—	—	0.90	0.90	—	—
Rb	—	0.70	—	—	—	—
Sr	1.60	0.80	0.60	0.50	1.20	1.20
Th	0.30	0.20	1.00	0.90	0.50	0.30
U	0.20	—	0.70	0.30	0.50	0.50
V	21.00	10.00	16.00	13.00	27.00	31.00
Zr	1.60	0.90	—	—	0.90	6.00
Y	1.70	2.30	2.70	3.00	116.80	45.60
Cu	2.60	17.40	2.50	1.60	5.90	6.10
Pb	0.50	2.50	0.50	0.40	0.90	0.70
Zn	5.00	6.00	1.00	1.00	2.00	2.00
La	3.90	1.60	3.20	3.00	4.20	15.20
Ce	3.70	1.90	4.70	8.10	10.80	27.00
Pr	0.53	0.25	0.47	0.58	1.49	3.03
Nd	2.10	1.20	1.60	1.10	9.90	12.90
Sm	0.40	0.20	0.30	0.40	8.40	4.30
Eu	0.45	0.29	0.29	0.34	3.98	1.82
Gd	0.62	0.45	0.57	0.30	18.72	8.63
Tb	0.07	0.10	0.09	0.08	3.94	1.55
Dy	0.35	0.33	0.27	0.38	20.19	8.00
Ho	—	—	—	0.20	3.81	1.50
Er	0.11	0.16	0.20	0.22	9.14	3.45
Tm	0.07	—	—	—	1.12	0.44
Yb	0.06	—	0.05	0.06	6.40	2.59
Lu	0.03	0.04	0.02	0.02	0.94	0.33
Eu/Eu*	2.77	2.88	2.13	2.89	0.95	0.90
ΣETR	12.39	6.52	11.76	14.78	103.03	90.74

Appendix 3. Stable and radiogenic isotopes data.

Oxygen Isotopes	Carbon and Strontium Isotopes	Sulfur Isotope
Distal alteration zone (V1 vein-breccias) $\delta^{18}O_{V\text{-}SMOW}$ (Least-altered jaspilite) 6.6 to 15.2‰ (n=8) $\delta^{18}O_{V\text{-}SMOW}$ (mag) –0.4 to 4.3‰ (n=5) $\delta^{18}O_{V\text{-}SMOW}$ (calcite) 9.1 to 10.6‰ (n=6) $\delta^{18}O_{V\text{-}SMOW}$ (kutnahorite) 11.7 to 15.5‰ (n=3) $\delta^{18}O_{V\text{-}SMOW}$ (quartz) 10.1 to 13.1‰ (n=3) Intermediate alteration zone (V2-V3 veins) $\delta^{18}O_{V\text{-}SMOW}$ (quartz) 13.7 to 18.8‰ (n=12) Proximal alteration zone V4 vein-breccias $\delta^{18}O_{V\text{-}SMOW}$ (kutnahorite) 17.5 to 15.2‰ (21.8‰) (n=15) $\delta^{13}C_{PDB}$ (dolomite) 15.7 to 20.0‰ (n=5); Hematite-martite ore $\delta^{18}O_{V\text{-}SMOW}$ (martite) –5.9 to –3.9 ‰ (n=4) Hematite ore $\delta^{18}O_{V\text{-}SMOW}$ (MpHem) –7.1 to –2.7‰ (n=7) $\delta^{18}O_{V\text{-}SMOW}$ (AnHem) –8.5 to –4.9‰ (n=6) $\delta^{18}O_{V\text{-}SMOW}$ (TbHem) –9.5 to –5.9‰ (n=4) Intermediate alteration zone – Mafic wall rocks $\delta^{18}O_{V\text{-}SMOW}$ (calcite) 8.7 to 17.5‰ (n=6)	Distal alteration zone (V1 vein-breccias) $\delta^{13}C_{PDB}$ (calcite) –5.5 to –2.3‰ (n=6); $^{87}Sr/^{86}Sr$ = 0.7165 to 0.7460 (n=4) $\delta^{13}C_{PDB}$ (kutnahorite) –8.2 to –4.8‰ (n=3); $^{87}Sr/^{86}Sr$ = 0.7226 to 0.7247 (n=3) Proximal alteration zone (V4 vein-breccias) $\delta^{13}C_{PDB}$ (kutnahorite) –5.0 to –4.0‰ (n=15); $^{87}Sr/^{86}Sr$ = 0.7116 and 0.7137 $\delta^{13}C_{PDB}$ (dolomite) –5.1 to –3.4‰ (n=5); $^{87}Sr/^{86}Sr$ = 0.7158 Intermediate alteration zone – Mafic wall rocks $\delta^{13}C_{PDB}$ (calcite) –4.0 to 0.2‰ (n=6); $^{87}Sr/^{86}Sr$ = 0.7260 to 0.7145 (n=6)	Distal alteration zone V1 vein-breccias $\delta^{34}S$ (pyrite) 2.7 to 10.8‰ (n=11) Intermediate alteration zone – Mafic wall rocks (Zucchetti 2007) $\delta^{34}S$ (chalcopyrite) –4.3 to 5.7‰ (n=9) $\delta^{34}S$ (pyrite) –1.2 to 4.9‰ (n=8)

ANEXO 3

Laser-ablation ICP-MS analyses on oxides of hypogene iron ore from the giant Serra Norte jaspilite-hosted iron ore deposits, Carajás Mineral Province, Brazil

Resumo expandido publicado no 10th SGA meeting 2009

Laser-ablation ICP-MS analyses on oxides of hypogene iron ore from the giant Serra Norte jaspilite-hosted iron ore deposits, Carajás Mineral Province, Brazil

Rosaline Cristina Figueiredo e Silva, Lydia Maria Lobato

CPMTC-IGC, Universidade Federal de Minas Gerais, Av. Antônio Carlos, 6627, Campus Pampulha, 31270901, Belo Horizonte, Brazil; rosalinecris@yahoo.com.br

Steffen Hagemann

Center for Exploration Targeting, School of Earth and Environment, The University of Western Australia, Crawley, Western Australia 6009, Australia; shageman@cyllene.uwa.edu.au

Leonid Danyushevsky

ARC-Centre of Excellence in Ore Deposits, University of Tasmania, Private Bag 79, Hobart, Tasmania 7001, Australia; l.dan@utas.edu.au

Abstract. Laser ablation inductively coupled plasma mass spectrometry (LA ICP-MS) on different iron oxide species from the Serra Norte iron ore deposits in Carajás revealed a systematic variation of trace elements, mainly rare earth, from the early to late stage iron oxides: magnetite → martite → microplaty or -platy hematite → anhedral hematite → euhedral and/or tabular- hematite. The variation of trace element concentrations and REE patterns, such as decrease in Co and Ni from hydrothermally altered jaspilites to iron ores, and a general REE enrichment with near-horizontal HREE patterns in iron ores, suggest a hydrothermal fluid evolution from the earliest hydrothermal oxide magnetite to the latest tabular hematite.

Keywords. LA-ICP-MS, oxides, iron ore, Carajás

1 Introduction

The Carajás iron ore deposits located in the eastern part of the state of Pará in Brazil were discovered in 1967 and have produced in the last 5 years about 70 million tons of iron ore annually. The deposits are hosted by the Archean metavolcanic-sedimentary sequence of the Grão Pará Group. The protoliths to iron mineralization are jaspilites, under- and overlain by basalts, both metamorphosed to greenschist-facies. The basal contact of the high-grade iron ores is defined by a hydrothermally altered basaltic rock (chlorite-microplaty hematite). The major Serra Norte N1, N4E, N4W, N5E and N5S iron ore deposits are distributed along, and structurally controlled by, the northern flank of the Carajás fold.

Varying degrees of hydrothermal alteration have affected jaspilites to form iron ores (Figueiredo e Silva et al., 2008; Lobato et al., 2008). Variably altered jaspilites may be brecciated, containing a range of hematite types (e.g. microplaty and anhedral), and vein-associated quartz, carbonate and sulfide minerals. A hydrothermal paragenetic sequence for the oxides is established from the earliest (magnetite) to the latest (tabular hematite) oxide (Fig. 1).

Based on the widespread occurrence of relatively high salinity fluid inclusions (~20 to 30 eq. wt % $CaCl_2$), ranges of sulfur isotope ratios in sulfides (–0.7 to 3.0 ‰), and strontium isotopes in carbonates (0.7116 and 0.7247), and the high oxygen isotopes values in paragenetically early-stage oxides (0 to 4 ‰), when compared to later-stage low oxygen isotope ratios (-10 to -4 ‰), it is interpreted that magmatic fluids played an important role mainly during the early alteration stage. The existence of low-salinity inclusions and decrease in oxygen isotopic values of hematite suggest interaction with meteoric waters, which must have acted mainly during the late mineralization stage, with tabular hematite precipitation in veins (Figueiredo e Silva et al., 2008).

This contribution provides: (a) detailed petrography of oxide types and (b) investigation of the trace element concentrations based on preliminary results and interpretation on in situ laser ablation ICP-MS analyses on the different iron oxide species. These data are used to constrain the mineralogical and hydrothermal evolution at the Serra Norte iron ore deposits in Carajás.

2 Petrography of oxides

Detailed petrography, Scanning Electron Microprobe (SEM) analyses and images of iron oxides from hydrothermally altered jaspilites and hard iron ores were used to establish the following paragenesis (Fig. 1) for the iron oxides (cf. Figueiredo e Silva et al., 2008), from the early to the late alteration and mineralization stages: microcrystalline hematite; magnetite – kenomagnetite; martite; microplaty-platy hematite; anhedral hematite; and euhedral and/or tabular- hematite.

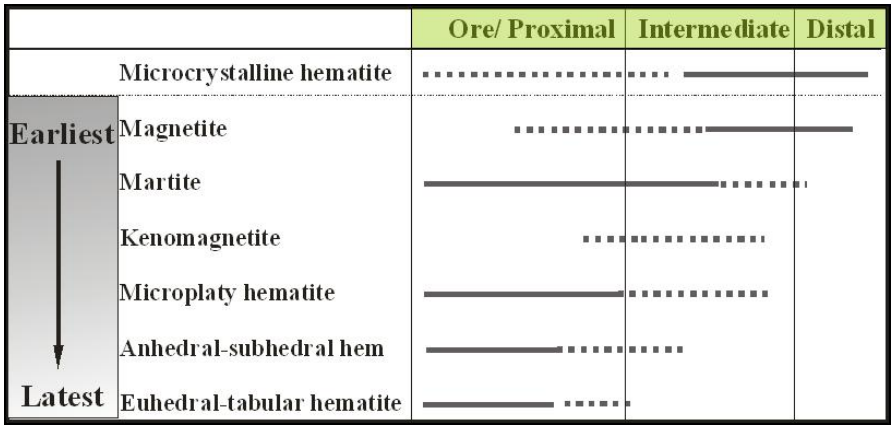

Figure 1. Paragenetic sequence of oxides from the earliest magnetite to the latest euhedral-tabular hematite.

Microcrystalline hematite is represented by very fine-grained crystals (<0.004 mm), typical of the jaspilite bands, as the original iron oxide. In incipiently altered jaspilites (early alteration stage), microcrystalline hematite is overgrown by magnetite crystals (Fig. 2a), but it is maintained even in the more advanced alteration stages (Fig. 2b). Magnetite is also associated with carbonate-sulfide veins-breccias. Martitisation follows, with an intermediate phase confirmed by the presence of kenomagnetite. Martitic magnetite crystals (Fig. 2b) vary from 100 to 300 μm. Their original shape is destroyed by progressive martite development, resulting in abundant agglomerates of anhedral hematite (Fig. 2c) with crystals of about 20 μm in diameter and lobate borders. Microplaty hematite has commonly diamond sections of *ca.* 4-8 μm length and, where coarser (platy), from 100 to 400 μm (Fig. 2d). Space opening enhanced by quartz-jasper dissolution lead to very porous, locally brecciated rocks, which is also indicated by the precipitation of platy hematite in the open spaces or vugs. Fine- to medium-grained, euhedral and bladed tabular hematite, some 200 to 300 μm and locally up to 500 μm, form internal selvages to discordant and banding-parallel milli- to centimetric veins in iron ores (advanced alteration stage). It is commonly comb textured, exhibits growth lines, and partially cements open spaces or vugs.

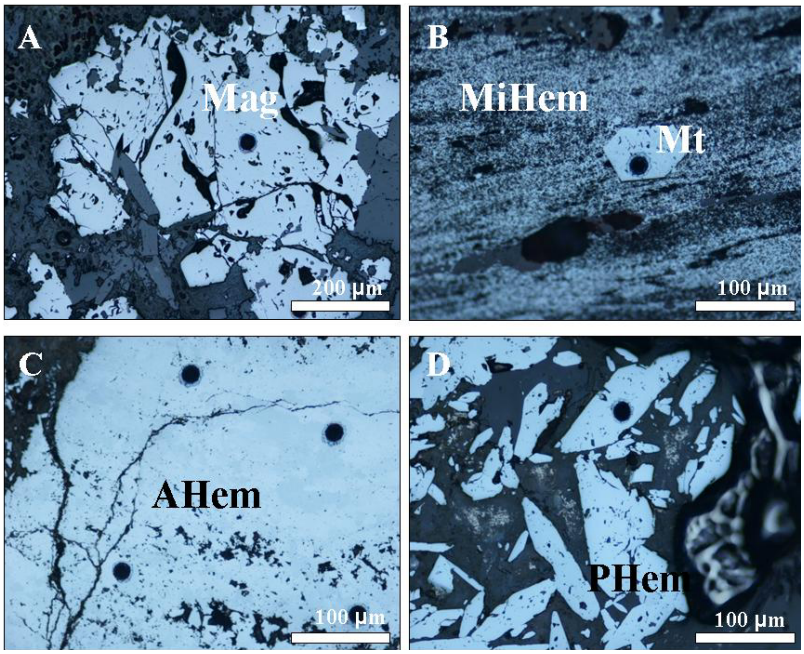

Figure 2. Photomicrographs showing iron oxide types (with analyzed laser spots): A. magnetite (Mag); B. martite (Mt) overgrown original microcrystalline hematite (MiHem); C. anhedral hematite (AHem); and D. platy hematite (PHem).

3 Laser-ablation ICP-MS analyses on oxides

3.1 Methods

Detailed SEM images on oxide minerals were produced to identify zoning and inclusions of minerals such as monazite and xenotine, prior to in situ laser ICP-MS analyses. The latter was performed at the ARC- Centre of Excellence in Ore Deposits, University of Tasmania, using a New Wave UP-213 Nd:YAG Q-switched Laser Ablation System coupled to a Agilent HP4500 Quadrapole ICP-MS. Samples were ablated in an ultra-high purity He atmosphere, later mixed with Ar to aid the transport of ablated material, before flowing into the ICP-MS. The standard STDGL2b-2 was used for oxide analyses (Danyushevsky et al. 2004). The LA ICP-MS analyses were obtained with different spot sizes varying (8 to 110 µm), depending on the size of the crystal. Most analyses were run for a total of 100 seconds, which includes an initial 30 seconds of analysing the gas background before commencing sample ablation. Detection limits vary for each element and analyzed spot. In the case of REE analyses, detection limit values vary from 0.03 to 0.59 ppm.

3.2 Results

Based on the paragenetic sequence established, 25 iron oxides samples were selected from hydrothermally altered jaspilites and mafic wallrocks, and iron ores, including magnetite and various hematite types (Fig. 1). Trace elements Ti, V, Mn, Co, Ni, Cu, As, Sr, Y, Zr, Nb, Mo, Ba, W, Au, Pb, Th, and U, including REE La, Ce, Nd, Sm, Eu, Gd, Dy, Er, Yb, and Lu, abundances were determined. Selected trace elements (Co, Ni, Cu, Zn, and Pb) and REE concentrations are shown in Figs. 3 and 4.

Hydrothermal magnetite crystals from the early alteration stage contain Co and Ni > 100 ppm each, Zn between 23 and 70 ppm, and Cu and Pb below 10 ppm (Fig. 3A). Cobald and Ni are substantially higher when compared to other hematite types, whereas Zn and Pb are relatively similar to martite (Fig. 3B). Microplaty hematite crystals exhibit Co, Zn and Pb content of up to 40 ppm and the highest contents of Cu (up to 65 ppm) and Ni (up to 33 ppm), when compared to other hematite types (Fig. 3c). Anhedral and tabular hematite (Figs. 3 D and E) have similar concentrations of selected trace elements, excepted Zn, which is higher (up to 64 ppm) in the former.

Magnetite crystals show the lowest REE abundance and concentrations (up to 3.8 ppm), followed by martite (up to 9.2 ppm) (Figs. 4A and B), and both display a significantly increased LREE pattern when compared to LREE pattern of the other oxides (Figs. 4C-F). Anhedral, platy and tabular hematite crystals present different REE patterns (ΣREE contents vary from 4 to 40 ppm), which are characterized by a small increase in HREE resulting in a flat pattern, when compared to paragentically earlier magnetite-martite oxides. Platy hematite and martite from hydrothermally altered (chlorite-hematite) mafic wallrocks have the highest total REE contents (Fig. 4E). It is also noticed that the late-stage euhedral-tabular hematite has a more regular REE distribution pattern (Fig. 4F).

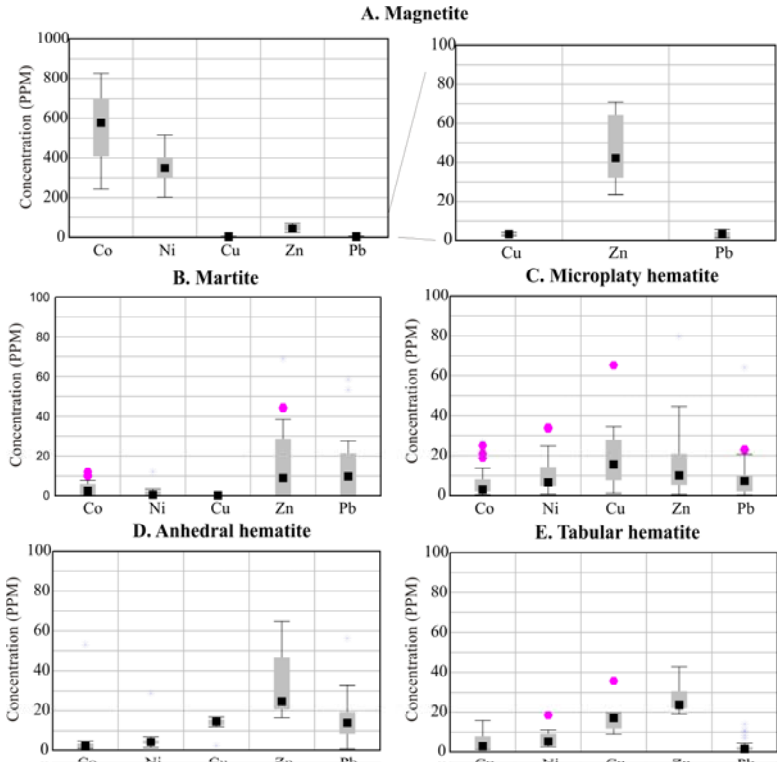

Figure 3. Box diagrams showing concentrations (ppm) of selected trace elements (Co, Ni, Cu, Zn and Pb) obtained in crystals from: A. magnetite; B. martite; C. microplaty hematite; D. anhedral hematite; and E. tabular hematite. Pink dots correspond to outliers; black dots to mean values; gray area to mean values ± standard deviation; and black lines mean values ± 1.5 standard deviation.

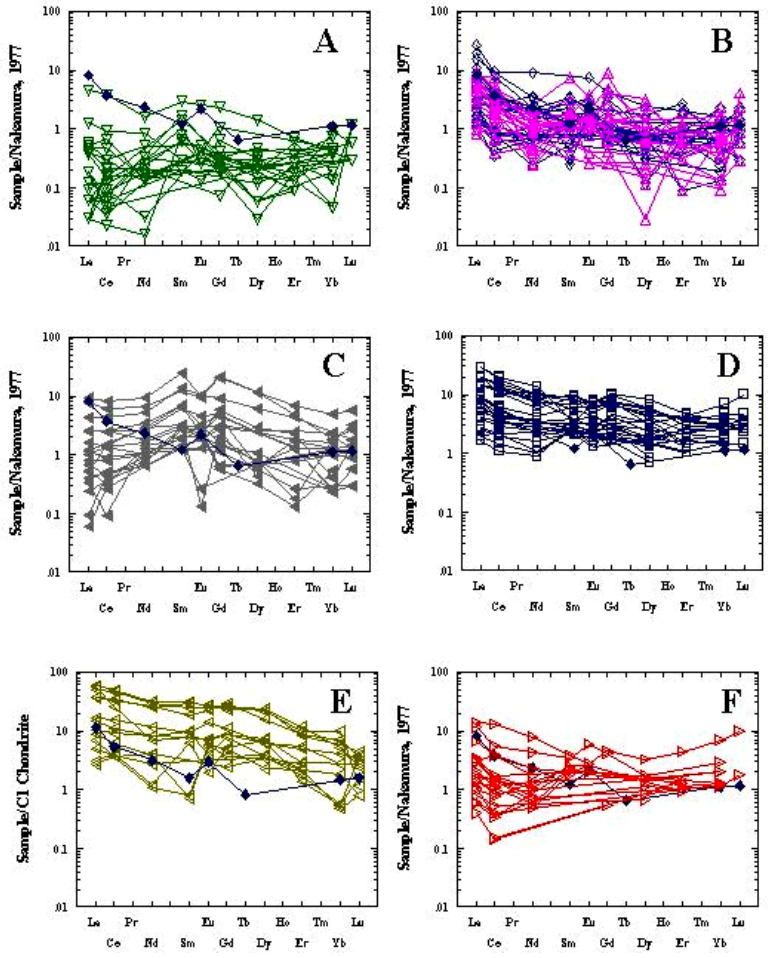

Figure 4. Distribution of REE, normalized against chondrite (Nakamura 1974), in crystals from: A. magnetite; B. martite; C. martite and microplaty hematite; D. anhedral hematite; E. platy hematite and martite from hydrothermally altered (chlorite-hematite) mafic wallrock; and F. tabular hematite.

4 Discussion and Conclusions

In situ laser ICP-MS analyses of trace elements in various oxides from the Serra Norte iron ore deposits revealed two important aspects that needs further discussion: (i) the relative increase of REE and change of their patterns from paragenetically early oxides–magnetite/martite to late oxides–platy, anhedral and tabular hematite, and (ii) the decrease of Co and Ni contents from magnetite to different hematite types.

To (i): The small increase in HREE of the late stage anhedral, platy and tabular hematite types when compared to earlier magnetite-martite, results in a relatively flat REE pattern. The advance of martitization, forming anhedral hematite, and also precipitation of platy and tabular hematites, may have favoured the relative increase of HREE in the residual fluid. The increase in REE in the late-stage oxides also indicates a switch in the fluid composition, mainly favored by fixation of HREE. This general REE enrichment with near-horizontal HREE patterns has also been documented for

iron ores from the Mt. Tom Price deposit in Western Australia, also containing anhedral and microplaty hematite (Lobato et al., 2007).

To (ii) The decrease in the magmatic elements Co and Ni may reflect increased fluid-rock reactions from magmatic fluids dominant early in the evolution of the hydrothermal system to meteoric waters dominant in the later stages (c.f., Figueiredo e Silva et al., 2008). However, the possibility of partial incorporation of these elements from the mafic wallrocks can not be excluded.

The results of this study are compatible with previous whole-rock REE analyses of iron ores (Figueiredo e Silva et al., 2008) and strongly support a magmatic fluid component principally during the early hydrothermal mineralization stage of the upgrade from jaspilite BIF to high-grade iron ore.

Acknowledgements

We wish to thank Vale for logistical, technical and finantial support, UFMG, UWA and, UTAS, especially Sarah Gilbert for the support during data acquisition. We greatly acknowledge the Grants received from the CNPq and scholarships from CAPES.

References

Danyushevsky L., Robinson P., McGoldrick P., Large R. and Gilbert S., (2004) Quantitative multi-element analysis of sulphide minerals by laser ablation ICPMS, 17th AGC, Hobart, p. 260.

Figueiredo e Silva, R.C., Lobato, L.M., Rosière, C.A., Hagemann, S., Zucchetti, M., Baars, F.J., Morais, R., and Andrade, I., (2008) Hydrothermal origin for the jaspilite-hosted, giant Serra Norte iron ore deposits in the Carajás mineral province, Para State, Brazil, *in* Hagemann, S.G., Rosière, C.A., Gutzmer, J., and Beukes, N.J. (eds.), BIF-Related High-Grade Iron Mineralization: Reviews in Economic Geology, v. 15, p. 255-290.

Figueiredo e Silva R.C., (2009) Evolução e gênese do minério de ferro hidrotermal nos depósitos da Serra Norte, Província Mineral Carajás, PhD. Thesis, Universidade Federal de Minas Gerais, Departamento de Geologia, Belo Horizonte, Brazil, 256 p.

Lobato, L.M., Figueiredo e Silva, R.C., Hagemann, S., Thorne, W., and Zucchetti, M., (2008) Hypogene Alteration Associated with High-Grade BIF-related Iron Ore, *in* Hagemann, S.G., Rosière, C.A., Gutzmer, J., and Beukes, N.J. (eds.), BIF-Related High-Grade Iron Mineralization: Reviews in Economic Geology, v. 15, p. 107-128.

Lobato, L.M., Figueiredo e Silva, R.C., Hagemann, S., and Thorne, W., (2007) Mineralizing fluid evolution and REE patterns for the hydrothermal Carajás iron ores, Brazil, and for selected

Hamersley iron deposits, Australia [ext. abs.]: Biennial Meeting of the Society for Geology Applied to Mineral Deposits 9. Proceedings, SGA, Dublin, v. 2, p. 1227-1230.

Nakamura, N., (1974) Determination of REE, Ba, Fe, Mg, Na and K in carbonaceous and ordinary chondrites: Geochimica Cosmochimica Acta, v. 38, p. 757-775.

ANEXO 4

Hypogene Alteration Associated with High-Grade BIF-related Iron Ore

Separata do artigo publicado na Reviews of Economic Geology em Junho de 2008

SEG Reviews vol. 15, p. 107–128

Chapter 4

Hypogene Alteration Associated with High-Grade Banded Iron Formation-Related Iron Ore

Lydia Maria Lobato,† Rosaline Cristina Figueiredo e Silva,

Universidade Federal de Minas Gerais, Centro de Pesquisas Prof. Manoel Teixeira da Costa-Instituto de Geociências. Av. Antônio Carlos 6627, Campus Pampulha, Belo Horizonte, MG, 31270.901, Brazil

Steffen Hagemann, Warren Thorne,

Centre for Exploration Targeting, School of Earth and Geographical Sciences, University of Western Australia, 35 Stirling Highway, Crawley, WA 6009, Australia

and Márcia Zucchetti

Companhia de Pesquisas e Recursos Minerais-CPRM, Serviço Geológico do Brasil, Av. Brasil 1731, Funcionários, Belo Horizonte, MG 30140.002, Brasil

Abstract

Hydrothermal alteration in structurally controlled, high-grade banded iron formation (BIF)-related iron deposits at Carajás (Brazil), Hamersley (Australia), and Thabazimbi and the Zeekoebaart prospect (South Africa) exhibit significant similarities and differences in geologic setting and hypogene alteration. In Carajás, Paleoproterozoic hematite deposits are hosted in low-metamorphic grade Archean jaspilites that are encased in metabasalts. The Paleoproterozoic BIF-hosted deposits of the Hamersley district, the Thabazimbi deposit, and the Zeekoebaart prospect are surrounded by shales.

At Carajás, the hydrothermal alteration of jaspilites is characterized by a distal alteration zone with magnetite-calcite-quartz-pyrite where the primary microcrystalline hematite → magnetite (±kenomagnetite). The intermediate alteration zone consists of martite-microplaty hematite-quartz with magnetite → martite, whereas the proximal alteration zone contains hematite ± carbonate ± quartz with martite → microlamellar hematite → anhedral hematite → euhedral-tabular hematite. The proximal alteration zone represents the high-grade ore (i.e., porous hard to soft and hard ores). Hydrothermal alteration also affected mafic wall rocks with chlorite-quartz-carbonate ± hematite in distal alteration zones, and chlorite-hematite-quartz-albite-mica-carbonate ± titanite ± magnetite ± sulfides and hematite-chlorite-quartz-albite-mica-carbonate ± titanite ± magnetite ± sulfides in intermediate and proximal alteration zones, respectively.

At the Mount Tom Price deposit in the Hamersley district, three spatially and compositionally distinct hydrothermal alteration zones are distinguishable: (1) distal magnetite-siderite-iron silicate, where the shape of the magnetite is suggestive of it being pseudomorphous after preexisting minerals, likely siderite; (2) intermediate hematite-ankerite-magnetite, with euhedral and bladed magnetite showing minor replacement by martite along crystal boundaries and replacement of iron-silicates by anhedral and microplaty hematite; and (3) proximal martite-microplaty hematite zones, where carbonate is removed. Martite and anhedral hematite replace magnetite and iron silicates of the intermediate alteration assemblage, respectively.

The Thabazimbi deposit and the Zeekoebaart prospect lack unequivocal evidence for the formation of paragenetically early hydrothermal magnetite. Chert in ore zones has been replaced by microplaty hematite or has been leached, giving rise to porosity. Veins contain coarse tabular hematite and coarse crystalline quartz. High-grade hematite-martite orebodies are the result of SiO_2 leaching and associated volume loss that created widespread brecciation of the high-grade hematite ore. In addition to high-grade hematite-martite ores, four mineralogically distinct types of iron ore have been recognized: (1) goethite-rich, (2) low-grade dolomite-hematite, (3) low-grade calcite-hematite, and (4) talc-hematite.

The comparison of hydrothermal alteration characteristics in the three case study areas revealed: (1) a similar paragenetic sequence of iron oxides, marked by an abundance of open-space filling and replacement textures; (2) distinct lack of a penetrative fabric in alteration lithologic units and high-grade ores; and (3) the importance of porosity and brecciation to accommodate volume loss. Differences include: (1) the formation of carbonate in different hydrothermal alteration zones of each deposit; (2) the presence of stilpnomelane in BIF that is surrounded by shales and hosted in sedimentary basins but absence in BIF that is bounded by mafic rocks; (3) the presence of significant amount of siderite in distal alteration zone in the Hamersley deposits but absence in the Carajás and Thabazimbi deposits; (4) the presence of significant amount of sulfides in the Carajás deposits but absence in the Hamersley and Thabazimbi deposits; and (5) significant amounts of chlorite, talc, white mica, and albite in basalt-hosted iron ore deposits (e.g., Carajás) or mafic dikes that are spatially and temporally associated with iron mineralization (e.g., in the Hamersley province).

† Corresponding author: e-mail, lobato@netuno.lcc.ufmg.br

The systematic documentation of hydrothermal-alteration minerals and assemblages has significant implications for the exploration of concealed high-grade iron orebodies, because key hydrothermal alteration minerals such as chlorite, talc, carbonates or iron silicates are an expression of the hydrothermal footprint of the BIF iron-ore mineral system and, therefore, can be used as mineral vectors.

Introduction

THIS CONTRIBUTION aims to critically review the effects of hydrothermal alteration on BIF host rock and associated wall-rock lithologic units in the Carajás (Brazil), Hamersley (Australia), Thabazimbi, and Zeekoebaart (South Africa) areas. The study of the hydrothermal alteration has provided important insights into the nature of hydrothermal fluids and the formation of hydrothermal ore deposits (i.e., Reed, 1997). Recent studies have revealed the presence of hydrothermal alteration zones associated with and surrounding high-grade BIF-hosted iron ore deposits of the Carajás district (Figueiredo e Silva et al., 2008), the Hamersley district (Thorne et al., 2008), the Thabazimbi deposit (Netshiozwi, 2002), and the Zeekoebaart prospect (Harding, 2004). Although the effects of hydrothermal alteration may be recorded by BIF, they are often more prominent in associated lithologic units such as volcanic rocks (Lobato et al., 2005b) or sills and dikes (Dalstra and Guedes, 2004). The scarcity of studies of the hydrothermal alteration associated with most high-grade BIF-hosted iron deposits can be attributed to the difficulty of recognizing it through the effects of intense supergene weathering (i.e., Beukes et al., 2003).

This contribution describes and compares the effects of hydrothermal alteration on BIF and associated wall-rock lithologic units in the Carajás and Hamersley districts, Thabazimbi deposit, and Zeekoebaart prospect. The parageneses and textures of hydrothermal alteration zones, veins and breccias related to hydrothermal alteration, and lateral and vertical transitions of the alteration zones are described for these districts and/or deposits. Finally, implications for exploration are provided and questions for further research are discussed.

Hydrothermal Alteration in BIF-Hosted Iron Deposits

High-grade iron orebodies are almost monomineralic and composed essentially of hematite (and martite-textured hematite), with minor magnetite, goethite, quartz, and trace amounts of apatite (Taylor et al., 2001). In most mining districts, high-grade orebodies are in sharp contact with oxidized BIF that consists of subequal amounts of hematite and quartz. This oxidized BIF has been categorized as altered in only a few districts where it has been traced laterally into unaltered BIF host rock (Barley et al., 1999; Thorne et al., 2004).

We have attempted to delineate zones of hydrothermal alteration with distinct textures and/or mineral associations and apply the terms distal, intermediate, and proximal to indicate their position relative to high-grade iron orebodies. In general, distal alteration is weaker and proximal is stronger.

Iron oxides change in form through the mineralogical sequence and hydrothermal alteration zones from diagenetic microcrystalline or dusty hematite, locally followed by hydrothermal magnetite (Mag) in distal alteration zones. Magnetite may be replaced by martite (Mt) exhibiting kenomagnetite (KMag) nuclei and finally hematite, both characterizing the intermediate zones. Hematite types are classified according to their morphology into microplaty (MpHem), platy, euhedral to anhedral, patchy (similar to anhedral), bladed, and tabular (see Fig. 1), which are typical of the proximal alteration zones.

Carajás Iron District, Brazil

Regional geologic setting

The Carajás mineral province is in an Archean through Paleoproterozoic portion of the Amazon craton. The Carajás mineral province is dominated by metavolcano-sedimentary rocks and granitoids, formed from 2.76 to 2.68 Ga, and also includes the Meso-Archean igneous and metamorphic Pium and Xingu Complexes (Santos, 2003).

The Carajás mineral province is host to a wealth of mineral deposits (Figueiredo e Silva et al., 2008), which are associated with a range of metavolcano-sedimentary rocks that overlie

FIG. 1. Photomicrographs of polished thin sections, all in reflected light except (A) which is transmitted light and (K) which is an SEM photograph. A. Reddish jasper bands in poorly altered jaspilite, rich in microcrystalline (or dusty) hematite and martite streaks, Carajás, N4W deposit. B. Brecciated magnetite microband with matrix of siderite and iron silicates, Mount Tom Price deposit. C. Radial and individual bladed magnetite, with kenomagnetite nuclei that is partially oxidized to microplaty hematite within siderite matrix, Mount Tom Price deposit. D. Magnetite band in contact with a band of microcrystalline (or dusty) hematite in poorly altered jaspilite, with magnetite forming at the expense of microcrystalline hematite, Carajás N4E deposit. E. Martite "blasts" within microcrystalline hematite, exhibiting kenomagnetite centers and that are surrounded by voids, Carajás N4W deposit. F. Incipient oxidation illustrated by kenomagnetite occurring next to hematite pseudomorph after grunerite in quartz (QTZ) matrix, oxidized Penge Iron Formation, Thabazimbi deposit. G. Aggregate of microplaty hematite in high-grade ore, Mount Tom Price deposit. H. Aggregate of microplaty hematite surrounded by microcrystalline hematite, high-grade ore, Carajás N1 deposit. I. Goethite replacing chert, as fine-grained aggregates in laminated hematite ore, Zeekoebaart deposit. J. Dissolution collapse effect shown by coarse-grained hematite in chert microbands, hematitized iron formation of the Zeekoebaart deposit. K. Homogeneous microplaty hematite (MpHem) laths in voids. Scanning electron microscope (EDS), Mount Whaleback deposit shaley ore. L. Typical appearance of patchy hematite with lobate grain boundaries (crossed nicols and oil immersion); massive high-grade hematite ore, Thabazimbi deposit. M. Anhedral hematite crystals displaying growth lines, Carajás, N5E deposit. N. Comb-textured, tabular hematite veinlets filling pores in brecciated portions of high-grade hard ore, which contains banded fragments of relict microcrystalline hematite, Carajás, N5E deposit. O. Tabular hematite veinlets filling pores in brecciated portions of high-grade hard ore, which contains banded fragments of relict microcrystalline hematite, Carajás, N5E deposit (all photos taken from Netshiozwi, 2002; Harding, 2004; Figueiredo e Silva, 2004; Thorne et al., 2004; Webb et al., 2004). Mineral abbreviations: AHem = anhedral hematite, FeSil = iron silicate, Gt = goethite, Hem = hematite, KMag = kenomagnetite, Mag = magnetite, MiHem = microcrystalline hematite, MpHem = microplaty hematite, Mt = martite, Sd = siderite, THem = tabular hematite.

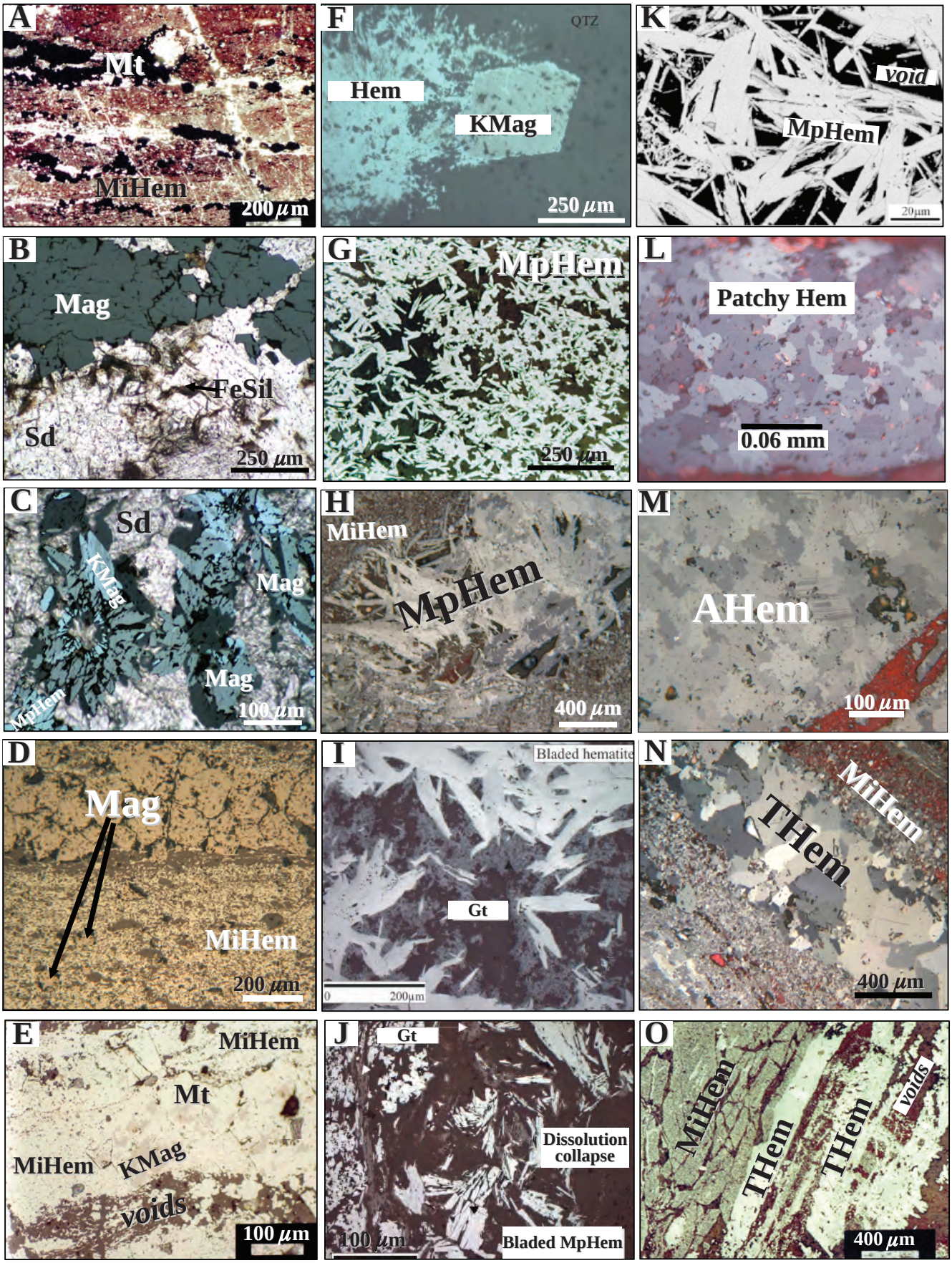
A
Mt
MiHem
200 μm
F
QTZ
Hem
KMag
250 μm
K
void
MpHem
20μm
B
Mag
FeSil
Sd
250 μm
G
MpHem
250 μm
L
Patchy Hem
0.06 mm
C
Sd
KMag
Mag
Mag
MpHem
100 μm
H
MiHem
MpHem
400 μm
M
AHem
100 μm
D
Mag
MiHem
200 μm
I
Bladed hematite
Gt
0
200μm
N
MiHem
THem
400 μm
E
MiHem
Mt
MiHem
KMag
voids
100 μm
J
Gt
Dissolution collapse
100 μm
Bladed MpHem
O
MiHem
THem
THem
voids
400 μm

what is considered as the tonalite-trondhjemite-granodiorite basement terranes of the Xingu Complex (ca. 2.86 Ga; Silva et al., 1974; Tassinari et al., 2000). The Carajás metavolcano-sedimentary and metasedimentary units belong to the Itacaiúnas Supergroup (DOCEGEO, 1988), formally subdivided into the Grão Pará, Igarapé Salobo, and Igarapé Pojuca Groups, although a better stratigraphic definition is still required (Figueiredo e Silva et al., 2008). Geochronological data indicate two main volcano-sedimentary periods, at 2.76 Ga and 2.75 to 2.73 Ga (Machado et al., 1991; Galarza et al., 2001). Jaspilites (plus the iron ores) of the Carajás Formation and their surrounding mafic volcanic rocks (Beisiegel, 1982) are part of the Grão Pará Group dated at 2740 ± 8 Ma by Trendall et al. (1998). The volcano-sedimentary rocks are covered by sedimentary psammo-pelitic rocks (e.g., arenites, calcarenites, siltites, and conglomerates) of the Águas Claras Formation (fig. 1 of Figueiredo et al., 2008), which yielded zircon U-Pb ages of 2708 ± 37 Ma (Mougeot, 1996) and 2645 ± 12 Ma (Dias et al., 1996).

Archean syntectonic, calc-alkaline intrusions include the Estrela (2763 ± 7 Ma; Barros et al., 2001) and Planalto Granite massifs. Examples (see Santos, 2003) of Paleoproterozoic (1.88 Ga) A-type intrusions are the Velho Guilherme (Silva et al., 1974) and the Serra dos Carajás batholiths (1.88 Ga; Gibbs et al., 1986). These are the subject of discussion by Dall'Agnol et al. (2005) and Dall'Agnol and de Oliveira (2007).

A recent summary of the structural framework of the Carajás area is provided by Rosière et al. (2006). The authors proposed that the dominant structure is a flattened flexural fold system intersected by several strike-slip faults subparallel to the axial plane of the fold system (fig. 1 of Figueiredo e Silva et al., 2008). Further details of the geology of the Carajás mineral province are presented by Figueiredo e Silva et al. (2008).

Hydrothermal alteration zones

Hydrothermal alteration associated with the transformation of jaspilite to high-grade iron ore affected jaspilites to varying degrees and at different times during the evolution of the iron deposits (Table 1A; Guedes et al., 2002; Figueiredo e Silva, 2004; Figueiredo e Silva et al., 2004, 2007, 2008; Lobato et al., 2004, 2005a, b, 2007; fig. 7 of Figueiredo e Silva et al., 2008). The mineralogical sequence for iron oxides in the distal hydrothermal alteration zone is microcrystalline hematite → magnetite (kenomagnetite; Fig. 1A, D, E). The intermediate alteration zone is characterized by widespread martitization, and the proximal alteration zone has martite → microlamelar hematite → anhedral hematite → euhedral-tabular hematite (Fig. 1H, M-O; fig. 7 of Figueiredo e Silva et al., 2008). Microcrystalline hematite (<4 μm; Fig. 1A) is typical of the jasper layers in nonmineralized jaspilites. It represents the original iron oxide and is stable even in the more advanced alteration stages in desilicified, banded ore-breccia fragments.

Distal and intermediate alteration zones (Figs. 2, 3; Tables 1A, 2) are characteristic of variously altered jaspilites, whereas the proximal alteration zone represents the ore zone (high-grade porous hard to soft and hard ores). The distal zone is up to 80 m wide in the N4E deposit, whereas the intermediate alteration zone is about 100 m wide (e.g., the N5S

TABLE 1. Characteristic Hydrothermal Alteration Assemblages in Distal, Intermediate, and Proximal Alteration Zones for Selected Iron Deposits in the Carajás and Hamersley Iron Districts in Brazil and Australia, Respectively, Thabazimbi Deposit and Zeekoebaart Prospect in South Africa[1]

A	Carajás	Hamersley, Tom Price		South Africa	
Alteration zones	Serra Norte deposits (in jaspilite)	North deposit	Southern Ridge deposit	Thabazimbi deposit	Zeekoebaart prospect
BIF	Jasper-MiHem	Mag-Chert-Sd/Fe Dol-Stp-Py	Qtz-Mag-Stp-Dol	Chert/Micro Qtz-Mag-Stp-Carb-Gru	Hem-Mag-Sd(Ank)-Chert-Stp
Distal	Mag-Carb-Qtz-Py(Ccp)	Mag-Sd-FeSil (Py-Ap-Qtz)	Mag-Sd-Stp	KMag-Mt-Platy Hem ± Red Chert-THem	Hem(KMag)-Chert-Mega Qtz-
Intermediate	Mt-MpHem-Qtz(Sulf-Mag)	Hem-Ank-Mag(Ap-Py)	Hem-Mag-Tlc-Chl	_____	_____
Proximal and/or high-grade ore	Hem[2]-Carb-Qtz-(Sulf-Mag)	Mt-MpHem-Ap	Mt-MpHem-Ap	Hem[3]-Carb	Patchy Hem-MpHem±Mt

B	Carajás Serra Norte deposits (in mafic wall rock)	
Prealteration	Alteration zones	
Ol-Aug-Pl-Ilm-Sulf	Distal	Chl-Qtz-Carb(Hem) (±Ol-Aug-Pl-Ilm)
	Intermediate	Chl-Hem-Qtz-Ab-Mica-Carb(Ttn-Mag-Sulf)
	Proximal	Hem-Chl-Qtz-Ab-Mica-Carb(Ttn-Mag-Sulf)

[1] Adapted from data by Thorne (2001), Netshiozwi (2002), Harding (2004), Lobato et al. (2005b), Thorne et al. (2007), Zucchetti, 2007; Figueiredo e Silva et al. (2008); minerals in parentheses represent minor phases

[2] These include martite, anhedral, tabular, microplaty, and microcrystalline hematite

[3] These include martite, patchy, microplaty, anhedral, and tabular hematite

Mineral abbreviations: Ab = albite, Ank = ankerite, Ap = apatite, Aug = augite, Carb = carbonate, Ccp = chalcopyrite, Chl = chlorite, Dol = dolomite, FeSil = iron silicate, Gru = grunerite, Ilm = ilmenite, KMag = kenomagnetite, Mag = magnetite, MiHem = microcrystalline hematite, MpHem = microplaty hematite, Mt = martite, Ol = olivine, Pl = plagioclase, Py = pyrite, Qtz = quartz, Sd = siderite, Stp = stilpnomelane, Sulf = sulfide, THem = tabular hematite, Tlc = talc, Ttn = titanite

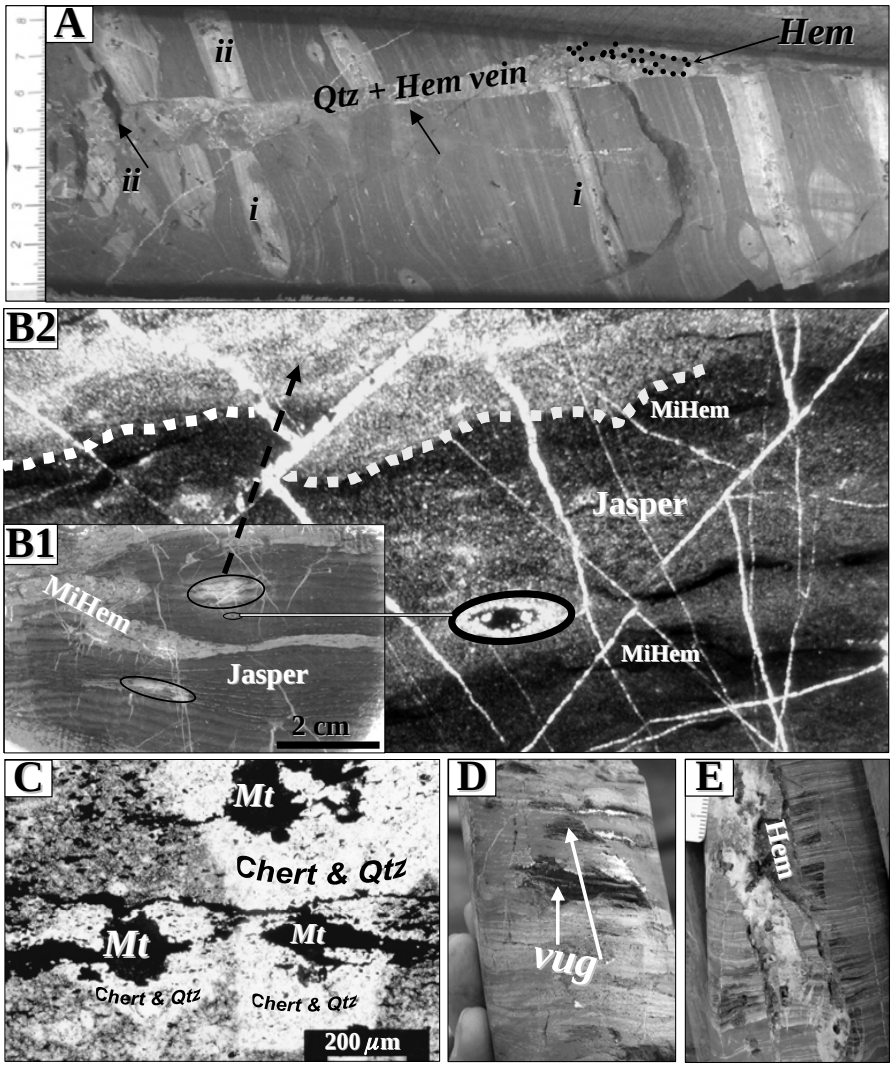

FIG. 2. Carajás iron deposits, Brazil. A. Core sample of quartz-hematite veins within incipiently hydrothermally altered banded jaspilite from the N5S deposit. Note the light-colored streaks, parallel to banding, *(i)* which emerged due to quartz and hematite (dashed lines) veins. These have white nuclei composed of fine-grained quartz that are invariably vuggy, and their contacts with jaspilite are darker and devoid of vugs *(ii)*. B1. Scanned surface of a thin section of a least altered, intensely veined jaspilite sample, showing light-colored patches (highlighted) associated with both microcrystalline hematite and jasper bands. The patches are located in regions of crosscutting veinlets. B2. Photomicrograph of B1 showing (arrows) the two patches marked on B1, highlighted by dashed and continuous lines, where most of the jasper is transformed to recrystallized quartz and microcrystalline hematite is lost (polished thin section, natural transmitted light; N5S deposit). C. Jasper bands with overgrown martitic magnetite (after microcrystalline hematite), displaying halos of clear, hematite-free or -poor chert and quartz, with quartz having formed due to chert recrystallization (polished thin section, natural transmitted light; N4W deposit). D. and E. Core samples of quartz-hematite veins, banded jaspilite that are considerably vuggier than sample (A). Note that vugs are concordant to banding and are rooted in veins (N5S deposit). Mineral abbreviations: Qtz = quartz, Hem = hematite, MiHem = microcrystalline hematite, Mt = martite.

deposit). The proximal alteration zone includes the porous hard to soft ore and the hard, massive ore itself (the latter is about 20 to 50 m in width). Their mineralogical composition and general characteristics are depicted in Tables 1 and 2.

Distal alteration zone—magnetite-calcite-quartz-pyrite: The distal alteration zone (Tables 1A, 2A; Fig. 3) contains microcrystalline hematite, which is overgrown by magnetite (± martite) "blasts" (Fig. 1A). Magnetite-rich jaspilite ores (Fig. 1D) are present in the N5S deposit. Jasper bands may display discoloration resulting in clear halos of recrystallized chert or fine-grained, clear granoblastic quartz (Fig. 2A-C) that surrounds martite (Fig. 2C). The halos may represent leaching of iron from jasper due to chert that recrystallized into quartz.

Sulfide minerals, mainly pyrite and chalcopyrite, may be located in vein breccias in association with carbonate minerals, viz. calcite (Figueiredo e Silva et al., 2008), and magnetite and quartz that are discordant to layering in the jaspilite. Pyrite-magnetite assemblage locally overgrows microcrystalline hematite-rich jaspilite layers; monomineralic pyrite veins are also observed.

Jasper recrystallization to quartz is associated with the formation of abundant quartz veins and veinlets (fig. 9, table 3 of

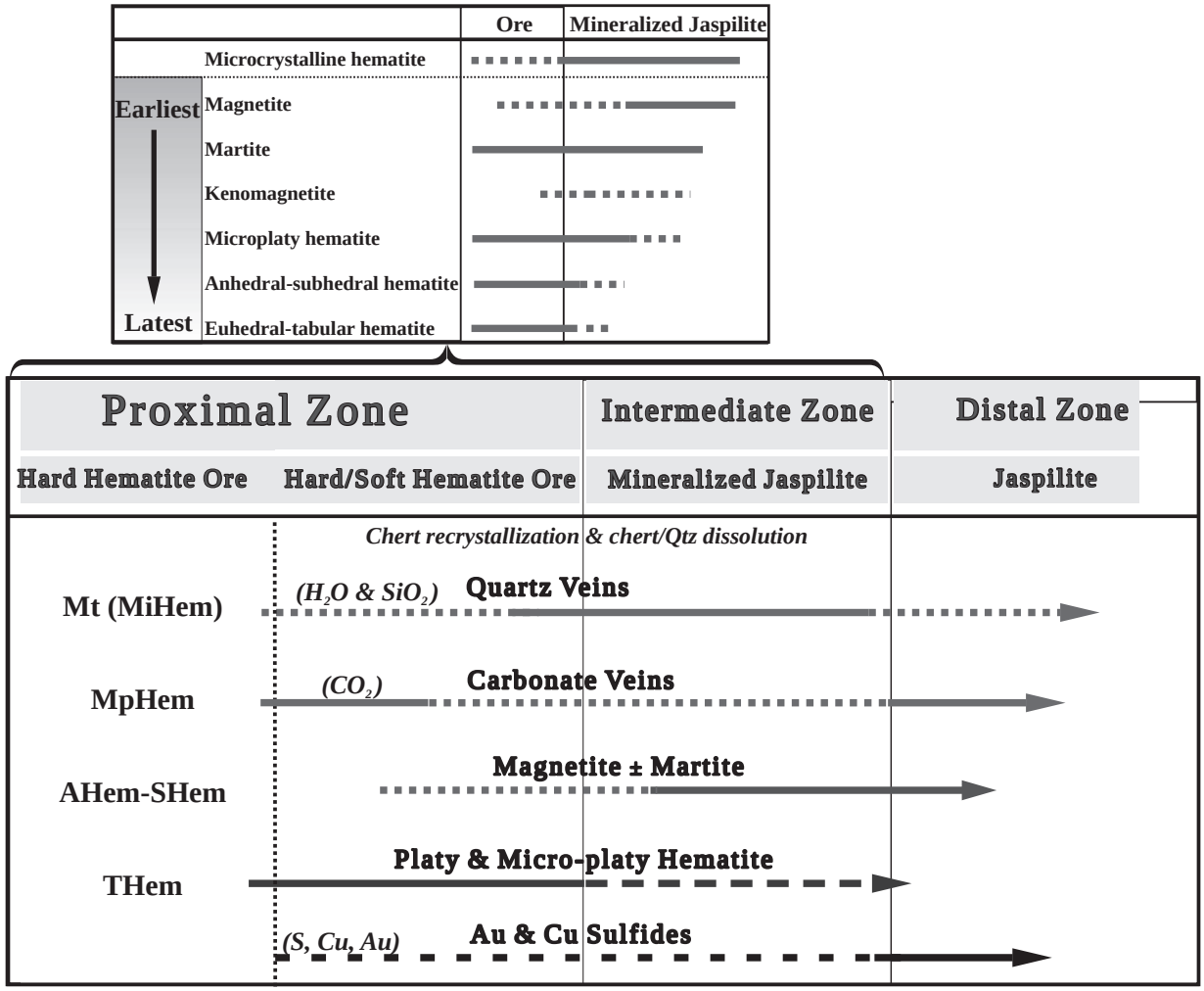

FIG. 3. Paragenetic sequence for the Carajás N4 and N5 iron ore deposits. Table at bottom displays variation from hard hematite (Hem) ore zone through proximal, intermediate, and distal alteration zones. Note that chert recrystallization to quartz and their dissolution are associated with the intermediate and proximal zones, whereas quartz vein deposition is observed mainly in the zone of hydrothermally altered jaspilites (intermediate and distal alteration zones). Top table displays oxide mineral variation from early- to late-stage hydrothermal alteration. Mineral abbreviations: AHem-SHem = anhedral and subhedral hematite, MiHem = microcrystalline hematite, MpHem = microplaty hematite, Mt = martite, THem = tabular hematite (adapted after Lobato et al., 2005b).

Figueiredo e Silva et al., 2008) and porosity development (Fig. 2A-E). The dominant V1a and V1b veins (table 3 of Figueiredo e Silva et al., 2008) in the distal alteration zone contain quartz ± sulfide or calcite ± chalcopyrite (pyrite)-magnetite, and either crosscut or are parallel to jaspilite bands. The jaspilite adjacent to V1 veins is locally brecciated.

Intermediate alteration zone—martite-microplaty hematite-quartz: Martite characterizes the martite-microplaty hematite-quartz assemblage of this alteration zone (Tables 1, 2; Fig. 3), with or without kenomagnetite. Martite (grain size 100–300 μm, exceptionally 600 μm) may preserve kenomagnetite relicts (e.g., at the N4W deposit; Fig. 1E). Quartz-jasper dissolution led to porous, locally brecciated rocks, and to the precipitation of lamellar (microplaty or platy) hematite (Fig. 1H) that fills the open spaces or vugs (Fig. 2D, E). The size range of this hematite is 4 to 8 μm (microplaty) and 100 to 200 μm, locally 400 μm (platy). The microplaty or platy hematite also formed at the expense of martite edges. Rare gold particles are included in quartz or associated with martite in altered jaspilite (Figueiredo e Silva, 2004).

There are two vein types (fig. 9, table 3 of Figueiredo e Silva et al., 2008) in the intermediate alteration zone: V2—quartz ± microcrystalline hematite bedding-discordant and vuggy veins, and V3—microcrystalline hematite-quartz veins that crosscut and/or are parallel the jaspilite bedding. Quartz is granoblastic, zoned, and comb textured in the vugs. Carbonates are absent.

Proximal alteration zone—hematite (carbonate-quartz): The proximal alteration zone (Tables 1A, 2; Fig. 3) is characterized by various types of hematite and/or by the presence of martite. The destruction of martitic magnetite "blasts" results from their recrystallization forming abundant eye-shaped agglomerates of anhedral hematite (~20 μm), especially in the N5E deposit hard ores (Fig. 1M). Some anhedral hematite

TABLE 2. Summary Hydrothermal Alteration Chart, Displaying Commonalities and Differences in Hypogene Alteration for Selected Iron Ore Deposits of the Carajás and Hamersley Iron Districts in Brazil and Australia, Respectively, Thabazimbi Deposit and Zeekoebaart Prospect in South Africa[1]

A	Carajás	Hamersley	South Africa	
Alteration zones	Serra Norte deposits (in jaspilite)	North deposit (Tom Price)	Thabazimbi deposit	Zeekoebaart prospect
Distal	(1) Chert-Qtz leached; abundant vein Qtz ± Carb ± Sulf (2) Mag after MiHem & in veins (3) Qtz-Carb veins may have Py and Ccp but lack Hem	(1) Distal magnetite-siderite-iron silicate zone (2) Chert bands partially replaced by bladed Mag, Sd and Fe silicates (3) Mag after Dol or Sd (4) Breccia and vein formation	(1) Fe silicates, Carb and Mag replaced by KMag and Mt (2) Chert is partly leached and also replaced by MpHem (3) Collapse breccias cemented by late THem, with angular fragments of oxidized BIF (4) Microcrystalline Qtz and Hem replace Gru and Ank	(1) Mag replaced by fine-grained Hem to form KMag that develops into Mt (2) Leaching of silicate layers results in collapse structures (3) MpHem in iron-poor cherty layers (4) PH replaces Mt (5) Qtz veins
Intermediate	(1) Intense Mag martitization (2) Advanced chert recrystallization to Qtz and chert-Qtz leaching (3) Intense Qtz-Hem and Hem-Qtz formation with MpHem and less Sulf (4) Significant porosity increase; vugs partially filled by MpHem	(1) Intermediate hematite-ankerite-magnetite zone (2) Sd replaced by Ank; liberated Fe precipitates MpHem (3) Breccias, veins; complete absence of chert mesobands (pseudomorphous after Carb) (4) Qtz is absent	Not described	Not described
Proximal and/or high-grade ore	(1) Progressive martitization to form AnHem (2) Rare Qtz veins with MpHem (3) Stockwork-style, "Christmas-tree"-type veins contain THem, and crosscut rocks of all alteration stages (4) Hematite-martite and hematite ore types, with MpHem, AnHem, Them, and preserving MiHem (5) Intense Carb alteration results in ore breccias cemented by Dol (N5 deposit) and Kut (6) Late-stage, AnHem- and Them-rich ore lacks Qtz and Carb veins	(1) Proximal martite-microplaty hematite-apatite zone (2) Mt and AnHem replace Mag and Fe silicates, respectively (3) Proportion of Mt increases with proximity to high-grade ore (4) Increased oxidation of Mt is accompanied by increase in voids and Gt formation (5) MpHem important constituent of both hard and soft high-grade iron ores (6) All Carb are dissolved (7) Ap occurs mainly within the inter-granular space of Mt mesoband	(1) Efficient leaching and replacement of chert (2) Two hypogene, high-grade iron ore types that grade into one another: (a) hard hematite that may be massive, laminated, and brecciated; (b) carbonate-hematite 3) (a) Contain fine-grained Hem and minor Mt-laminated ores dominated by MpHem, which is abundant in brecciated and massive ores; (b) Encompasses various breccia ore types, cemented by sparry Carb, and developed in response to fracturing of high-grade hematite ores	(1) Complete replacement of KMag to form Mt (2) Efficient leaching of SiO_2 led to laminated and massive hematite ores (3) Mt recrystallization resulting in PH in former Fe-rich bands in BIF (4) MpHem develops within Fe-poor or microcrystalline Qtz microbands at the expense of chert that is effectively leached (5) Small patches of chert almost entirely replaced by MpHem

B	Carajás
Alteration zones	Various deposits in the Serra Norte (in mafic wall rock)
Distal	(1) Igneous, variolitic texture partially preserved (2) Abundant Chl replaces prealteration silicates forming chloritites (3) Qtz-Carb veins (4) Some Hem, white mica AND comb-textured Ab (5) Also Mag, minor MpHem, fibrous vein filling Tlc, Ttn, and Brk in veins; rare Zrn
Intermediate	(1) Pervasive Chl; also Hem development along veins and replacing amygdales, locally forming Hem chloritites (2) Important Carb and Qtz development (3) Also white mica, Ab, Ttn, Mag, subordinate Sulf
Proximal	(1) Pervasive and abundant Hem; further Chl development (2) Presence of Hem chloritites (3) Also Carb, Qtz, white mica, Ab, Ttn, Mag, subordinate Sulf

[1] Adapted from data in Thorne (2001), Netshiozwi (2002), Harding (2004), Lobato et al. (2005b), Thorne et al. (2007), Zucchetti (2007); Figueiredo e Silva et al., (2008)

Mineral abbreviations: Ab = albite, AHem = anhedral hematite, Ank = ankerite, Ap = apatite, Carb = carbonate, Ccp = chalcopyrite, Chl = chlorite, Dol = dolomite, FeSil = iron silicate, Gru = grunerite, Gt = goethite, Hem = hematite, KMag = KMagnetite, Kut = kutnahorite, MiHem = microcrystalline hematite, Mag = magnetite, MpHem = microplaty hematite, Mt = martite, PH = patchy hematite, Py = pyrite, Qtz = quartz, Sd = siderite, Sulf = sulfide, THem = tabular hematite, Tlc = talc, Ttn = titanite, Zrn = zircon

also developed by recrystallization of microcrystalline hematite, where it was in contact with euhedral and/or tabular hematite veins. Fine- to medium-grained (200–300 μm, locally up to 500 μm), euhedral and blade-tabular hematite (Fig. 1N, O) forms internal selvages to discordant and layering-parallel milli- to centimeter veins. The euhedral and blade-tabular hematite appears to correspond to the latest oxide stage and is located in discordant veins and veinlets without quartz. They are commonly comb-textured, exhibit growth zones, and further fill the vugs created by chert-quartz dissolution. Growth lamellae are common in euhedral hematite (Fig. 1M) but also are observed in anhedral, tabular, and, rarely, in lamellar (microplaty or platy) hematite.

Pyrite is located as inclusions in hematite (martite and/or anhedral types) and, in the case of mafic rocks, also as rings around amygdale fillings. Locally pyrite is surrounded by chalcopyrite, which in places is overgrown by covellite. Rare gold is encountered in this zone as inclusions in tabular hematite. Rare chalcopyrite is observed in anhedral hematite bands of high-grade ore.

The proximal alteration zone is characterized by vein filling (vein types in table 3 of Figueiredo e Silva et al., 2008) in breccias classified as V4—carbonate-quartz breccia, and V5—quartz ± microplaty hematite breccia; both are located in high-grade ore (Table 3). In this alteration zone, carbonate is predominantly dolomite impregnated by hematite dust (fig. 9 of Figueiredo e Silva et al., 2008) that may be associated with (crystalline) hematite. Quartz and dolomite may contain hematite inclusions.

Mafic rocks: Hydrothermal alteration also affected mafic wall rocks surrounding jaspilites and ores, including mostly basalts, and to a lesser degree gabbro and diabase. Basalts display features indicative of seawater hydrothermal alteration (e.g., Meirelles, 1986; Meirelles and Dardenne, 1991; Teixeira et al., 1997). Amphiboles (± epidote), relict plagioclase laths and augite may occur as prealteration minerals (Tables 1B, 2B, Fig. 4) in samples that still preserve their original textures. These rocks were subsequently affected by a regional greenschist-facies metamorphism. Finally, the mafic rocks were chloritized and hematitized at their top portion where in contact with the base of the hard iron ores, particularly at the N4 and N5 deposits, as a result of the hydrothermal alteration associated with the formation of high-grade iron ore (Zucchetti and Lobato, 2004; Lobato et al., 2005a; Zucchetti, 2007; Zucchetti et al., 2007).

In the distal alteration zone, igneous textures are partially preserved, such as varioles and amigdales (Table 2B, Fig. 5). The hydrothermal alteration is defined by chlorite-quartz-carbonate ± hematite assemblage (Table 1B). The color of the rocks is light pinkish-green due to the impregnation of very fine-grained hematite (Fig. 5A-F). This alteration was initiated via fluid influx in amygdales or varioles, which acted as nuclei to fluid dispersion (Fig. 5A-C).

The intermediate alteration zone is characterized by chlorite-hematite-quartz-albite-mica-carbonate ± titanite ± magnetite ± sulfides assemblage, whereas the proximal alteration zone displays hematite-chlorite-quartz-albite-mica-carbonate ± titanite ± magnetite ± sulfides assemblage (Figs. 4, 5; Tables 1B, 2B). In both intermediate and proximal alteration zones hematite is dominantly acicular, microlamellar, and lamellar. Anhedral hematite (developed after martite) agglomerates in veins and random crystals located in the breccia matrices; carbonate, quartz, and rare sulfides dominate in veins. As shown in Figure 5D and E, the rupturing of amygdale margins gave place to hematite-rich chloritites, with concomitant to late development of hematite ± chlorite-filled fractures.

Hamersley Iron District, Australia

Regional geologic setting

Banded iron formation-hosted high-grade iron ores of the Hamersley province in northwestern Australia (fig. 1 of Thorne et al., 2008) are located in the Neo-Archean to Paleoproterozoic (2.6–2.4 Ga) Mount Bruce Supergroup, a succession of volcanic and sedimentary rocks that overlie the granitoids and greenstone belts of the Archean Pilbara craton (e.g., summary in Martin et al., 1998). The Hamersley province contains a resource of about 25 billion metric tons (Bt) of iron ore and includes several deposits dominated by martite-microplaty hematite ore. The two most important examples are the giant Mount Tom Price and Mount Whaleback deposits (Thorne et al., 2008).

TABLE 3. Characteristics of Vein Types in the Serra Norte N4 and N5 Deposits in the Carajás Province and in the North Deposit in the Hamersley Province[1]

	Serra Norte deposits: Carajás		North deposit: Hamersley	
Vein type	Vein mineralogy	Alteration zone	Vein mineralogy	Alteration zone
V_1			Dol, Cal, Sd	Unaltered BIF
		Distal alteration zone		
	Qtz, Py; Cal, Ccp-Py, Mag			
V_2	Qtz, MpHem (Ccp)	Intermediate alteration zone	Sd, Fe silicates	Distal alteration zone.
V_3	MpHem, Qtz	Intermediate alteration zone	Ank, MpHem	Intermediate alteration zone
V_4	Kut-Dol (Cal), MpHem	Proximal alteration zone	Py	Brittle fracture zones that postdate intermediate alteration zone (rare)
V_5	Qtz, MpHem (Ccp)	Proximal alteration zone (high-grade ore)	Absent	

Mineral abbreviations: Ank = ankerite, Cal = calcite, Ccp = chalcopyrite, Dol = dolomite, Kut = kutnahorite, MpHem = microplaty hematite, Py = pyrite, Qtz = quartz, Sd = siderite

[1] Adapted with data from Thorne (2001), Lobato et al. (2005b), Thorne et al. (2007), Figueiredo e Silva et al. (2008)

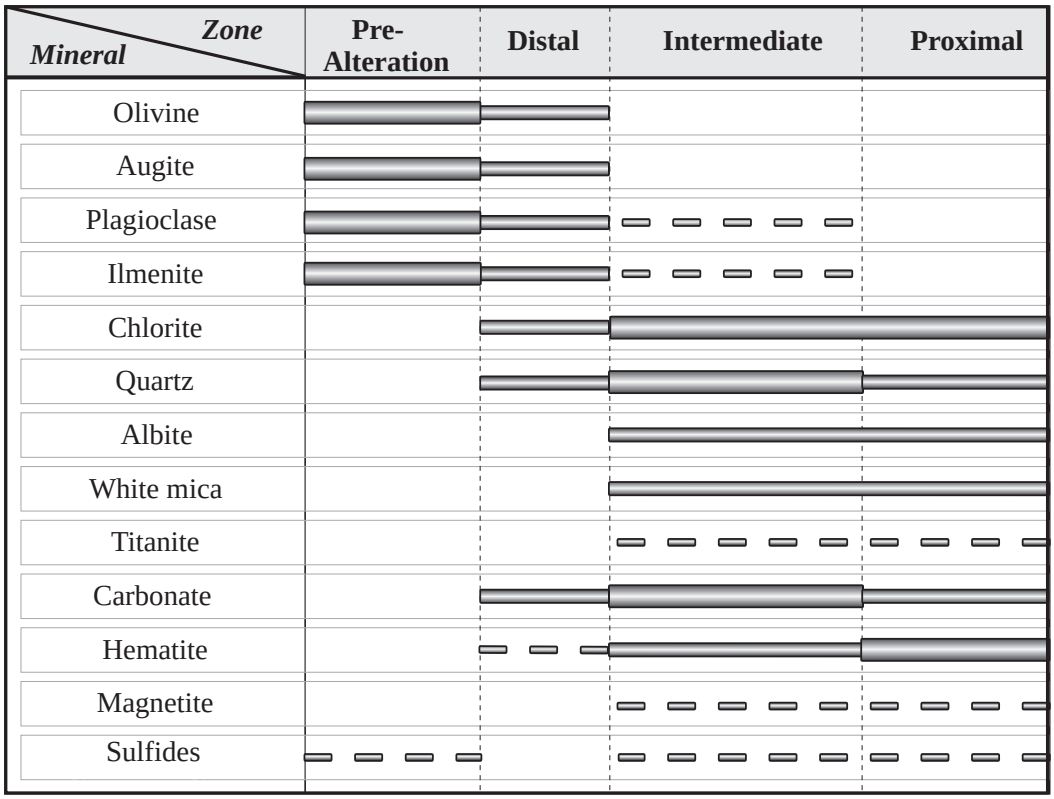

FIG. 4. Paragenetic sequence according to the distal, intermediate, and proximal hydrothermal alteration zones of the basaltic wall rocks. The intermediate zone reaches about 30 m in width, and the proximal zone is approximately 60 m wide. Minerals are shown as major (thick bar), common (thin bars), or minor (dashed line) phases (adapted after Lobato et al., 2005b; Zucchetti, 2007).

The Neo-Archean Marra Mamba (ca. 2.6 Ga, Beukes and Gutzmer, 2008) and Early Paleoproterozoic Brockman (ca. 2.46–2.5 Ga, Beukes and Gutzmer, 2008) iron formations of the Hamersley Group, Mount Bruce Supergroup are host to the main iron ore deposits (Martin et al., 1998). A thick succession of shales and dolostones separate these two iron formations (e.g., Martin et al., 1998). Minor amounts of shale and tuffaceous beds are intercalated with the iron formations (Trendall and Blockley, 1970; Blake and Barley, 1992; Barley et al., 1997). The iron formations are typically microbanded, composed of microcrystalline quartz (chert), iron oxides, iron silicate, and carbonate minerals (Trendall and Blockley, 1970; Barley et al., 1999) that reflect greenschist-facies metamorphism. Dolerite sills and dikes locally intrude into the iron formations. Some of these mafic intrusions predate ore formation and are affected by intense hydrothermal alteration (Dalstra and Guedes, 2004), whereas others postdate ore formation (Müeller et al., 2005).

Iron ore deposits and types

The iron ores exploited in the Hamersley province can be subdivided into three distinct types: (1) high-grade martite-microplaty hematite deposits developed predominantly within the Brockman Iron Formation, with minor deposits within the Marra Mamba Iron Formation; (2) martite-goethite deposits hosted within the Marra Mamba and Brockman Iron Formations; and (3) detrital deposits and goethite-rich pisolitic accumulations in Tertiary paleochannels. The latter two ore types are rather convincingly related to geologically recent weathering processes, whereas a hydrothermal origin, followed by supergene modification, is now widely accepted for most high-grade martite-microplaty hematite ores.

The identification and investigation of hydrothermal alteration is summarized based on detailed work by a number of authors on the Mount Whaleback (Powell et al., 1999; Brown et al., 2004; Webb et al., 2004; Oliver et al., 2007), Mount Tom Price (Barley et al., 1999; Hagemann et al., 1999; Ridley, 1999; Taylor et al., 2001; Dalstra et al., 2002; Cochrane, 2003; Thorne et al., 2004, 2005, 2007, 2008) and Paraburdoo deposits (Taylor et al., 2001; Dalstra, 2005).

With a premining resource in excess of 1800 Mt at 65 wt percent Fe the Mount Whaleback deposit is the largest known iron ore accumulation in Australia (Clout, 2005). The deposit is structurally complex (fig. 4 of Thorne et al., 2008), with the orebody constrained by the westerly plunging overturned East and South synclines (Powell et al., 1999; Taylor et al., 2001; Webb et al., 2003, 2004; Thorne et al., 2008). High-grade iron ore (Fig. 3B) is hosted predominantly in the Dales Gorge Member of the Brockman Iron Formation (fig. 4 of Thorne et al., 2008), with lesser amounts in the underlying Colonial Chert Member of the Mount McRae Shale and the overlying Joffre Member of the Brockman Iron Formation (Webb et al., 2003). The ore in the Dales Gorge Member

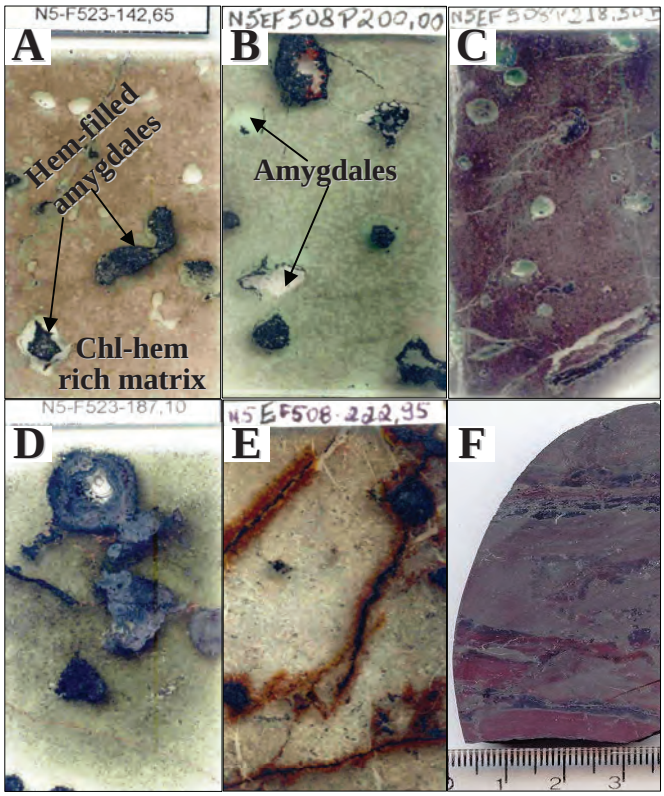

FIG. 5. Scanned surfaces of thin and polished sections of the N5E deposit, Carajás, showing the progressive hydrothermal alteration of volcanic mafic rocks, which is initiated via fluid infiltration into amygdales, shown on the surface of thin sections. A. B. and C. Chlorite-dominated alteration, with associated platy (microlamellar) hematite; the matrix is impregnated by a hematite dust covering all phases. D and E. Hematite(Hem)-dominated alteration via rupturing of amygdale margins, resulting in pervasive iron enrichment (i.e., hematite development), with sample (F) representing the most advanced alteration stage (from Lobato et al., 2005a, b; Zucchetti, 2007).

consists of medium to hard martite and microplaty hematite. Ore in the Joffre Member consists of soft, fissile microplaty hematite containing locally elevated amounts of goethite.

The Mount Tom Price deposit is located near the eastern closure of the Mount Turner syncline (fig. 5 of Thorne et al., 2008). More than 90 percent of the ore at Mount Tom Price is located in the Dales Gorge Member. Locally iron ore extends into the Joffre Member (fig. 5 of Thorne et al., 2008), where it is in faulted contact with the Dales Gorge Member (Barley et al., 1999). The entire thickness of the Dales Gorge Member consists of high-grade ore at the eastern end of the deposit (e.g., South East Prongs deposit; fig. 5 of Thorne et al., 2008), with only the upper portion of this unit reaching ore grade farther west (e.g., North deposit). Major structures that control the distribution of high-grade iron ore include the Southern Batter, the Box Cut (fig. 5 of Thorne et al., 2008), and the North East Prong faults (Taylor et al., 2001). A set of northwest-trending dolerite dikes extends through the Southern Ridge and syncline deposits and are influenced by F_2 and F_3 folds.

The Paraburdoo deposit consists of two orebodies: 4 West and 4 East (Harmsworth et al., 1990; fig. 6 of Thorne et al., 2008). High-grade iron ore is equally distributed between the Dales Gorge and Joffre Members of the Brockman Iron Formation. Lesser amounts of iron ore are associated with flat-lying faults within the Yandicoogina Shale and the lowermost section or the Weeli Wolli Formation (fig. 6 of Thorne et al., 2008). Structural reconstruction of the Paraburdoo deposit suggests that the flat fault zones that now underlie the deposit were steeply dipping normal faults, prior to late tilting (Dalstra, 2005). Northwest-trending dikes (ca. 2008 Ma; SHRIMP $^{207}Pb/^{206}Pb$ baddeleyite; Müller et al., 2005), which limit the aerial extent of iron orebodies at Paraburdoo (fig. 6 of Thorne et al., 2008), intrude extensional faults active during the mineralization processes and were hydrothermally altered to a talc-chlorite assemblage during ore formation (Barley et al., 1999; Dalstra, 2005) but do not intrude the Mount McGrath Formation. This indicates that the hypogene alteration and iron ore formation took place during or shortly after emplacement of the Paleoproterozoic dikes.

Hydrothermal alteration zones

Evidence for hydrothermal alteration is surprisingly scant at the Mount Whaleback deposit. Webb et al. (2004) reported that the chemical and mineralogical composition of the Mount McRae Shale beneath the iron orebody (fig. 4 of Thorne et al., 2008) at Mountt Whaleback at depth is chemically and mineralogically distinct from the regional black and red shales produced during regional metamorphism. The shale is locally intensely carbonate altered and adjacent to high-grade ore consists of fine- to medium-grained dolomite cut by numerous chlorite and ferroan-dolomite and/or ankerite veinlets (cf. Webb et al., 2004; fig. 4 of Thorne et al., 2008). Fine-grained ferroan-dolomite and ankerite crystals are spatially associated with many of these veins (fig. 3A of Thorne et al., 2008). Powell et al. (1999) and Brown et al. (2004) studied at least five generations of quartz ± hematite veins surrounding the Mount Whaleback deposit. At least one generation of hematite ± quartz veins that is locally enclosed by microplaty hematite ore (Fig. 1K) was suggested to be synchronous to the main ore-forming event.

Three compositionally distinct zones of hydrothermal alteration have been described at the Mount Tom Price deposit (Taylor et al., 2001; Thorne et al., 2004, 2005, 2008), distal magnetite-siderite-iron silicate (Fig. 6A, B), intermediate hematite-ankerite-magnetite, and proximal martite-microplaty hematite-zones (Figs. 6C-F, 7A, B; Tables 1A, 2). The distal alteration zone (Fig. 6D, Fig. 7A) is about 30 m wide and characterized by replacement of chert layers by bladed magnetite (50–200 μm), siderite (800–1,500 μm), and iron silicates (20–110 μm; Fig. 1B). The shape of the magnetite is atypical, suggesting that it is pseudomorphous after preexisting minerals, likely siderite (Fig. 1C). Where preserved, microcrystalline quartz is intergrown with euhedral magnetite and forms inclusions within siderite blades. Pyrite crystals (50–300 μm) are finely disseminated within shale layers. Apatite is observed as euhedral crystals intergrown with anhedral chlorite (Fig. 7A). Veins in the distal alteration zone (V2 veins, Table 3) are observed in orientations both crosscutting and parallel to the lamination of the BIF host rock and are filled by siderite and stilpnomelane (Table 3). The wall rock adjacent to these veins is locally brecciated with clasts (5–60 mm) of magnetite-rich mesobands in a matrix of bladed magnetite, siderite, and iron silicates.

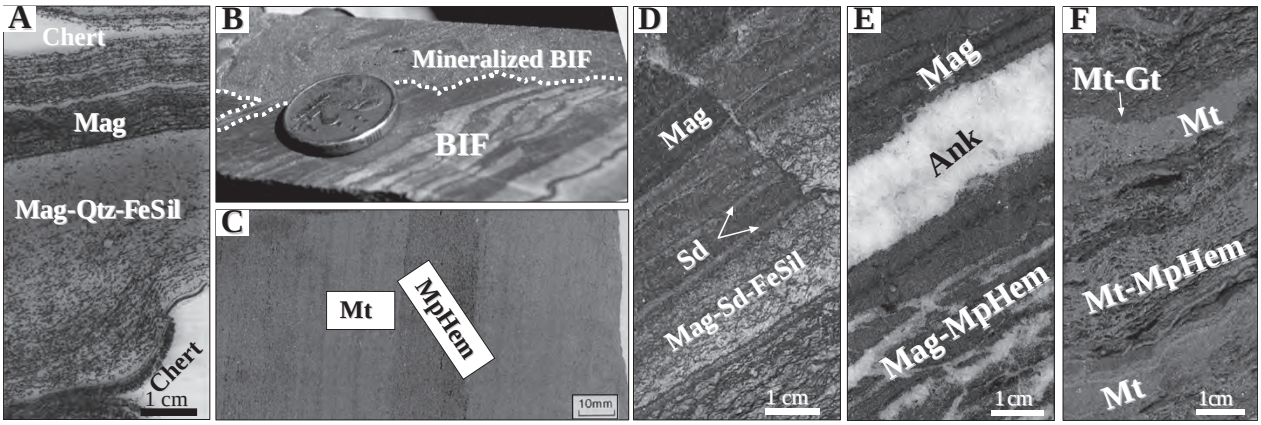

FIG. 6. Core samples from the North deposit, Mount Tom Price. A. Least altered BIF showing chert and magnetite banding. B. Least altered BIF showing hematitized portion. Note that hematite invades bands of BIF. C. Hard hematite ore, with preservation of bands characterized by alternating martite- and microplaty hematite-rich bands. D. Magnetite-siderite-iron silicate distal alteration zone showing preservation of bands. E. Hematite-ankerite-magnetite intermediate alteration zone with localized brecciated magnetite bands. F. Martite-microplaty hematite ore (supergene). Note preservation of banding and goethite infill. Abbreviations: FeSil = iron silicate, Gt = goethite, Mag = magnetite, MpHem = microplaty hematite, Mt = martite, Sd = siderite (adapted after Thorne et al., 2004).

A

Zone / Mineral	Least-altered BIF	Hypogene: Distal	Hypogene: Intermediate	Hypogene: Proximal	Supergene: High-grade iron ore (Fe>60 %, P>0.05 64%)
IRON OXIDES					
Magnetite	■	■	■	■	
Anhedral hematite			■	■	■
Microplaty hematite			■	■	■
Martite				■	■
Goethite					■
CARBONATES					
Dolomite	■	■			
Siderite	■	■			
Ankerite			■	■	
SILICATES					
Chert	■	■	■	■	■
Iron Silicates	■	■	■	■	
Chlorite		■	■		
SULFIDE					
Pyrite	■	■	■	■	

B

	Euhedral Magnetite (*Mg*)	Platy Magnetite (pMg)	Bladed Hematite (*pHm*)	Microplaty Hematite (*mpH*)	Martite (*Mr*)	Anhedral hematite (*aHm*)
Unmineralised BIF						
Dales Gorge Member	■					■
Joffre Member	■					■
Protore						
Mt Tom Price						
Distal	■	■				▪
Intermediate	■			■		▪
Proximal				■	■	■
Talc altered				▪	■	■
Paraburdoo						
Proximal				■	■	■
High-grade ore						
Channar			■	■	■	■
Ratty Springs			■			
Paraburdoo				■	■	■
Mt Tom Price			■	■	■	▪

▪ <5 wt% ■ >5 and <10 wt% ■ >10 and <20 wt% ■ >20 wt%

FIG. 7. A. Paragenetic alteration sequence in BIF at the North deposit, Mount Tom Price. Proximity to iron mineralization increases to the right. Zone widths shown here do not relate to actual widths observed in the field (adapted after Thorne et al., 2004). B. Paragenetic sequence of oxide minerals between nonmineralized BIF and high-grade ore for various deposits in the Hamersley province (Thorne et al., 2007).

Intermediate alteration zones are about 15 m in width (Figs. 6E, 7A) and characterized by the mineral assemblage microplaty hematite-ankerite-martite that replaces quartz, siderite, magnetite, and iron silicates (Fig. 6). Microplaty hematite (10–60 μm) forms both individual blades and dense clusters as overgrowth on magnetite (Fig. 1C) and as individual plates within ankerite crystals. Euhedral and bladed magnetite show minor replacement by martite along crystal boundaries, whereas iron silicates are replaced by anhedral and microplaty hematite (Fig. 7B). Ankerite crystals (0.20–4 mm) form variably recrystallized mosaics with irregular grain boundaries. Apatite is present as inclusions within magnetite and microplaty hematite and as anhedral crystals within ankerite crystals.

There are two vein sets associated with the intermediate alteration zone. These are ankerite-hematite (V3, Table 3) and pyrite veins (V4, Table 3). The V3 veins are especially abundant and crosscut BIF and shale bands, whereas pyrite veins are rare and are in the fracture zones that postdate hematite-ankerite-magnetite alteration. Breccias are matrix supported and consist of angular and rotated clasts (5–40 mm) of altered iron formation within an ankerite-microplaty hematite matrix.

The proximal alteration zone is about 15 to 30 m wide and characterized by the mineral assemblage martite-microplaty hematite-apatite. Martite and anhedral hematite replace magnetite and iron silicates of the intermediate alteration assemblage, respectively. Minor amounts of apatite and chlorite are located in thin layers, together with some fine-grained martite. Intergranular porosity increases significantly. Locally, late-stage talc alteration crosscuts the proximal alteration zone.

The high-grade ore consists of martite and microplaty hematite, with the ore preserving the meso- and microlayering of the primary BIF bands. The ore is characteristically porous and consists of randomly oriented, fine-grained platy hematite and martite. Individual microplates (0.001–0.25 mm) are bladed or cigar shaped with sharp terminations (Taylor et al., 2001) that exhibit intensive overgrowth on subhedral martite grain margins. High-grade martite-microplaty ore was formed by the interaction of supergene fluids with the proximal martite-microplaty hematite-apatite assemblage. Magnesium silicates were converted to a kaolinitic residue, thereby significantly thinning the shale layers, apatite was dissolved, and both calcium and phosphorus were leached from the ore. Dolerite dikes that bound the high-grade ore are intensely altered and largely composed of chlorite and talc, with accessory leucoxene and pyrite. The chlorite (diabantite) forms pseudomorphs after primary phases such as pyroxene and amphibole, whereas talc or chlorite form pseudomorphs after feldspar.

As for Paraburdoo, preliminary work at the deposit has identified at least one hydrothermal alteration zone transitional between the BIF protolith and the high-grade iron ore (Thorne et al., 2007; fig. 6 of Thorne et al., 2008). The proximal alteration zone is characterized by a hematite-dolomite-chlorite-pyrite assemblage, is at least 20 m wide, and is emplaced below the depth of modern weathering. It forms by the replacement of magnetite by hematite and the replacement of quartz by dolomite, chlorite, and pyrite. Matrix-supported BIF breccias are observed locally and consist of angular and rotated clasts of altered BIF in a dolomite-microplaty hematite-chlorite-pyrite cement. The mineral assemblage is similar to that of the intermediate alteration zone at Mount Tom Price. The entire orebody at Paraburdoo now lies within the Tertiary weathering profile and some high-grade martite-goethite ore is mixed with the martite-microplaty hematite ore. The latter ore is also very similar to that described at Mount Tom Price.

South African Iron Deposits

Regional geologic setting

The Late Archean to Paleoproterozoic (2.06–2.65 Ga) Transvaal Supergroup on the Kaapvaal craton is comprised of lowermost protobasinal volcano-sedimentary deposits, followed by platform carbonate rocks (dolostone, minor limestone), and BIF of the Ghaap-Taupone-Chuniespoort Groups. These are unconformably overlain by clastic sedimentary and volcanic rocks of the Postmasburg-Segwagwa-Pretoria Groups (Eriksson et al., 1995). Voluminous iron formations of the Asbesheuwels Subgroup in the Griqualand West subbasin and the laterally correlative Penge Formation of the Transvaal subbasin of the Transvaal Supergroup (2.43–2.45 Ga, Pickard, 2003) host all economically important high-grade iron ore deposits of South Africa. The Asbesheuwels Subgroup thickness ranges from 250 (platform facies) to 750 m (basinal facies), with a complex mineralogical and textural facies architecture that is documented in detail by Beukes (1983) and Beukes and Gutzmer (2008). Mineralogical and textural iron formation facies can be correlated over large distances, suggesting deposition on a continental platform (i.e., a submerged Kaapvaal craton) in a very stable depositional and/or tectonic environment (Beukes, 1983).

The most important South African high-grade hematite ore deposits are hosted by the Manganore Iron Formation, an extensively oxidized remnant of the Asbesheuwels Subgroup, in the Griqualand West subbasin. The Manganore Iron Formation and associated high-grade iron ores are preserved in depressions that are related to Paleoproterozoic (2.1–2.2 Ga) peneplenation, lateritic weathering, and karstification (Gutzmer and Beukes, 1998). High-grade iron ores within the Manganore Iron Formation are developed immediately below the erosional unconformity that marks this peneplenation event and are thought to be of ancient supergene origin (Beukes et al., 2003). These are, therefore, not the subject of this contribution.

In contrast, high-grade iron orebodies exploited at the Thabazimbi deposit in Limpopo province, which are hosted by the basal portion of the Penge Iron Formation, as well as the Zeekoebaart prospect of the basal portion of the Kuruman Iron Formation near Nauga in Griqualand West, are regarded to be of hydrothermal origin. The orebodies of the Thabazimbi deposit are particularly well documented (Strauss, 1964).

The Thabazimbi deposit

The Thabazimbi iron deposit comprises a series of tabular, strata-bound orebodies aligned along the faulted basal contact between the Neo-Archean to Paleoproterozoic Penge Iron Formation and the dolostones of the Malmani Subgroup, immediately above a chert-rich, black carbonaceous shale unit that is intensely sheared and highly oxidized (Van

Deventer et al., 1986; Gutzmer et al., 2002). The concentration of high-grade hematite orebodies near the structural, basal contact of the Penge Iron Formation suggests an ore-forming process that was both structurally and lithologically controlled. Formation of the high-grade iron ores took place after contact metamorphism related to the intrusion of the Bushveld complex (2.05 Ga) but before the deposition of red beds of the Waterberg Group at ca. 1.9 Ga (age of ore formation by de Kock et al., 2008).

The hydrothermal alteration attending ore formation has been described by Netshiozwi (2002) and Netshiozwi et al. (2002) and much of the present review is based on their work (Tables 1, 2). The origin of the Thabazimbi ores is also discussed by Beukes et al. (2002) and (Gutzmer et al., 2002, 2006).

The metamorphosed Penge Iron Formation is very fine grained with alternating dark iron oxide bands and light gray laminae containing chert, grunerite, and ankerite, with the following main assemblage (Fig. 8A, B): chert and/or microquartz-magnetite (±dusty hematite inclusions)-stilpnomelane-calcite-ankerite-grunerite. Variations in the amounts of these phases characterize different mineralogical facies of BIF. Reddish chert (QTZ-I) and microquartz (QTZ-II) are the most abundant constituents (Fig. 9), and these enclose dusty hematite (He-I). Diagenetic magnetite probably formed by the reduction of dusty hematite is the dominant iron oxide. Stilpnomelane and closely associated calcite (CC-I, Fig. 9) and ankerite are also interpreted to be of diagenetic origin. Carbonates and stilpnomelane predate the formation of grunerite that is thought to be a product of contact metamorphism related to the intrusion of the giant Bushveld layered igneous complex. Minor to trace amounts of pyrite, apatite, and chlorite are also present (Fig. 9).

All high-grade iron orebodies at the Thabazimbi deposit are surrounded by a halo of oxidized and partly enriched BIF, i.e., alteration of the Penge Iron Formation (Figs. 1F, 8C; Tables 1A, 2A). Platy hematite (He-II, Fig. 9) is disseminated in chert, imposing a distinctive pinkish color, and probably represents recrystallization of primary dusty hematite and replacement of grunerite and ankerite by hematite and the formation of martite at the expense of magnetite. Locally, chert has been either replaced by microplaty hematite or it has been leached, thus giving rise to porosity. Veins and veinlets are filled by coarse tabular hematite (referred to as specularite by

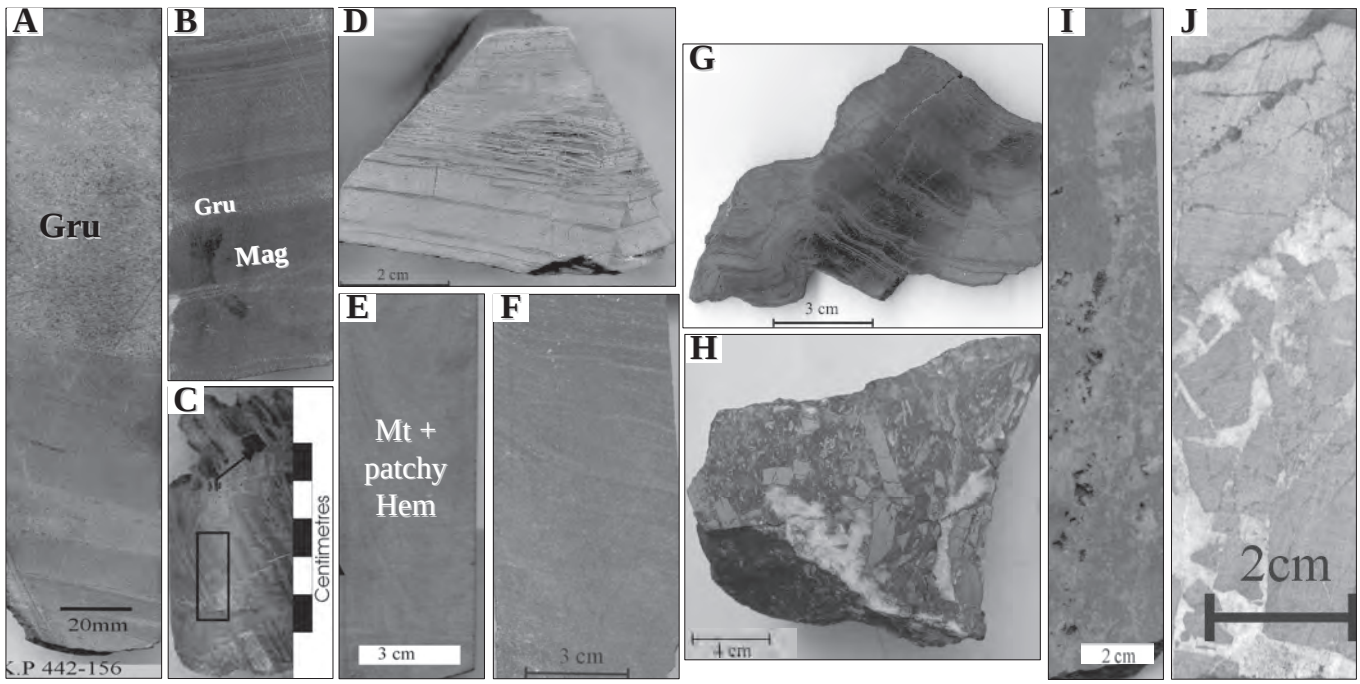

FIG. 8. Photographs illustrating the typical appearance of the least altered and oxidized Penge Iron Formation, South Africa (from Netshiozwi, 2002). A. Mesobanded iron formation characterized by thick grunerite-chert mesobands closely intercalated by thick magnetite-rich laminae. This type of iron formation is likely to produce a massive hematite ore during the ore-forming process. B. Magnetite-rich grunerite-chert iron formation. Note that grunerite-chert mesobands are characterized by thin laminae of magnetite. C. Oxidized cherty facies of the Penge Iron Formation. Note porosity developed where chert was leached. D. Laminated hematite ore comprised of massive hematite beds closely alternating with thin porous hematite laminae. Note minor brecciation toward bottom right of the sample. The breccia fragments are cemented by porous hematite. Photographs (E) to (J) display different types of high-grade hematite ore at the Thabazimbi mine. E. Typical appearance of massive hard hematite ore, mainly comprised of fine-grained martite (Mt) and patchy hematite. F. Finely laminated hematite ore characterized by very thin (millimeter-thick) massive hematite laminae alternating with dusty hematite laminae of distinctly greater thickness (3–5 mm). G. Folded, laminated high-grade hematite ore. Note that the folding of the ore preceded iron mineralization. Photos (H), (I), and (J) show samples of carbonate-hematite ore. H. Hematite-calcite breccia with rectangular to angular hematite fragments cemented by sparry calcite. I. Dolomite breccia defined by irregular outlines of hematite ore fragments, cemented and replaced by sparry dolomite. J. Hydraulic hematite breccia with well-defined angular fragments of hematite cemented by sparry calcite.

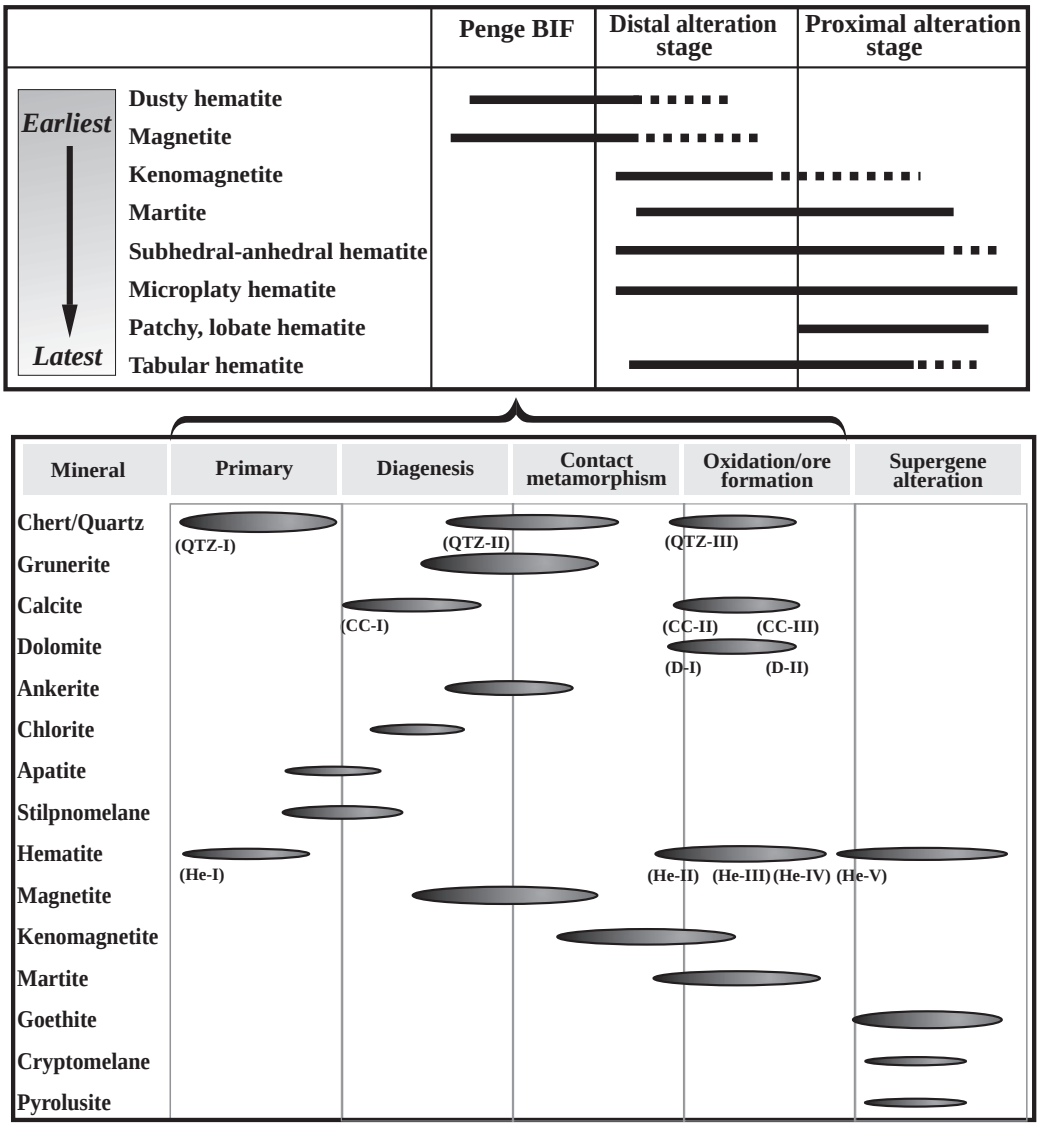

FIG. 9. Paragenetic sequence for the Penge Iron Formation and iron ores developed at the Thabazimbi deposit, according to Netshiozwi (2002). The distribution of oxide minerals along the alteration path is shown in the upper figure. Abbreviations: CC-I = diagenetic calcite; CC-II = C sparry calcite, CC-III = C sparry calcite, D-I = D sparry 1 2 1 dolomite, D-II = D sparry dolomite, He-I = dusty hematite, He-II = microplaty hematite, He-III = specularite, He-IV = patchy hematite, He-V = supergene fine-grained hematite, QTZI = chert, QTZ-II = recrystallized microquartz, QTZ-III = megaquartz. The size of the ellipsoid is a relative measure of abundance.

Gutzmer et al., 2002, and Netshiozwi, 2002) and coarse crystalline quartz fills fractures and veinlets. The effects of hydrothermal alteration are similar to the intermediate alteration zone in the Carajás iron district.

The formation of high-grade hematite orebodies at the Thabazimbi deposit are the result of the gradually increasing degree of SiO_2 leaching (Fig. 8D-J) and closely associated volume loss that created widespread brecciation of the high-grade hematite ore (Fig. 8D; Gutzmer et al., 2005). The presence of finely laminated and massively textured iron ores devoid of brecciation, on the other hand, suggests either the introduction of iron and replacement of silica-rich laminae by porous aggregates of microplaty hematite or the remobilization of iron during the ore-forming process. The formation of such high-grade hematite-martite ores at the Thabazimbi deposit corresponds to the proximal alteration zones described in the Hamersley and Carajás iron districts.

Hard hematite ores dominate at the Thabazimbi deposit. They may be massive, laminated, and brecciated and are mainly composed of martite, patchy (He-IV), and microplaty hematite. Massive ores may have originated by replacement of the banded Penge Iron Formation, including fine-grained microplaty hematite. These ores are either devoid of sedimentary lamination or may display traces of mesobanding. Patchy hematite and martite constitute the massive bands of these laminated hematite ores. Anhedral, patchy hematite is defined by lobate grain boundaries, and it is interpreted to have formed during the recrystallization of martite. Tabular

hematite is observed in laminated hematite ore, infilling porosity, and also in crosscutting quartz veins. There is a gradual transition from laminated through weakly fragmented to brecciated ore types. Breccias evolved from hard hematite ores that were reduced by collapse and secondary tabular hematite infill. Breccia fractures are variously cemented by very fine grained anhedral hematite, microplaty hematite, and tabular hematite.

In addition to high-grade hematite-martite ores, four mineralogically distinct types of iron ore have been recognized: (1) goethite-rich, (2) low-grade dolomite-hematite, (3) low-grade calcite-hematite, and (4) talc-hematite. Goethite-rich ores are restricted to the geologically recent weathering environment, whereas carbonate-rich ores interfinger with high-grade hematite-martite ore at depth. Talc-rich ores are found locally along the fringes of the high-grade iron orebodies and along the contact of high-grade iron ore with the basal shale.

The iron oxides in the low-grade carbonate- and talc-rich hematite ores are of very similar texture and mineralogy (i.e., hematite, martite, remnant magnetite) to high-grade ores and are intimately intergrown with sparry carbonates and talc (Fig. 8H-J; Tables 1A, 2A). This led Netshiozwi (2002) and Gutzmer et al. (2005) to the conclusion that ore formation was genetically associated with the formation of calcite, dolomite, and talc. It is interesting to note that despite the fact that both sparry calcite and dolomite appear to be cogenetic with the ore-forming microplaty hematite, these carbonates are not observed in close spatial association or even intergrown. Indeed, they appear always to be separated by either an oxidized shale bed or a bed of high-grade hard hematite ore.

Supergene alteration of both high-grade hematite and carbonate-hematite ores is common and leads to friable, often goethite-bearing high-grade ores.

The Zeekoebaart prospect

The Zeekoebaart prospect is in an area of intense deformation along the southwestern margin of the Kaapvaal craton in Griqualand West (Harding, 2004). It consists of a stratabound lens of hard hematite ore located near the basal contact of the iron formation to the underlying Klein Naute Shale (Beukes and Gutzmer, 2008). The present account of the high-grade iron ores of the Zeekoebaart prospect and its relationship to the surrounding Kuruman Iron Formation is based on the work by Harding (2004).

The high-grade iron ore at the Zeekoebaart prospect is surrounded by a wide halo of oxidized iron formation. This oxidized BIF is comprised essentially of alternating layers of iron oxide (hematite and martite) and fine-grained quartz (Fig. 10; Tables 1A, 2A). Microplaty hematite laths form in the iron-poor or cherty layers, whereas patchy hematite is observed to replace martite in the iron oxide-rich layers. Overall, the oxidized BIF compares well to oxidized BIF at the Thabazimbi deposit and the intermediate alteration zone in the Carajás iron district. Short veins of coarse-grained quartz crosscut the oxidized BIF; hematite and carbonates are conspicuously absent. Unaltered BIF is known to crop out at a distance of ca. 1 km from the Zeekoebaart prospect. This unaltered basinal facies of the Kuruman Iron Formation encompasses alternating iron-rich magnetite-hematite-siderite (ankerite) and iron-poor chert-siderite-stilpnomelane mesolayers (Beukes, 1983). Comparison of this unaltered protolith to oxidized BIF reveals the effects of marked oxidation as well as SiO_2 leaching (Fig. 10).

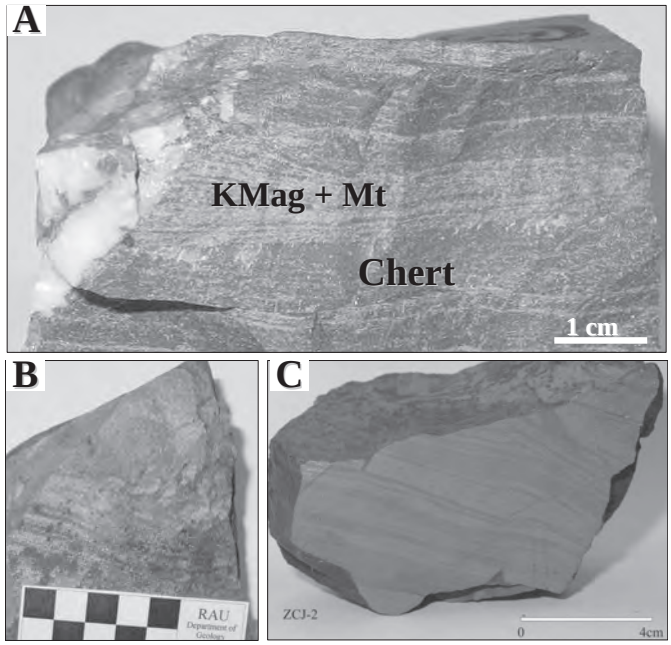

FIG. 10. Photographs illustrating typical samples from the Zeekoebaart iron deposit. A. Oxidized iron formation showing alternating oxide (kenomagnetite-KMag, and martite-Mt) and darker reddish chert bands. B. Laminated hematite ore with alternating, more porous bands (formerly chert) and brighter, less porous (formerly iron oxides) bands. C. Massive hematite ore, with discrete lamination (Harding, 2004).

Proximal alteration at the Zeekoebaart prospect around the high-grade iron orebody involved leaching of SiO_2 from oxidized iron formation and formation of laminated and massive hard hematite ores (Fig. 11; Tables 1A, 2A). The laminated ore is composed of dense layers of fine-grained patchy hematite (former iron oxide bands) that alternate with layers of coarser grained, microplaty hematite (former chert layers; Fig. 11). Patchy hematite is interpreted to be the product of recrystallization of martite. Massive hematite ores, in contrast, develop at the expense of thicker mesobanded BIF and lacks the clear separation of microplaty and patchy hematite. Thin quartz veins, up to 5 cm wide and containing minor amounts of coarse blades of hematite, are randomly distributed in the high-grade ore.

Goethite appears only in minor amounts and is attributed to the influx of oxidizing meteoric water along pore spaces and microfractures. The goethite forms as open-space infill but also as a replacement product of hematite and even quartz.

Commonalities and Differences in Hypogene Alteration of BIF

Mineral associations

The most obvious common attribute of all deposits included in this review (Tables 1, 2; Figs. 3, 7, 9, 11) is a very similar paragenetic sequence of iron oxides. Microcrystalline hematite and fine-grained magnetite, associated with Fe-rich

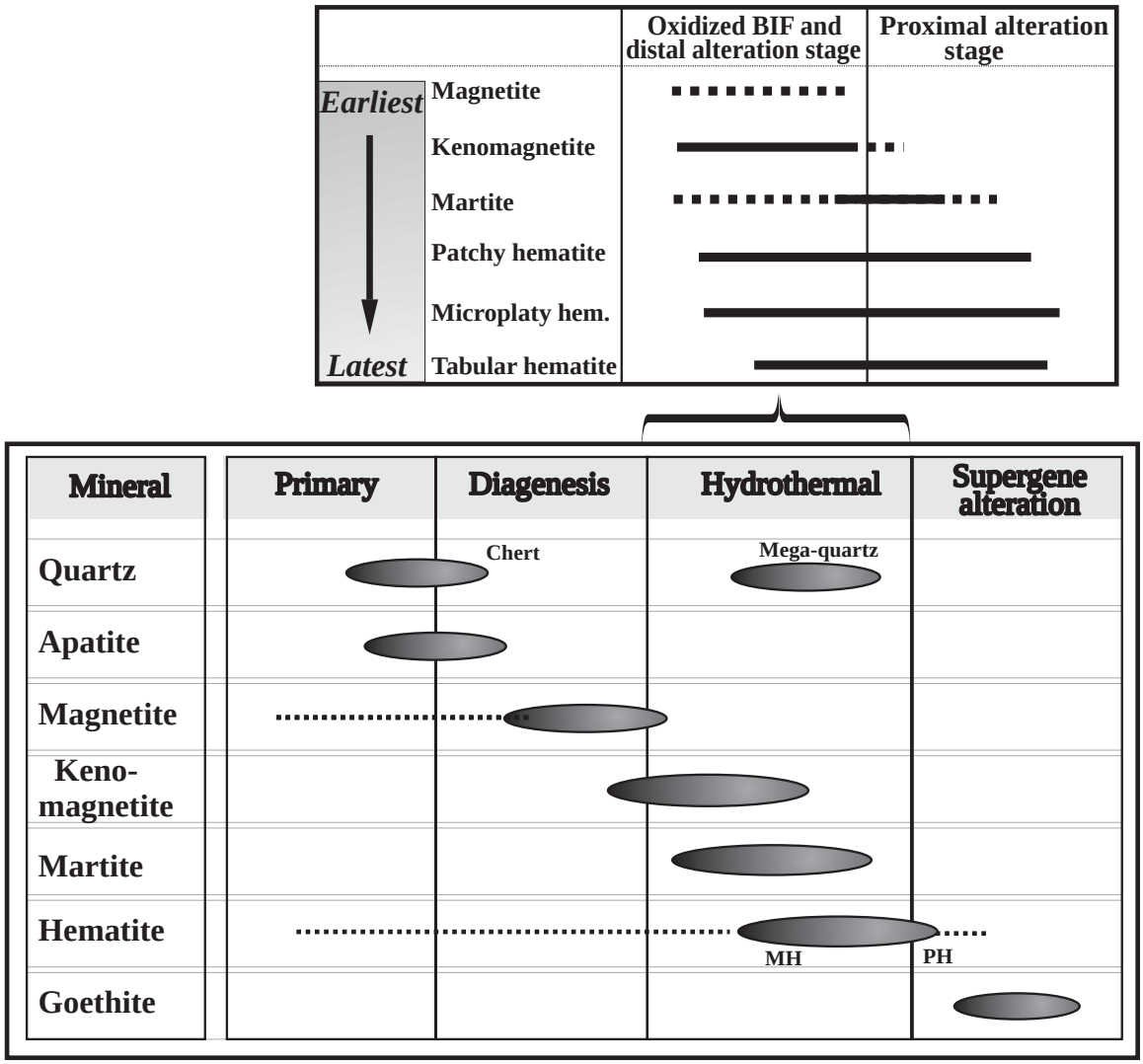

FIG. 11. Mineral paragenesis chart for the hematitized iron formation and hematite iron ore types from the Zeekoebaart deposit, as determined from the study by Harding (2004). The distribution of oxide minerals along the alteration path is shown in the upper figure; the 1st and the 2nd alteration stages represent the distal and proximal alteration zones, respectively. Mineral abbreviations: Hem = hematite, MH = microplaty hematite, PH = patchy hematite

silicates, siderite, and ankerite, dominate the least altered protolith BIF. In distal alteration zones of the Carajás and Hamersley districts hematite and locally iron-rich silicates and carbonates are replaced by euhedral hydrothermal magnetite (Tables 1, 2). This magnetite is typically more abundant and coarse grained than magnetite formed during metamorphism. The Thabazimbi deposit and Zeekoebaart prospect lack unequivocal evidence for the formation of paragenetically early hydrothermal magnetite (Figs. 9, 11). At the Hamersley and South African districts, extensive oxidation is reflected by martitization and the formation of hematite at the expense of Fe^{2+}-rich carbonates and silicates, marking the intermediate alteration zones, which in Carajás is characterized by oxidation of magnetite. Several textural types of hematite, including martite, are located in the oxidized BIF and are similar in appearance to hematite in associated high-grade iron ores. This may be used to support the cogenetic relationship between oxidized BIF and high-grade hematite ore.

In order to transform an altered and/or oxidized BIF to high-grade ore very effective removal of SiO_2 needs to take place. Our case studies revealed that the removal of SiO_2 can take place in two ways. The simplest process involves direct leaching of SiO_2, which is accompanied by widespread oxidation. The second process involves leaching of hydrothermal carbonate that replaced SiO_2 during hydrothermal alteration. The dissolution of these carbonates can be caused by meteoric water influx into fault zones or geologically recent deep chemical weathering.

Hydrothermal carbonates are observed in all our case studies, located in veins and breccias (Table 3), with the notable exception of the Zeekoebaart prospect. They are present in the distal (siderite) and intermediate (ankerite) alteration zones at Mount Tom Price, whereas only the proximal

alteration zone at Thabazimbi displays calcite and dolomite. In both deposits, carbonates effectively replaced chert in altered BIF surrounding high-grade orebodies; in the proximal alteration zones carbonate is then replaced by hematite. In Carajás, calcite dominates in the distal alteration zone, with dolomite and kutnahorite in the proximal alteration zone (the complete hydrothermal alteration assemblages are listed in Table 1). Carbonate-altered BIF has, as yet, not been identified at the Mount Whaleback deposit. This is tentatively attributed to a lack of geologic information on the deeper parts of the ore-forming system, as the closely associated Mount Silvia shale has at least locally provided evidence for extensive carbonate alteration (Webb et al., 2004) Textural relationships between the iron oxides in carbonate-altered BIF and high-grade iron ores in the Hamersley district strongly suggest that carbonate alteration preceded the formation of high-grade iron ore, and that the transformation of carbonate-altered BIF to high-grade hematite-martite ore is due to oxidation and complete decomposition of the hydrothermal carbonates.

In the Carajás iron district, only the intermediate alteration stage (martite-microplaty hematite-quartz assemblage) lacks carbonate. Calcite dominates in the distal alteration zone (magnetite-calcite-quartz-pyrite assemblage; Fig. 3) in veins and breccias. The proximal zone (hematite ± carbonate-quartz assemblage) has dolomite and kutnahorite, covered by hematite dust, in equilibrium with hematite and rare quartz. In addition, carbonate-bearing, late-stage veins and breccias may also be associated with the proximal alteration zone, replacing the martite-rich layers. Sulfides are only significant in the Carajás district where these, together with rare gold, form in quartz-carbonate veins associated mainly with distal hydrothermal alteration zones.

Finally, it is important to note common patterns in the hydrothermal alteration of mafic wall rocks, dikes, and sills, and even shales associated with our case studies. Dalstra and Guedes (2004) were the first to point out that in several important deposits and/or districts mafic dikes and sills that intruded BIF protolith prior to hydrothermal ore formation display marked hydration as expressed by the formation of abundant Mg chlorite and talc. Mafic wall rocks, sills, and dikes in the Carajás district show very similar alteration effects, as they were transformed into hematite- and talc-bearing chloritites. Even the formation of talc-rich iron ores along the contact between high-grade iron orebodies and basal shale at the Thabazimbi deposit may be attributed to intensive hydration. At Carajás, the widespread and dominant chlorite, talc, white mica, and albite in the hydrothermally altered mafic wall rocks that surround the high-grade ores is a function of the mafic wall rocks which are typical of the granite-greenstone belt setting. This is in contrast to the Hamersley district and Thabazimbi deposit, where iron silicates are common and reflect the sedimentary host rocks typical for the host sedimentary basins. Iron silicates are absent at Carajás.

Vein formation, brecciation, and volume loss

Evidence for multiple events of hydrothermal fluid flow and associated remobilization is provided at all the studied sites by different sets of veins. It is important to point out, however, that veins and breccias can also form pre- and post-the transformation of BIF to high-grade iron ore. Detailed geologic mapping, diamond core logging, and a combination of petrographic and geochemical analyses of veins in the three case studies provide specific evidence for the contemporaneous emplacement of particular vein and breccia types during the hydrothermal alteration and mineralization processes in the BIF, but also in the surrounding wall rocks. Veins emplaced synchronous with iron mineralization processes display typically crack-seal, massive, or brecciated textures, and their formation may be genetically linked to deformation that can coincide with the ore-forming fluid-flow event. However, veins rarely are observed within high-grade iron ore. The formation of high-grade iron ore is related to the advanced stage of the mineralization process where desilicification, with or without carbonate alteration, makes the preservation of veins unlikely.

Moreover, it is pervasive rather than focused fluid flow that is required to transform a large volume of BIF into high-grade iron ore. Because unaltered BIF is typically impervious, the generation of porosity (i.e., produced by the dissolution of quartz and/or carbonate) is regarded as instrumental for the progress of alteration and iron ore formation. It comes thus as no surprise that a marked increase in porosity (and, by inference permeability) is associated with all hydrothermal alteration zones in all the districts under consideration.

Provided that an average iron formation contains between 25 and 45 wt percent SiO_2 (Klein, 2005), and that quartz and silicates have a distinctly lower density than magnetite and hematite, a volume loss of 60 to 70 vol percent is expected to be associated with the complete removal of SiO_2 from the protolith BIF. Similarly, this would apply for the dissolution of hydrothermal carbonate that may have replaced chert prior to high-grade ore formation. This massive volume loss could be accommodated by a combination of (1) porosity increase, (2) collapse brecciation, (3) bedding-parallel compaction, and (4) the introduction of additional iron by the hydrothermal fluid. A marked porosity increase and collapse brecciation have been described in all of the deposits included in this review. Bedding-parallel compaction has to be inferred to explain the origin of high-grade iron ores sporting laterally continuous fine lamination reminiscent of the protolith. In deposits for which simple SiO_2 leaching is invoked (Carajás, Thabazimbi, Zeekoebaart), the increase of porosity was gradual. However, although it is readily noted during incipient alteration, a rapid increase of porosity accompanies the transition from intermediate to proximal alteration zones, i.e., the contact of oxidized BIF to high-grade iron ore. The marked porosity of the high-grade ore is due to a very open, scaffold-like intergrowth of microplaty or platy hematite that is thought to have formed as open-space infill. This very porous intergrowth often is observed along distinct layers that are tentatively identified as former chert layers, which are separated by much less porous hematite-martite laminae that are thought to represent iron-rich layers of the protolith BIF. In contrast, no such gradual increase of porosity has been noted for deposits that have experienced carbonate metasomatism as an integral part of high-grade ore formation (Hamersley district, possibly Thabazimbi). Instead, the increase of porosity is almost entirely associated with the contact of carbonate-altered BIF to high-grade iron ore. This increase is due to the dissolution of the hydrothermal carbonate. Carbonate dissolution may be

attributed either to most intense hydrothermal alteration (Hamersley district, Thabazimbi deposit) or, alternatively, be due to geologically recent chemical weathering processes.

Dissolution collapse brecciation is another important process that accommodates the volume loss during the hydrothermal transformation of BIF protolith to high-grade hematite ore. It has been described in all the deposits and/or districts, with the notable exception of the Zeekoebaart prospect (Taylor et al., 2001). Typically, brecciation is noted already during incipient alteration, although it may be restricted to the immediate vicinity of veins (Hamersley and Carajás districts). At Thabazimbi brecciation is usually found to increase gradually toward the high-grade iron ore, likely reflecting the increasing amount of volume loss (Gutzmer et al., 2005). In the high-grade iron orebodies, dissolution collapse brecciation usually abounds. It is observed at different scales and intensity, ranging from mild mosaic breccias restricted to a hand specimen scale to large volumes of iron ore marked by chaotic collapse brecciation (Netshiozwi, 2002). An open scaffold of microplaty or somewhat coarser grained platy hematite usually forms the cement of such breccias. At the Thabazimbi deposit, abundant brecciation is not restricted to the high-grade iron orebody but is also locally observed in low-grade ores with hydrothermal carbonate cement (Netshiozwi, 2002; Gutzmer 2005). The presence of talc as breccia cement appears to be unique to the Thabazimbi deposit. In Thabazimbi, this is a synore process. In Carajás, brecciation is associated with the early to advanced, including late, stages, with these breccias being cemented by quartz, carbonate, and hematite in the ore-proximal zone; locally, this carbonate cement constitutes close ≥50 vol percent, thereby decreasing the ore grade (Figueiredo e Silva et al., 2008). Interpretations regarding the relationship of such hydrothermal carbonate and talc cement differ considerably and indicate the need for more detailed investigations.

Discussion

Three aspects of the hypogene alteration processes described for the selected case studies above warrant further discussion. These are the (1) significance of the early hydrothermal magnetite, (2) origin of soft ore in the Carajás district, and (3) question of whether iron is introduced or simply remobilized with the Carajás iron deposits as an example.

Hydrothermal magnetite

Regardless of the iron xide sequence, magnetite is an early oxide phase in the alteration paragenesis (Tables 1, 2), followed by various types of hematite. The South African deposits are an exception, since in these magnetite is considered to have formed as a prealteration phase (Figs. 9, 11). The formation of hydrothermal magnetite suggests that the early-stage fluid had a f_{O_2} at the magnetite equilibrium conditions (Lobato et al., 2005a) and interacted with rocks that variably contained dominant ferric (Carajás) or ferrous (Mount Tom Price) phases.

Silica leaching

The leaching of SiO_2 can be attained by solutions that are oxidizing enough to render ferric oxide immobile; such is the case for hydrothermal fluids or low-temperature supergene fluid. In the case of hydrothermal fluids mildly alkaline and silica-undersaturated conditions enhance effectively the SiO_2 transport (Barnes, 1997). Remobilization of SiO_2 to form quartz-rich veins, paired by a distinct increase in porosity (documented for the Carajás district, Thabazimbi and Zeekoebaart), lend important support to the concept of SiO_2 leaching. Carbonates, silicates, and sulfide minerals are conspicuously absent from the oxidized BIF. This model would require very high fluid/rock ratios and is thus likely to apply to orebodies emplaced along major dilational structures acting as important fluid pathways. The Zeekoebaart prospect may be regarded as the most plausible example for simple SiO_2 leaching. For Carajás, Lobato et al. (2005a) and Figueiredo e Silva et al. (2008) suggest relatively hot magmatic fluids interacting with a colder, exhumed rock sequence, to account for SiO_2 leaching, with some parallels to a model proposed by Gruner (1930, 1937) for the Lake Superior region.

Hypogene soft ore in Carajás

We propose that a hypogene, porous hard to soft, but relatively cohesive hematite ore evolved as a result of porosity enhancement and quartz-chert leaching at Carajás. The ore preserves martite; microplaty and anhedral hematite partially fills the existing pores (Lobato et al., 2005a, b). Following early-stage jaspilite alteration, with significant SiO_2 leaching, jasper discoloring and porosity development (Fig. 2), vugs were initially filled predominantly by microplaty hematite as seen in figure 9E of Figueiredo e Silva et al. (2008). The hard hematite ore that is enveloped by this soft ore, which itself is in contact with jaspilite (fig. 6 of Figueiredo e Silva et al., 2008), would thus represent an evolutionary stage of the hypogene soft ore., This is because it developed due to advanced cavity filling via precipitation of additional microplaty (after martite), platy (Fig. 1H), and also euhedral and comb-textured, bladed and/or tabular hematites (Fig. 1M-O), with the latter ones especially in veins. The possibility for a hypogene origin for soft hematite ores was also indicated by Gruner (1937) and Mann (1953) for the Lake Superior region and the Marquette and Gogebic ranges, respectively.

Conclusions

Comparison of hydrothermal alteration at Carajás, Hamersley, Thabazimbi, and Zeekoebaart revealed important similarities (Tables 1, 2), including: (1) a similar paragenetic sequence of iron oxides, marked by an abundance of open-space filling and replacement textures; (2) the lack of a penetrative fabric of alteration lithologic units and high-grade ores; and (3) the importance of porosity and brecciation to accommodate volume loss.

Marked differences include the following:

1. Carbonate metasomatism in hydrothermal alteration zones: Hydrothermal carbonate is observed in all three case studies and located in veins and breccias. At Tom Price in distal and intermediate alteration zones, in the Thabazimbi deposits in the proximal alteration zone, and in Carajás in the distal and proximal alteration zones in jaspilites. The Mount Whaleback deposit lacks significant carbonate alteration; however, this may be due to lack of information on the deeper

parts of the orebody. At Tom Price the transformation of carbonate-altered BIF in the intermediate alteration zones to high-grade martite-microplaty hematite ore in the proximal alteration zone is due to oxidation of magnetite and leaching of carbonate. In contrast, at Carajás dolomite and kutnahorite veins and breccias are stable in the proximal alteration zone and locally replace martite-rich layers. Significant amount of siderite as the dominant carbonate species is only recorded in the Hamersley iron deposits.

2. Silicate-alteration phases such as stilpnomelane are only present where hydrothermally altered BIF is part of a sedimentary basin, such as the Hamersley basin or the Asbesheuwels Subgroup in the Griqualand West subbasin, and the laterally correlative Penge Formation of the Transvaal subbasin of the Transvaal Supergroup. The basalt-hosted Carajás iron deposits are devoid of these alteration minerals.

3. Chlorite, talc, white mica, and albite are part of the alteration assemblage in basalt-hosted iron deposits, for example, in Carajás (Tables 1B, 2B) or mafic dikes that are spatially and temporally associated with iron mineralization, for example, in the Hamersley province.

4. Hydrothermal sulfides present in significant quantities are recorded only in Carajás. Their appearance may relate to the more sulfur-rich basaltic wall rocks (Zucchetti, 2007) and/or to the magmatic hydrothermal fluids postulated to be one major fluid source for the ore-forming event in the Carajás district (Lobato et al., 2005a, b; Figueiredo e Silva et al., 2008). Possible similarities of these iron ore-forming fluids with those associated with the formation of hydrothermal magmatic deposits, dominantly rich in the ore elements Cu and Au, and that are present in the same district (including IOCG-type deposits), need to be carefully evaluated (Lobato et al., 2005a, b).

Exploration Significance

The acknowledgment that complex and possibly polyphase hydrothermal systems, including both ascending and descending hydrothermal fluids, cause the transformation of BIF (including jaspilite) to high-grade hematite-martite ore has significant implications for the exploration of blind orebodies (Hagemann et al., 2006). Structures such as fault zones, shear zones, and/or isoclinal folds serve as fluid pathways for the hydrothermal fluids and, therefore, can be used to constrain areas of maximum fluid flow and associated hydrothermal alteration and iron mineralization. Hydrothermal alteration minerals, such as carbonates, chlorite, and magnetite, may form distinct alteration zones, both lateral and above and below the high-grade iron orebodies, thereby providing a hydrothermal alteration footprint that can be used in the search for new high-grade iron deposits or extensions of existing orebodies; in particular, those that are located concealed below cover sequences or nonmineralized BIF. These hydrothermal alteration indicator minerals in both nonmineralized BIF and surrounding wall rocks can thus be used as vectors toward iron mineralization.

In the Hamersley-type deposits, the identification of hydrothermal alteration minerals, veins, and breccias at the contact between nonmineralized BIF and low- and high-grade iron ore are commonly subtle and require detailed mapping, core logging, and petrographic and textural work. Of particular importance is the petrography and geochemistry of carbonate and quartz-carbonate veins. With increasing proximity to high-grade iron ore, the carbonate species change from siderite to ankerite and calcite to dolomite at the Mount Tom Price (Fig. 7) and Paraburdoo deposits, respectively. The manganese content of the carbonates (up to 10 wt %) also increases with increased proximity to high-grade ore (Hagemann et al., 2006).

The hydrothermal alteration of dolerite dikes that are spatially and temporally related to iron mineralization (cf. Taylor et al., 2001) provide another vector toward iron ore mineralization. The dikes commonly display intense talc-chlorite alteration, particularly where in close proximity to the iron orebodies. Although rarely containing significant iron enrichment, they bound the mineralization at several orebodies at the Paraburdoo, Channar, and Mount Tom Price deposits (Dalstra et al., 2005; Taylor et al., 2005, Thorne et al., 2006). The identification of quartz ± carbonate veins and/or breccias that are emplaced contemporaneous with the iron mineralizing event, and often in distal alteration zones, serves as another vector toward iron mineralization.

In the Carajás deposits the contact between nonmineralized and hydrothermally altered and mineralized jaspilites can be gradational. In this case a distal alteration zone can be defined by magnetite, quartz, and carbonate veins that may locally be layer-parallel or crosscutting with respect to the jaspilite (Fig. 3). The intermediate alteration zone is made up of variable proportions of quartz ± hematite veins, magnetite, microplaty hematite, anhedral-subhedral hematite, euhedral-tabular hematite, and locally sulfides and gold (Fig. 3). Hydrothermal alteration minerals and zonation are particularly well distributed in the basalts that surround the nonmineralized jaspilites and iron orebodies (Zucchetti et al., 2007; Figueiredo e Silva et al., 2008). The distal alteration zone, which contains carbonate and locally hematite, can extend up to 80 m away from the iron orebodies and, therefore, can be used as vectors toward iron mineralization. The intermediate alteration zones are characterized by chlorite, quartz, albite, white mica, carbonate, hematite, and traces of magnetite and sulfides (Fig. 4). Therefore, any drilling program that aims to identify either deep extensions of existing orebodies or new, concealed iron mineralization can utilize these distal alteration minerals and veins as vectors toward iron mineralization.

Geologic mapping, core logging, and understanding key hydrothermal alteration (i.e., indicator) minerals in three dimensions may provide important constraints on the geometry of the hydrothermal footprint of any given iron mineral system (Hagemann et al., 2006; Figueiredo e Silva et al., 2008; Thorne et al., 2008). Therefore, the rapid identification of these indicator minerals in the field and in diamond core is crucial. Besides sound petrographic analyses, methods such as PIMA analyses, airborne HyMap™, and satellite ASTER imagery, both handheld on diamond core and airborne have been developed in the past years. These techniques significantly assist not only in identifying these often fine-grained hydrothermal alteration minerals but also constraining their three-dimensional distributions. The analyses of diamond core using the new Fe HyLogger™ system can assist in the rapid identification and calculation of modal mineralogy, rapidly differentiating between minerals and products of

chemical weathering (e.g., clay and goethite). The presence and distribution of the latter is particularly important in exploring in arid areas or areas with significant lateritic cover, such as in Brazil, India, and Australia (Morris, 1985).

Future Work

This contribution highlights the limited amount of detailed mineralogical and petrographic studies of high-grade BIF-hosted iron deposits that take cognizance of the presence of alteration halos. Detailed delineation of the distribution of distinct alteration mineral assemblages are required to delineate the true size and extent of distinct, mappable alteration zones in three dimensions both in BIF and wall rocks. The processes that characterize the transformation of unaltered to hydrothermally altered BIF need to be better constrained, in particular with respect to the role of iron-rich carbonates (siderite and ankerite) that often abound in unaltered BIF protolith or ore formation (Hamersley). Detailed alteration studies need to be extended to deposits and districts that have been affected by high-grade, sometimes polyphase regional metamorphism, i.e., the Quadrilátero Ferrífero (Rosière and Rios, 2004; Rosière et al., 2008) and Krivoy Rog districts (Plotnikov, 1994; Dalstra and Guedes, 2004). Finally, the possibility that not all porous, friable and soft high-grade iron ores are supergene in origin, as suggested for the Carajás district by Lobato et al. (2005a, b), needs to be further investigated.

Geochronological data are urgently required to advance our understanding of the different alteration zones, as defined in this study, and their relationship to each other. Case in point is the strongly divergent opinions regarding the genetic significance of hydrothermal carbonate metasomatism. Geochronological constraints can be obtained by radiogenic isotope dating of hydrothermal alteration minerals (i.e., SHRIMP U-PB dating of monazite in high-grade ores from Mount Tom Price, Rasmussen et al., 2007). Alternatively, ores and alteration assemblages may be indirectly dated by careful paleomagnetic analyses (cf. de Kock et al., 2008).

Acknowledgments

We thank the many iron mining and exploration companies in Australia, Brazil (Vale), and South Africa that allowed us to access their field camps, databases, and analyses of rocks. Without their logistical and intellectual support, this paper would not have been written and our ongoing research would have not been possible. RCFS and MZ were recipients of scholarships from Coordenação de Aperfeiçoamento de Pessoal de Nível Superior (CAPES) as part of their Ph.D. degrees. LML acknowledges her grant from the Conselho Nacional de Desenvolvimento Científico e Tecnológico (CNPq). Jens Gutzmer significantly contributed to this paper with very detailed information on the South African iron deposits and also greatly assisted in straightening out our arguments; his editing of an earlier version was very much appreciated. Thanks are due to Franciscus J. Baars for revising the English. Finally, we would like to express our appreciation to the reviewers Nick Oliver and Phil Brown and the editorial staff of this special volume, including Steve Kesler, for constructive criticism of an earlier version of this manuscript.

REFERENCES

Barley, M.E., Pickard, A.L., and Sylvester, P.J., 1997, Emplacement of a large igneous province as a possible cause of banded iron formation 2.45 billion years ago: Nature, v. 385, p. 55–58.

Barley, M.E., Pickard, A.L., Hagemann, S.G., and Folkert, S.L., 1999, Hydrothermal origin for the 2 billion year old giant iron ore deposit, Hamersley province, Western Australia: Mineralium Deposita, v. 34, p. 784–789.

Barnes, H.L., ed., 1997, Geochemistry of hydrothermal ore deposits (3rd ed.): New York, John Wiley and Sons, 972 p.

Barros, C.E.M., Macambira, M.J.B., and Barbey, P., 2001, Idade de zircão do Complexo Granítico Estrela: Relações entre magmatismo, deformação e metamorfismo na Província Metalogenética Carajás [ext. abs.]: Simpósio de Geologia da Amazônia, 7th, Belém, Brazil, Proceedings, p. 17–20.

Beisiegel, V.R., 1982, Distrito ferrífero da Serra dos Carajás: Simpósio de Geologia da Amazônia, 1st, Belém, Brazil, Proceedings, p. 21–46.

Beukes, N.J., 1983, Paleoenvironmental settings of iron formation in the depositional basin of the Transvaal Supergroup, South Africa, *in* Trendall, A.F., and Morris, R.C., Iron-formations: Facts and problems: Amsterdam, Elsevier, p. 131–209.

Beukes, J.B., and Gutzmer, J., 2008, Origin and paleoenvironmental significance of major iron formations at the Archean-Paleoproterozoic boundary: Reviews in Economic Geology, v. 15, p. 5–48.

Beukes, N.J., Gutzmer, J., and Mukhopadhyay, J., 2002, The geology and genesis of high-grade hematite iron ore deposits: Australasian Institute of Mining and Metallurgy, Publication Series 7, p. 23–29.

——2003, The geology and genesis of high-grade hematite iron ore deposits: Transactions of the Institute of Mining and Metallurgy, sec. B, v. 112, p. 18–25.

Blake, T.S., and Barley, M.E., 1992, Tectonic evolution of the Late Archean to Early Proterozoic Mount Bruce Megasequence, Western Australia: Tectonics, v. 11, p. 1415–1425.

Brown, M.C., Oliver, N.H.S, and Dickens, G.R., 2004, Veins and hydrothermal fluid flow in the Mount Whaleback iron ore district, eastern Hamersley province, Western Australia: Precambrian Research, v. 128, p. 441–474.

Clout, J.M.F., 2005, Iron formation-hosted iron ores in the Hamersley province of Western Australia: Australasian Institute of Mining and Metallurgy Publication Series 8, p. 9–19.

Cochrane, N., 2003, Phosphorus behavior during banded iron-formation enrichment: Unpublished B.Sc. (Honours) thesis, Brisbane, University of Queensland, 86 p.

Dall'Agnol, R., and de Oliveira, D.C., 2007, Oxidized, magnetite-series, rapakivi-type granites of Carajás, Brazil: Implications for classification and petrogenesis of A-type granites: Lithos, v. 93, p. 215–233.

Dall'Agnol, R., Teixeira, N.P., Rämo, O.P., Moura, C.A.V., Macambira, M.J.B., and de Oliveira, D.C., 2005, Petrogenesis of the Paleoproterozoic rapakivi A-type granites of the Archean Carajás metallogenic province, Brazil: Lithos, v. 80, p. 121–129.

Dalstra, H.J., 2005, Structural controls of bedded iron ore in the Hamersley province, Western Australia—an example from the Paraburdoo Ranges: Australasian Institute of Mining and Metallurgy Publication Series 8, p. 49–55.

Dalstra, H.J., and Guedes, S., 2004, Giant hydrothermal hematite deposits with Mg-Fe metasomatism: A comparison of the Carajás, Hamersley, and other iron ores: Economic Geology, v. 99, p. 1793–1800.

Dalstra, H.J., Harding, A.E. and Taylor, D., 2002, Genesis of high-grade hematite orebodies of the Hamersley province—a reply: Economic Geology, v. 97, p. 179–181.

de Kock, M.O., Evans, D.A.D., Gutzmer, J., Beukes, N.J., and Dorland, H.C., 2008, Origin and timing of banded iron formation-hosted high-grade hard hematite deposits—a paleomagnetic approach: Reviews in Economic Geology, v. 15, p. 49–71.

Dias, G.S., Macambira, M.J.B., Dall'Agnol, R., Soares, A.D.V., and Barros, C.E.M., 1996, Datação de zircões de *sill* de metagabros: comprovação da idade arqueana da Formação Águas Claras, Carajás-Pará [ext. abs.]: Simpósio de Geologia da Amazônia, 5th, Belém, Brazil, Proceedings, p. 376–379.

DOCEGEO, 1988, Revisão litoestratigráfica da Província Mineral Mineral de Carajás: Congresso Brasileiro de Geologia, 35th, Sociedade Brasileira de Geologia: Belém, Brazil, Annex to Proceedings, p. 11–54.

Eriksson, P.G., Hattingh, P.J., and Altermann, W., 1995, An overview of the geology of the Transvaal Sequence and Bushveld Complex, South Africa: Mineralium Deposita, v. 30, p. 98–111.

Figueiredo e Silva, R.C., 2004, Caracterização petrográfica e geoquímica de jaspilitos e minérios de ferro, Província Mineral Carajás, Pará: Implicações para a mineralização de ferro: Unpublished M.Sc. dissertation, Belo Horizonte, Brazil, Universidade Federal de Minas Gerais, 151 p.

Figueiredo e Silva, R.C., Lobato, L.M., Rosière, C.A., Guedes, S.C., Monteiro, A.M., Meireles, H., and Matias, P.H., 2004, Estudos petrográficos microscópicos e geoquímicos em jaspilitos e minérios de ferro dos depósitos N1, N4E, N4W e N5E, Província Mineral Carajás, Pará [abs.]: Simpósio Brasileiro de Exploração Mineral, 1st, Ouro Preto, Brazil, Agência para o Desenvolvimento Tecnológico da Indústria Mineral Brasileira (ADIMB), CD-ROM.

Figueiredo e Silva, R.C., Hagemann S.C., Lobato, L.M., and Venemann T., 2007, Iron oxide paragenesis, quartz vein chronology, and hydrothermal fluid evolution at the giant North Range Carajás iron deposits in Brazil [ext. abs.]: Biennial Meeting of the Society for Geology Applied to Mineral Deposits 9th, SGA, Dublin, Ireland, Proceedings, v. 2, p. 1223–1226.

Figueiredo e Silva, R., Lobato, L.M., Rosière, C.A., Zucchetti, M., Hagemann, S., Zucchetti, M., Baars, F.J., Morais, R., and Andrade, I., 2008, Hydrothermal origin for the jaspilite-hosted, giant Serra Norte iron ore deposits in the Carajás mineral province, Para State, Brazil: Reviews in Economic Geology, v. 15, p. 255–290.

Galarza, M.A.T, Macambira, M.J.B., Maurity, C.W., and Meireles, H.P., 2001, Idade do depósito Igarapé Bahia (Província Mineral de Carajás, Brasil), com base em isótopos de Pb [ext. abs.]: Simpósio de Geologia da Amazônia, 7th, Belém, Brazil, Proceedins, p. 116–119.

Gibbs, A.K., Wirth, K.R., Hirata, W.K., and Olszewski, W.J., Jr., 1986, Age and composition of the Grão Pará Group volcanics, Serra dos Carajás: Revista Brasileira de Geociências, v. 16, p. 201–211.

Gruner, J.W., 1930, Hydrothermal oxidation and leaching experiments: Their bearing on the origin of Lake Superior hematite-limonite ores: Part II: Economic Geology, v. 25, p. 837–867.

——1937, Hydrothermal leaching of iron ores the Lake Superior type—a modified theory: Economic Geology, v. 32, p. 121–130.

Guedes, S.C., Rosière, C.A., Barley, M., and Lobato, L.M., 2002, The importance of carbonate alteration associated with the Carajás high-grade hematite deposits, Brazil: Australasian Institute of Mining and Metallurgy Publication Series 7, p. 63–66.

Gutzmer, J., and Beukes N.J., 1998, Earliest laterites and possible evidence for terrestrial vegetation in Paleoproterozoic: Geology, v. 26, p. 263–266.

Gutzmer, J., Netshiozwi, S., and Beukes, N.J., 2002, Hydrothermal origin of high-grade iron orebodies hosted by the Paleoproterozoic Penge Iron Formation, Thabazimbi, South Africa [abs]: International Sedimentological Congress, 16th, Auckland Park, Abstract Volume 2002, CD-ROM.

Gutzmer, J., Beukes, N.J., Kock, M.O. de, and Netshiozwi, S.T., 2005, Origin of high-grade iron ores at the Thabazimbi deposit, South Africa: Australasian Institute of Mining and Metallurgy Publication Series 8, p. 99–110.

Gutzmer, J., Mukhopadhyay, J., Beukes, N.J., Pack, A., Hayashi, K., and Sharp, Z.D., 2006, Oxygen isotope composition of hematite and genesis of high-grade BIF-hosted iron ores: Geological Society of America, Memoir 198, p. 257–268.

Hagemann, S.G., Barley, M.E., Folkert, S.L., Yardley, B.W., and Banks, D.A., 1999, A hydrothermal origin for the giant Tom Price iron ore deposit, *in* Stanley, C.J. et al., eds., Mineral deposits: Processes to processing: Rotterdam, Balkema, p. 41–44.

Hagemann, S.G., Rosière, C.A., Lobato, L.M., Baars, F.J., Zucchetti, M., and Figueiredo e Silva, R.C., 2006, Controversy in genetic models for high-grade BIF related Fe deposits: Unifying or discrete model(s)?: Transactions of the Institute of Mining and Metallurgy, sec. B, v. 115, p. 147–151.

Harding, C.J., 2004, Origin of the Zeekoebaart and Nauga East high-grade iron ore deposits, northern Cape Province, South Africa: Unpublished M.Sc. thesis, Auckland Park, South Africa, Rand Afrikaans University, 128 p.

Harmsworth, R.A., Kneeshaw, M., Morris, R.C., Robinson, C.J., and Shrivastava, P.K., 1990, BIF-derived iron ores of the Hamersley province: Australasian Institute of Mining and Metallurgy Monograph 14, p. 617–642.

Klein, C., 2005, Some Precambrian banded iron-formations (BIFs) from around the world: Their age, geologic setting, mineralogy, metamorphism, geochemistry, and origins: American Mineralogist, v. 90, p. 1473–1499.

Lobato, L.M., Rosière, C.A., Baars, F.J., Figueiredo e Silva, R.C., Zucchetti, M., Rios, F.J., Seoane, J.C.S., Pimentel, M., Lindenmayer, Z.G., Mendes, G.E., and Maciel, A.L., 2004, Timing of hydrothermal iron mineralisation, Carajás province, PA [abs.]: Simpósio Brasileiro Exploração Mineral, 1st, Ouro Preto, Brazil, Agência para o Desenvolvimento Tecnológico da Indústria Mineral Brasileira (ADIMB), CD-ROM.

Lobato, L.M., Figueiredo e Silva, R.C., Rosière, C.A., Zucchetti, M., Baars, F.J., Seoane, J.C.S., Rios, F.J., and Monteiro, A.M., 2005a, Hydrothermal origin for the iron mineralisation, Carajás province, Pará State, Brazil: Australasian Institute of Mining and Metallurgy Publication Series 8, p. 99–110.

Lobato, L.M., Rosière, C.A., Figueiredo e Silva, R.C., Zucchetti, M., Baars, F.J., Seoane, J.C.S., Rios, F.J., Pimentel, M., Mendes, G.E., and Monteiro, A.M., 2005b, A mineralização hidrotermal de ferro da Província Mineral de Carajás—controle estrutural e contexto na evolução metalogenética da província, *in* Marini, O.J., de Queiroz, E.T., and Ramos, B.W., eds., Caracterização de depósitos minerais em distritos mineiros da Amazônia: Brasília, Brazil, Departamento Nacional da Produção Mineral (DNPM)/Fundo Setorial Mineral (CT-Mineral/FINEP)/Agência para o Desenvolvimento Tecnológico da Indústria Mineral Brasileira (ADIMB), p. 25–92.

Lobato, L.M., Figueiredo e Silva, R.C., Hagemann, S., and Thorne, W., 2007, Mineralizing fluid evolution and REE patterns for the hydrothermal Carajás iron ores, Brazil, and for selected Hamersley iron deposits, Australia. [ext. abs.]: Biennial Meeting of the Society for Geology Applied to Mineral Deposits, 9th, SGA, Dublin, Proceedings, v. 2, p. 1227–1230.

Machado, N., Lindenmayer, Z., Krogh, T.E., and Lindenmayer, D., 1991, U-Pb geochronology of Archean magmatism and basement reactivation in the Carajás area, Amazon shield, Brazil: Precambrian Research, v. 49, p. 329–354.

MacLeod, W.N., 1966, The geology and iron deposits of the Hamersley Range area, Western Australia: Geological Survey of Western Australia Bulletin 117, 170 p.

Mann, V.I., 1953, The relation of oxidation to the origin of soft iron ores of Michigan: Economic Geology, v. 48, p. 251–281.

Martin, D.McB, Li, Z.X., Nemchin, A.A., and Powell, C.McA., 1998, A pre-2.2 Ga age for giant hematite ores of the Hamersley province, Australia: Economic Geology, v. 93, p. 1084–1090.

Meirelles M.R., 1986, Geoquímica e petrologia dos jaspilitos e rochas vulcânicas associadas, Grupo Grão-Pará, Serra dos Carajás, Pará: Unpublished M.Sc. thesis, Instituto de Geociências, Universidade de Brasília, 171 p.

Meirelles, M.R., and Dardenne, M.A., 1991, Vulcanismo basáltico de afinidade shoshonítica e ambiente de arco arqueano, Grupo Grão-Pará, Serra dos Carajás, Pará: Revista Brasileira de Geociências, v. 21, p. 41–50.

Morris, R.C., 1985, Genesis of iron ore in banded iron-formation by supergene and supergene-metamorphic processes—a conceptual model, *in* Wolf, K.H., ed., Handbook of strata-bound and stratiform ore deposits: Amsterdam, Elsevier, v. 13, p. 73–235.

Mougeot, R., 1996, Estude de la limite Archeen-Proterozoique et des mineralizations Au, +/_U associees. Exemples de la region de Jacobina (Etat de Bahia, Bresil) et de Carajás (Etat de Para, Bresil), Unpublished thesis, University of Montpellier II, 301 p.

Müller, G.M., Krapez, B., Barley, M.E., and Fletcher, I.R., 2005, Giant iron-ore deposits of the Hamersley province related to the breakup of Paleoproterozoic Australia: New insights from in situ SHRIMP dating of baddeleyite from mafic intrusions: Geology, v. 33, p. 577–580.

Netshiozwi, S.T., 2002. Origin of high-grade hematite ores at Thabazimbi mine, Limpopo province, South Africa: Unpublished M.Sc. thesis, Auckland Park, South Africa, Rand Afrikaans University, 135 p.

Netshiozwi, S.T., Beukes, N.J., and Gutzmer, J., 2002, Petrographic constraints on the transformation of the Penge Iron Formation into high-grade hematite ores at Thabazimbi mine, Limpopo province [abs]: International Sedimentological Congress, 16th, Auckland Park, Abstract Volume 2002, CD-ROM.

Oliver, N.H.S., Cleverley, J.S., Dipple, G.M., and Broadbent, G.C., 2007, Giant BIF-hosted hematite ores: Geochemical and isotopic modeling of meteoric and basinal fluid-rock reactions. [ext. abs.]: Biennial Meeting of the Society for Geology Applied to Mineral Deposits, 9, SGA, Dublin, Proceedings, v. 2, p. 1219–1222.

Pickard, A.L., 2003, SHRIMP U-Pb zircon ages for the Palaeoproterozoic Kuruman Iron Formation, northern Cape Province, South Africa: Evidence for simultaneous BIF deposition on Kaapvaal and Pilbara cratons: Precambrian Research, v. 125, p. 275–315.

Plotnikov, A.V., 1994, Tectonical structure and development of the Krivoy Rog ore region as a deep fault zone: Geotectonics, v. 28, p. 121–135 (English Translation).

Powell, C.M., Oliver, N.H.S., Li, Z.X., Martin, D.M., and Ronaszeki, J., 1999, Synorogenic hydrothermal origin for giant Hamersley iron oxide ore bodies: Geology, v. 27, p. 175–178.

Rasmussen, B., Fletcher, I.R., Muhling, J.R., Thorne, W.S., and Broadbent, G.C, 2007, Prolonged history of episodic fluid flow in giant hematite ore bodies: Evidence from in situ U-Pb geochronology of hydrothermal xenotime: Earth and Planetary Science Letters, v. 258, p. 249–259.

Reed, M.H., 1997, Hydrothermal alteration and its relationship to ore fluid composition, *in* Barnes, H.L., ed., Geochemistry of hydrothermal ore deposits: New York, John Wiley and Sons, p. 303–365.

Ridley, M, 1999, Evidence for the hydrothermal origin of iron ore, Southern Ridge, Mount Tom Price, Western Australia: Unpublished B.Sc. thesis, Nedlands, University of Western Australia, 93 p.

Rosière, C.A., and Rios, F.J., 2004, The origin of hematite in high-grade iron ores based on infrared microscopy and fluid inclusion studies: the example of the Conceição mine, Quadrilátero Ferrífero, Brazil: Economic Geology, v. 99, p. 611–624.

Rosière, C.A., Baars, F.J., Seoane, J.C.S., Lobato, L.M., da Silva, L.L., de Souza, S.R.C., and Mendes, G.E., 2006, Structure and iron mineralisation of the Carajás province: Transactions of the Institute of Mining and Metallurgy, sec. B, v. 115, p. 126–136.

Rosière, C.A., Spier, C.A., Rios, F.J., and Suckau, V.E., 2008, The itabirites of the Quadrilátero Ferrífero and related high-grade iron ore deposits: An overview: Reviews in Economic Geology, v. 15, p. 223–254.

Santos, J.O.S., 2003, Geotectônica dos Escudos das Guianas e Brasil-Central, *in* Bizzi, L.A., Schobbenhaus, C., Vidotti, R.M., and Gonçalves, J.H. eds., Geologia, Tectônica e Recursos Minerais do Brasil: Brasília, Brazil, Companhia de Pesquisa e Recursos Minerais, p. 169–226.

Silva, G.G., Lima, M.I.C., Andrade, A.R.F., Issler, R.S., and Guimarães, G., 1974, Geologia das folhas SB-22 Araguaia e parte da SC22 Tocantins, Levantamento de Recursos Minerais, Projeto Radam, Brazil.

Strauss, C.A., 1964, The iron ore deposits at Thabazimbi, Transvaal, *in* Haughton, S.H., ed., Geology of some ore deposits of southern Africa: Johannesburg, Geological Society of Southern Africa, p. 383–392.

Tassinari, C.C.G., Bettencourt, J.S., Geraldes, M.C., Macambira, M.J.C., and Lafon, J.M., 2000, The Amazonian craton, in tectonic evolution of South America: International Geological Congress, 31st, Rio de Janeiro, Brazil, Proceedings, p. 41–99.

Taylor, D., Dalstra, H.J., Harding, A.E., Broadbent, G.C., and Barley, M.E., 2001, Genesis of high-grade hematite orebodies of the Hamersley province, Western Australia: Economic Geology, v. 96, p. 837–875.

Teixeira, J.B.G., Ohmoto, H., and Eggler, D.H., 1997, Elemental and oxygen isotope variations in Archean mafic rocks associated with the banded iron-formation at the N4 iron deposit, Carajás, Brazil, *in* Costa, M.L., and Angélica, R.S., coords., Contribuições à Geologia da Amazônia, FINEP/SBG, Brazil, p. 161–203.

Thorne, W.S., 2001, Genesis of the North deposit, Mount Tom Price: Unpublished B.Sc. thesis, Perth, Australia, University of Western Australia.

Thorne, W.S., Hagemann, S.G., and Barley, M.E., 2004, Petrographic and geochemical evidence for hydrothermal evolution of the North deposit, Mount Tom Price, Western Australia: Mineralium Deposita, v. 39, p. 766–783.

——2005, Hydrothermal alteration zonation and fluid chemistry of the Southern Ridge and North deposits at Mount Tom Price: Australasian Institute of Mining and Metallurgy Publication Series 8, p. 151–158.

Thorne, W.S., Hagemann, S.G., and Vennemann T., 2007, Oxygen isotope compositions of iron oxides from high-grade (>63 wt % Fe) BIF-related iron deposits of the Pilbara province, Western Australia [ext. abs.]: Biennial Meeting of the Society for Geology Applied to Mineral Deposits, 9th, SGA, Dublin, Ireland, Proceedings, v. 2, p. 1215–1218.

Thorne, W., Hagemann, S., Webb, A., and Clout, J., 2008, Banded iron formation-related iron ore deposits of the Hamersley province, Western Australia: Reviews in Economic Geology, v. 15, p. 197–221.

Trendall, A.F., and Blockley, J.G., 1970, The iron formations of the Precambrian Hamersley Group, Western Australia, with special reference to the associated crocidolite: Geological Survey of Western Australia, Bulletin, v. 119, 366 p.

Trendall, A.F., Basei, M.A.S., Laeter, J.R., and Nelson, D.R., 1998, SHRIMP zircon U-Pb constraints on the age of the Carajás Formation, Grão Pará Group, Amazon craton: Journal of South American Earth Sciences, v. 11, p. 265–277.

Van Deventer, J.L., Eriksson, P.G., and Synyman, C.P., 1986, The Thabazimbi iron ore deposit, North Western Transvaal, *in* Annhaeusser, C.R., and Maske, S.S. eds., Mineral deposits of southern Africa: Geological Society of South Africa, p. 923–930.

Webb, A.D., Dickens, G.R., and Oliver, N.H.S., 2003, From banded iron-formation to iron ore: Geochemical and mineralogical constraints from across the Hamersley province, Western Australia: Chemical Geology, v. 197, p. 215–251.

——2004, Carbonate alteration of the Upper Mount McRae Shale beneath the martite-microplaty hematite ore deposit at Mount Whaleback, Western Australia: Mineralium Deposita, v. 39, p. 632–645.

Zucchetti, M., 2007, Rochas máficas do Supergrupo Grão Pará e sua relação com a mineralização de ferro dos depósitos N4 e N5, Carajás, (PA): Unpublished Ph.D. thesis, Belo Horizonte, Brazil, Universidade Federal de Minas Gerais, Departamento de Geologia, 125 p.

Zucchetti, M., and Lobato, L.M., 2004, Alteração hidrotermal a hematita das rochas máficas associadas aos depósitos de ferro N4 e N5, Província Mineral de Carajás, PA [abs.]: Simpósio Brasileiro de Exploração Mineral, 1st, Ouro Preto, Brazil, Agência para o Desenvolvimento Tecnológico da Indústria Mineral Brasileira (ADIMB), CD-ROM.

Zucchetti, M., Lobato, L.M., and Hagemann, S.G., 2007, Hydrothermal alteration of basalts that host to the giant Northern Range Carajás iron deposits, Brazil [ext. abs.]: Society for Geology Applied to Mineral Deposits Meeting, 9th, SGA, Dublin, Ireland, Proceedings, v. 2, p. 1231–1234.

ANEXO 5. Relação de amostras estudadas por depósito e procedimentos analíticos aplicados.

Sample	Rock	Vein type	Vein mineral	WR Geoch	Micro-probe (SEM)	LA-ICP-MS	FLINCS	C, O & Sr isotopes in carbonate	Sulphur isotopes	Oxygen isotopes	IC	LA-ICP-MS Flincs	δD in Flincs Qtz
N1F08P54,30	HO			X	X	Mt							
N1F08P61,00	HO			X	X	Mt							
N1F08P66,00	HO			X									
N1F14P197,20	HO			X									
N1F36P25,55	HO	V5	MpHem	X						MpHem	X		
N1F36P28,90	HO			X									
N1F82P107,70	HO	V5	THem		X	THem				THem			
N4E2A2BC	Jp	V1	Cal	X	Cal			C, O & Sr					
N4E3A, 3B, 3C	Jp	V1	Cal	X	Cal			C, O & Sr					
N4EF603P20,70	HO			X									
N4EF603P21,70	HO			X									
N4EF603P30,00	HO			X									
N4EF603P38,60	HO				Kut	Mt &carb							
N4EF603P43,40	HO	V4	Kut(Cal)-Qtz		Kut	Mt & carb	Qtz; Kut	C, O & Sr		Mt	X	X	
N4EF603P53,50	HO	V4	Kut(Cal)-Qtz	X	Kut	Mt & carb		C, O & Sr		Mt	X		
N4EF603P55,50	HO	V5	Qtz-MpHem	X	X	Mt	Qtz				X	X	
N4EF621P50,15	HO	V5	Qtz-MpHem	X	X	Platy hem	Qtz			MpHem	X	X	
N4EF621P55,40	Hematitised mafic	V5	Qtz-MpHem	X			Qtz			Qtz		X	
N4EF703P77,60	Jp	V1b	Kut(Cal)-Qtz-Mag-Py-Ccp		Cal		Cal; Qtz	C-O & Sr (carb)	Pyrite	Mag	X	X	
N4EF703P77,60B	Jp	V1b	Kut(Cal)-Qtz-Mag-Py-Ccp		Cal			C, O & Sr		Mag			
N4EF703P78,10	Jp	V1b	Kut(Cal)-Qtz-Mag-Py-Ccp		Cal		Qtz; Cal		Ccy & Py	Mag			

Sample	Rock	Vein type	Vein mineral	WR Geoch	Micro-probe (SEM)	LA-ICP-MS	FLINCS	C, O & Sr isotopes in carbonate	Sulphur isotopes	Oxygen isotopes	IC	LA-ICP-MS Flincs	δD in Flincs Qtz
N4EF703P89,35	Jp	V1b	Kut(Cal)-Qtz-Mag-Py-Ccp	X	X	Mag, carb							
N4EF703P98,35	Jp	V1b	Kut(Cal)-Qtz-Mag-Py-Ccp		Cal-Dol	Mag, sulphides		C, O & Sr			X		
N4EF703P123,90	Jp		Kut(Cal)-Qtz-Mag-Py-Ccp	X	Kut	Mag, sulphides		C, O & Sr	Pyrite	Mag			
N4EF703P152,90	Jp	V1b	Kut(Cal)-Qtz-Mag-Py-Ccp				Qtz					X	
N4EF703P157,00	Jp	V1b	Kut(Cal)-Qtz-Mag-Py-Ccp				Cal					X	
N4WF588P144,00	Jp	V1a	Qtz	X						Qtz	X		X
N4WF613P168,70	Jp			X									
N4WF617P233,60	Jp	V1a	Qtz				dirty			Qtz	X		X
N4WF617P267,10	Jp	V2a		X									
N4WF618P113,90	Jp	V1	Qtz	X									
N4WF618P161,00	Jp			X									
N4WF618P166,00	Jp			X									
N4WF618P176,80	Jp	V1b	Qtz	X						Qtz	X		X
N4WF618P96,60	Jp			X						Jp			
N4WF660P176,45	Jp	V1a	Qtz	X			Qtz			Qtz		X	
N4WF693P103,00	Jp				X	Mt, KMag				Mag			
N4WF693P108,50	Jp	V2	Qtz-Platy Hem										X
N5EF040P251,80	Hematitised mafic	V5	MpHem		X	Mt & Hem				Mt (MpHem-THem)	X		
N5EF284P27,90	Jp	V5	Qtz-MpHem	X						Jp			
N5EF284P31,00	HO									MpHem(MiHem)	X		

Sample	Rock	Vein type	Vein mineral	WR Geoch	Micro-probe (SEM)	LA-ICP-MS	FLINCS	C, O & Sr isotopes in carbonate	Sulphur isotopes	Oxygen isotopes	IC	LA-ICP-MS Flincs	δD in Flincs Qtz
N5EF284P29,15A				X									
N5EF284P32,65	HO	V5	Qtz-MpHem	X	X	MpHem	Qtz			AHem	X	X	
N5EF318P160,70	HO			X									
N5EF318P172,70	HO	V5	THem	X						THem	X		
N5EF405P19,40	Jp			X									
N5EF405P24,75	Jp	V1	Qtz	X						Qtz			
N5EF414P246,10	HO	V5		X	X	THem				THem			
N5EF414P247,70	HO	V5		X	X	THem				THem			
N5EF414P252,00A	HO	V5		X	X	THem				THem			
N5EF414P251,70	HO									MpHem			
N5EF414P257,00	HO			X	X	AHem & MpHem				AHem			
N5EF439P247,00	HO	V4	Dol-Qtz	X	Dol	AHem & Carb	Dol	C, O & Sr		AHem(Platy Hem)	X	X	
N5EF439P249,80	HO	V4	Dol-Qtz	X	Dol	AHem				AHem			
N5EF440P96,00	HO				X	AHem-SubHem & THem				AHem & THem	X		
N5EF561P156,70	HO			X							X		
N5EF529P100,40	HO	V4	Carb-Qtz	X							X		
N5EF529P120,70	HO	V4	Carb-Qtz	X						AHem	X		
N5EF571P90,55	HO			X							X		
N5EF572P214,30	HO			X						AHem (THem)	X		
N5EF572P267,90	HO	V5	MpHem	X							X		
N5EF572P382,85	HO	V5	MpHem-THem	X						MpHem-THem	X		
N5EF577P222,25	HO			X							X		
N5EF577P232,40	HO										X		
N5EF577P242,25	porous HO	V5		X						AHem(Mt)-MiHem	X		

Sample	Rock	Vein type	Vein mineral	WR Geoch	Micro-probe (SEM)	LA-ICP-MS	FLINCS	C, O & Sr isotopes in carbonate	Sulphur isotopes	Oxygen isotopes	IC	LA-ICP-MS Flincs	δD in Flincs Qtz
N5EF577P257,86	HO			X							X		
N5EF577P261,55	HO-mafic contact			X						Mt(MpHem)	X		
N5EF577P445,40	HO	V5	MpHem-THem	X						MpHem-THem	X		
N5SF700P274,60	HO-mafic contact										X		
N5SF771P182,25	Jp	V3	Hem-Qtz		X	Sub-AHem & THem				MpHem (AHem)			
N5SF686P136,60	HO			X									
N5SF686P152,65	Jp			X									
N5SF686P163,15	Jp	V1b	Mag	X						Mt(MiHem)	X		
N5SF686P163,40	Jp	V3-V2	Qtz-Mag	X						Mt(Mag)	X		
N5SF686P169,90	HO			X									
N5SF686P172,20	HO									THem(Mag)	X		
N5SF817P111,10	BIF				X	Mag				Mag			
N5SF817P158,85	Jp	V3(V2)	Qtz-Hem							Qtz			X
N5SF817P169,50	Jp	V2	Qtz-Hem							Qtz			X
N5SF817P232,75	Jp	V3	Hem-Qtz				Qtz			Platy Hem(THem)		X	
N5SF817P252,45	Jp	V1/V2a	Qtz-Hem							Qtz			X
N5SF817P265,50	Jp	V2b	Qtz-Hem										
N5SF817P271,40	Jp	V2b	Qtz-Hem	X			Qtz			Jp; Qtz	X	X	X
N5SF817P278,85	Jp-mafic contact	V3	Hem-Qtz	X						Qtz			X
N5SF817P296,60	Jp	V2	Qtz	X									X
N5SF817P308,57	HO			X						MpHem			
N5SF817P320,90	Jp	V3	Hem-Qtz							Qtz			X
N5SF817P349,83	HO			X							X		
N5SF817P361,90	Jp	V2	Qtz-Hem	X						Platy Hem			

Sample	Rock	Vein type	Vein mineral	WR Geoch	Micro-probe (SEM)	LA-ICP-MS	FLINCS	C, O & Sr isotopes in carbonate	Sulphur isotopes	Oxygen isotopes	IC	LA-ICP-MS Flincs	δD in Flincs Qtz
N5SF825P235,25	Jp	V1	Qtz		Kut	Mag		C, O & Sr	Ccp	Qtz			
N5SF825P276,40	Jp-mafic contact	V1b	Kut-Qtz-Py		Kut		Kut	C, O & Sr		Jp	X	X	
N5SF825P239,20	Jp	V2	Qtz-Hem								X		
N5SF825P86,05	Jp	V2b	Qtz-Hem							Qtz	X		
N5SF825P88,95	Jp	V2a	Qtz-Hem	X			Qtz					X	
N5SF825P98,55	Jp	V2a	Qtz-Hem										
N5SF836P156,25	Jp	V2a	Qtz-Hem	X						Qtz	X		
N5SF836P157,00	Jp	V2a	Qtz-Hem				Qtz					X	
N5SF836P226,00	Jp	V3	Hem-Qtz								X		
N5SF836P232,45	Porous HO			X							X		
N5SF836P234,80	Porous HO			X						MpHem (AHem)	X		
N5SF837P132,20	Jp	V1a	Qtz	X						Qtz	X		
N5SF897P132,20	Porous HO			X						MpHem(Mt)	X		
N5SF897P183,20	HO			X									
N5SF904P107,65	HO			X							X		
N5SF904P134,85	HO			X						AHem (MpHem)	X		
N5SF910P252,50	HO			X							X		
N5SF910P253,35	HO			X						AHem (MpHem)	X		
N5WF556P121,90	Jp				X	Mt							

Abbreviations: Jp – jaspilite; HO – hard ore; BIF – banded iron formation; Mag – magnetita; mt – martite; MpHem – microplaty hematite; AHem – anhedral hematite; Sub – subhedral; THem – tabular hematita; Qtz – quartz; Cal – calcite; Kut – kutnahorite; Dol – dolomite; Ccp – chalcopyrite; Py – pyrite; WR – whole rock; Flincs – fluid inclusions.
In sample colunm: F – drill hole; P - depth

CURRICULUM VITAE

ROSALINE CRISTINA FIGUEIREDO E SILVA recebeu o título de bacharel em Geologia em 2002, com trabalho final de graduação sobre o depósito orogênico de ouro Engenho D Água localizado no *greenstone belt* arqueano Rio das Velhas, e o título de mestre em 2004, ambos na Universidade Federal de Minas Gerais. Recentemente recebeu o título de doutora, sob supervisão da Profa. Lydia M. Lobato, pesquisando a gênese do minério de ferro tipo compacto dos depósitos de ferro da Província Mineral Carajás, também seu tópico de mestrado. De 2005 a 2006, a doutorando esteve como estudante visitante na University of Western Australia sob supervisão do Prof. Steffen Hagemann, como parte do doutorado. Neste período foram desenvolvidos estudos de inclusões fluidas, análises de isótopos estáveis, as últimas desenvolvidas na Universidade de Hobart e Universidade de Lausanne; ablação a *laser* e íon cromatografia em inclusões fluidas foram realizados na Universidade de Leeds. Ao longo dos anos, Sra. Figueiredo e Silva tem atuado como colaboradora na disciplina de graduação Geologia Econômica. Desde 2000 também tem realizado estudos petrográficos de variados tipos litológicos associados a minérios hidrotermais, como em depósitos de: ouro orogênico e epitermal (região do Quadrilátero Ferrífero, Tocantins, Tapajós & Lavras do Sul); ferro (Serra Norte, Carajás, Mato Grosso, Piauí); e manganês (Morro da Mina). Atualmente é bolsista da FAPEMIG do projeto de pesquisa “Projetos Estruturantes para as Linhas de Atuação do Pólo de Excelência Mineral e Metalúrgico – PEMM”, atuando no Centro de Microscopia da UFMG, sob coordenação de Renato Ciminelli, Prof. Carlos Alberto Rosière e Profa. Karla Balzuweit.